

Thermodynamics of Micellar Lyotropic Liquid Crystals

A DISSERTATION
SUBMITTED TO THE FACULTY OF THE
UNIVERSITY OF MINNESOTA
BY

Ashish Jayaraman

IN PARTIAL FULFILLMENT OF THE REQUIREMENTS
FOR THE DEGREE OF
DOCTOR OF PHILOSOPHY

Mahesh K. Mahanthappa

June 2020

© Ashish Jayaraman, 2020

Acknowledgements

I would like to thank my advisor, Prof. Mahesh Mahanthappa, for his constant enthusiasm, ideas and encouragement throughout my Ph.D. His constant inputs have greatly influenced how I think about science and safety. He has been proactive in pointing out opportunities for my professional development, which have been of immense help throughout my time in graduate school.

I wish to thank all the Mahanthappa group members, present and past, for their continuous support. Their presence made brainstorming ideas, designing experiments, writing manuscripts, and even working night shifts at the Argonne National Lab merry. I appreciate the time and effort put in by Dr. Grayson Jackson, Dr. Sung Kim, and Dr. Carlos Baez-Cotto to train me in the laboratory and teach me all about lyotropic self-assembly. I cherish the shared learning with Beth Dewing, Hongyun Xu, and John O'Donnell since we all joined the group as first years. We have gone through times of joy as well as frustration together and the value of great companionship in those times cannot be overstated. I am thankful to Dr. Tyler Mann for his expertise in organic chemistry, which saved me immeasurable time in the lab, and for our vivid conversations as fume hood neighbors on topics ranging from politics to chess. Michelle Hoard, Mike Karavolias, Ankita Naik, Andreas Mueller, Tianyi Zhu, and Parth Bhide helped me appreciate the joys of being a senior student and pushed me to think about new proposals and experiments tangential to my research, which have helped widen my scientific horizons. I really appreciate the company of all the undergraduate students in the group, including Nick Bible, Karsten Poulsen, Diana Zhang, and Leah Wofford, who made me relearn and test my own understanding of various topics. I was fortunate to supervise Diana and Leah, whose work has been presented in Chapters 3 and 4. From talking about Broadway shows, to finding restaurants with the best cheese curds in Wisconsin, the topics of discussion with my group members have been more disparate than the micelle-size distributions in the Laves phases.

I would also like to thank Dr. Byeongdu Lee, Dr. Xiaobing Zuo, Dr. Soenke Seifert, Janae Ernst, and Alexis Quental for their support while running experiments at Sector 12-IDB at the Advanced Photon Source. My thesis would have been considerably harder without the small-angle X-ray scattering (SAXS) data that I obtained from the synchrotron. I wish to thank Dr. Javier Garcia Barriocanal and Dr. Seema Thakral at the Characterization Facility at the University of Minnesota for managing the Ganesha SAXS instrument and providing me the freedom to experiment with different sample stages and automation procedures. I would also like to thank Dr. Peter Schmidt for training me on the shear cell, which culminated in new interesting findings with respect to the shear behavior of the complex phases, which have not been included in this thesis. I would like to thank Connor Valentine and Prof. Lynn Walker for their collaboration on the shear aspects of the project and for helping me learn a lot about the rheology of the complex phases.

I would also like to thank the entire polymer group including the Bates, Lodge, Reineke, and Morse groups for the use of shared equipment, willingness to discuss ideas, and for being a cohesive unit, which helped removed many hurdles associated with research. Specifically, everyone who has worked on the sphere-forming projects including Dr. Ron Lewis, Aaron Lindsay, Andreas Mueller, Tianyi Zhu, Dr. Akash Arora, Dr. Kyungtae Kim, and Dr. Alice Chang have helped further our understanding about micellar phase formation in different material classes through extensive discussions, collaborative experiments, and even model building using ping-pong balls.

The Department of Chemical Engineering and Materials Science has been home far away from home (12,747 km) and in many ways, became family. First, I would like to thank Julie Prince and Teresa Bredahl for being awesome. I would also like to thank Jennifer Harris, Susan Wermager, and Danny Williams for help with purchasing and ordering. I appreciate the stringent gym routines with Bryan Voigt every morning, where I became truly Minnesotan. The daily lunch with Matheus de Mello, Pavlos Pachidis, and Sagar Udyavara added sparks to even the dullest of days. I will miss

the weekend Indian buffets and movies with Aditya Banerji and Suvam Das. The enjoyable times spent with everyone in my class as well as the rest of the CEMS community has always been rejuvenating and enjoyable and I will always be thankful for that.

I would also like to thank Raju Peripa for looking out for me when I first moved to the U.S.A. His constant encouragement and advice about how to navigate life in a foreign country was helpful. I am extremely grateful for my awesome family back home, including Amma, Appa, and Vignesh, as they have always been there for me through stressful and happy times alike. They have been the most influential people in regard to how I approach life and are the reason why I strive to be a better version of myself every day.

This thesis has been written during the shelter-at-home period of the COVID-19 pandemic. My thoughts and appreciation go out to the nurses, doctors, delivery, sanitation and construction personnel, grocery and restaurant workers, and everyone else who have worked tirelessly to prevent the disease from completely overwhelming life as we know it.

Finally, I am thankful to my committee members Professors Frank Bates, Timothy Lodge, and Kevin Dorfman for their advice and guidance.

Financial Support

I acknowledge financial support from the National Science Foundation (NSF) through grants CHE-1608115 and CHE-1807330. Beth L. Dewing, Diana Y. Zhang and Leah Wofford were supported by the University of Minnesota and the Materials Research Science and Engineering Centers (MRSEC) of the NSF under DMR-1559833 and DMR-1420013. This thesis presents NMR spectra acquired using instruments in the Chemistry NMR laboratory, which is partly supported by the Office of the Director, National Institutes of Health under award number S10OD011952. This content is solely the responsibility of the authors and does not necessarily represent the official views of the National Institutes of Health. Preliminary X-ray scattering patterns were acquired at the Characterization Facility of the University of Minnesota, which receives partial support from the NSF through the MRSEC program (DMR-1420013). Synchrotron small-angle X-ray scattering analyses were performed at the Advanced Photon Source, a U.S. Department of Energy (DOE) Office of Science User Facility operated for the DOE Office of Science by Argonne National Laboratory under contract no. DE-AC02-06CH11357. I also wish to acknowledge the Minnesota Supercomputing Institute (www.msi.umn.edu) at the University of Minnesota for providing computational resources to reconstruct real-space electron densities of the structures shown in this thesis.

Dedication

To தாத்தா and பாட்டி

,

Abstract

Aqueous lyotropic liquid crystals (LLCs) comprise a class of ordered morphologies formed by self-assembly of amphiphiles in water. LLCs assume a variety of concentration- and temperature-dependent structures including lamellae (bilayers), bicontinuous networks, hexagonally-packed cylindrical micelles, and spherical micelles packed on a lattice. Typically, LLC sphere packings include high-symmetry body-centered cubic (BCC), face-centered cubic (FCC), and hexagonally closest-packed (HCP) structures. Recently, a giant tetragonal σ phase containing 30 micelles of five different sizes was discovered in the aqueous LLC self-assembly of dianionic alkylphosphonate surfactants. The σ phase belongs to a class of tetrahedrally close-packed structures called Frank-Kasper (FK) phases, which possess ≥ 7 particles of two or more types situated at 12-, 14-, 15-, or 16-fold coordination environments in low-symmetry unit cells. Ubiquitous in intermetallic alloys, FK phases have been recapitulated in other soft materials including dendritic thermotropic liquid crystals, giant-shape surfactants, and block polymers. The observation of these complex morphologies across different soft material classes stabilized by varying non-covalent interactions begs the question of universality in the principles that govern FK phase formation.

The formation of the σ phase in LLCs of ionic surfactants was rationalized based on maximizing counterion-mediated intermicellar cohesion, while minimizing expensive local variations in headgroup-counterion solvation. However, molecular design principles guiding FK phase selection in LLCs are lacking. FK phases are periodic approximants of dodecagonal quasicrystals (DDQCs), structures which possess 12-fold rotational symmetry yet lack translational symmetry. DDQCs have been observed in self-assembled micelles of neat, neutral amphiphiles in regions of phase space adjacent to FK morphologies. However, quasiperiodic ordering of micelles in LLC self-assembly is surprisingly unknown given the pervasiveness of the periodic approximants.

This thesis elucidates the amphiphile structural motifs that stabilize FK phases and related

DDQCs in aqueous LLCs. We first establish the molecular design criteria for the formation of σ phases in ionic amphiphiles by investigating the LLC phase behavior of alkylmalonate dianionic surfactant analogous to the alkylphosphonate amphiphiles. FK phase formation was observed to depend on the nature of the counterions and length of the alkyl tail. Using real-space electron density reconstructions, we find that the preference for local micellar symmetry in the σ phase is dictated by the extent of headgroup-counterion association. We next report the formation of a well-ordered DDQC in oil-swollen micelles of alkylphosphonate surfactants, and we use high-resolution small-angle X-ray scattering data to determine the space group symmetry of this quasiperiodic structure. The formation of the DDQC was contingent on the sample-processing protocols employed, indicating the metastability of this mesophase.

We further illustrate the non-specific nature of FK phase formation in soft materials by the discovery of a σ phase on self-assembly of hydrated non-ionic polyethylene-*block*-poly(ethylene oxide) surfactants. For the hydroxyl terminated surfactant, access to the σ phase depends on sample thermal history, indicating its metastability with respect to the A15 structure. Finally, the hydroxyl end-group of the amphiphile was synthetically modified with ionic and strongly H-bonding moieties. We find that strongly interacting terminal groups provide increased temperature- and composition-windows of σ phase stability. Moreover, cationically-terminated oligomers surprisingly self-assembled into a DDQC. These findings are rationalized based on the drive to minimize local variations in intramicellar chain-chain interactions, while maximizing intermicellar cohesion.

These fundamental studies of the thermodynamics of micellar morphologies in solvated amphiphiles provide insights into the general underlying principles which stabilize these complex packings of soft reconfigurable particles.

Preface

Chapter 1 includes a thorough overview of complex micellar phases in different classes of soft materials with varied interaction parameters and length-scales of self-assembly. Chapter 2 explores molecular design criteria of ionic surfactants to access Frank-Kasper phases upon minimal hydration. The chapter has been reprinted with permission from Jayaraman A. & Mahanthappa M. K., *Langmuir* **2018**, *34*, 2290-2301. ©American Chemical Society, 2018. Chapter 3 reports the discovery of dodecagonal quasicrystal in the self-assembly of hydrated dianionic surfactants. Sample preparation and experimental analyses were performed in collaboration with Dr. Tyler J. Mann and Dr. Carlos M. Baez-Cotto. Chapter 4 describes the discovery of a FK σ phase in the aqueous self-assembly of non-ionic oligomers and has been reprinted with permission from Jayaraman A.; Zhang D. Y.; Dewing B. L.; Mahanthappa M. K. *ACS Central Science* **2019**, *5*, 619-628. © American Chemical Society, 2019. Diana Y. Zhang and Beth L. Dewing made the initial discovery mentioned in the chapter and the author of the thesis performed additional thermodynamic experiments. Chapter 5 investigates the effect of end-groups on the micellar structures formed by the non-ionic amphiphile utilized in Chapter 4. The synthetic aspects of the work were performed in collaboration with Leah Wofford. Chapters 3 and 5 are intended to be submitted for peer-reviewed publication.

Table of Contents

Acknowledgements	i
Financial Support	iv
Dedication	v
Abstract.....	vi
Preface.....	viii
Table of Contents	ix
List of Tables	xii
List of Figures.....	xiv
List of Schemes.....	xxxii
Chapter 1. Introduction.....	1
1.1 Amphiphile self-assembly in aqueous solution.....	1
1.2 Lyotropic liquid crystals (LLCs).....	4
1.3 Historical perspective.....	7
1.4 Sphere packings in metals.....	8
1.5 Micellar packings of dendritic molecules	12
1.6 Micellar self-assembly of giant-shape amphiphiles	20
1.7 Complex sphere-packings in neat block polymers.....	28
1.8 Micellar lyotropic liquid crystals	42
1.9 Quasicrystalline structures in soft materials.....	56
1.10 Conclusions and Outlook	66
Chapter 2. Counterion-Dependent Access to Low-Symmetry Lyotropic Sphere Packings of Ionic Surfactant Micelles.....	68
2.1 Introduction	68

2.2 Experimental Section	73
2.3 Results and Analysis	78
2.4 Discussion	89
2.5 Conclusions	95
Chapter 3. Quasiperiodic Ordering of Oil-Swollen Ionic Surfactant Micelles	96
3.1 Introduction	96
3.2 Experimental section	97
3.3 Results and Discussion.....	100
3.4 Conclusions	112
Chapter 4. Path-Dependent Preparation of Complex Micelle Packings of a Hydrated Diblock Oligomer	114
4.1 Introduction	114
4.2 Results	116
4.3 Discussion	128
4.4 Conclusions	134
Chapter 5. End Group-Dependent Complex Micellar Self-assembly of Hydrated Diblock Oligomers.....	137
5.1 Introduction	137
5.2 Experimental Section	141
5.3 Results	146
5.4 Discussion	158
5.5 Conclusions	163
Chapter 6. Conclusions.....	165
References.....	170

Appendix 1. Supporting Information for Chapter 2: Counterion-Dependent Access to Low-Symmetry Lyotropic Sphere Packings of Ionic Surfactant Micelles.....	188
Appendix 2. Supporting information for Chapter 3: Quasiperiodic ordering of oil-swollen ionic surfactant micelles	212
Appendix 3. Supporting information for Chapter 4: Path-dependent Preparation of Complex Micelle Packings of a Hydrated Diblock Oligomer.....	223
A3.1 Experimental Section	223
Appendix 4. Supporting information for Chapter 5. End Group-Dependent Complex Micellar Self-assembly of Hydrated Diblock Oligomers	246

List of Tables

Table 1.1. Self-assembled morphology as a function of <i>CPP</i>	3
Table 5.1. Molecular characterization of the modified oligomers used in this study.....	147
Table A1.1. List of the observed and calculated peak positions for Frank-Kasper σ phase of C₁₀Mal-TMA₂ with $w_{0_s} = 22.21$ at 25 °C using the tetragonal space group symmetry <i>P4₂/mnm</i> (#136) and unit cell parameters $a = 13.30$ nm and $c = 6.99$ nm.	189
Table A1.2. List of the observed and calculated peak positions for Frank-Kasper σ phase of C₈Mal-TMA₂ with $w_{0_s} = 15.91$ at 25 °C using the tetragonal space group symmetry <i>P4₂/mnm</i> (#136) and unit cell parameters $a = 11.41$ nm and $c = 5.99$ nm.....	191
Table A1.3. Key to molecules: Notebook page numbers and APS trips when data were collected	211
Table A2.1. List of the observed and calculated peak positions for the Frank-Kasper σ phase formed by a LLC with $w_0 = 35.2$ at $T = 25$ °C prepared by hydration of C₁₂PA-Dec10 . The corresponding tetragonal space group is <i>P4₂/mnm</i> (#136) with the unit cell parameters are $a = 15.24$ nm and $c = 8.01$ nm ($c/a = 0.526$).....	214
Table A2.2. List of observed and calculated peak positions for the lyotropic dodecagonal quasicrystal formed by hydration of C₁₂PA-Dec10 to $w_0 = 29.1$ at $T = 25$ °C. The observed Miller indices correspond to the 5D space group <i>P12₆/mmc</i> (or <i>P12₆/mcm</i>) for the quasicrystal. The DDQC has a intermicellar distance as $a = 7.91$ nm and the interplanar distance as $c = 8.02$ nm, such that $c/a = 1.01$	217
Table A3.1. List of the observed and calculated peak positions for the Frank-Kasper σ phase formed by quenching an aqueous LLC with 58.7 wt% C ₁₆ E ₂₀ from 70 °C to 25 °C and annealing at 25 °C for 50 min. The corresponding tetragonal space group symmetry is <i>P4₂/mnm</i> (#136) and unit cell parameters are $a = 28.37$ nm and $c = 14.89$ nm ($c/a = 0.525$).	237

Table A4.1. List of observed and calculated peaks positions obtained for the σ phase formed by LLCs containing 66.2 wt% $\text{C}_{16}\text{E}_{21}\text{-C}$ at 25 °C using the tetragonal space group $P4_2/mnm$ and unit cell parameters $a = 142.1 \text{ \AA}$ and $c = 271.2 \text{ \AA}$	251
Table A4.2. List of observed and calculated peaks positions obtained for the σ phase formed by LLCs containing 63.0 wt% $\text{C}_{16}\text{E}_{19}\text{-S}$ at 25 °C using the tetragonal space group $P4_2/mnm$ and unit cell parameters $a = 149.4 \text{ \AA}$ and $c = 283.5 \text{ \AA}$. The sample was cooled from 100 to 25 °C and annealed for 9 h at 25 °C before data acquisition.	256
Table A4.3. List of observed and calculated peak positions and residuals for a dodecagonal quasicrystal formed by an LLC with $[\text{C}_{16}\text{E}_{21}\text{-N}] = 60.0 \text{ wt\%}$ at 25 °C. The miller indices correspond to the 5D space group $P12_6/mmc$ (or $P12_6/mcm$) for the quasicrystal. The intermicellar distance in the quasiperiodic plane of the DDQC is $a = 15.1 \text{ nm}$ with an interlayer stacking distance of $c = 15.4 \text{ nm}$ ($c/a = 1.02$).	263
Table A4.4. List of laboratory notebook page numbers and synchrotron trips corresponding to molecules shown in Chapter 4.	265

List of Figures

- Figure 1.1.** LLC phase progression observed with decreasing water content from left to right showing the formation of the micelles packed on a lattice (I), hexagonally-packed cylinders (H), bicontinuous structures (e.g., G), and lamellar bilayers (L_a). The mean interfacial curvature is positive for Type I mesophases and negative for Type II mesophases..... 6
- Figure 1.2.** FK polyhedra with Z12, Z14, Z15, and Z16 coordination environments..... 9
- Figure 1.3.** Examples of some canonical, FK, and Laves phases with the corresponding crystal structures. The different colors of particles correspond to the different symmetry-equivalent coordination environments present in each lattice. The structure files were obtained from Mehl et al.⁶⁵ and Hicks et al.⁶⁶ and were visualized using the VESTA crystallographic software.⁶⁷. 11
- Figure 1.4.** All the experimentally observed FK phases on a plot of fraction of Z15 polyhedra *versus* average *CN* of the structure. The A15, Laves, and Z phase constitute the vertices of the triangle within which all the other morphologies lie. Adapted by permission from Springer Nature: Nature Chemistry - Su, Z.; Hsu, C.-H.; Gong, Z.; Feng, X.; Huang, J.; Zhang, R.; Wang, Y.; Mao, J.; Wesdemiotis, C.; Li, T.; Seifert, S.; Zhang, W.; Aida, T.; Huang, M.; Cheng, S. Z. D., Identification of a Frank-Kasper Z phase from shape amphiphile self-assembly. *Nature Chemistry* **2019**, *11* (10), 899-905. Copyright 2019..... 12
- Figure 1.5.** Mesophases formed by thermotropic dendritic gallic acid-based liquid crystals as a function of the molecular shape. (A) Singly-substituted phenyl-ring affords a flat-tapered molecule which self-assembles into a 2D hexagonal phase. (B) Increasing the number of substitutions yields conical molecules that form spherical micelles with a hydrophobic corona and a hydrophilic core that arrange on an A15 lattice. Reprinted (adapted) from Balagurusamy, V. S. K.; Ungar, G.; Percec, V.; Johansson, G., Rational design of the first spherical supramolecular dendrimers self-organized in a novel thermotropic cubic liquid-crystalline phase

and the determination of their shape by X-ray analysis. *J. Am. Chem. Soc.* **1997**, *119*, 1539-1555. Copyright (1997) American Chemical Society..... 15

Figure 1.6. Triply-substituted carbohydrate-derived molecules that were observed to form the A15 structure. The three alkyl chains render the molecule conical analogous to Percec's dendrons. 16

Figure 1.7. Poly(ethyleneimine) with pendant dendritic groups that form micelles with an ionic core that self-assemble into a BCC lattice. 18

Figure 1.8. (A) The third-generation dendritic molecule that forms a σ phase at temperatures intermediate to the A15 and BCC structures. (B) 1D SAXS pattern obtained from a polycrystalline sample of the σ phase. (C) Diffraction patterns obtained along the $\langle 001 \rangle$ and $\langle 010 \rangle$ directions of a monodomain of the σ phase grown by slowly cooling from the high temperature disordered state. (D) Electron density maps obtained for the dense ($z = 0,1$) and sparse ($z = \frac{1}{4}, \frac{3}{4}$) layers of the σ phase. From Ungar, G.; Liu, Y.; Zeng, X.; Percec, V.; Cho, W. D., Giant Supramolecular Liquid Crystal Lattice. *Science* **2003**, *299* (5610), 1208-11. Reprinted with permission from American Association for the Advancement of Science. 19

Figure 1.9. (A) A substituted POSS cage. Use of an isobutyl terminating group yielded a hydrophobic cage whereas substituting with the carboxylic acid or hydroxy groups made them hydrophilic. (B) Azimuthally-integrated SAXS profile obtained for the A15 structure formed from self-assembling tetrahedra. (C) Fourier-filtered TEM image of the FK phase along the $\langle 100 \rangle$ direction. (D) Formation mechanism of the A15 structure. The hydrophobic POSS cages initially crystallize to yield lamellae, which upon melting form micelles that self-assemble into the cubic structure. From Huang, M.; Hsu, C. H.; Wang, J.; Mei, S.; Dong, X.; Li, Y.; Li, M.; Liu, H.; Zhang, W.; Aida, T.; Zhang, W. B.; Yue, K.; Cheng, S. Z., Selective Assemblies of Giant Tetrahedra via Precisely Controlled Positional Interactions. *Science* 2015, *348* (6233),

424-428. Reprinted with permission from American Association for the Advancement of Science..... 22

Figure 1.10. (A) POSS cage substituted with four PS chains that exhibits FK phase formation. (B, C, D, E) The scattered intensity *versus* wavevector (q) plots obtained for the HEX, A15, σ , and BCC structures respectively. The cartoon inset in each panel represents the increase in PS chain length in the phase progression: HEX \rightarrow A15 \rightarrow σ \rightarrow BCC. Reprinted (adapted) from Yue, K.; Huang, M.; Marson, R. L.; He, J.; Huang, J.; Zhou, Z.; Wang, J.; Liu, C.; Yan, X.; Wu, K.; Guo, Z.; Liu, H.; Zhang, W.; Ni, P.; Wesdemiotis, C.; Zhang, W.-B.; Glotzer, S. C.; Cheng, S. Z. D., Geometry induced sequence of nanoscale Frank–Kasper and quasicrystal mesophases in giant surfactants. *Proc. Natl. Acad. Sci. U.S.A.* **2016**, *113* (50), 14195-14200, with permission..... 24

Figure 1.11. (A) POSS cages covalently bonded to a triphenylene core forming the triangular structure. (B) 1D SAXS trace obtained for the Z phase at 170 °C formed by the amphiphile with no methylene linkers. Reprinted by permission from Springer Nature Customer Service Centre GmbH: Nature Chemistry - Su, Z.; Hsu, C.-H.; Gong, Z.; Feng, X.; Huang, J.; Zhang, R.; Wang, Y.; Mao, J.; Wesdemiotis, C.; Li, T.; Seifert, S.; Zhang, W.; Aida, T.; Huang, M.; Cheng, S. Z. D., Identification of a Frank-Kasper Z phase from shape amphiphile self-assembly. *Nature Chemistry* **2019**, *11* (10), 899-905. Copyright 2019..... 28

Figure 1.12. Schematic depiction for an AB diblock polymer with block lengths N_A and N_B . The phase diagram as predicted by SCFT is plotted as segregation strength (χN) *versus* the volume fraction of A (f_A). Micellar BCC and close packings are predicted for high compositional asymmetries. Reprinted (adapted) with permission from Cochran, E. W.; Garcia-Cervera, C. J.; Fredrickson, G. H., Stability of the Gyroid Phase in Diblock Copolymers at Strong Segregation. *Macromolecules* **2006**, *39* (7), 2449-2451. Copyright 2006, American Chemical Society..... 31

Figure 1.13. (A) Structure of the PI-PLA diblock polymer, which forms the σ phase. (B) Evolution

of the σ phase upon extended annealing at 25 °C after quenching from the disordered state. Peaks corresponding to BCC are marked in the SAXS trace obtained at 4.7 h. From Lee, S.; Bluemle, M. J.; Bates, F. S., Discovery of a Frank-Kasper σ Phase in Sphere-Forming Block Copolymer Melts. *Science* **2010**, *330* (6002), 349-353. Reprinted with permission from American Association for the Advancement of Science. 32

Figure 1.14. Diblock phase diagrams obtained as a function of conformational asymmetry of the two blocks. (A) SCFT predicts an increase in the composition window for the σ phase when ε increases from 2.25 to 4 for an AB diblock. Reprinted (adapted) with permission from Xie, N.; Li, W.; Qiu, F.; Shi, A.-C., σ Phase Formed in Conformationally Asymmetric AB-Type Block Copolymers. *ACS Macro Letters* **2014**, *3* (9), 906-910. Copyright 2014 American Chemical Society. (B) The σ phase window is experimentally observed to increase for diblock polymers with greater ε . The asymmetry values required to observe a σ phase experimentally are much lower than those predicted by SCFT. Reprinted with permission from Schulze, M. W.; Lewis III, R. M.; Lettow, J. H.; Hickey, R. J.; Gillard, T. M.; Hillmyer, M. A.; Bates, F. S., Conformational Asymmetry and Quasicrystal Approximants in Linear Diblock Copolymers. *Phys. Rev. Lett.* 2017, *118* (20), 207801. Copyright 2017 by the American Physical Society. DOI: <http://dx.doi.org/10.1103/PhysRevLett.118.207801>. 37

Figure 1.15. Thermal processing of PI-PLA diblock polymers. (A) Quenching into liquid nitrogen and rapidly heating the IL-58-15 polymer leads to the formation of C14 and DDQC structures. (B) Processing the more symmetric IL-52-20 with the same protocol yields the C15 and σ phases. Both samples remain arrested in a LLP when heated to 25 °C. From Kim, K.; Schulze, M. W.; Arora, A.; Lewis, R. M.; Hillmyer, M. A.; Dorfman, K. D.; Bates, F. S., Thermal processing of diblock copolymer melts mimics metallurgy. *Science* **2017**, *356* (6337), 520-523. Reprinted with permission from American Association for the Advancement of Science. 39

Figure 1.16. Molecular structures of molecules used in study by Martiel et al.¹⁸⁰. Mixtures of PC and limonene form a Type II FCC structure whereas using tocopherol as the dopant leads to the formation of the inverse Laves C15 structure..... 44

Figure 1.17. (A) Bis(alkyltrialazolium sulfobetaine) surfactants that form an inverse A15 structure in aqueous LLCs. (B) Azimuthally integrated 1D SAXS trace obtained from the well-ordered cubic FK phase and indexed using $Pm3n$ symmetry. The inset shows the 2D scattering pattern. (C) Electron density reconstruction obtained from the SAXS data, clearly displaying the two kinds of micelles expected for the structure. Republished with permission from Royal Society of Chemistry, from Inverse $Pm3(-)n$ Cubic Micellar Lyotropic Phases from Zwitterionic Triazolium Gemini Surfactants, Perroni, D. V.; Mahanthappa, M. K., *Soft Matter* **2013**, 9 (33), 7919-7922; Copyright 2013; permission conveyed through Copyright Clearance Center, Inc. 47

Figure 1.18. (A) Temperature *versus* hydration number phase diagram constructed for aqueous LLCs containing tetramethylammonium decanoate and 40 wt% decane using temperature-dependent SAXS analyses. (B) Electron density reconstructions obtained for the C15 and C14 structures showing the different classes of highly faceted micelles. Reprinted (adapted) with permission from Baez-Cotto, C. M.; Mahanthappa, M. K., Micellar Mimicry of Intermetallic C14 and C15 Laves Phases by Aqueous Lyotropic Self-Assembly. *ACS Nano* **2018**, 12 (4), 3226-3234. Copyright 2018 American Chemical Society..... 51

Figure 1.19. (A) 1D Intensity *versus* q traces obtained for the BCC, A15 and σ phases for LLCs of DPA-TMA₂. (B) An LLC phase portrait of the entire temperature- and concentration-dependent phase behavior of the surfactant. The water content is expressed as $w_0 = (\text{moles of water})/(\text{moles of surfactant})$. At 25 °C, the following phase behavior is observed with increasing hydration: H₁ → A15 → σ → BCC → Dis. (C) Electron density reconstructions of the σ and A15 phase

derived from experimental SAXS data showing highly faceted micelles in different coordination environments. Reprinted (adapted) from Kim, S. A.; Jeong, K.-J.; Yethiraj, A.; Mahanthappa, M. K., Low-symmetry sphere packings of simple surfactant micelles induced by ionic sphericity. *Proc. Natl. Acad. Sci. U.S.A.* **2017**, *114* (16), 4072-4077, with permission. 55

Figure 1.20. Square-triangle tiling elements that form the FK A15 and σ phases, and the DDQC.

The spheres indicate the positions of the particles at $z = 0, \frac{1}{4}, \frac{1}{2}, \frac{3}{4},$ and 1. The unit cells of the FK phases are marked with red dashed lines. 59

Figure 1.21. (A) Molecular structure of third generation dendron that forms a DDQC. (B) 2D-

SAXS pattern normal to the quasicrystalline layers clearly showing the 12-fold rotational symmetry. The open circles indicate calculated reflections for a monodomain of the DDQC. (C) Azimuthally-integrated SAXS trace obtained from a polycrystalline sample of the QC. (D) Arrangement of micelles in a hexagonal antiprism motif of the 3D DDQC structure. The 2D layers of the QC are constructed using the three tiling elements shown in Figure 1.20. Reprinted by permission from Springer Nature Customer Service Centre GmbH: Nature - Zeng, X.; Ungar, G.; Liu, Y.; Percec, V.; Dulcey, A. E.; Hobbs, J. K., Supramolecular dendritic liquid quasicrystals. *Nature* **2004**, *428* (6979), 157-160. Copyright 2004. 60

Figure 1.22. Time-temperature transformation diagram obtained for micellar phases of PI-PLA

constructed using DMS and SAXS. The σ phase is the thermodynamically stable structure for $T < 40$ °C. Reprinted (adapted) from Gillard, T. M.; Lee, S.; Bates, F. S., Dodecagonal Quasicrystalline Order in a Diblock Copolymer Melt. *Proc. Natl. Acad. Sci. U.S.A.* **2016**, *113* (19), 5167-5172, with permission. 63

Figure 2.1 (A) Chemical structure of dianionic surfactant DPA-TMA₂, which (B) forms

tetrahedrally close-packed aqueous lyotropic Frank–Kasper σ and A15 mesophases. In the low-symmetry σ phase unit cell that contains 30 particles, 5 discrete micelle sizes spontaneously

form to maximize electrostatic cohesion in the LLC while minimizing variations in surfactant hydration..... 72

Figure 2.2 Aqueous lyotropic liquid crystalline phase behavior for **C₁₀Mal-TMA₂**. (A) Synchrotron SWAXS powder patterns illustrating the formation of A15, σ , HCP, and BCC ordered phases at various headgroup hydration numbers w_{0s} . (B) Temperature versus w_{0s} phase diagram depicting the lyotropic mesophase progression of ordered phases to disordered micellar solutions with increasing w_{0s} 81

Figure 2.3 (A) Synchrotron SWAXS powder patterns for aqueous LLCs derived from **C₈Mal-TMA₂**, illustrating the formation of A15 and σ ordered phases and the coexistence of BCC and disordered micelles at 25 °C. (B) Temperature versus surfactant hydration number w_{0s} phase diagram showing the lyotropic phase progression: disordered micelles \rightarrow BCC + disordered micelles \rightarrow σ \rightarrow A15 with decreasing w_{0s} 84

Figure 2.4 (A) Synchrotron SWAXS powder patterns for **C₈Mal-K₂** LLCs illustrating the formation of hexagonally packed cylinders (H_1), H_1 /A15 two-phase coexistence (* demarcates peaks corresponding to the H_1 phase), and pure A15 sphere packing phases. (B) Temperature versus w_{0s} phase diagram, which notably lacks an FK σ phase..... 85

Figure 2.5 Temperature versus surfactant hydration number w_{0s} phase diagram for aqueous LLCs of (A) **C₈Mal-Cs₂** and (B) **C₁₀Mal-Cs₂**, which shows that the soft and somewhat hydrophobic Cs⁺ counterions allow σ phase formation in narrow composition windows. 88

Figure 2.6. (A) 90% isosurface electron density reconstructions of the A15 phase unit cells for **C₈Mal-TMA₂** and **C₈Mal-K₂** at $w_{0s} = 8.25$ and 9.85 , respectively. (B) Normalized linear electron density profile in the $z = 0$ plane along the [010] direction passing through the centers of the platelet micelles and in the [100] direction along the unit cell edge. The peaks correspond to the micelle cores, and the troughs correspond to the counterion distribution between

neighboring micelles. The relative depth and breadth of the troughs in the [010] and [100] directions indicate that the counterions are more localized along the Voronoi cell boundaries in the case of TMA⁺ (blue) than with K⁺(red)..... 94

Figure 3.1. (A) Synchrotron 1D-SAXS intensity profiles for aqueous LLCs prepared by **C₁₂PA-Dec10**, illustrating formation of canonical FCC, HCP, and BCC micellar cubic packings, tetrahedrally close-packed σ and A15 phases, as well as a glassy LLP state. All data were acquired at 25 °C, except where indicated. (B) Temperature versus amphiphile hydration number (w_0) phase diagram from aqueous LLCs of **C₁₂PA-Dec10**, derived by SAXS analyses of samples on their first heating. Solid lines indicate approximate phase boundary locations. 103

Figure 3.2. (A) SAXS pattern obtained by **C₁₂PA-Dec10** hydrated to $w_0 = 29.1$ at 25 °C corresponding to a well-ordered DDQC with interlayer spacing $c = 8.02$ nm and in-plane intermicellar distance $a = 7.91$ nm. Miller indices for the first ten peaks corresponding to the 5D space group symmetry $P12_6/mmc$ are provided (red tick marks correspond to peaks that could not be unambiguously assigned). (B) Schematic Stampfli tiling depiction of the in-plane, aperiodic order of the oil-laden micelles of an ideal, defect-free DDQC..... 105

Figure 3.3. Synchrotron SAXS data for as-prepared **C₁₂PA-Dec10** LLCs formed at $w_0 = 32.1$ on heating, during which samples were equilibrated at each temperature for ≥ 10 min. The as-made sample that exhibits DDQC/ σ two-phase coexistence irreversibly transforms on heating to 100 °C into a pure FK σ phase, which persists on cooling to 25 °C. The reflections corresponding to the σ phase are indicated by the tick marks in pattern in the initial obtained at 25 °C. Note the coincidence of the respective (00002) and (002) spacings of the DDQC and the σ phase (*dashed line*)..... 106

Figure 3.4. Temperature *versus* w_0 LLC phase portrait obtained from samples produced by mixing

10 wt% decane relative to amphiphile into pre-formed, C₁₂PA-TMA₂ aqueous LLCs, in which the DDQC is entirely absent. 108

Figure 4.1. Aqueous LLC phase behavior of C₁₆E₂₀: (A) Synchrotron SAXS patterns exhibiting the formation of H_I, A15 + H_I, A15, BCC, and FCC phases at diblock oligomer concentrations ranging 30–65 wt% C₁₆E₂₀. (B) Temperature *versus* wt% C₁₆E₂₀ phase portrait depicting the composition-dependent LLC phases that form, based on synchrotron SAXS analyses of as-prepared samples at 22 °C on the first heating. The solid lines delineate the approximate locations of the phase boundaries. 119

Figure 4.2. (A) Electron density map (90% isosurface) of an A15 phase reconstructed from a 1D-synchrotron SAXS pattern derived from a LLC with 58.9 wt% C₁₆E₂₀, comprising six coordination number *CN* = 14 micelles (*blue*) and two *CN* = 12 micelles (*red*). (B) 2D electron density map of the *z* = 0 and 1 planes of the A15 phase showing faceted micelles, which face each other and mimic the underlying Wigner-Seitz cell structure of each corresponding lattice position. 120

Figure 4.3. SAXS patterns obtained from a LLC having 58.7 wt% C₁₆E₂₀, upon quenching from 70 °C to 25 °C. The H_I phase rapidly transforms into BCC, evidenced by the 7 sharp SAXS maxima recorded 2 min after quenching. The BCC phase then evolves into a well-developed FK σ phase on further isothermal annealing at 25 °C for 50 min. 122

Figure 4.4. (A) Electron density reconstruction (90% isosurface) depicting the FK σ phase formed by a sample with 58.7 wt% C₁₆E₂₀ on quenching from 60 °C to 25 °C, followed by isothermally annealing at 25 °C for 2 d. The 30 particles within the tetragonal unit cell belong to five symmetry-equivalent classes exhibiting coordination numbers *CN* = 12 (*red* and *blue*), 14 (*green* and *purple*), and 15 (*yellow*). (B) 2D-electron density map of the *z* = 0 and 1 planes of the σ phase, illustrating the more modest faceting of the micelles as compared to the A15 phase

in Figure 4.2B. 123

Figure 4.5. SAXS patterns of the σ phase obtained from a quenched LLC with 58.7 wt% $C_{16}E_{20}$ upon ambient temperature annealing for 60 d shows the development of peaks which index to A15 (*red markers*). Extended annealing for 150 d reveals that the σ phase completely reverts to the original A15 phase of the as-prepared sample, indicating that the σ phase is a long-lived metastable liquid crystalline state at 25 °C. 124

Figure 4.6. SAXS traces obtained by two different LLC sample cooling protocols from 70 °C to 25 °C: (1) quenching a sample formed at 58.7 wt% $C_{16}E_{20}$ at > 60 °C/min and isothermally annealing for > 3 days at 25 °C (*blue*), and (2) cooling a sample comprising 57.9 wt% $C_{16}E_{20}$ at 0.1 °C/min followed by isothermal annealing for 2 h at 25 °C (*black*). The rapid quench yields a pure σ phase, whereas slow cooling yields coexisting A15 and σ phases. The red lines correspond to (200), (210), (211) and (400) peak positions of A15 structure, which are present in the black trace and are absent in the blue trace. 126

Figure 4.7 SAXS traces depicting the nucleation of the FK σ and A15 phases from a BCC morphology, upon quenching an aqueous LLC comprising 58.7 wt% $C_{16}E_{20}$ from 70 to 30 °C with subsequent isothermal annealing. BCC/ σ phase coexistence is observed after 20 min of isothermal annealing at 30 °C, after which the BCC peak intensities (*dashed lines*) decrease with concomitant growth of an A15 LLC morphology indicated by the appearance of the (110), (200), (210), and (211) SAXS peaks (*red triangles*). 128

Figure 4.8. Summary of the results of various thermal processing protocols applied to an LLC with 58.7 wt% $C_{16}E_{20}$. The progression of phases upon quenching to 50, 40, 30, and 20 °C is depicted as a function of log(time). Dotted arrows represent time intervals where no SAXS data were obtained. Numerical values in the parentheses correspond to the unit-cell parameters (in nm) of the respective phases. The unit cell parameters of the BCC phase were obtained immediately

following the quench ($t = 0$ s). The unit cell parameter of the A15 phase as-formed by centrifugation is equal to that of samples that were quenched and subsequently annealed at 25 and 30 °C for 150 d and 19.5 h, respectively..... 130

Figure 5.1. (A) Temperature *versus* amphiphile weight fraction phase portrait of hydroxyl-terminated $C_{16}E_{20}$ reported by Jayaraman et al., documenting formation of FCC, BCC, FK A15, and H_I phases on decreasing hydration. (B) Aqueous LLCs formed at 54–59 wt% $C_{16}E_{20}$ adopt A15 structures that undergo OOTs to BCC and H_I morphology at elevated temperatures, yet quenching the H_I phase to 25 °C nucleates a FK σ phase that only slowly reverts to the original A15 phase over 150 days. Reprinted (adapted) with permission from Jayaraman A.; Zhang D. Y.; Dewing B. L.; Mahanthappa M. K. Path-Dependent Preparation of Complex Micelle Packings of a Hydrated Diblock Oligomer. *ACS Central Science* **2019**, 5 (4), 619-628. Copyright 2019 American Chemical Society. 141

Figure 5.2. (A) Representative synchrotron small-angle scattering intensity profiles obtained from $C_{16}E_{21}-C$ aqueous LLCs at the specified compositions, annotated with Miller indices for the corresponding diffraction peaks for the FCC, BCC, and H_I phases; see Figure A4.5 for a fully indexed σ phase pattern. (B) Phase diagram depicting the LLC morphology progression of $C_{16}E_{21}-C$ as a function of hydration and temperature, which demonstrates the formation of disordered micelles, FCC, BCC, σ and H_I phases with increasing amphiphile content in LLCs. Solid black lines indicate approximate phase boundary locations within the ~2 wt% phase mapping protocol..... 152

Figure 5.3. Temperature *versus* wt% $C_{16}E_{19}-S$ morphology diagram derived from temperature-dependent synchrotron SAXS phase mapping on the first heating cycle from 25 to 100 °C. As-made σ phase samples exhibit thermoreversible OOTs to H_I phases, and all samples exhibit greater thermal stabilities (higher ODTs) than aqueous LLCs of $C_{16}E_{21}-C$ 153

Figure 5.4. (A) SAXS traces obtained from LLCs formed by $C_{16}E_{21}-N$. Dispersions containing 60.0 wt% $C_{16}E_{21}-N$ self-assemble into DDQCs, which transform to H_I phases at elevated temperatures. However, cooling the mesophase to 25 °C leads to the hysteretic formation of a poorly ordered DDQC that coexists with the H_I . LLCs containing 61.8 wt% amphiphile coexist as $H_I/DDQC$ phases and transition into a pure H_I at 60 °C. (B) LLC phase portrait obtained for $C_{16}E_{21}-N$ obtained on the first heating cycle, which reveals a narrow composition window of 12-fold aperiodic ordering of micelles in the vicinity of the periodic FK σ phase approximant. 156

Figure A1.1 Fully indexed lyotropic s phase formed by $C_{10}Mal-TMA_2$ with $w_{0_s} = 22.21$ at 25 °C shown in Figure 3.2A. The complete assignment of the Miller indices for the observed reflections are explicitly tabulated in Table A1.1..... 188

Figure A1.2 An enlarged and fully indexed SWAXS pattern for the σ phase formed by $C_8Mal-TMA_2$ with $w_{0_s} = 15.91$ at 25 °C shown in Figure 3A. The complete assignment of the Miller indices for the observed reflections are explicitly tabulated in Table A1.2..... 191

Figure A1.3. An enlarged and indexed SWAXS pattern for the A15 phase ($Pm3(-)n$ symmetry) formed by $C_8Mal-TMA_2$ with $w_{0_s} = 8.25$ at 25 °C shown in Figure 2.3A..... 194

Figure A1.5. (A) 90% isosurface of the electron density reconstruction of the FK σ phase of $C_{10}Mal-TMA_2$ at $w_{0_s} = 22.21$ at 25 °C. (B) 90% isosurface of the electron density reconstruction of the FK σ phase of $C_8Mal-TMA_2$ at $w_{0_s} = 15.91$ at 25 °C..... 211

Figure A2.1. Synchrotron SAXS traces obtained from LLCs prepared by hydration of mixtures of $C_{12}PA-Dec10$ at 25 °C showing the phase coexistences observed at intermediate hydrations relative to the pure phase SAXS patterns in Figure 1A. Specific indices corresponding to the reflection planes of the phases observed are color-coded with the color of the respective text.

.....	212
Figure A2.2. Enlarged and fully-indexed scattering pattern of the FK σ phase obtained from LLC with $w_0 = 35.2$ and $T = 25$ °C prepared by hydration of C₁₂PA-Dec10 that exhibits > 50 synchrotron instrument resolution-limited peaks. A complete list of peak positions and residuals are given in Table A2.1.	213
Figure A2.3. Azimuthally-integrated synchrotron SAXS patterns C₁₂PA-Dec10 LLCs with $w_0 = 16.2$ and 24.0 at 25 °C depicting the appearance of DDQC-like features in the LLP scattering trace ,and LLP-like features in a DDQC scattering trace. The red arrows correspond to low-intensity correlations, which likely correspond to those in the DDQC.	218
Figure A2.4. Scattering traces obtained from H _I morphology formed by LLCs of C₁₂PA-Dec10 with $w_0 = 6.1$ at 25 °C. The Miller indices corresponding to the 2D lattice are marked.	219
Figure A2.5. Synchrotron SAXS patterns obtained from the σ and A15 phases formed by oil addition into pre-made aqueous LLCs of C₁₂PA-TMA₂ at 25 °C.	220
Figure A2.6. (A) Synchrotron SAXS patterns of aqueous LLCs formed by DDPA-TMA₂ , in the absence of any hydrocarbon oil additive, showing the formation of H _I , A15, A15 + σ , σ , and HCP phases at 25 °C, unless otherwise noted. All traces are vertically shifted for clarity. (B) Temperature <i>versus</i> $w_0 = (\text{moles of H}_2\text{O}/\text{moles of surfactant})$ phase portrait of for DDPA-TMA₂ obtained from the synchrotron SAXS analyses of the as-prepared samples at 22 °C. Solid lines indicate the approximate locations of the phase boundaries with the resolution of the phase map, indicated by the data points.	221
Figure A3.1. H ¹ NMR of C₁₆E₂₀ in CDCl ₃ . The spectrum is calibrated such that there are three methyl protons (<i>a</i>). The integration of the protons on the PEO chain (<i>e</i>) are used to calculate the number of EO units. The integration of the hydrocarbon fragments (<i>a,b,c,d</i>) is consistent with a 16 carbon alkyl chain (33 protons). M_n is calculated as the sum of masses of the hydrocarbon	

and PEO blocks.	224
Figure A3.2. SEC trace obtained using differential refractive index detection for C ₁₆ E ₂₀ in tetrahydrofuran. The dotted lines represent the bounds of the peak from the amphiphile.	225
Figure A3.3. Temperature–dependent synchrotron SAXS patterns obtained from a LLC sample with 32.9 wt% C ₁₆ E ₂₀ in water. This LLC sample transitions from an FCC micellar packing at 25 °C to BCC/FCC coexistence at 60 °C, which melts into a disordered solution of micelles at 74 °C. In the SAXS trace at 60 °C, the green marker indicates the peak corresponding to the coexisting BCC phase. At 68 °C, we observe an intervening window of two-phase coexistence between a micellar BCC phase and disordered micellar solution as expected based on Gibbs’ Phase Rule.	228
Figure A3.4. 1D-SAXS intensity profiles for the LLC formed at 46.5 wt% C ₁₆ E ₂₀ showing the formation of a body-centered cubic (BCC) phase at $25 \leq T \leq 80$ °C, and H ₁ + disordered micelles at 100 °C.	229
Figure A3.5 An enlarged and fully indexed SAXS pattern for the LLC FK σ phase obtained on quenching a sample comprising 58.7 wt% C ₁₆ E ₂₀ from 70 °C to 25 °C and isothermally annealing it at 25 °C for 50 min. The complete assignment with indices for observed reflections are tabulated in Table A3.1. <i>Inset:</i> 2D scattering pattern which was azimuthally integrated to give the 1D plot	236
Figure A3.6 1D-SAXS intensity profiles obtained every 2 °C, on heating the aqueous LLC with 58.7 wt% C ₁₆ E ₂₀ heated from 25 °C to 70 °C. Samples were equilibrated at each temperature for at least 5 min. A LLC BCC phase nucleates at 37 °C and it completely transforms to H ₁ at 60 °C. The σ phase is notably absent on heating, and it can only be accessed upon cooling the H ₁ phase.	242
Figure A3.7 Time-resolved 1D-SAXS patterns obtained upon quenching LLC sample with 58.7	

wt% C₁₆E₂₀ from 70 °C to 50 °C. H₁ rapidly transforms into a BCC morphology on quenching, the latter of which remains stable for up to 10 h after annealing at 50 °C with no signs of either FK A15 or σ phase nucleation. Changes in the peak intensities with time upon extended monitoring suggest changes in the average micelle aggregation number (N_{agg}) within the BCC phase. 243

Figure A3.8 1D-SAXS patterns obtained upon quenching an LLC with 58.7 wt% C₁₆E₂₀ from 70 °C to 40 °C after various 40 °C isothermal annealing times. Prolonged annealing at 40 °C leads to decreased intensities of the “forest” or peaks which correspond to σ phase, and the peaks corresponding to BCC remain intense even after a long annealing time. 244

Figure A3.9 SAXS analyses of an aqueous LLC sample comprising 58.7 wt% C₁₆E quenched from 70 °C to 0 °C demonstrate the lack of nucleation of either FK σ or A15 phases upon annealing at 0 °C for > 3 days. The Miller indices corresponding to the observed peaks are marked on the plot. 245

Figure A4.1. ¹H NMR spectrum obtained for C₁₆E₂₁-C in CDCl₃. The peaks of the spectrum are indexed to the protons in the structure using alphabets. The integral obtained from the methyl protons (*a*) is calibrated to 3. Completion of carboxylation of the amphiphile is apparent due to the presence of two methylene protons at 4.17 ppm (*f*). 246

Figure A4.2. ¹H NMR spectrum of sulfonate C₁₆E₂₀ (C₁₆E₁₉-S) in CD₄OD-*d*₄. The peaks of the spectrum are assigned to the protons in the structure using alphabets. The proton integrals are calibrated such that the number of methyl protons (*a*) are 3. Integral of the methylene protons (*f* and *g*) is approximately 2 indicating complete modification of the -OH endgroup of C₁₆E₂₀. The number of EO units are calculated using the integral of peak *e*. 247

Figure A4.3. ¹H NMR spectrum of C₁₆E₂₁-N in CD₄OD-*d*₄. The number of methyl protons at 0.92 ppm (*a*) is calibrated to 3 to reference the other protons. Substitution of the ammonium groups

is indicated by the multiplet at 3.98 ppm (*f*) and the singlet corresponding to the methyl protons attached to N at 3.24 ppm (*g*). The extent of ion-exchange was assessed by disappearance of the tosylate peak at $\delta = 7.80$ ppm 248

Figure A4.4. (A) 1D SAXS traces obtained from LLCs containing 30.2 wt% $C_{16}E_{21}-C$ showing the transition of an FCC arrangement of micelles to an isotropic micellar solution upon heating from 25 to 60 °C. (B) 2D SAXS pattern obtained on cooling the micellar solution from above the ODT temperature to 25 °C yields a FCC structure riddled with stacking faults, which manifest as Bragg rods..... 249

Figure A4.5. Enlarged and fully indexed pattern of a σ phase formed by LLCs containing 66.2 wt% $C_{16}E_{21}-C$ shown in Figure 5.2A. Complete peak assignments and residuals are presented in Table A4.1. 250

Figure A4.6. Azimuthally integrated scattering patterns obtained for an LLC containing 70.4 wt% $C_{16}E_{21}-C$. Coexisting σ and H_I phase formed at 25 °C transitions to pure H_I at $T = 40$ °C. Cooling the cylindrical morphology to 25 °C leads to reformation of the σ phase, which coexists with a BCC structure. SAXS maxima consistent with a BCC lattice are marked with the corresponding miller index. The sample relaxes over 6 h at 25 °C to form the initial $H_I + \sigma$ morphology as evidenced by the disappearance of the (200) peak. Inverted triangles mark the peaks commensurate with the H_I phase. 253

Figure A4.7. LLCs containing 20.1 wt% $C_{16}E_{19}-S$ exhibiting coexisting FCC and BCC phases. The miller indices corresponding to the two phases are marked on the plot. 254

Figure A4.8. Fully indexed σ phase SAXS pattern obtained from LLC containing 63.0 wt% $C_{16}E_{19}-S$. The sample was cooled from 100 to 25 °C and annealed at 25 °C for 9 h before data acquisition. The list of miller indices and residuals are given in Table A4.2. 255

Figure A4.9. SAXS patterns obtained for LLCs containing 65.2 wt% $C_{16}E_{19}-S$ as a function of

temperature. The sample initially exhibits a non-equilibrium coexistence of A15, H_I, and σ phases at 25 °C. The peaks corresponding to A15 and H_I morphologies are indicated using blue and yellow markers respectively. Cooling the sample from the H_I structure at 100 °C to 25 °C leads to a transition to coexisting σ and H_I phases indicating the metastability of the A15 structure. 258

Figure A4.10. Small-angle X-ray scattering traces obtained for aqueous dispersions containing 49.7 wt% C₁₆E₂₁-N. The LLC exhibits the formation of a BCC phase at 25 °C, which upon heated to 100 °C transforms into coexisting σ + H_I phases. The peaks corresponding to the H_I phase are marked using green triangles. Cooling the sample back to 25 °C leads to retention of the σ phase while the H_I phase transitions to a BCC structure, as evidenced by the appearance of the (200) peak. 259

Figure A4.11. Azimuthally-integrated scattering traces obtained from LLCs containing 54.1 wt% C₁₆E₂₁-N. At 25 °C, the sample coexists as BCC/DDQC phases, and transitions to a pure DDQC at 60 °C. 260

Figure A4.12. SAXS patterns obtained from sample containing 60.0 wt% C₁₆E₂₁-N as a function of temperature. The sample was equilibrated at each temperature for 5 mins before data acquisition. The sample exhibits a direct DDQC→H_I transition when heated to 37 °C without the observation of a σ phase. 261

Figure A4.13. 1D SAXS patterns obtained from LLCs containing 76.3 wt% C₁₆E₂₁-N exhibiting the formation of H_I and G_I phases at 25 and 80 °C respectively. The miller indices corresponding to the G_I morphology are marked on the plot 262

Figure A4.14. ¹H NMR spectrum obtained from precipitated C₁₆E₂₀ in CDCl₃ in the presence of trifluoroacetic acid. The integrals of the spectrum are calibrated such that number of methyl protons (*a*) is 3. The total number of EO units is obtained by summation of *e*, *f* and *g* protons. A

peak from residual acetone in the NMR tube is observed at $\delta = 2.18$ ppm. 264

Figure A4.15. Temperature *versus* wt% diagram generated by SAXS analyses of LLCs containing $C_{16}E_{20}$ that was precipitated from hexanes twice. Only the canonical FCC, BCC and H_1 phases are observed with no evidence of any FK phases. 265

List of Schemes

Scheme 2.1 Synthesis of 2-Alkylmalonates Surfactants	79
Scheme 5.1. Synthetic modification of hydroxy-terminated $C_{16}E_{20}$ to access $C_{16}E_{21}-C$, $C_{16}E_{19}-S$, and $C_{16}E_{21}-N$	147

Chapter 1.

Introduction

1.1 Amphiphile self-assembly in aqueous solution

Supramolecular architectures resulting from self-assembly of nanoscopic building blocks possess properties beyond those of their individual components. Amphiphiles are a class of self-assembling molecules comprising two or more dissimilar moieties covalently bonded with each other. Surfactants are the earliest class of amphiphilic molecules dating back to 2800 BC¹ and are comprised of a hydrophilic headgroup attached to a long hydrophobic alkyl tail.² Hydration of amphiphiles induces self-assembly, where the hydrophilic groups shield the hydrophobic tails to alleviate unfavorable interactions with water.³ Typical aggregates in dilute solution include micelles of different shapes, such as spheres and cylinders as well as vesicles. The headgroups can be non-ionic, (e.g., monoolein), cationic (e.g., cetylammmonium bromide), anionic (e.g., sodium dodecyl sulfate), or zwitterionic (e.g., dipalmitoylphosphatidylcholine: DPPC), and dictate the strength of the headgroup-water interactions.⁴ The structure of the aggregate depends on the surfactant molecular architecture, extent of hydration, temperature, pH, and the presence of exogenous additives, amongst other factors. Directing the aqueous self-assembly behavior of surfactants is important for various applications in detergency, enhanced oil recovery, and rheological modification and emulsification.² The ensemble properties that enable these applications are derived from the structure of the self-assembled morphology of the surfactants. Hence, a fundamental understanding of the factors that guide amphiphile self-assembly in water is essential to realize these important applications.

The structure of the supramolecular aggregates formed upon hydration of amphiphiles can be predicted by considering the bending and elastic energies and the interfacial tension associated with

the hydrophobic-hydrophilic interface. This introduction provides a brief overview of the principles, while extensive details may be found elsewhere.⁵⁻⁹ Consider a monolayer of solvated amphiphiles with two orthogonal principal curvatures, c_1 and c_2 . The curvature of the membrane can be defined using two averaging schemes: Mean curvature $H = \frac{1}{2}(c_1 + c_2)$ and Gaussian curvature $K = c_1 c_2$, such that $H, K = 0$ for a flat layer. By convention, increasing the curvature of the surfactant layer by bending the interface gives $H, K > 0$ on curving the interface towards the hydrophobic domain and $H, K < 0$ for an interface curved towards the hydrophilic domain. The interface is stabilized by a balance of three forces: interfacial tension, which drives packing of amphiphiles in as tight a layer as possible; headgroup pressure, which generally consists of repulsive interactions due to electrostatic or steric repulsions between the headgroups; and repulsive hydrophobic chain pressure, due to excluded volume interactions between the alkyl tails. At equilibrium, the stress profile, $t(z)$ is zero when integrated over the length of the monolayer (z).^{5,8}

The total free energy of the monolayer can be expressed as: $G_{\text{tot}} = G_C + G_p + G_{\text{inter}}$, where G_C stems from the curvature elasticity, G_p accounts for the hydrophobic chain packing and G_{inter} includes all interactions associated with the headgroups. The free energy contribution of membrane elasticity is a function of the mean curvature and assumes the form: $G_C = 2\kappa(H-H_0)^2 + \kappa_G K$, where κ and κ_G are respectively the mean and Gaussian bending moduli of the monolayer and H_0 is the mean curvature when the membrane is fully relaxed.⁹ The moduli are a measure of the resistance of the membrane to bend. The penalty to form surfaces with non-uniform principal curvatures is contained in κ_G , which is negligible for constant mean curvature aggregates such as micelles and cylinders.

The curvature of an interface formed by surfactants can then be understood as follows: amphiphiles with large headgroups are forced away from each other due to the headgroup pressure. However, the free energy penalty of increased contacts between the hydrophilic and hydrophobic

domains and decreased cohesion between the alkyl tails forces the membrane to curve such that it minimizes interfacial area while preventing large variations in tail packing density in the hydrophobic domain. As the headgroup pressure increases, the amphiphiles transition from flat layers in vesicles to high curvature cylindrical and spherical micelles. The precise free energy calculations for measuring the extent of curvature and hence the self-assembled morphology, require specific knowledge about all the interacting forces. While the membrane moduli^{5,10} and interfacial tension are experimentally accessible,⁴ the interheadgroup interactions are generally complex and present a challenge to perform the full analyses for all surfactants.

Israelachvili and co-workers proposed a simple geometric model based on amphiphile shape to lump some of the complexities of the full mathematical treatment.^{5,11} The prediction of the self-assembled morphology is based on the relative dimensions of the hydrophobic and hydrophilic components. A critical packing parameter (*CPP*) was defined based on the molecular characteristics of the amphiphile.

$$CPP = \frac{v}{a_0 l_0}$$

where, v = effective volume of the hydrocarbon chain; a_0 = effective interfacial area per molecule and l_0 = length of the fully extended hydrophobic tail. The *CPP* utilizes the relative geometric volume constraints of the hydrophobic and hydrophilic components of an amphiphile to anticipate the structure of the aggregate. Table 1.1 lists the expected supramolecular architecture based on the *CPP* of a surfactant.⁵

Table 1.1. Self-assembled morphology as a function of *CPP*

Morphology	
$CPP < \frac{1}{3}$	Spherical micelles
$\frac{1}{3} < CPP < \frac{1}{2}$	Cylindrical micelles

$\frac{1}{2} < CPP < 1$ Bilayers and vesicles

$CPP > 1$ Inverse architectures

Amphiphiles with $CPP < \frac{1}{3}$ are comprised of large polar groups (a_0) and a relatively small hydrophobic tail (v/l_0), which tend to self-assemble into spherical micelles such that the tails are accommodated in the core and the large headgroups occupy the corona. As the tail volume increases, aggregates with larger hydrophobic volumes such as cylinders and vesicles are preferred. At larger tail volumes and CPP s, the hydrophobic/hydrophilic interface curves towards the hydrophilic domain due to the relatively small headgroups leading to dispersed water pools in a matrix of alkyl tails.

Although the simplicity of this model is enticing, the CPP presents multiple complications for its effective use as a predictive tool across all amphiphile classes. The interfacial area is a strong function of the extent of hydration and the nature of headgroups present in the surfactant. For example, solvation of ionic endgroups presents a much greater interfacial area per chain as compared to non-ionic headgroups at the same water content. As hydration increases the headgroups are hydrated with a greater number of water molecules, thereby increasing a_0 and subsequently the CPP , despite no change in actual the amphiphile molecular structure. Furthermore, the use of the length of the fully-stretched chain leads to underestimation of the CPP since the hydrophobic tails are never fully-stretched in practice.¹² Nevertheless, the CPP presents an initial prediction of the self-assembled morphology based on the surfactant molecular structure, but it should be used with due caution.

1.2 Lyotropic liquid crystals (LLCs)

In dilute solutions, the self-assembled aggregates formed by hydrated amphiphiles remain uncorrelated with each other, similar to disordered gas molecules. However, upon decreasing the

water content, the inter-aggregate distance decreases, leading to an increase in amphiphile-amphiphile interactions. This causes the surfactants to structure into mesophases that exhibit long-range crystallographic order, known as lyotropic liquid crystals (LLC). The cooperative self-assembly of the aggregates prevents unfavorable inter-headgroup interactions while maximizing cohesion among the amphiphiles. Consider the simple case of normal spherical micelles, where lowering the water content forces self-assembly on a lattice akin to hard spheres. Decreasing the hydration further leads to fusion of the spheres to form cylindrical micelles, which arrange on a 2D hexagonal lattice (H_I).¹³⁻¹⁴ Additional reduction in the water content leads to wrinkling of the hydrophobic-hydrophilic interface, enabling formation of non-constant mean curvature bicontinuous network phases (e.g., double gyroid: G_I),¹⁵⁻¹⁶ which ultimately transition to flat lamellar bilayers at even lower hydrations (Figure 1.1).¹⁷ Further decreasing the water content leads to the formation of inverse or Type II LLCs, where analogous to the dilute case, the hydrophobic/aqueous interface is curved towards the hydrophilic domain.¹⁸ The nanoscopic ordering in LLCs has found numerous applications in drug delivery,^{17,19-21} rapid ion and proton conduction membranes,²²⁻²³ and as templates for mesoporous silica synthesis.²⁴⁻²⁷ A similar phase progression has been observed for neat diblock polymers as a function of the relative composition of the two dissimilar polymeric blocks.²⁸

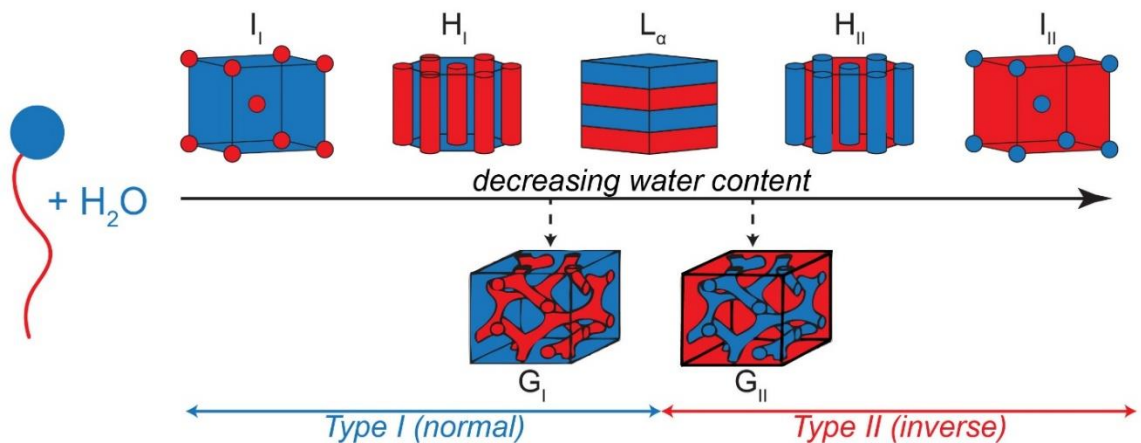


Figure 1.1. LLC phase progression observed with decreasing water content from left to right showing the formation of the micelles packed on a lattice (I), hexagonally-packed cylinders (H), bicontinuous structures (e.g., G), and lamellar bilayers (L_a). The mean interfacial curvature is positive for Type I mesophases and negative for Type II mesophases.

Hydrated micelles, analogous to hard spheres, pack into lattices such as the face-centered cubic (FCC), hexagonally closest-packed (HCP), and body-centered cubic (BCC) structures. However, some amphiphiles have been observed to form low-symmetry spherical packings, which involve micelles of different sizes and aggregation numbers packed on giant unit cells.²⁹⁻³¹ For example, the A15 structure that comprises two types of micelles arranged on a cubic lattice with $Pm\bar{3}n$ symmetry is a common Type I LLC morphology.³² Similarly, inverse micelles with sizes that vary by 20% about the mean have been observed to arrange in $Fd\bar{3}m$ symmetry.³³ These mesophases have been recapitulated in other soft material systems such as neutral dendrons,³⁴⁻³⁵ block polymers,³⁶⁻³⁸ and giant-shape surfactants.³⁹⁻⁴¹ These observations suggest universality in the principles guiding formation of particle packings in soft matter, which remain poorly understood.

The ordered lattices formed by soft micelles mimic the crystal structures found in metallic systems. Elemental metals typically contain atoms of one size, and crystallize into high symmetry FCC, HCP, and BCC structures. Packing of multiple sphere sizes, pervasive in intermetallic alloys, yields more complicated low-symmetry lattices, analogous to formation of disparate micelle size distribution in soft materials. Remarkably, sphere packings exist in all classes of matter, span orders of magnitude in length scales from 1 to 200 Å and are stabilized by nanoscopic interaction energies that range from strong metallic bonds to weak van der Waals forces in neutral soft materials. This universality is intriguing and poses a fundamental problem to decipher its origins. First, it is essential to understand how amphiphile structure and interactions affect the formation of micellar packings in soft materials. The complexity in this endeavor arises from the initial self-assembly of

amphiphiles into aggregates and additional inter-aggregate interactions, which dictate phase selection. A fundamental understanding of the thermodynamics, kinetics, and mechanism of phase formation in soft matter will hold us in good stead to establish analogies in particle packings across hard and soft matter. Specifically, this thesis aims to determine the molecular design criteria required for formation of low-symmetry micellar lattices in LLC assembly.

The first section explores the historical aspect of partitioning space through spheres and froth surfaces. The insights gained from these problems are valuable to understand nanoscale phase separation driven by unfavorable interfacial interactions between different soft material domains. Next, a brief overview of complex crystal structures formed in intermetallic alloys is provided to understand analogous phase formation in soft materials and to explore common themes across a range of material classes. The next three sections extensively review the low-symmetry particle packings observed in neutral thermotropic liquid crystals formed by dendritic molecules, giant shape-based surfactants, and block polymers in the melt that are stabilized by van der Waals forces. Following this, the rich micellar morphology space of LLC self-assembly of surfactants and polymers will be considered. The principles governing the formation and thermodynamics of the complex mesophases in all the material classes are discussed. Finally, a brief overview of the chapters in this thesis is provided.

1.3 Historical perspective

The variety of configurations available to pack spheres in space has fascinated scientists throughout centuries. Kepler conjectured in 1611 that a face-centered cubic packing of spheres, i.e. stacked 2D hexagonally closest-packed layers, presents the maximal density for a periodic arrangement of monodisperse spheres in 3D. Physically, maximal density is preferred to minimize void space and hence, maximize the cohesive energy in the structure. A rigorous proof for the

conjecture was provided by Hales in 2005 through the process of elimination,⁴² and was only formalized in 2017.⁴³ The problem becomes more fascinating if two or more sized spheres are involved.⁴⁴ The ratio between the sphere diameters and their relative numbers decide the maximal possible density and can be optimized to exceed that of an FCC packing.⁴⁵

Minimal surface tessellations in 3D have presented a similar historical puzzle. This problem physically manifests itself in soap froths, where the lowest interfacial area is preferred to minimize unfavorable air-water contacts. Hales proved that partitioning of a plane into equal hexagonal cells yields the least perimeter in 2D.⁴⁶ The 3D analog of the problem currently lacks a formal proof. Kelvin proposed an arrangement of truncated octahedrons of equal volumes as the optimal solution to the problem in 1887.⁴⁷ However, Kelvin's hypothesis was formally disproven in 1994 when Weaire and Phelan (W&P) found an arrangement of tetrakaidekahedron and irregular dodecahedron of equal volumes to present an interfacial area that was 0.4% lower than Kelvin's proposed structure.⁴⁸ The arrangement of the polyhedra in the W&P solution corresponds to the Wigner-Seitz (W-S) cells in an A15 lattice.

The initial two-fold nature of packing micelles formed by amphiphiles is apparent: maximization of packing density is preferred for cohesion of the structure, but simultaneous partitioning of space to yield the minimal interfacial area to alleviate unfavorable core-corona interactions is also essential. Hence, the new micellar arrangements can present insights into optimal solutions for these historically interesting problems.

1.4 Sphere packings in metals

Metals provide a model system to understand packing of interacting hard spheres. As expected by the Kepler conjecture, most elemental metals self-assemble into the dense face-centered cubic (FCC) (e.g., Ca, Pt) or hexagonally closest-packed lattice (e.g., Ti, Os) to maximize the atomic

packing fraction in 3D.⁴⁹ The atoms in FCC and HCP packings have the largest possible coordination number (CN) of 12 for equal-sized spheres. However, some elements, including all the alkali metals, self-assemble into the high-symmetry body-centered cubic (BCC) structure. Note that the W-S cell of a BCC lattice is a truncated octahedron, the initial proposed solution for the Kelvin problem.

Dense packing of atoms with $CN = 12$ is possible in cubo-octahedral, twinned cubo-octahedral and icosahedral arrangements.⁵⁰ The former two particle packings are the building blocks of the FCC and HCP lattices, comprised of a mixture of tetrahedral and octahedral atomic clusters. On the other hand, icosahedra contain only slightly distorted tetrahedra and cannot tessellate space alone while maintaining translational periodicity on account of their five-fold rotational symmetry.⁵¹ Frank and Kasper realized that topologically close-packed (TCP) structures containing only tetrahedral interstitial sites may be constructed if the icosahedral coordination is supplemented with $CN = 14, 15$, or 16 triangulated coordination shells (Figure 1.2).⁵²⁻⁵³ A total of 24 Frank-Kasper (FK) phases have been identified in metal alloys and many more have been predicted in computer simulations.^{50,54}

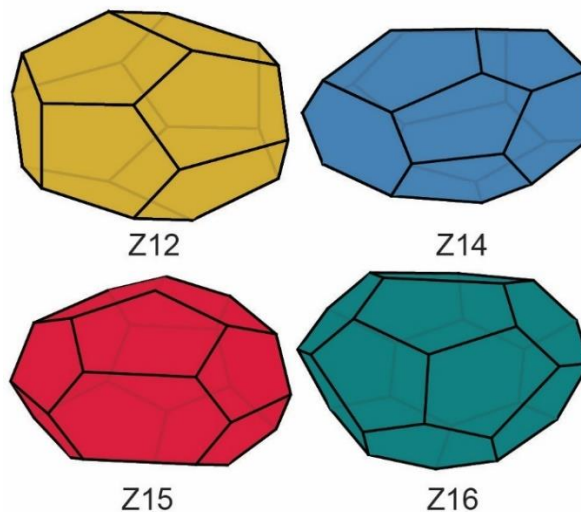


Figure 1.2. FK polyhedra with Z12, Z14, Z15, and Z16 coordination environments.

FK phases involve ≥ 7 particles situated at two or more symmetry equivalent positions on gigantic low-symmetry lattices. The structures present a periodic space-filling strategy that uses different permutations of the four coordination polyhedra. For example, FK σ phases ($P4_2/mnm$ symmetry) observed in Fe-Cr alloys,⁵⁵ β -U,⁵⁶ and β -Ta⁵⁷ consist of 30 atoms at five different coordination environments, with one Z15 polyhedron and two Z12 and Z14 polyhedra each, on a tetragonal lattice. A σ phase with equal volumes of all polyhedra has been proposed to present a more optimal solution to the Kelvin problem than the W&P structure.⁵⁸ A list of binary and ternary alloys where the σ phase has been observed can be found elsewhere.⁵⁹ The FK A15 phase ($Pm\bar{3}n$ symmetry), found Cr₃Si alloys,⁶⁰ is comprised of two atoms (Z12) arranged on a body-centered cubic lattice and four atoms (Z14) on the face centers. The closely related Z phase ($P6/mmm$ symmetry) contains Z12, Z14, and Z15 polyhedra and is common in metal alloys with A₄B₃ (e.g., Zr₄Al₃) stoichiometry.⁶¹ Anderson has used crystallographic operations such as translation, rotation, reflection, and intergrowth to describe the relationships of the σ and Z phase with the simpler A15 structure.⁶²

The Laves phases comprise a subset of the FK phases that only include Z12 and Z16 FK polyhedra. Typically, these structures are formed by alloys with AB₂ stoichiometry with ~20% difference in the atomic radii.⁴⁹ MgCu₂ and MgZn₂ were the first two structures studied in this subclass. The MgCu₂ structure, also known as the C15 phase ($Fd\bar{3}m$ symmetry), comprises of Mg atoms on a diamond structure with Cu atoms in the corresponding tetrahedral interstices.⁴⁹ The C14 structure ($P6_3/mmc$ symmetry) formed by MgZn₂ contains an arrangement of 12 atoms on three symmetry equivalent positions of a hexagonal lattice.⁶³ The atoms in different symmetry positions are represented with different colors in Figure 1.3. The C36 structure (MgNi₂ type, $P6_3/mmc$ symmetry) is a double-hexagonal representation of the C14 morphology and forms the third Laves polytype.⁶⁴ The ratio of the atomic radii of the elements and the alloy composition is critical for the

formation of FK structures in metallic systems.⁵¹

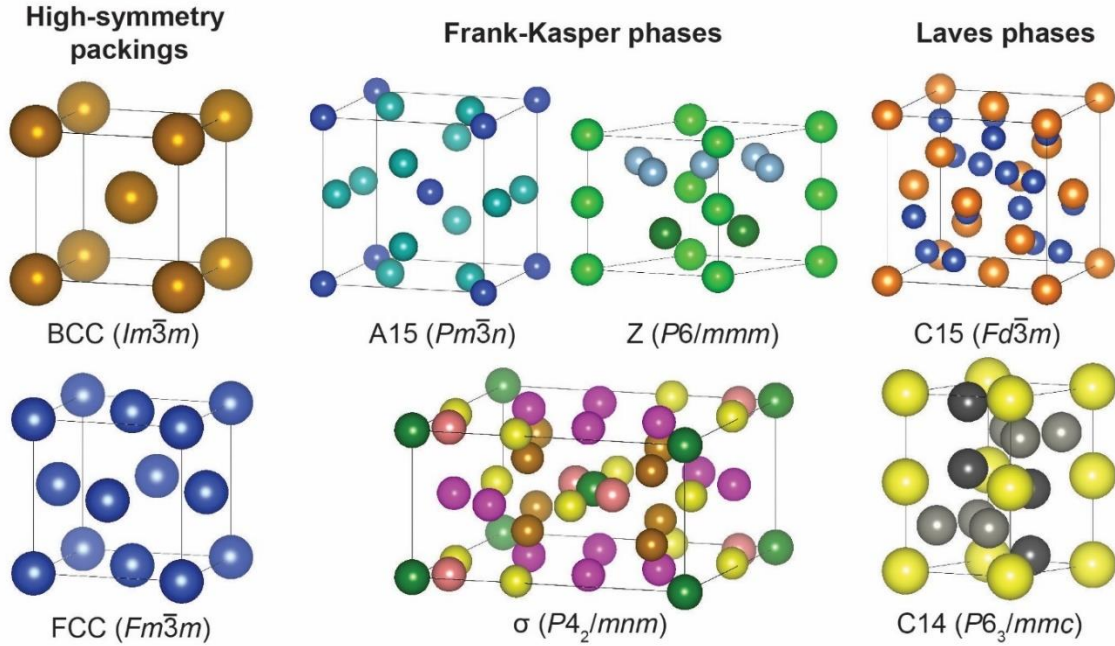


Figure 1.3. Examples of some canonical, FK, and Laves phases with the corresponding crystal structures. The different colors of particles correspond to the different symmetry-equivalent coordination environments present in each lattice. The structure files were obtained from Mehl et al.⁶⁵ and Hicks et al.⁶⁶ and were visualized using the VESTA crystallographic software.⁶⁷

Figure 1.4 shows a plot of number fraction of Z15 polyhedra (f_{Z15}) versus average coordination of the structure (CN_{avg}) on which all the FK phases have been marked.⁶⁸ The A15 structure has the maximum average coordination number of 13.5 with no Z15 polyhedra. The C15 and C14 structures possess the least $CN_{avg} = 13.3$ and lack Z15 polyhedra. The Z phase contains the largest fraction of the Z15 polyhedra at $2/7$ with $CN_{avg} = 13.429$. The structures form the vertices of the triangle with one of its bases on the x -axis, and the Z phase at the apex. All other FK phases lie within the triangle and can be constructed entirely using a linear combination of the polyhedral arrangements present in the A15, C14 and C15, and Z phases.⁵⁰

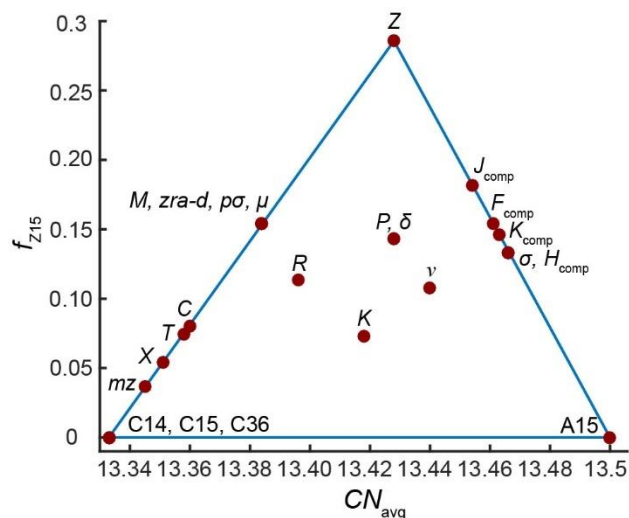


Figure 1.4. All the experimentally observed FK phases on a plot of fraction of Z15 polyhedra *versus* average CN of the structure. The A15, Laves, and Z phase constitute the vertices of the triangle within which all the other morphologies lie. Adapted by permission from Springer Nature: Nature Chemistry - Su, Z.; Hsu, C.-H.; Gong, Z.; Feng, X.; Huang, J.; Zhang, R.; Wang, Y.; Mao, J.; Wesdemiotis, C.; Li, T.; Seifert, S.; Zhang, W.; Aida, T.; Huang, M.; Cheng, S. Z. D., Identification of a Frank-Kasper Z phase from shape amphiphile self-assembly. *Nature Chemistry* **2019**, *11* (10), 899-905. Copyright 2019.

The observation of FK phases is not limited to intermetallic alloys. The FK A15, σ , and Z phases have been observed in water clathrate gas hydrates.⁶⁹ The current solution to the Kelvin conjecture is a FK phase, but other TCP structures have been identified as more optimal solutions.⁷⁰⁻⁷¹ The formation of A15 and C15 structures in LLCs harbinger the possibility of identifying additional FK phases in the self-assembly of LLCs and other soft materials. The ubiquity of the FK phases indicates universality in the periodic packing of spherical objects of different sizes in disparate fields of study.

1.5 Micellar packings of dendritic molecules

Dendrons are a widely studied class of thermotropic liquid crystals (LCs), in which self-assembly is governed by the spatial extent of the molecules. The structure of the amphiphiles

resembles a tree emanating from a root (the core), where each additional set of branches forms a new generation of the dendron.⁷² The primary scaffold consists of multiply substituted aromatic groups to create the dendritic structure. The molecules are terminated using aliphatic, fluorinated, or poly(ethylene oxide) chains to imbue an amphiphilic nature.⁷³ The convergent and divergent synthetic strategies allow the creation of a variety of molecular shapes, including wedges,³⁴ cylinders,⁷⁴ spheres,⁷⁵ and rod-coil conformations.⁷⁶⁻⁷⁷ The self-assembly of dendritic molecules is largely driven by packing of the molecular shape and less by the amphiphilic nature of the molecule. Hence, addition of new generations results in increased complexity in the molecular self-assembly. A variety of liquid crystalline phases have been observed in dendron self-assembly including nematic and smectic assemblies,⁷²⁻⁷³ bicontinuous phases,⁷⁸⁻⁷⁹ cylinders,⁸⁰ and spherical micelle packed on a lattice.⁸¹⁻⁸²

Percec and co-workers³⁴ and Tschierske and co-workers⁸³ independently reported the self-assembly of dendritic molecules into an A15 structure in the 1990s. Percec's group used gallic acid to grow multiple generations and obtain a library of dendritic molecules with varying architectures. Addition of singly-substituted phenyl rings in the second dendritic generation yielded flat tapered molecules, which self-assembled into cylinders that packed on a 2D hexagonal lattice (HEX) (Figure 1.5A). In contrast, molecules containing triply substituted phenyl rings in the second generation acquired a conical structure, which guided self-assembly into spherical micelles that subsequently arranged on a FK A15 lattice as shown in Figure 1.5B. The similarities between the formation of these structures and those in Type II LLCs are evident. Molecules with smaller interfacial areas (lower *CPP*) form the cylindrical phase. Increasing the effective area (increasing *CPP*) by adding additional alkyl tails, causes the dendrons to form high curvature micelles. Based on the W&P solution of the Kelvin problem, the preference for the A15 lattice was rationalized based on minimization of the micellar interfacial area.

The formation of the A15 structure was elucidated through a combination of electron-density reconstructions obtained from small-angle X-ray scattering (SAXS) data and transmission electron microscopy analyses (TEM).^{34,84-85} Stacking faults and grain boundaries were also identified using TEM.⁸⁶ The proposed micellar assembly was isostructural to the intermetallic Cr₃Si lattice and included two micelles arranged on a body-centered cubic unit cell and six highly deformed micelles on the faces of the cube. This arrangement of micelles was similar to that proposed for the Type I lyotropic A15 structure.²⁹

The phase behavior of the dendrons depended on the volume pervaded by micellar cores relative to the aromatic corona.⁸² Changing the –COOH moiety of the A15 forming dendron to either high M_n polystyrene (PS) or poly(methyl methacrylate) (PMMA) groups triggered self-assembly into a HEX morphology instead of an A15 structure. However, using lower molecular weight polymers led to recovery of the original phase behavior. The large volume occupied by the polymer chains in the core decreases the effective molecular asymmetry of the dendrons. As a result, the amphiphile shape becomes less conical causing the molecules to pack on the lower curvature cylindrical phase. The addition of polymer chains to the dendritic molecules is analogous to decreasing the *CPP* of an amphiphile forming inverse phases by increasing the size of the headgroups.

Molecules containing additional dendritic generations formed cones with larger base diameters. The fourth generation dendrons, where the molecular shape was almost spherical, yielded an A15 structure with decreased long-range order as compared to the second and third generations.³⁴ The apparent barrier to ordering was rationalized based on the dependence of the aggregation number (N_{agg}) of the micelles on the size of the molecules. The fourth-generation molecule exhibited an average of two molecules per micelle as compared to 12 and six for the second and third generations respectively. The calculated taper required for packing two fourth generation molecules into a micelle deviated from the actual taper of the molecule, which was argued to increase the penalty

for FK phase formation.

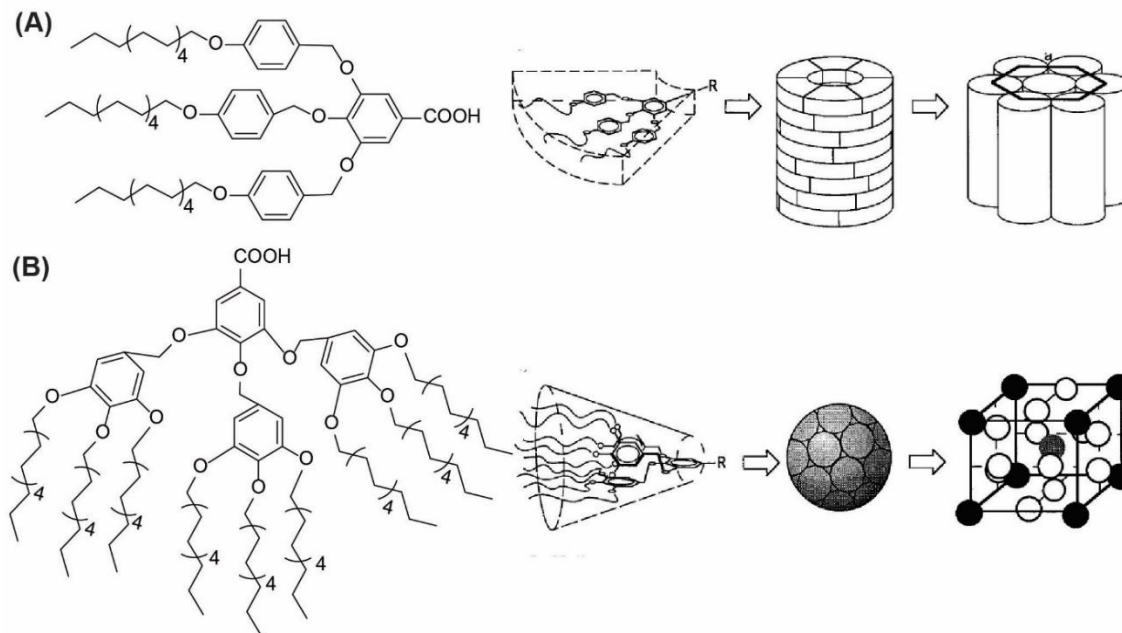


Figure 1.5. Mesophases formed by thermotropic dendritic gallic acid-based liquid crystals as a function of the molecular shape. (A) Singly-substituted phenyl-ring affords a flat-tapered molecule which self-assembles into a 2D hexagonal phase. (B) Increasing the number of substitutions yields conical molecules that form spherical micelles with a hydrophobic corona and a hydrophilic core that arrange on an A15 lattice. Reprinted (adapted) from Balagurusamy, V. S. K.; Ungar, G.; Percec, V.; Johansson, G., Rational design of the first spherical supramolecular dendrimers self-organized in a novel thermotropic cubic liquid-crystalline phase and the determination of their shape by X-ray analysis. *J. Am. Chem. Soc.* **1997**, *119*, 1539-1555. Copyright (1997) American Chemical Society.

Concurrently, Tschierske and co-workers studied the self-assembly of phenyl-N-methyl glucamide, where the aromatic ring was substituted with one, two or three dodecyl chains. The thermotropic behavior of the triply-substituted phenyl ring exhibited the following phase progression with increasing temperature: Crystalline \rightarrow Cubic lattice \rightarrow Disorder (Figure 1.6).⁸³ The cubic structure was later identified as A15 using SAXS⁸⁷ and the phase behavior of the

molecule was mapped systematically as a function of the number and length of the alkyl tails.⁸⁸ The micellar structure was accessible only for molecules comprising triply-substituted alkyl tails with nine or more carbons. Decreasing the length and the number of hydrophobic tails is equivalent to lowering the *CPP* of an amphiphile forming Type II LLCs, which is expected to destabilize micellar structures.⁵ Increasing the length of the hydrophobic tail also resulted in the formation of larger A15 unit cells with higher order-disorder transition temperatures (T_{ODT}). Additionally, an unknown micellar structure was obtained in these systems, which was observed to be sensitive to the sample preparation protocol.⁸⁹ The structure was metastable and was prone to recrystallization after extended time periods. Despite the rich mesophase behavior displayed by this class of carbohydrate-derived liquid crystals,⁹⁰ the observation of new micellar structures has been limited.

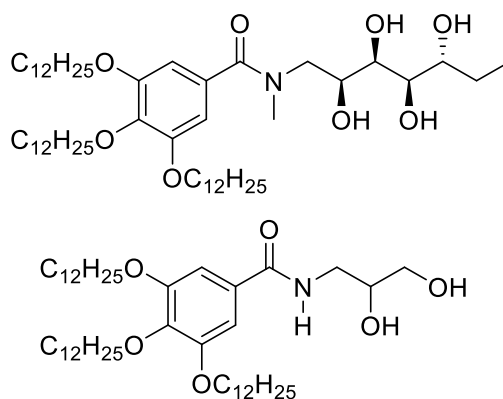


Figure 1.6. Triply-substituted carbohydrate-derived molecules that were observed to form the A15 structure. The three alkyl chains render the molecule conical analogous to Percec's dendrons.

Alternatively, the micellar self-assembly of Percec-type dendrons has been extensively studied and has led to the discovery of a variety of new structures.⁸⁰ A BCC structure ($Im\bar{3}m$ symmetry) was discovered in the self-assembly of poly(ethyleneimine) with pendant dendritic groups (Figure 1.7).⁷⁵ The structure melted into a disordered solution of micelles when heated to 131 °C with no intervening phase transitions. The rationale for the preference of a BCC structure instead of an A15 lattice is not clearly apparent. It possibly stems from the ionic core group, which increases the

interfacial area per chain. As discussed later in sections section 1.7 and 1.8, the effective amphiphile area is greater for micelles in the BCC structure than the A15 phase in both neat diblock polymers and aqueous LLCs.

The BCC packing was also discovered in the wedge-shaped dendrons, where the A15 arrangement was initially observed. The micellar sizes, T_{ODTS} and order-order transition temperatures (T_{OOTS}) of the BCC and A15 structures formed in the wedge-shaped dendrons can be modulated by addition of new dendritic generations,⁷⁴ increasing the length of the alkyl tails in the corona,⁹¹ or by adding ionic interactions in the core.⁹²⁻⁹⁴ The carboxylic acid group (Figure 1.5B) was deprotonated with alkali metal hydroxides to introduce intra-core electrostatic forces. The general phase progression: HEX \rightarrow A15 \rightarrow BCC \rightarrow Dis was observed with increasing temperature for dendrons containing dodecyl tails and alkali metal cations except Li^+ . Molecules with lithium carboxylate cores or alkyl tails with ≥ 14 carbons only formed HEX and BCC structures, with two exceptions. Amphiphiles with tetradecyl tails containing Rb^+ and Cs^+ counterions form A15 structures. The extent of headgroup-counterion dissociation controls the deformability of micellar cores, which was deemed an essential parameter affecting complex phase formation in polymers and lyotropic liquid crystals (See Section 1.7 and Chapter 2 for details).⁹⁵⁻⁹⁶ The larger Rb^+ and Cs^+ ions are highly dissociated, forming rigid cores lined with repulsive carboxylate headgroups. The formation of an A15 lattice can then be rationalized based on the W&P solution of the Kelvin problem to partition space with minimal interfacial area to reduce unfavorable interactions between the ionic core and the lyophilic corona.

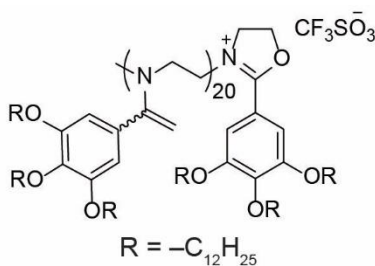


Figure 1.7. Poly(ethyleneimine) with pendant dendritic groups that form micelles with an ionic core that self-assemble into a BCC lattice.

In 2003, Ungar, Percec and coworkers discovered the formation of a new structure in the self-assembly of third-generation wedge-shaped dendrons with dodecyl peripheral groups and a carboxylic acid core (Figure 1.8A).³⁵ Note that molecules with $-\text{CH}_2\text{OH}$ core only formed the A15 structure and the new mesophase was not observed. This amphiphile belongs to the same family of molecules shown in Figure 1.5B. The new structure was obtained at temperatures intermediate to the A15 and BCC structures. Powder and single-domain SAXS analyses indicated the formation of a thermotropic LC FK σ phase (Figure 1.8B).³⁵ The single-crystals were grown by slow cooling from the disordered state. Electron density reconstructions obtained from SAXS data confirm the presence of 30 micelles at five symmetry-equivalent positions on a tetragonal unit cell with $CN = 12, 14, \text{ and } 15$ in accordance with FK topology (Figure 1.8D).

The formation of the σ phase was rationalized based on the ideal taper of the conical dendron to form the micelle sizes required for the TCP structure. However, the model based on molecular shape could not discern a difference in stability between the A15 and σ phases.³⁵ The FK σ and A15 structures in metals are formed by alloys where the sizes of atoms only marginally differ.⁵⁰⁻⁵¹ The low N_{agg} of the micelles formed in these systems prevent subtle changes in micellar size. For example, the A15 structure formed by the molecule shown in Figure 1.5 exhibits $\langle N_{\text{agg}} \rangle = 6$, so adding or subtracting one molecule from a micelle will result in a $\sim 16\%$ change in micellar volume. However, the σ and A15 structures display a particle size variation of less than $\pm 9\%$ about the mean. Hence, the formation of these phases in dendritic systems is tolerated due to this minor disparity in micelle-sizes which is overcome by non-uniform deformation of the particles at different symmetry positions.⁹⁷ The observation of dendron-based σ and A15 structures with $N_{\text{agg}} < 5$ lends additional support to this hypothesis.⁹⁸⁻¹⁰⁰

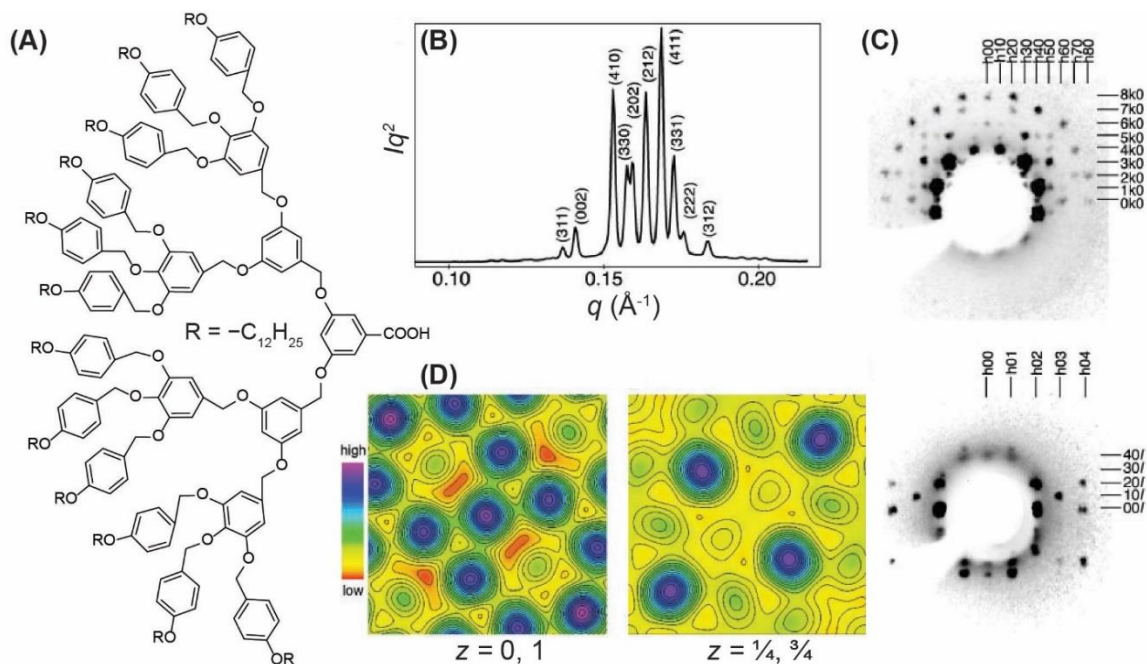


Figure 1.8. (A) The third-generation dendritic molecule that forms a σ phase at temperatures intermediate to the A15 and BCC structures. (B) 1D SAXS pattern obtained from a polycrystalline sample of the σ phase. (C) Diffraction patterns obtained along the $\langle 001 \rangle$ and $\langle 010 \rangle$ directions of a monodomain of the σ phase grown by slowly cooling from the high temperature disordered state. (D) Electron density maps obtained for the dense ($z = 0, 1$) and sparse ($z = 1/4, 3/4$) layers of the σ phase. From Ungar, G.; Liu, Y.; Zeng, X.; Percec, V.; Cho, W. D., Giant Supramolecular Liquid Crystal Lattice. *Science* **2003**, 299 (5610), 1208-11. Reprinted with permission from American Association for the Advancement of Science.

As dendrons self-assemble, organization at length scales below that of the self-assembled structure also emerge. Percec et al. illustrated the formation of chiral aggregates that self-assembled into A15 and σ phases.¹⁰¹⁻¹⁰² Micelles formed by achiral dendrons were observed to be chiral but racemic, while inherent chirality of the molecules led to amplified chirality in the micelles. An orientational memory effect was also observed for BCC \rightarrow HEX¹⁰³ and A15 \rightarrow HEX transitions.¹⁰⁴⁻¹⁰⁵ Cooling a monodomain of BCC aligned along the $\langle 111 \rangle$ direction yielded the expected epitaxial relationship with the $\langle 10 \rangle$ direction of the cylinders phase. However, repeated heating and cooling

cycles led to broadening of the (10) reflection in the SAXS patterns obtained from the HEX morphology, indicative of hysteresis from partially mismatched cylinder orientations. The A15 structure yielded three orientations of cylinders corresponding to the micelles on the face-centers of the cubic lattice. Other dendronized architectures including rod-coil conformations⁷⁷ and dendronized nanoparticles¹⁰⁶ have been reported to form complex spherical morphologies. However, no close-packed structures (FCC/HCP) or Laves phases have been observed in dendritic systems. The absence of the C14 and C15 morphologies probably stems from the low N_{agg} of the micelles, which precludes a large variation in micelle sizes while maintaining constant mass density.

1.6 Micellar self-assembly of giant-shape amphiphiles

FK phases can be visualized as periodic packing of distorted tetrahedra, where the particles occupy the vertices of the polyhedron. Simulations from Haji-Akbari et al.¹⁰⁷ and Damasceno et al.¹⁰⁸ illustrated the ability of hard tetrahedra to self-assemble into various low-symmetry structures, including a σ phase. Inspired by these results, Cheng and co-workers synthesized tetrahedral analogs using soft-material building blocks and studied their self-assembly behavior.³⁹ Four polyhedral oligomeric silsesquioxane (POSS) cages were covalently tethered to each other using a rigid linker consisting of a tetraphenyl methane group. POSS cages were rendered hydrophobic by complete substitution with isobutyl groups, whereas hydrophilic cages were obtained by using terminal $-OH$ and $-COOH$ groups (Figure 1.9A). A combination of the two types of cages was utilized to synthesize amphiphilic tetrahedra.

The phase behavior of the ‘soft’ polyhedra was governed by the relative positions of the hydrophilic and hydrophobic POSS cages. Molecules containing one hydrophilic cage attached to three isobutyl substituted cages initially self-assembled into crystalline lamellae (Figure 1.9D).

Heating the structure above the melting temperature (T_m) of the POSS cages leads to the formation of micelles that arranged on a A15 lattice as evidenced by the corresponding 1D SAXS trace (Figure 1.9B). TEM analyses of the cubic FK phase revealed the formation of two different sphere sizes with a 4-16% variation in their volumes. Figure 1.9C shows the Fourier-filtered TEM image obtained along the $\langle 100 \rangle$ direction of the A15 lattice. The observation of two coordination environments is expected for the cubic structure and the authors calculated an average of 38 and 50 tetrahedra in the two different micelles. This observation is in stark contrast to the A15 structure formed by wedge-shaped dendrons where $N_{agg} < 15$. The stability of the mesophase in the POSS-containing molecules was argued to stem from strong H-bonding interactions in the hydrophilic cores of the spheres. Weakening the intra-core interactions by using a $-OH$ substituted hydrophilic POSS cage leads to the formation of a high-symmetry BCC structure. The decreased intermolecular forces within the core possibly reduces the enthalpic gain due to reduced interfacial area afforded by packing the micelles into an A15 structure. Moreover, any other permutations of the relative number of hydrophilic and hydrophobic cages yielded tetrahedra that remained semicrystalline or exhibited the formation of canonical lamellar, HEX or double gyroid phases.³⁹ Note that all samples were annealed for extended time periods above the melting point, after which they were quenched in $N_{2(l)}$ to prevent recrystallization of the POSS cages.³⁹

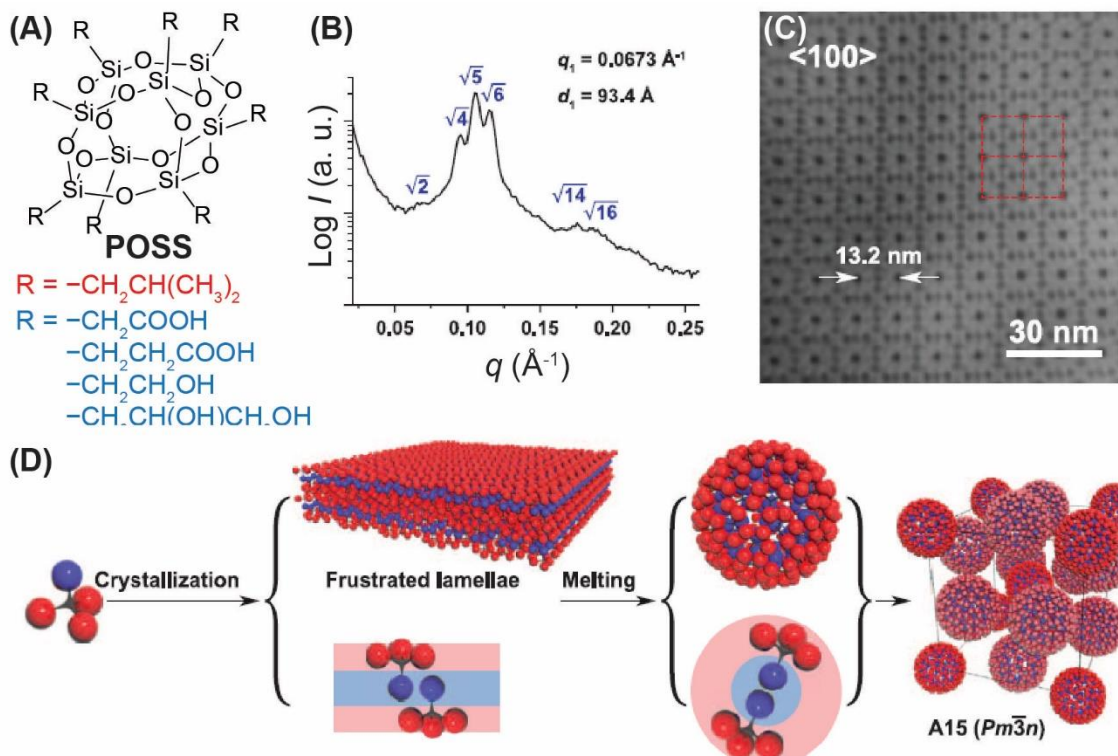


Figure 1.9. (A) A substituted POSS cage. Use of an isobutyl terminating group yielded a hydrophobic cage whereas substituting with the carboxylic acid or hydroxy groups made them hydrophilic. (B) Azimuthally-integrated SAXS profile obtained for the A15 structure formed from self-assembling tetrahedra. (C) Fourier-filtered TEM image of the FK phase along the $\langle 100 \rangle$ direction. (D) Formation mechanism of the A15 structure. The hydrophobic POSS cages initially crystallize to yield lamellae, which upon melting form micelles that self-assemble into the cubic structure. From Huang, M.; Hsu, C. H.; Wang, J.; Mei, S.; Dong, X.; Li, Y.; Li, M.; Liu, H.; Zhang, W.; Aida, T.; Zhang, W. B.; Yue, K.; Cheng, S. Z., Selective Assemblies of Giant Tetrahedra via Precisely Controlled Positional Interactions. *Science* 2015, 348 (6233), 424-428. Reprinted with permission from American Association for the Advancement of Science.

The molecular asymmetry achievable in a tetrahedron is limited by the angular positioning of the four POSS cages. Yue et al. circumvented this problem by tethering PS chains at a single position on the POSS cage.⁴⁰ A library of giant-shape surfactants was synthesized with one to four PS chains of varying molecular weights to systematically modulate the molecular asymmetry. The

molecules containing three and four PS chains self-assembled into the FK A15 and σ phases upon extended annealing above T_m of the POSS cages and T_g of the PS domains (Figure 1.10).⁴⁰ The authors observed no order-order phase transitions at elevated temperatures for any of the structures. The micelles formed by these molecules consist of rigid POSS cores with relatively flexible coronae.

Consider the mesophase formation for surfactants containing four PS chains as shown in Figure 1.10A. The following phase progression was observed with increasing PS molecular weight (volume fraction): HEX \rightarrow A15 \rightarrow σ \rightarrow BCC (Figure 1.10). The inset cartoons for Figures 1.10B, C, D, and E represent molecules containing successively larger PS chains. This phase progression with increasing molecular asymmetry is reminiscent of the complex micellar phase behavior of hydrated surfactant LLCs with increasing water content (see Section 1.8 and Chapter 2).^{31,38,95,109} Since the length of the PS chains dictates the N_{agg} , the average micelle size necessarily needs to change for each structure.¹¹⁰ Brownian dynamics simulations revealed that the change in particle size in the neat giant-shape surfactants was effected by intermicellar chain exchange. The simulations also captured the bimodal distribution of micelle sizes in the A15 structure and the presence of a unimodal particle-size distribution in the BCC lattice. The authors argued for the stabilization of the FK phases based on a subtle free energy balance between the interfacial tension of the core and coronae and the chain stretching penalty of the PS chains.¹¹¹⁻¹¹³ This rationale has been extensively explored in neat diblock polymer self-assembly and will be discussed in detail in Section 1.7. Note that the more symmetric molecular architectures involving POSS cages attached to ≤ 2 PS chains only formed the canonical lamellar (L), double gyroid (G), HEX, and BCC phases. This observation is consistent with decreasing the *effective* ‘CPP’ of these molecules, leading to formation of lower curvature structures.

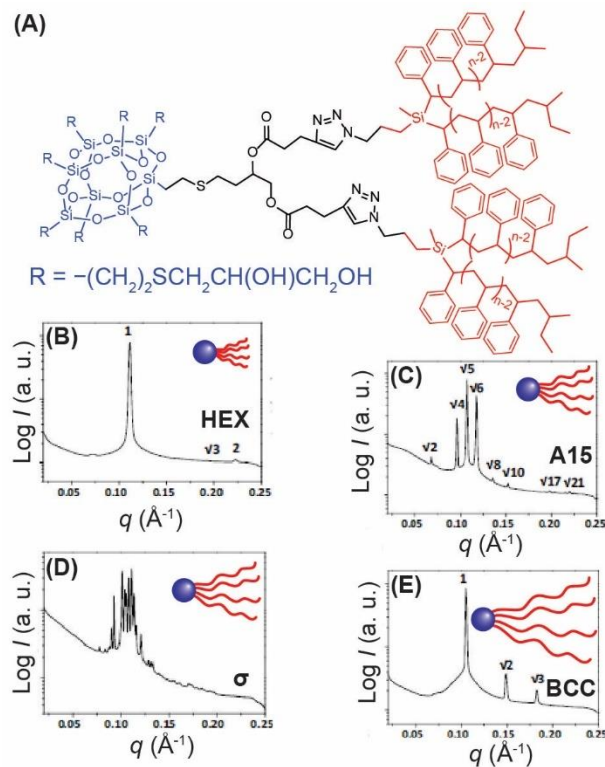


Figure 1.10. (A) POSS cage substituted with four PS chains that exhibits FK phase formation. (B, C, D, E) The scattered intensity *versus* wavevector (q) plots obtained for the HEX, A15, σ , and BCC structures respectively. The cartoon inset in each panel represents the increase in PS chain length in the phase progression: HEX \rightarrow A15 \rightarrow σ \rightarrow BCC. Reprinted (adapted) from Yue, K.; Huang, M.; Marson, R. L.; He, J.; Huang, J.; Zhou, Z.; Wang, J.; Liu, C.; Yan, X.; Wu, K.; Guo, Z.; Liu, H.; Zhang, W.; Ni, P.; Wesdemiotis, C.; Zhang, W.-B.; Glotzer, S. C.; Cheng, S. Z. D., Geometry induced sequence of nanoscale Frank-Kasper and quasicrystal mesophases in giant surfactants. *Proc. Natl. Acad. Sci. U.S.A.* **2016**, *113* (50), 14195-14200, with permission.

Cheng and co-workers have exploited the modularity of alkene-substituted POSS cages to synthesize various architectures including pseudo-bottlebrush oligomers^{110,114} and conical,¹¹⁵⁻¹¹⁷ spherical,^{41,118} and pizza-slice shaped dendrons.^{116,119} The self-assembly of bottlebrush (BB) polymers with linearly-tethered majority hydrophobic (DPOSS) and minority hydrophilic

(HPOSS) POSS cages was studied to investigate how the sequence of the cages and the total length of the bottlebrush backbone guides phase formation.¹¹⁴ Bottlebrushes containing one terminal HPOSS unit and multiple DPOSS units formed L, G, and HEX morphologies at low molecular anisotropies. Increasing the number of DPOSS cages to > 3 triggered the formation of a micellar A15 structure. However, moving the HPOSS cage to the second position of a BB containing five DPOSS units (sequence: DHD₄) led to the formation of a σ phase. Alternatively, the D₂HD₃ sequence of cages, where the hydrophilic cage occupies the third position, yields BBs that form an A15 lattice. The formation of micelles by the BB polymers was rationalized as follows: The unfavorable interactions between the DPOSS and HPOSS cages cause microphase separation along the backbone of the BB. This leads to the formation of tapered cones for BBs containing sequences with large compositional asymmetry,¹¹⁴ which self-assemble into micelles in a manner similar to dendritic cones formed by Balagurusamy et al.³⁴⁻³⁵ But, the preference between the σ and A15 structures and the sequence-mediated control of the phase behavior is not well understood.

Percec, Ungar, and co-workers established a framework to understand the complex micellar phase formation in dendron-shaped molecules. Cheng and co-workers synthesized analogous POSS-based dendritic amphiphiles by covalently linking multiple hydrophobic POSS cages to a single hydrophilic POSS unit.¹¹⁵⁻¹¹⁶ Increasing the number of hydrophobic units progressively changed the molecular structure of POSS-conglomerate from a linear giant-surfactant to a cone-shaped moiety. An A15 structure was formed by molecules containing 4, 5, and 6 DPOSS cages attached to one HPOSS cage, whereas addition of a seventh cage led to the formation of a σ phase, concurrent with results obtained for neat wedge-shaped dendrons.³⁵ Further increase in the number of DPOSS cages yielded a disordered state. At the limit of forming completely spherical dendrons containing 16 or 24 POSS cages, a non-ergodic molecular glass with no apparent periodic order was observed.¹¹⁸ The decrease in periodic order associated with the large molecular size is similar

to observations made by Percec and co-workers, where increasing the number of dendritic generations led to fewer SAXS peaks obtained for an A15 structure.⁹⁹ This behavior stems from the decrease in the N_{agg} of the micelles for large amphiphiles, which prevents achieving the micelle volume distribution required for forming FK phases. The stability of complex phases in the dendritic giant-shape surfactants emerges from intra-core H-bonding among the HPOSS cages. Nuclear Overhauser Effect nuclear magnetic resonance spectroscopy (NOE-NMR) revealed that the linker moieties were largely localized within the core, which was strongly segregated from hydrophobic DPOSS cages. The authors posit that the core regions containing the linker is deformable and aids in the formation of the different micelle sizes required for σ and A15 mesophase formation.¹¹⁵ Interestingly, shifting the position of the junction of the dendrons towards the hydrophilic POSS cage leads to disordering of the micellar structure.¹¹⁶

The molecular shape and nanoscale packing of amphiphiles containing POSS cages is dictated by the rigid moieties. Su et al. tethered six DPOSS cages to a triphenylene core forming a triangular molecule with branched arms with lengths that were synthetically controlled (Figure 1.11A).⁴¹ At 150 °C, the shape amphiphile with the shortest linker formed micelles that self-assembled into a FK A15 phase. Heating and annealing the sample at 170 °C for 12 h yielded a 1D SAXS trace as shown in Figure 1.11B, which conforms to the Z phase. The A15 and Z phases are structurally related through a stacking fault as evidenced by the proximity of the (110) maximum of the Z phase and the (200) reflection of the A15 structure in their respective SAXS traces.^{41,62} The transition between the two FK phases was observed to be thermoreversible, indicating their temperature-dependent thermodynamic stability. However, the recovery of a pure A15 lattice upon cooling the Z phase to 150 °C was sluggish and happened over several days.

The amphiphiles with methylene groups linking the phenyl ring with the DPOSS cages only formed a BCC structure at 170 °C. The phase behavior of the molecules at 150 °C was not reported.

This observation suggests that the rigid linker is essential to realize the Z phase in this class of shape amphiphiles. In intermetallic alloys, the Z phase is characterized by a ~20% variation of particle sizes about the mean. The micelles formed by triangular amphiphiles possessed $N_{\text{agg}} = 3-5$, approaching the limit of N_{agg} found in dendritic systems. The small N_{agg} enables such a large variation by the intermicellar exchange of one or two molecules. However, the exact origins directing the formation of the structure in this system are unknown. Additionally, this suggests the possibility of forming Laves C14 and C15 phases, which exhibit similar variations in micelle size distributions. Additionally, the absence of these morphologies in the low N_{agg} micelles formed by wedge-shaped dendrons is intriguing.

dissimilar polymeric blocks. A number of varied molecular architectures can be obtained based on the number of blocks and the different ways the blocks are linked.¹²⁰ Diblock polymers present the simplest case in this amphiphile class, where two chains are linked at one junction point.¹²¹ The unfavorable enthalpic interactions between the two blocks causes microphase separation at nanometer length scales. The morphology of the nanostructure is dictated by the entropic penalty of stretching the individual blocks while filling space at constant density.^{28,120} The phase behavior of diblock polymers is determined by the temperature-dependent interaction parameter ($\chi \sim 1/T$) between the blocks, the segment density-normalized degree of polymerization (N), and the volume fraction of the individual blocks defined as $f_A = N_A/(N_A + N_B)$, where N_A and N_B are the degrees of polymerization of the individual blocks.¹²² A thermodynamic phase diagram for an AB diblock polymer obtained from self-consistent field theory (SCFT) calculations is shown in Figure 1.12. The phases are plotted as functions of segregation strength (χN) and f_A . At low segregation strengths, diblock polymers form a disordered melt. Symmetric diblocks ($f_A = 0.5$) microphase separate to form lamellae at sufficiently high χN . As the volume asymmetry ($f_A \neq 0.5$) is increased, the enthalpic drive to maintain uniform mass density forces the formation of higher curvature morphologies such as bicontinuous double gyroid (G), hexagonally-packed cylinders (HEX) and spherical micelles packed on various lattices.¹²³⁻¹²⁴ For $f_A < 0.5$, the interface between the two polymers curves towards the A domain whereas for $f_A > 0.5$, the curvature is towards the B domain. This phase behavior is analogous to that observed with increasing hydration for LLCs discussed in Section 1.1. Given the large library of homopolymers and architectures, block polymers offer infinite possibilities to access varied nanoscopic morphologies and aided with theory present an expansive class of soft materials that form complex micellar arrangements.

At large volume asymmetries, individual diblock chains in the melt aggregate to form micelles which in turn self-assemble on lattices to yield supramolecular structures.¹²⁵ Leibler predicted an

arrangement of closest-packed spheres at the vicinity of the compositional order-disorder transition (ODT) using SCFT.¹²² In contrast, Dormidontova & Lodge predict a direct Dis \rightarrow BCC transition upon increasing the segregation strength using the strong segregation theory. The closest-packed structure was found to be thermodynamically unstable as compared to the disordered state.¹²⁵ In 1982, a BCC packing of micelles was established in the self-assembly of asymmetric polystyrene-*block*-poly(1,4-butadiene) (PS-PB) using small-angle neutron scattering (SANS) and TEM near the T_{ODT} .¹²⁶ However, Hashimoto and co-workers later reported the observation of an FCC lattice formed by micelles of poly(1,4-butadiene)-*block*-poly(ethylene oxide) (PB-PEO) for $T > 200$ °C in the vicinity of ODT.¹²⁷ Broad low- q features were observed in SAXS traces upon extended annealing at high T , which could suggest some extent of sample degradation or crosslinking of the PB cores.¹²⁸ Thus, the preferred sphere-packing near the diblock polymer ODT remains an open question.

FCC arrangement of micelles has also been observed in compositionally symmetric PB-PEO doped with PB.¹²⁹ The following phase progression was observed for the blends with increasing temperature: BCC \rightarrow FCC \rightarrow Dis, where all transitions were thermoreversible. The homopolymer was argued to relieve chain packing frustration in the coronal domain of the closest-packed morphology. The homologous HCP structure has also been observed for the blends upon heating the FCC structure to $T = 220$ °C.¹³⁰ Note that the earlier report probed the phase behavior only for $T \leq 183$ °C,¹²⁹ which probably precluded the observation of the high- T HCP structure. FCC packing contains alternating spatial arrangement of octahedral and smaller tetrahedral voids. In contrast, the HCP lattice comprises solely octahedral voids that are linearly connected. Hence, Chen et al. rationalized the preference for the hexagonal structure based on the increased translational entropy of the homopolymer localized in the octahedral voids.¹³⁰ Despite the high temperature employed for sample annealing, no artifacts were observed in the obtained SAXS patterns. However, no

molecular characterization was reported after the scattering analyses to assess the thermal stability of the polymer. Micellar morphologies in neat diblock polymer self-assembly remained limited to the canonical packings until 2010.

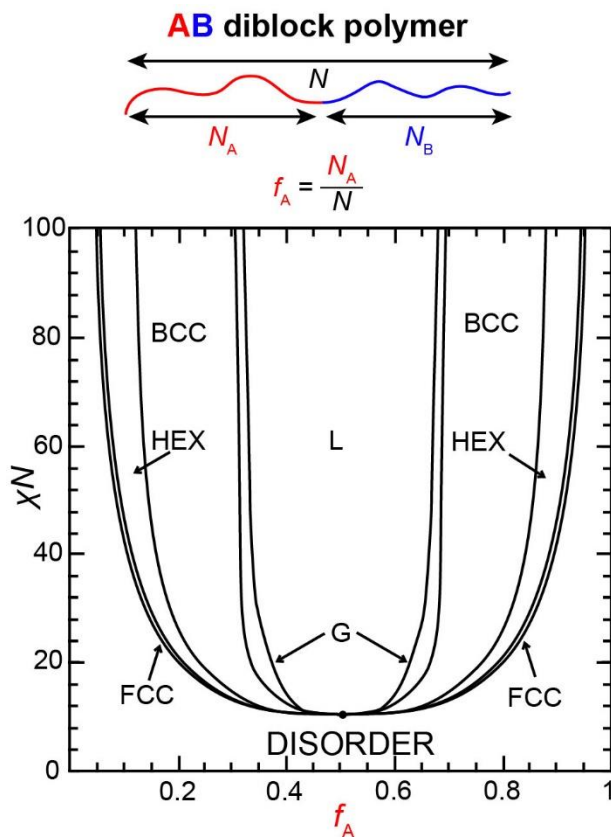


Figure 1.12. Schematic depiction for an AB diblock polymer with block lengths N_A and N_B . The phase diagram as predicted by SCFT is plotted as segregation strength (χN) versus the volume fraction of A (f_A). Micellar BCC and close packings are predicted for high compositional asymmetries. Reprinted (adapted) with permission from Cochran, E. W.; Garcia-Cervera, C. J.; Fredrickson, G. H., Stability of the Gyroid Phase in Diblock Copolymers at Strong Segregation. *Macromolecules* **2006**, 39 (7), 2449-2451. Copyright 2006, American Chemical Society.

Bates and co-workers were investigating the effect of blending low molecular weight poly(1,4 isoprene)-*block*-poly(D, L-lactide) (PI-PLA) with PLA-PI-PLA as a strategy to tune thermoplastic

elastomer mechanical properties.¹³¹ A diblock sample with $M_n = 3.89$ kg/mol and $f_{PLA} = 0.22$ that nominally formed a BCC structure was heated above T_{ODT} and rapidly quenched to 25 °C. An expected BCC packing of micelles was initially observed, which surprisingly transformed into a complex scattering pattern over 37.7 h (Figure 1.13). Concurrently, a sample of polystyrene-*block*-poly(1,4-isoprene)-*block*-polystyrene-*block*-poly(ethylene oxide) (SISO) exhibited a similar SAXS trace for $T = 140$ – 224 °C. TEM analyses of the tetrablock sample and simultaneous Rietveld analyses of the scattering pattern obtained from PI-PLA helped confirm the formation of a FK σ phase in block polymer melts.³⁶

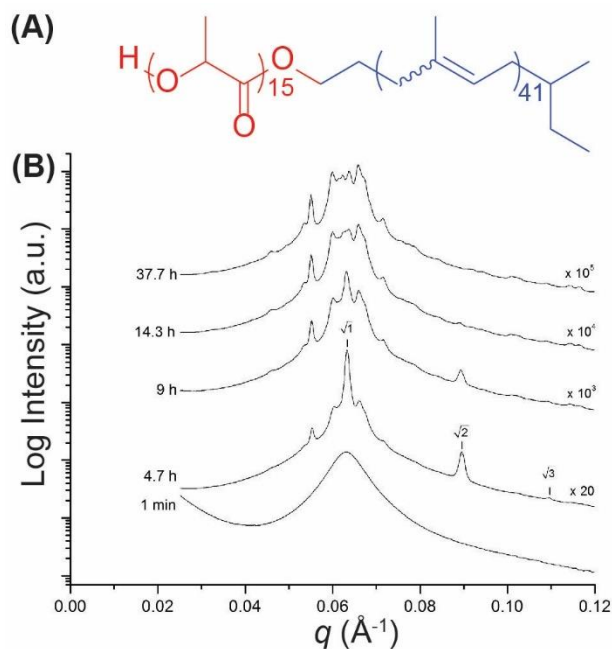


Figure 1.13. (A) Structure of the PI-PLA diblock polymer, which forms the σ phase. (B) Evolution of the σ phase upon extended annealing at 25 °C after quenching from the disordered state. Peaks corresponding to BCC are marked in the SAXS trace obtained at 4.7 h. From Lee, S.; Bluemle, M. J.; Bates, F. S., Discovery of a Frank-Kasper σ Phase in Sphere-Forming Block Copolymer Melts. *Science* **2010**, 330 (6002), 349-353. Reprinted with permission from American Association for the Advancement of Science.

The formation of a BCC structure immediately after the quench was argued based on

minimization of loss in translational entropy of the micelles upon ordering from a disordered state.¹³² A BCC lattice contains one micellar coordination environment, which is easily accessible from a uniformly homogenous disordered micellar melt. Packing of soft spheres on a lattice necessitates local particle deformations to maintain constant mass density and thus maximize van der Waals interactions between the polymeric chains.¹³³ Lee et al. recognized that micelles formed by diblock polymers deform and mirror the shape of the Wigner-Seitz (W-S) cell of each corresponding lattice position.¹¹³ The deviation from a spherical micellar shape leads to an increased enthalpic cost due to the interfacial tension between the blocks as well as an entropic penalty stemming from non-uniform stretching of individual chains to uniformly fill space. The sphericity of the W-S cells with volume V and surface area S was quantified using an isoperimetric quotient $IQ = 36\pi V^2/S^3$, defined such that $IQ_{\text{sphere}} = 1$. The number-averaged IQ s of the various lattices decreased as: $\sigma > A15 > BCC > FCC/HCP$, which implied that the micelles in the σ phase are most spherical (symmetrical). Thus, the formation of the structure was rationalized based on the preference for greater local micelle sphericity to minimize associated penalties of interfacial tension and chain stretching, while forgoing global lattice symmetry.¹¹³

The σ phase contains micelles of five different sizes which vary by $\pm 9\%$ about the mean, with $\langle N_{\text{agg}} \rangle \sim 200$ for micelles formed in the PI-PLA system. Hence, the $BCC \rightarrow \sigma$ transition necessarily involves a mass exchange mechanism to modify the unimodal size distribution of the high-symmetry lattice. The change in micelle-size distribution can be effected in two ways: micelle fusion and fission, and interparticle chain exchange. Any fusion or fission of the micelles in the BCC phase will induce a large deviation of sizes about the mean. Thus, the authors proposed intermicellar chain exchange as the primary mechanism to achieve the requisite sphere size distribution to facilitate σ phase formation. The dynamics associated with this exchange mechanism in diblock polymer micelles has recently been studied using X-ray photon correlation spectroscopy

and dynamic mechanical analyses (DMA).¹³⁴

The simple geometric construct of IQ provides a basis to understand the stabilization of the σ phase over the high-symmetry BCC structure. However, any reasonable applications sought from these complex architectures would require additional molecular design principles for diblock polymers. Using SCFT, Shi and co-workers showed that increasing conformational asymmetry (ε) between the blocks led to widening of the σ phase window for diblock polymers (Figure 1.14A).¹³⁵ Conformational asymmetry is defined as $(b_A/b_B)^2$ ($\varepsilon > 1$), where b is the statistical segment length of the blocks calculated at a constant reference volume. This parameter measures of the relative difference in the stretching penalties and pervaded volume of the two blocks. Increasing ε causes the core-corona interface to curve towards the more flexible block (higher statistical segment length) at lower compositional asymmetries, widening the sphere-forming window for $f_A < 1/2$.¹³⁶⁻
¹³⁷ The computational results were experimentally verified by the syntheses of three diblock polymers with different ε : poly[ethylene-*alt*-propylene]-*block*-poly(D,L-lactide) (PEP-PLA), polyethylene-*block*-poly(D,L-lactide) (PEE-PLA) and PI-PLA (Figure 1.14B). The less conformationally asymmetric PEP-PLA did not form a σ phase in the limit of the experimental resolution of diblock polymer compositions. However, PI-PLA and PEE-PLA both exhibited the formation of the complex structure. Moreover, the composition window of a stable σ phase was greater for the more conformationally asymmetric PEE-PLA.⁹⁶

The core-corona interface prefers to be spherical to reduce the energetic penalty from interfacial tension between the blocks at the expense of the entropic penalty incurred from the stretched chains in the core. As mentioned previously, the formation of micellar morphologies involves deformation of the micellar interface to adopt polyhedral shapes that mirror the W-S cell. Polyhedral interfacial warping allows the chains in the core to be less stretched than for a spherical interface. The increase in the chain stretching entropy of the core blocks ($S \sim 1/b^2$)¹³⁸ due to deformation of the interface

compensates for greater enthalpic penalty incurred for a polyhedral interface for diblock polymers with high $\varepsilon = (b_A/b_B)^2$. In other words, the imposition of the W-S cell on the micellar interface is facilitated by stiff corona blocks deforming a relatively flexible core. Consequently, phases with maximum local micelle sphericity are preferred to minimize the energy penalty stemming from interfacial tension and non-uniform core and corona chain stretching.

Despite the qualitative agreement between theoretical predictions and experimental analyses of the stabilization of the σ phase with increasing ε , two differences are apparent: First, the σ phase could be directly accessed from the disordered state experimentally, whereas theory predicted an intervening window of an equilibrium BCC structure. Second, the minimum ε value required for stabilization of the tetragonal structure was much higher in theory ($\varepsilon_{\min} \sim 2.25$) *versus* in experiment ($\varepsilon_{\min} \sim 1.32$). The first issue was rationalized based on the amplified fluctuation effects for these low- N diblock polymers, which causes truncation of the phase diagram at high $(\chi N)_{\text{ODT}}$.¹³⁹⁻¹⁴⁰

Lewis et al. sought to address the second disagreement by studying the phase behavior of polystyrene-*block*-poly(1,4-butadiene) (PS-PB) for $f_{\text{PB}} = 0.18 - 0.25$, between the HEX and BCC composition windows. This system was chosen as $\varepsilon = 1.7$ for the polymer pair compared well with the PEE-PLA diblock, which exhibited the formation of the σ phase over a wide composition window. However, high-resolution synchrotron SAXS analyses of the PS-PB samples revealed a complete absence of a σ phase for diblock compositions between the BCC and HEX forming regions, consistent with SCFT predictions for $\varepsilon = 1.7$.¹⁴¹

SCFT assumes Gaussian chain statistics to calculate the entropic penalty of chain stretching.¹⁴⁰ But, the finite extensibility of short diblock chains presents a limitation to the assumption. This physically manifests as an increased entropic penalty for stretching a significantly extended short diblock polymer chain. Hence, polyhedral warping of the micellar interface is amplified to address the additional requirement of uniformly filling space. The non-spherical micellar shape

subsequently stabilizes the locally more symmetric σ phase. In other words, the conformational asymmetry of short diblock polymers is apparently enhanced due to the finite extensibility of the short chains and the necessity to maintain constant mass density. On the other hand, long coronal polymers decrease the imposition of the polyhedral coronal shape onto the micellar interface due to decreased loss in the coronae chain stretching entropy. Thus, micelles have a nearly spherical core-corona interface and prefer a BCC structure over the σ phase to decrease non-uniform chain stretching.¹¹²

Bates and co-workers speculate that the transition where the amplification of conformational asymmetry occurs for short chains is concomitant with the transition from entanglement to Rouse dynamics in polymer melts. Calculation of the invariant entanglement degree of polymerization of a library of homopolymers: $\left(\bar{N}_x = \frac{N_e b^6}{v^2}\right)$, where N_e – entanglement degree of polymerization; v – reference volume; b – statistical segment length of the block, revealed a universal value of $\bar{N}_x \sim 400$. For PEE-PLA $\bar{N}_b \sim 80 < 400$, whereas for PS-PB, which in agreement with SCFT predictions does not form a σ phase, possesses $\bar{N}_b \sim 800 > 400$. Hence, the discrepancy between the predictions from Xie et al. and experiments from Schulze et al. can be reconciled based on the ostensible increase in the conformational asymmetry of short PI-PLA due to deviation from Gaussian chain statistics caused by the limited extensibility of the polymer chain. In the limit of $\bar{N}_b \sim 1$, the shape of the amphiphile dictates its self-assembly behavior as observed for solvated small-molecule surfactants described in Section 1.8. Accessing complex morphologies at large molecular weights will require polymer pairs with $\varepsilon > 2.25$ as predicted by SCFT. However, large molecular weights impose severe kinetic limitations on intermicellar chain exchange¹⁴² to achieve an ordered structure.¹⁰⁹

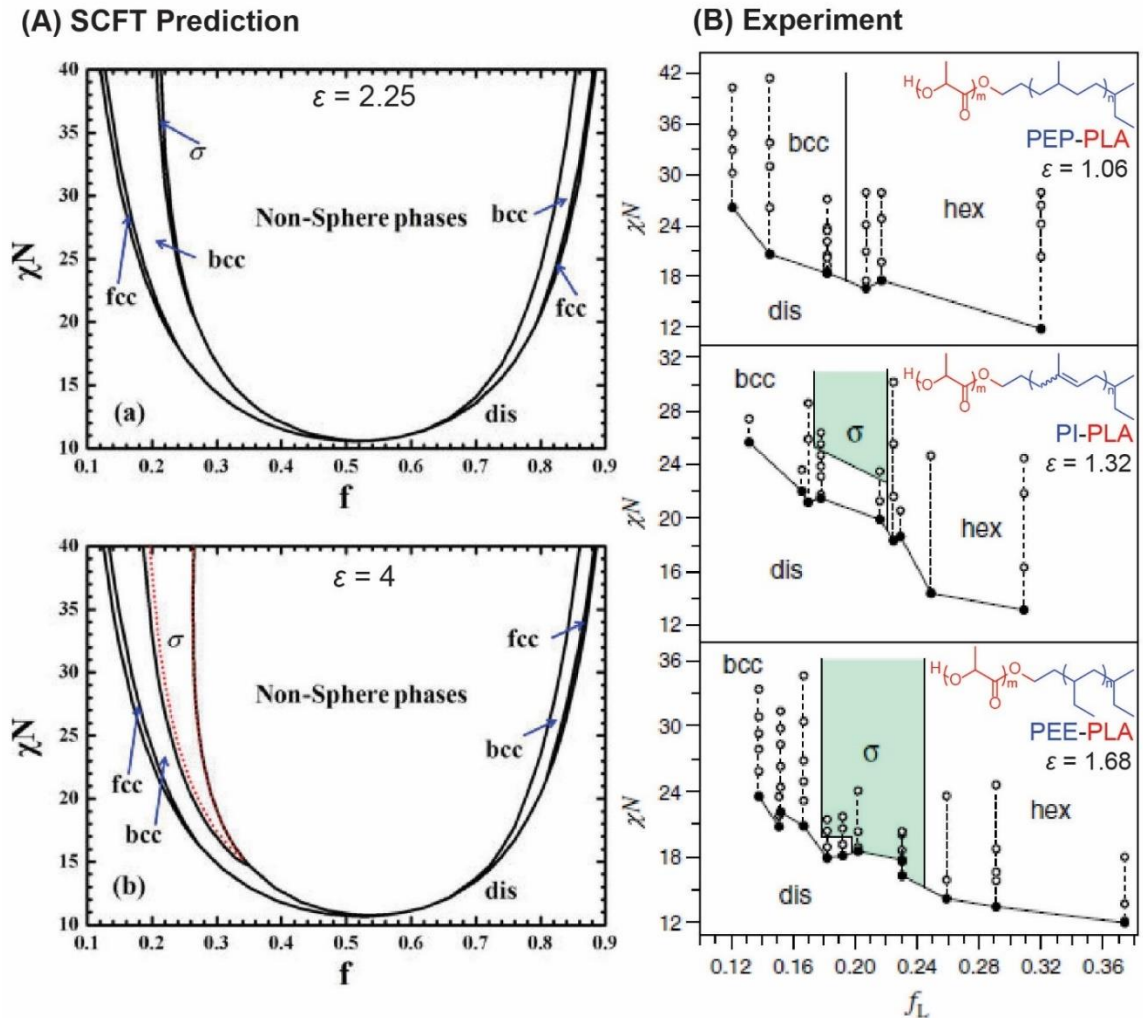


Figure 1.14. Diblock phase diagrams obtained as a function of conformational asymmetry of the two blocks. (A) SCFT predicts an increase in the composition window for the σ phase when ε increases from 2.25 to 4 for an AB diblock. Reprinted (adapted) with permission from Xie, N.; Li, W.; Qiu, F.; Shi, A.-C., σ Phase Formed in Conformationally Asymmetric AB-Type Block Copolymers. *ACS Macro Letters* **2014**, *3* (9), 906-910. Copyright 2014 American Chemical Society. (B) The σ phase window is experimentally observed to increase for diblock polymers with greater ε . The asymmetry values required to observe a σ phase experimentally are much lower than those predicted by SCFT. Reprinted with permission from Schulze, M. W.; Lewis III, R. M.; Lettow, J. H.; Hickey, R. J.; Gillard, T. M.; Hillmyer, M. A.; Bates, F. S., Conformational Asymmetry and Quasicrystal Approximants in Linear Diblock Copolymers. *Phys. Rev. Lett.*

The formation of FK phases inherently involves arrangement of different micelle sizes on low-symmetry lattices. Kim et al. used complex thermal processing strategies to modulate the micelle size distribution in PI-PLA.³⁷ Two diblock polymers IL-58-15 ($M_n = 5010$ g/mol, $f_{PLA} = 0.15$) and IL-52-20 ($M_n = 4830$ g/mol, $f_{PLA} = 0.2$), which exhibited the respective phase progressions with increasing temperature were chosen: $\sigma \rightarrow \text{BCC} \rightarrow \text{Dis}$ and $\text{HEX} \rightarrow \text{Dis}$ (Figure 1.15). Cooling the disordered state slowly led to reversible transitions to the original low- T phases. However, quenching the samples into liquid nitrogen (-196 °C) drastically changed the phase behavior at elevated temperatures. Heating a quenched IL-58-15 sample to 85 °C yielded a SAXS pattern that conformed to the Laves C14 structure (Figure 1.15A). Alternatively, heating an IL-52-20 sample to 85 °C led to nucleation and growth of the previously observed σ phase. However, another quenched sample of the same polymer exhibited the formation of a Laves C15 structure at $T = 100$ °C (Figure 1.15B).³⁷ The C14 structure involves AABBA... stacking of interstitial triangular nets with $\alpha\beta$... layering of Kagomé nets whereas the C15 phase is comprised of AABBCCAA... and $\alpha\beta\gamma$... stacking of layers.¹⁴³ These phases have been observed in phase space vicinity in intermetallic alloys, with no established methodologies to a priori determine the thermodynamically stable state.¹⁴⁴⁻¹⁴⁵ Hence, the observation of the two mesophases in diblock polymers of similar molecular weights and compositions is not surprising. Furthermore, calculations using SCFT yield free energy differences of $\sim 10^{-3}k_B T$ per chain between the various ordered structures, indicating the complex in phase space for these diblock polymers.

The Laves C14 and C15 phases possess disparate micelle volume distributions that vary $\pm 20\%$ about a mean value. In contrast, the σ phase exhibits a narrower size distribution of $\pm 9\%$ around the mean size. Kim et al. suggest that the large differences in the micelle core volumes of the Laves

structures can be accommodated by the dispersity of the PLA block. Additionally, the authors posit that violent quenching can cause micelle fission and fusion,¹⁴⁶ which in conjunction with intermicellar chain exchange allows the system to achieve the micelle size distribution required by the low-symmetry structures.¹⁴⁷ Corresponding SCFT simulations of simplified binary AB blends of different A block lengths indicate regions of stability for σ , A15, C14, and C15 structures as a function of blend composition and ratio of the chain lengths of A.¹⁴⁸⁻¹⁴⁹ These simulation results have recently found experimental validity with the observation of σ and A15 structures in blends of PS-PB diblock polymers containing PB core blocks of two different M_n .¹⁰⁹

The metastability of the Laves phases was probed by heating the samples to their respective T_{ODTs} . Surprisingly, the disordered states corresponding with different processing histories showed incongruent q positions for the correlation hole scattering maxima.¹⁴⁹ Moreover, cooling the disordered states of the C14 and C15 phases back to 85 and 100 °C led to reformation of the Laves phases. A difference in the q^* of the disordered structure factor profiles implies a dissimilarity in the micelle-size distribution, which apparently remains unaffected upon slow heating and cooling. This advocates for strong structuring of the disordered state, which preserves the memory of the initial ordered structure.

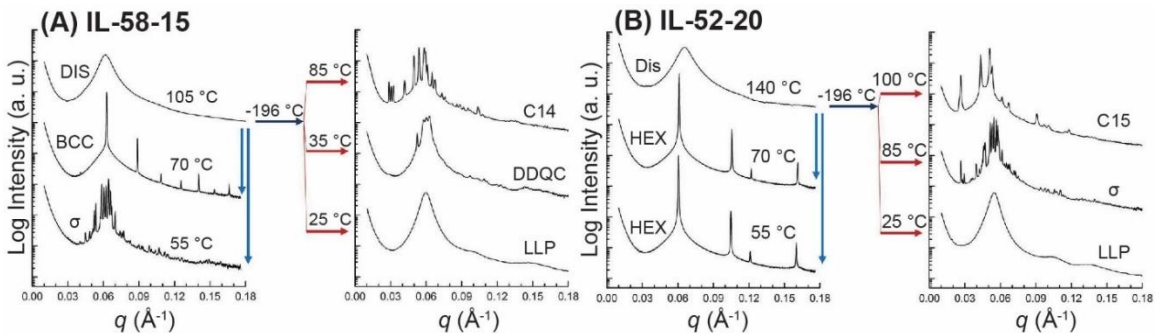


Figure 1.15. Thermal processing of PI-PLA diblock polymers. (A) Quenching into liquid nitrogen and rapidly heating the IL-58-15 polymer leads to the formation of C14 and DDQC structures. (B) Processing the more symmetric IL-52-20 with the same protocol yields the C15 and σ phases. Both samples remain

arrested in a LLP when heated to 25 °C. From Kim, K.; Schulze, M. W.; Arora, A.; Lewis, R. M.; Hillmyer, M. A.; Dorfman, K. D.; Bates, F. S., Thermal processing of diblock copolymer melts mimics metallurgy. *Science* **2017**, *356* (6337), 520-523. Reprinted with permission from American Association for the Advancement of Science.

Micelle-forming diblock polymers exhibit a T_{ODT} for disordering of micelles from a lattice followed by a high T_{MDT} for mean-field micelle dissociation into individual chains.¹²⁵ The free chain concentration progressively increases with temperature from T_{ODT} , until no micelles exist when T_{MDT} is reached. The distribution of the disordered state can be modified via interparticle chain exchange or micelle fission and fusion, which is energetically more expensive.¹⁴⁷ The authors argue that the slow rate of chain exchange even for $T > T_{ODT}$ possibly preserves the micelle-size distribution obtained after the initial quench from the disordered to the ordered state, allowing access to the metastable C14 and C15 structures after multiple heating and cooling cycles. Steurer & Deloudi have also hypothesized the formation of multiple precursor liquid states close to the T_m of metal alloys, which exhibit complex phase formation.¹⁵⁰ This observation warrants additional investigation of the disordered states of these complex morphologies across material classes.¹⁵¹ Understanding the structure of ‘disorder’ can provide additional insights into phase nucleation and growth of equilibrium and non-equilibrium low-symmetry structures.

Additional complexity in block polymer self-assembly can be induced by varying the molecular architectures to form multiblocks, star, and bottlebrush polymers.¹²⁰⁻¹²¹ SISO tetrablock polymers of similar compositions and molecular weights to Lee et al. were observed to self-assemble into the FK A15 phase¹⁵² as well as an intriguing assembly of micelles on a simple hexagonal lattice (HEX_s).¹⁵³ The following transition was observed: A15 \rightarrow σ \rightarrow Dis with increasing temperature, which agrees well with SCFT predictions except for an intervening window of the BCC structure between σ and disordered micelles.¹⁵⁴ However, cooling the disordered state initially led to the

formation of a BCC structure that slowly transformed into a σ phase upon extended annealing analogous to observations from Lee et al.³⁶

Increased ε also enabled access to additional intermediate complex structures. Highly conformationally asymmetric poly(dimethylsiloxane)-*block*-poly(2,2,2-trifluoroethyl acrylate) was reported to form well-ordered σ and C14 phases.¹⁵⁵ Recently, an A15 structure was also reported in the self-assembly of poly(dodecyl acrylate)-*block*-poly(D,L-lactide) at more symmetric compositions than the σ phase.³⁸ The observation of the cubic structure at lower compositional asymmetry than the σ phase has precedence in the self-assembly of .wedge-shaped dendrons,³⁵ giant surfactants,⁴⁰ and hydrated LLCs.³¹ The large dodecyl pendant group drives large ε (> 3), which enables compensation for the increased interfacial area of the micelles in the A15 structure by the gain in chain stretching free energy of the core block.¹¹² Miktoarm architectures have also been employed to amplify conformational and compositional asymmetries to access A15 and σ phases.¹⁵⁶⁻¹⁵⁷ Takagi and co-workers observed the formation of a σ phase in poly(1,4-butadiene)-*block*-poly(ε -caprolactone) corona-doped with homopolymer PB.¹⁵⁸ The complex structure was only observed for dopant $M_n < \text{block } M_n$. In contrast, using a larger molecular weight of the additive led to stabilization of only the BCC and HEX morphologies.¹⁵⁹ The smaller additives probably solubilize the corona, relieving the chain stretching penalty to form a σ phase instead of a BCC structure.¹¹² In a similar vein, Mueller et al. reported the formation of σ , C14, and C15 structures in PS-PB diblocks core-doped with PB homopolymer. This observation is expounded upon in Section 1.8. The σ and A15 phases have also been reported in the self-assembly of sugar-terminated polyolefins.¹⁶⁰⁻¹⁶¹ The alkyl tail consists of pendant groups, which increase the conformational asymmetry of the molecules and help stabilize the FK morphologies.

The simple geometric argument of IQ proposed by Bates and co-workers is insufficient to capture the rich complex phase behavior in neat diblock polymers. Inspired by the W&P solution

for the Kelvin problem, Kamien and Zihlerl proposed that the A15 structure should be the thermodynamic ground state of uniform self-assembling particles with a hard core and a deformable corona of large spatial extent.¹⁶²⁻¹⁶³ Note that the σ phase was not considered for the calculation. Grason and co-workers used a diblock foam model (DFM) to combine minimization of interfacial area and chain stretching penalties to mirror real polymeric systems.¹¹¹⁻¹¹² For short diblock polymers the conformational asymmetry leads to deformation of the micellar cores inducing polyhedral interfaces. At the polyhedral surface limit (PSL), the interface is warped to closely mirror the W-S cell shape of the corresponding coordination environment. The free energy of phase formation was calculated as functions of the entropic loss of chain stretching and the enthalpic penalty associated with the interfacial contacts between the core and corona domains while allowing for dissimilar volumes of the cells. The chain stretching penalty in the ordered phases increased as: $BCC < A15 < \sigma < C14/C15$, whereas the dimensionless area increased as: $C15/C14 < \sigma < A15 < BCC$. However, the overall free energy was minimum for the σ phase, insinuating its equilibrium nature for weakly conformationally asymmetric diblock polymers. In harmony with SCFT, results from DFM also indicated the near degenerate nature of these complex phases in block polymers. Hence, thermal or chemical processing are viable strategies to induce kinetically limited non-equilibrium structures. Guided by theory, materials discovery using diblock polymers is practically infinite and provides a vast phase space for accessing complex morphologies over varied length scales.^{120-121,164-165}

1.8 Micellar lyotropic liquid crystals

Section 1.1 details the principles that guide phase selection in solvated amphiphiles. This section explores the various micellar morphologies observed in aqueous LLCs and draws analogies with phase formation in neat dendrons, shape-amphiphiles, and block polymers. The formation of

bicontinuous LLC mesophases and their associated applications have been detailed elsewhere.^{17,166-}

167

Amphiphiles in water exist as unimers until the critical micelle concentration (CMC) is reached. As unimers, the hydrophobic tails are solvated by structuring of the water molecules around them. The entropic gain of releasing the water molecules at CMC leads to aggregation of the tails to form micelles.³ At high hydrations, micelles exist in a disordered solution, minimally correlated with each other. As the micelle concentration is increased, the coronae of these micelles impinge with each other, leading to unfavorable inter-coronal interactions. The increased micellar correlations then induce self-assembly into ordered morphologies.

BCC packing of micelles has been identified in the aqueous self-assembly of ionic^{13,31,95} and non-ionic amphiphiles,^{14,168-169} as well as in solutions of diblock polymers in a solvent selective to one of the blocks.¹⁷⁰⁻¹⁷¹ Note that BCC has not been observed as a Type II LLC phase in aqueous surfactant self-assembly. The closest-packed FCC structure has also been widely reported in the self-assembly of hydrated polyoxyethylenes^{14,172} and solvated diblock polymers.^{170,173-176} The formation of the BCC and FCC structures in non-ionic amphiphiles is dictated by the coronal structure. Short corona chains yield ‘crew-cut’ micelles, which are analogous to hard spheres, and pack on an FCC lattice to maximize the packing fraction. The molecular conformation of the coronae chains can be changed via surfactant solvation to yield ‘hairy’ micelles. Consequently, the micelles self-assemble into the lower packing fraction BCC lattice to reduce unfavorable intermicellar coronal chain overlap.¹⁷⁰⁻¹⁷¹ LLCs containing polyoxyethylenes typically form an FCC structure near the lyotropic ODT, an observation that was recently rationalized.¹⁷⁷ At high hydrations, the coronal poly(ethylene oxide) chains collapse onto the hydrophobic-hydrophilic interface so as to shield the core from unfavorable interactions with the aqueous domain.¹⁷⁸⁻¹⁷⁹ Hence, the micelles adopt an effectively crew-cut form and prefer to self-assemble onto an FCC

lattice.

Type II FCC packing of micelles was first reported in aqueous LLCs of soy bean phosphatidylcholine (PC) doped with cyclohexane, isooctane, or R-(+)-limonene (Figure 1.16).¹⁸⁰ On the other hand, using α -tocopherol as the dopant induced the formation of a C15 structure, which contains two differently-sized water pools arranged in a paraffin matrix with $Fd\bar{3}m$ symmetry. The dependence of the phase behavior on the additives was rationalized based on localization of the small hydrophobic molecules between the micelles to relieve chain packing frustration present in an FCC structure. In contrast, α -tocopherol probably acts as a cosurfactant due to its long hydrophobic tail, which allows for variations in micelle curvature that are required for the formation of two micelle sizes in the C15 structure. Deng & Zhao employed an alternative strategy to induce the formation of an inverse FCC mesophase using polar dopants.¹⁸¹ Addition of ionic sodium benzoate and sodium 2-bromoethanesulphonate to LLCs containing gemini dodecyltrimethylammonium bromide led to the stabilization of the closest-packed structure.¹⁸¹ However inclusion of long chain sodium hexanoate or sodium laurate triggered the formation of a Type II C15 morphology¹⁸² analogous to findings by Mezzenga and co-workers.¹⁸⁰

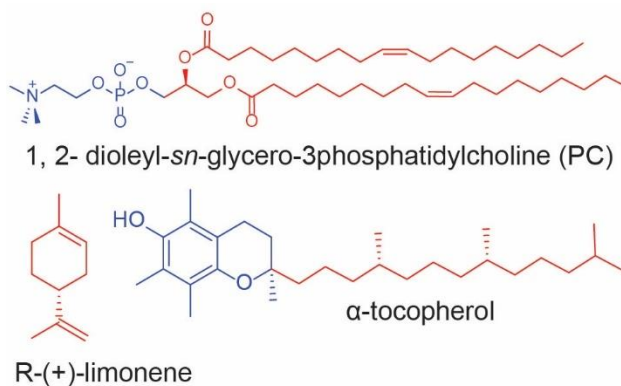


Figure 1.16. Molecular structures of molecules used in study by Martiel et al.¹⁸⁰. Mixtures of PC and limonene form a Type II FCC structure whereas using tocopherol as the dopant leads to the formation of the inverse Laves C15 structure.

The HCP and FCC structures differ only in the stacking of the hexagonally closest-packed layers. The cubic structure involves an ABCABC... stacking of layers whereas the hexagonal lattice is comprised of the entropically less favorable ABAB... stacking.¹⁸³ The packing fraction and *CN* of the micelles are identical for both morphologies. However, the HCP structure ($P6_3/mmc$) is rare in LLC self-assembly. Clerc discovered the formation of a Type I HCP structure in the packing of hydrated $C_{12}E_8$ micelles.¹⁸⁴⁻¹⁸⁶ Similar to the FCC lattice, the hexagonal phase was observed at high hydrations followed by a BCC structure at lower water contents.¹⁸⁶ Lee and co-workers observed the formation of a metastable HCP structure by thermally quenching aqueous PB-PEO micelles.¹⁷⁵ Extended annealing caused a transformation to the homologous FCC lattice via an intermediate randomly close-packed hexagonal structure. Formation of the HCP lattice was rationalized based on mechanical stresses inherent in the sample and the small crystallites formed after the violent quench.

Liu et al. reported an HCP structure in a systematic exploration of the phase behavior of alkyltrimethylammonium surfactants with varied tail lengths and counterions.¹⁸⁷ Highly hydrated phosphate, oxalate, and carbonate counterions displayed the following phase progression with decreasing hydration: HCP \rightarrow A15 \rightarrow H_I. Alternatively, the surfactants containing Br⁻ and Cl⁻ counterions only formed A15 and H_I morphologies. The authors argue that the micellar phase behavior is dictated by the extent of counterion-headgroup dissociation. However, the specific rationale guiding phase behavior in Type I ionic micelles was only established later by Mahanthappa and co-workers.^{31,95} A HCP arrangement of Type II micelles has been observed using SAXS by Seddon and co-workers in mixtures containing dioleoylphosphatidylcholine (DOPC), dioleoylglycerol (DOG), cholesterol, and water.¹⁸⁸ This presents a singular example of this type of inverse micellar packing.

The FK A15 structure has been the most prevalent Type I LLC morphology across all surfactant

classes.^{14,25,31-32} Balmbra et al. initially identified the TCP phase in the self-assembly of dodecyltrimethylammonium chloride at LLC hydrations intermediate between the H_I morphology and disordered micelles. The authors proposed a structure involving a BCC arrangement of rods, which was later found to be incorrect.¹⁸⁹ The currently accepted structure for A15 was proposed by Vargas et al. in 1992, which involves two quasispherical micelles arranged on a body-centered cubic lattice with six disc-shaped micelles on the face centers.²⁹ The A15 structure formed by neat dendrons, giant-shape surfactants, and block polymers shows an arrangement of micelles analogous to that proposed by Vargas et al., as evidenced by TEM and real-space electron density analyses.^{34,38,40} There is a solitary report about the formation of a Type II A15 structure, which was observed in aqueous LLCs of zwitterionic bis(alkyltriazolium sulfobetaine) surfactants.¹⁹⁰ Associated electron density reconstructions obtained from high-resolution SAXS data also conform with the two-micelle class model (Figure 1.17).

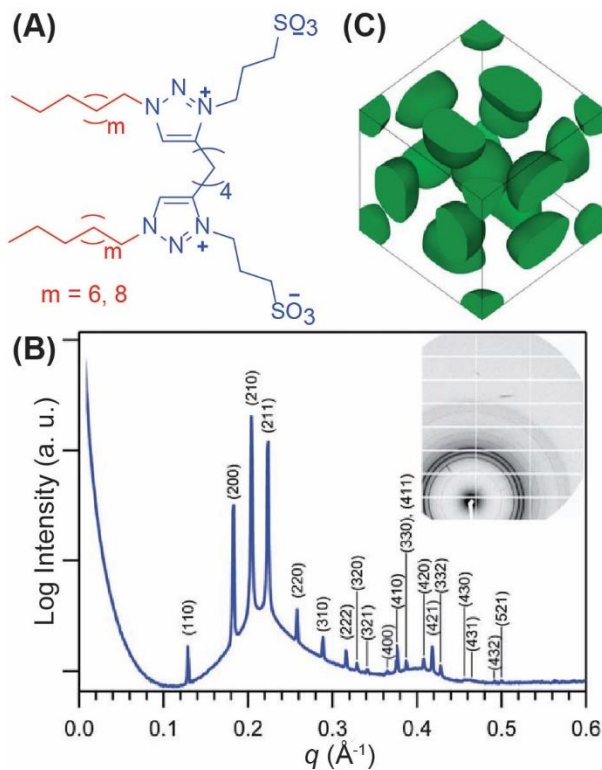


Figure 1.17. (A) Bis(alkyltriazolium sulfobetaine) surfactants that form an inverse A15 structure in aqueous LLCs. (B) Azimuthally integrated 1D SAXS trace obtained from the well-ordered cubic FK phase and indexed using $Pm\bar{3}n$ symmetry. The inset shows the 2D scattering pattern. (C) Electron density reconstruction obtained from the SAXS data, clearly displaying the two kinds of micelles expected for the structure. Republished with permission from Royal Society of Chemistry, from Inverse $Pm\bar{3}(-)n$ Cubic Micellar Lyotropic Phases from Zwitterionic Triazolium Gemini Surfactants, Perroni, D. V.; Mahanthappa, M. K., *Soft Matter* **2013**, 9 (33), 7919-7922; Copyright 2013; permission conveyed through Copyright Clearance Center, Inc.

The C15 structure is a common Type II LLC with inverse micelles of two sizes packed on a cubic lattice. Isostructural with the $MgCu_2$, the large micelles are situated on a diamond lattice with the smaller micelles present in the tetrahedral voids. The structure was first discovered in the lipid extract from *Pseudomonas fluorescens* by Luzzati et al.³⁰ The highly complex multicomponent lipid system precludes molecular level understanding of the factors that stabilize the Laves phase. The $Fd\bar{3}m$ structure has also been observed in LLCs of multicomponent neutral and charged lipid mixtures^{17,191-193} and binary non-ionic surfactants.¹⁹⁴⁻¹⁹⁵ Yagmur & Rappolt have compiled a list of lyotropic systems that self-assemble into C15 lattices.³³

The preference for the formation of the C15 morphology has been rationalized based on chain stretching considerations as compared to the canonical phases.¹⁹⁶ Using real-space electron density reconstructions obtained from SAXS data, Rappolt and co-workers showed that the soft micellar coronae deform to adopt the shape of the W-S cell of the lattice.¹⁹⁶ The polyhedral shape of the micelles necessitates non-uniform chain stretching to completely fill space in the hydrophobic domain inducing regions of packing stress at the corners of the polyhedra. Calculation of the micelle sphericity ($= IQ^{1/3}$ as calculated by Lee et al.¹¹³) of FCC, BCC, HCP, and C15 structures revealed that the Laves phase contains the most spherical W-S cells and hence presents the least

chain stretching penalty among the phases considered. This argument is analogous to that put forth by Bates and co-workers for short diblock polymers, as both systems involve filling space with covalently bonded chains with finite extensibilities. Note that Rappolt et al. did not compare the sphericity of C15 with the σ phase as the latter structure has not been observed in Type II LLCs.

The ternary systems that stabilize the Type II Laves phase conform to three classes: surfactant mixtures with a co-surfactant,^{180,182} LLCs with long-chain hydrophobic molecules as additives to lower curvature phases (H_{II} , $Pn\bar{3}m$),¹⁹⁷ and LLCs containing polar additives in the core.¹⁹⁸ As mentioned earlier, the co-surfactant locally segregates, probably aiding the stabilization of the two micelle curvatures required for formation of the C15 morphology.¹⁹⁶ The long chain additive provides another avenue by localizing between the micelles in the hydrophobic matrix to relieve packing frustration and locally modulate interfacial curvature. The inverse Laves phase was also observed in LLCs of monoolein, where the core was doped with ≤ 6 wt% of polar(amidoamine) dendrimers. Note that the micelles in the C15 lattice differ in volume by $\pm 20\%$ about the mean, which the low weight fraction of the dopant cannot fulfil. Molecular dynamics simulations showed strong interactions between the amine groups and the monoolein headgroups in the micellar core. The branched nature of the polar moiety possibly forces the interface to bend towards the hydrophilic domain to maximize interactions with the headgroups inducing micelle formation. Consequently, the micelles self-assemble into a C15 lattice as rationalized by Rappolt et al.¹⁹⁶ Interestingly, all single lipid systems that form the C15 Laves mesophase involve at least two lipidic chains attached to a single headgroup¹⁹⁹⁻²⁰⁰ or a highly branched hydrophobic tail.¹⁹⁴⁻¹⁹⁵ It is possible that the relative spatial orientation of the lipid chains and the branches stabilize the different curvatures corresponding to the two micelle sizes present in the structure.

Despite the ubiquity of the inverse micellar phase, Type I structures with $Fd\bar{3}m$ symmetry have been limited to two examples, both in ternary systems. Wang et al. reported the self-assembly of

hydrated Brij® 97 (10-oleyl ether) micelles doped with isopropyl myristate into a C15 lattice.²⁰¹ However, the 1D SAXS intensity pattern presented for the structure exhibits only three maxima corresponding to the (111), (220), and (331) reflections. Additionally, the relative peak intensities are unlike what has previously been observed for the C15 morphology. Higher-resolution scattering data are imperative for unambiguous phase assignment of these LLCs. Mahanthappa and co-workers definitively illustrated the formation of the Laves phase in decane-swollen micelles of tetramethylammonium decanoate using synchrotron SAXS analyses.²⁰²⁻²⁰³ The C15 structure was observed at LLC hydrations greater than that for the H_I mesophase. Increasing the water content further yielded a surprising discovery of a Laves C14 structure (Figure 1.18A), which consists of 12 TCP quasispherical micelles of three different volumes arranged on a hexagonal lattice (*P6₃/mmc* symmetry). Electron density reconstructions obtained for the two lattices clearly show the presence of disparate micellar volumes in different coordination environments (Figure 18B). The observation of the two structures in LLCs of similar hydrations is analogous to the observation of these phases in phase space vicinity in neat diblock polymers as well as in intermetallic alloys.^{37,149,204}

LLCs containing tetramethylammonium decanoate show the following phase progression with increasing water content: H_I → A15 → BCC. Addition of 40 wt% decane modifies the transitions as: H_I → C15 → C14 → BCC, where the A15 window has been replaced completely by the Laves phases. The matched carbon numbers of the surfactant and the hydrophobic additive has been shown to induce localization of the dopant at the center of the micellar cores leading to an increase in the micellar curvature.²⁰⁵⁻²⁰⁶ The authors argue for a preferential segregation of decane among the different particle classes via intermicellar exchange to yield the ± 20% variation in micelle volumes required for the formation of the C14 and C15 mesophases. This reasoning is comparable to that of Kim et al., where the core volume disparity was hypothesized to stem from the inherent

dispersity of the PLA block in PI-PLA diblocks.^{37,149}

The strategy of core-doping micelles to access Laves phases has been successfully applied to other soft material systems. Mueller et al. showed that PS-PB diblock polymer micelles doped with PB of the same molecular weight as the PB core block self-assemble into C14 and C15 morphologies.²⁰⁷ Additionally, Uddin et al. reported the formation of a C15 structure in neat diblock polymer micelles of PDMS-PEO, with residual unreacted PDMS monomer in the core.²⁰⁸ In addition to experimental evidence, Lindquist et al. discovered the formation of C14 and C15 structures in simulations containing moderately polydisperse hard spheres.²⁰⁹ Similarly, Engel and co-workers found that including an evolving dispersity of hard spheres to mimic interparticle chain exchange in MD simulations stabilizes the C15 structure as well as a complex AB₁₃ lattice.²¹⁰ Note that the AB₁₃ structure has been experimentally observed in mixed micelles of PS-PI and PS-PDMS in diethyl phthalate, a PS-selective solvent.²¹¹⁻²¹² These discoveries lend support to a notion of universality in the formation of Laves phases by core-doping soft, reconfigurable micellar systems. However, they raise questions about the apparent absence of a Type II C14 mesophase, given its close relationship with the C15 structure.

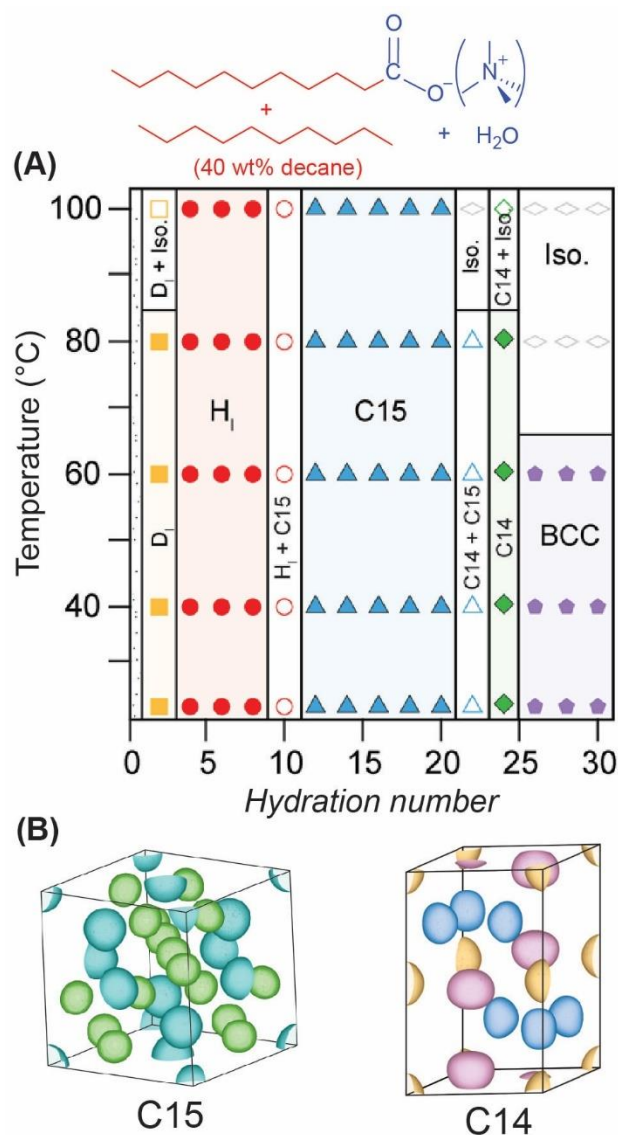


Figure 1.18. (A) Temperature *versus* hydration number phase diagram constructed for aqueous LLCs containing tetramethylammonium decanoate and 40 wt% decane using temperature-dependent SAXS analyses. (B) Electron density reconstructions obtained for the C15 and C14 structures showing the different classes of highly faceted micelles. Reprinted (adapted) with permission from Baez-Cotto, C. M.; Mahanthappa, M. K., Micellar Mimicry of Intermetallic C14 and C15 Laves Phases by Aqueous Lyotropic Self-Assembly. *ACS Nano* **2018**, *12* (4), 3226-3234. Copyright 2018 American Chemical Society

The FK σ and A15 phases have been observed in neat, undiluted self-assembly of charge-neutral

building blocks. The absence of a lyotropic σ phase is striking given the ubiquity of the related A15 structure in Type I LLCs. Kim et al. were investigating the lyotropic self-assembly of dianionic bis(tetramethylammonium) decylphosphonate (DPA-TMA₂) as a model system for rheological characterization of micellar LLCs. At low hydrations, LLCs exhibited the H_I and A15 mesophases and a BCC structure was obtained near the lyotropic ODT. However, samples with water contents intermediate to the A15 and BCC morphologies exhibited a SAXS pattern with at least 60 instrument-resolution limited maxima that was not previously reported for any LLC mesophase (Figure 1.19A). The pattern was qualitatively similar to traces obtained in the self-assembly of wedge-shaped dendrons,³⁵ di- and tetrablock polymers,^{36,113} and POSS-based giant surfactants.⁴⁰ Crystallographic analyses of the SAXS trace indicated the formation of a lyotropic FK σ phase with $P4_2/mnm$ symmetry.³¹ Concurrent electron density reconstructions showed the formation of the expected tetragonal unit cell with 30 micelles situated at five different symmetry-equivalent positions on the gigantic lattice.

The discovery of the σ phase in LLCs established its universality in different classes of self-assembling soft materials. The phase progression observed with increasing hydration $A15 \rightarrow \sigma \rightarrow BCC \rightarrow Dis$ is similar to that observed for wedge-shaped dendrons and diblock polymers with increasing temperature. The equivalency in hydration and temperature is easily understood based on their effects on interfacial tension. At low hydration, the ionic strength of the aqueous domain is high, leading to high interfacial tension with the hydrophobic core.⁵ The enthalpic penalty at the micellar interface reduces with increasing water content and decreasing overall concentration of ions in water. Similarly, the interfacial tension between the blocks in a diblock polymer is inversely dependent on temperature.²⁸ Hence, the observed phase sequence in both systems runs parallel to the decrease in interfacial tension, as dictated by hydration or temperature.

The LLCs of DPA-TMA₂ present a solvated, electrostatically stabilized FK phase as compared

to the neat, undiluted van der Waals force-stabilized σ forming systems discussed in the previous sections. The authors used MD simulations to understand the mechanisms that stabilize the σ phase in aqueous LLCs. Close inspection of the micellar shape from the MD simulations as well as the electron density reconstructions showed highly deformed hydrophobic micelle cores, which faceted to adopt the shapes of the W-S polyhedra of the corresponding lattice positions. The simulations also showed that the counterions were localized between the micellar facets, acting as the cohesive medium in the structure. The polyhedral shape of the micelle also implies a difference in micellar curvature at different positions on the hydrophobic-water interface leading to energetically expensive non-uniform counterion solvation. Inspired by the sphericity arguments of Rappolt et al.¹⁹⁶ and Bates and co-workers,¹¹³ the authors calculated the sphericity of the counterion cloud around each micelle in the MD simulations. The local ‘ionic sphericity’ followed this decreasing trend: $\sigma > A15 > BCC$, suggesting that the counterion distribution is most symmetrical in the tetragonal structure. The stability of the σ phase in LLCs is argued based on increased local particle symmetry, analogous to explanations provided for diblock polymers.

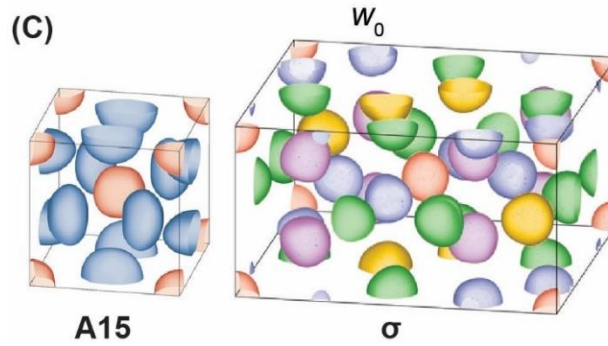
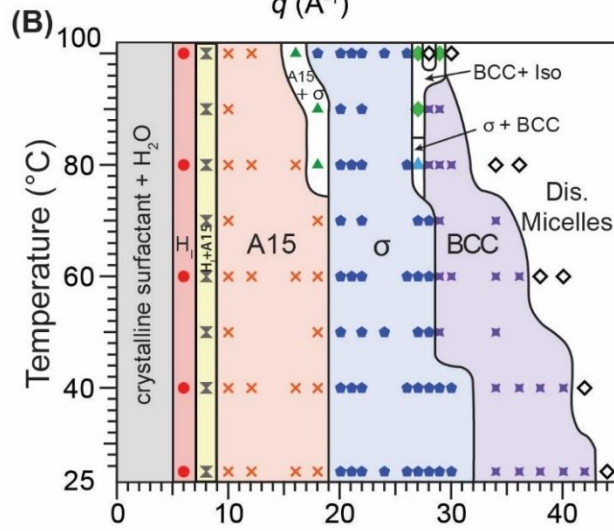
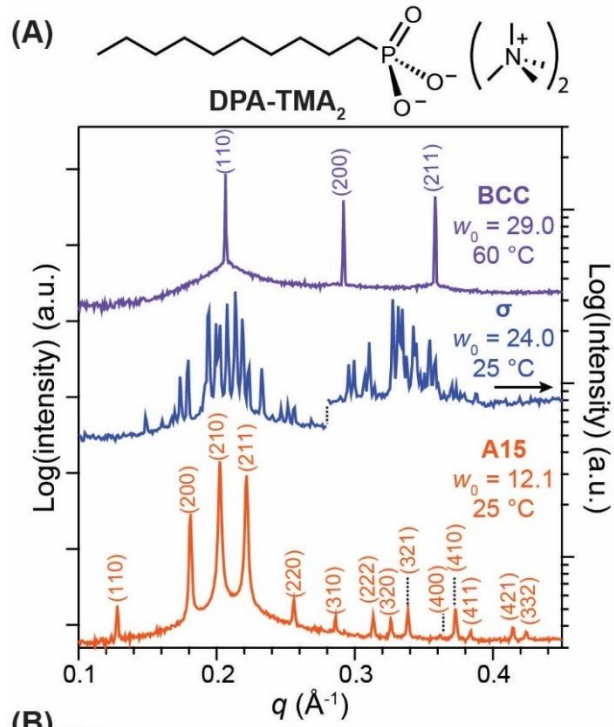


Figure 1.19. (A) 1D Intensity *versus* q traces obtained for the BCC, A15 and σ phases for LLCs of DPA-TMA₂. (B) An LLC phase portrait of the entire temperature- and concentration-dependent phase behavior of the surfactant. The water content is expressed as $w_0 = (\text{moles of water})/(\text{moles of surfactant})$. At 25 °C, the following phase behavior is observed with increasing hydration: $H_1 \rightarrow A15 \rightarrow \sigma \rightarrow BCC \rightarrow \text{Dis}$. (C) Electron density reconstructions of the σ and A15 phase derived from experimental SAXS data showing highly faceted micelles in different coordination environments. Reprinted (adapted) from Kim, S. A.; Jeong, K.-J.; Yethiraj, A.; Mahanthappa, M. K., Low-symmetry sphere packings of simple surfactant micelles induced by ionic sphericity. *Proc. Natl. Acad. Sci. U.S.A.* **2017**, *114* (16), 4072-4077, with permission.

The observed LLC phase behavior can then be understood as follows: as the hydration is lowered from the gas-like disordered micellar solution, a high-symmetry BCC structure nucleates so as to minimize the loss in translational entropy.¹³² Decreasing the hydration causes the counterion clouds of different micelles to impinge on one another causing a micellar rearrangement to maximize cohesion. Symmetry breaking ensues and the σ phase is preferred in this hydration state as the micelles in the structure have the most uniform counterion-headgroup solvation. Lowering the water content further triggers the formation of the A15 structure as the dearth of water to hydrate the headgroups forces the counterions to move closer to the core-corona interface, flattening micellar curvature and destabilizing the more spherical σ phase.³¹ Hence, formation of the high curvature tetragonal structure is induced by strong electrostatic interactions afforded by the dianionic headgroup. Few previous studies had explored the LLC phase behavior of ionic divalent surfactants,²¹³⁻²¹⁵ and none of them used synchrotron SAXS, which is essential for unambiguous identification of the complex structure.

The formation of FK and Laves phases present classic examples of global symmetry breaking in the lyotropic self-assembly of amphiphiles. The formation of the complex morphologies requires multiple micelle sizes with varying aggregation numbers. Core dopants and micelle curvature modifiers such as co-surfactants have yielded Laves phases, which exhibit large variations in

micelle sizes. In contrast, the A15 and σ phases contain micelles that involve narrower volume distributions. The discovery of a σ phase in the self-assembly of ionic surfactants leads to additional questions pivotal to understanding complex LLC phase selection: What molecular design rules govern Type I FK phase formation in ionic amphiphiles? Can non-ionic amphiphiles form other FK phases in addition to the already observed A15 structure? How do the phase stabilities and transitions compare with other soft material systems where these structures have been observed? This thesis aims to answer some of these questions and explore the rich phase space of micellar morphologies formed in lyotropic systems.

1.9 Quasicrystalline structures in soft materials

FK phases formed by intermetallic alloys present a glimpse into the complexity inherent to packing hard spheres of different sizes. The periodic nature of the structures yields sharp diffraction peaks, which are essential for definite phase assignment. This fundamental crystallographic principle was challenged by Dan Shechtman,²¹⁶ when he obtained a 10-fold rotational symmetric diffraction pattern from a deeply quenched Al-Mn alloy.²¹⁷ The high rotational symmetry precluded translational periodicity in the structure.²¹⁸ Levine & Steinhardt developed a model for the aperiodic crystal and calculated the diffraction pattern, which closely matched the experimental trace. They coined the term ‘quasicrystal’ (QC) for this class of aperiodic structures.²¹⁹ QCs involve an arrangement of particles that possess rotational symmetry yet lack translational periodicity. The discovery of the icosahedral quasicrystal (IQC), named for the major constituent motif of the aperiodic structure, marked a paradigm shift in formation of ordered structures in matter.

Following the discovery of the IQC, pentagonal, octagonal, decagonal, and dodecagonal QCs were discovered in a variety of binary and ternary metal alloys.²²⁰⁻²²² The IQC, pentagonal, and decagonal QCs have been obtained as thermodynamically stable structures.²²³ The IQC is the most

extensively studied QC in intermetallic alloys in terms of its structure, stability and formation. The morphology involves arrangement of atoms on a 3D icosahedral cage, which breaks symmetry due to its inability to tessellate space completely.²²⁴ The octagonal QC has only been observed in Ni-Si and Mn-Si alloys.²²⁵ Dodecagonal QCs (DDQCs), albeit with poor order, have been obtained in binary and ternary alloys including Ni-Cr,²²⁶ and Ta/V-Te²²⁷ systems. In contrast to the IQC, all other QCs are incommensurate in two directions. For example, the DDQC consists of quasiperiodic ordering of particles on a 2D plane. Aside from their novelty, metallic quasicrystals are potential candidates for applications such as low-friction surfaces,²²⁸ hydrogen storage materials,²²⁹ and heat insulators.²³⁰⁻²³¹

Mathematically, QCs can be treated as periodic crystals in nD space.¹⁵⁰ Projections of the structure into 3D yields periodic morphologies, called approximants. The FK phases comprise an important class of such periodic approximants. The alloy composition of the FK approximant differs only slightly with respect to the aperiodic structure suggesting a close structural relationship between the atomic arrangements. The library of periodic approximants for all QC classes in metal alloys is vast and has been extensively reviewed elsewhere.²²⁵ This section will focus on the formation, structure, and the approximants of DDQCs given their observation as soft material mesophases.

The FK A15 and σ phases are periodic approximants to the 12-fold rotationally symmetric DDQC. All three structures can be constructed using a square-triangle tiling scheme decorated with atoms at different coordinates in the third dimension (z) (Figure 1.20).²³²⁻²³³ The cubic A15 structure is composed of space-filling sets of four square tiles to yield a 4^4 arrangement. The σ phase consists repeating $3^2.4.3.4$ tiling of space i.e. an element consisting of three triangles and two squares. The unit cell of the two phases in tiling space has been marked with red dashed lines in Figure 1.20. In contrast, tiling in DDQC comprises a combination of $3^3.4^2$, $3^2.4.3.4$, 4^4 , and 3^6 tiling elements.²³⁴

The 3^6 tiling conforms to the FK Z phase, which is also a known approximant of the DDQC. The inability of the 12-fold symmetric structure to tile space completely causes symmetry breaking to generate the aperiodic 2D layers, which stack periodically in the z -direction to yield a DDQC.

In 2004, Percec, Ungar, and co-workers reported the discovery of a DDQC in the self-assembled wedge-shaped dendrons (Figure 1.21A).²³⁵ The molecules that initially formed the σ phase were observed to form the quasicrystalline structure albeit with some exceptions.^{35,236} The following phase progression was typically observed with increasing temperature: Crystalline \rightarrow DDQC \rightarrow σ \rightarrow Dis. Slow cooling from the disordered state produced an aligned QC, which exhibited 12-fold rotational symmetry in the 2D-SAXS patterns obtained upon impinging X-rays perpendicular to the quasiperiodic layers (Figure 1.21B). The proposed structure of the QC exhibits three hexagonal closest-packed layers at $z = 0, \frac{1}{2},$ and 1 each rotated successively by 30° with respect to each other to form a hexagonal antiprism with one micelle each at $z = \frac{1}{4}$ and $\frac{3}{4}$ (Figure 1.21D).²³⁶ The structure can be represented entirely by three tiling elements, consisting of a square and two triangles, decorated with micelles.²³⁴ This model differs from the DDQC formed in monoatomic liquids, where an additional rhombic tiling element was included.²³⁷⁻²³⁸ No phase transitions were observed upon annealing the DDQC at $T < T_\sigma$ for multiple days. This observation suggests that the QC formed in these dendritic systems is either a stable structure or a long-lived metastable state with a large activation barrier for transformation into a σ phase.^{234,239}

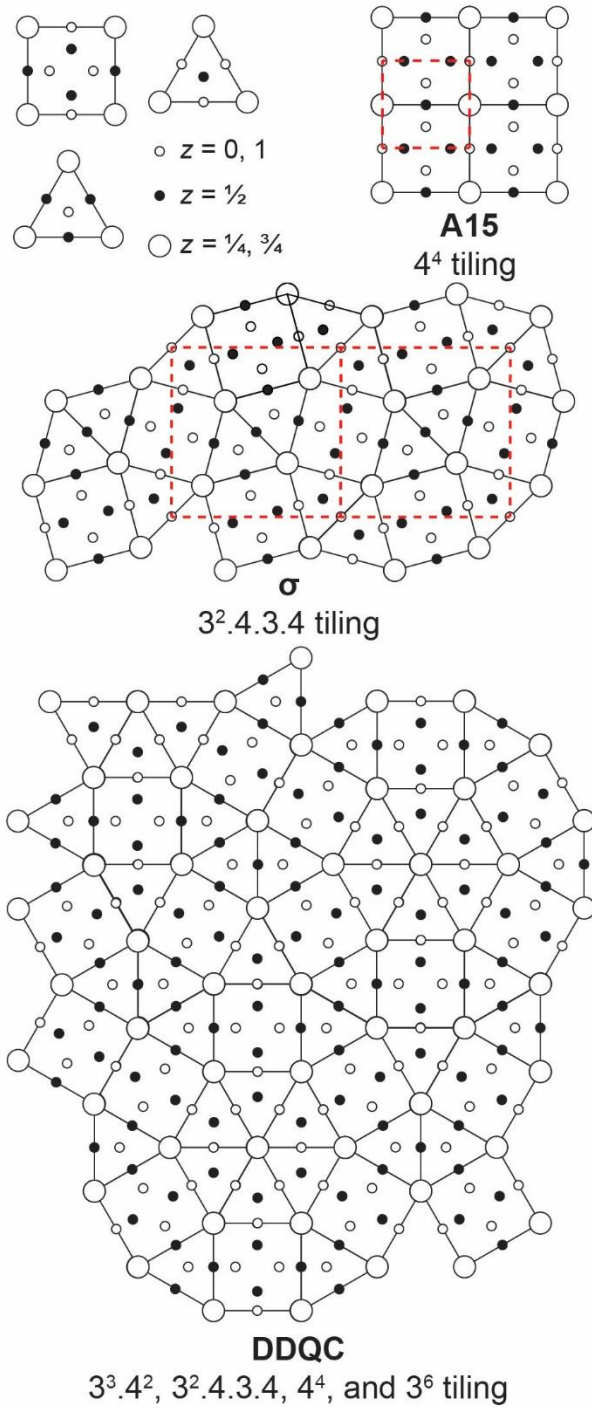


Figure 1.20. Square-triangle tiling elements that form the FK A15 and σ phases, and the DDQC. The spheres indicate the positions of the particles at $z = 0, 1/4, 1/2, 3/4,$ and 1 . The unit cells of the FK phases are marked with red dashed lines.

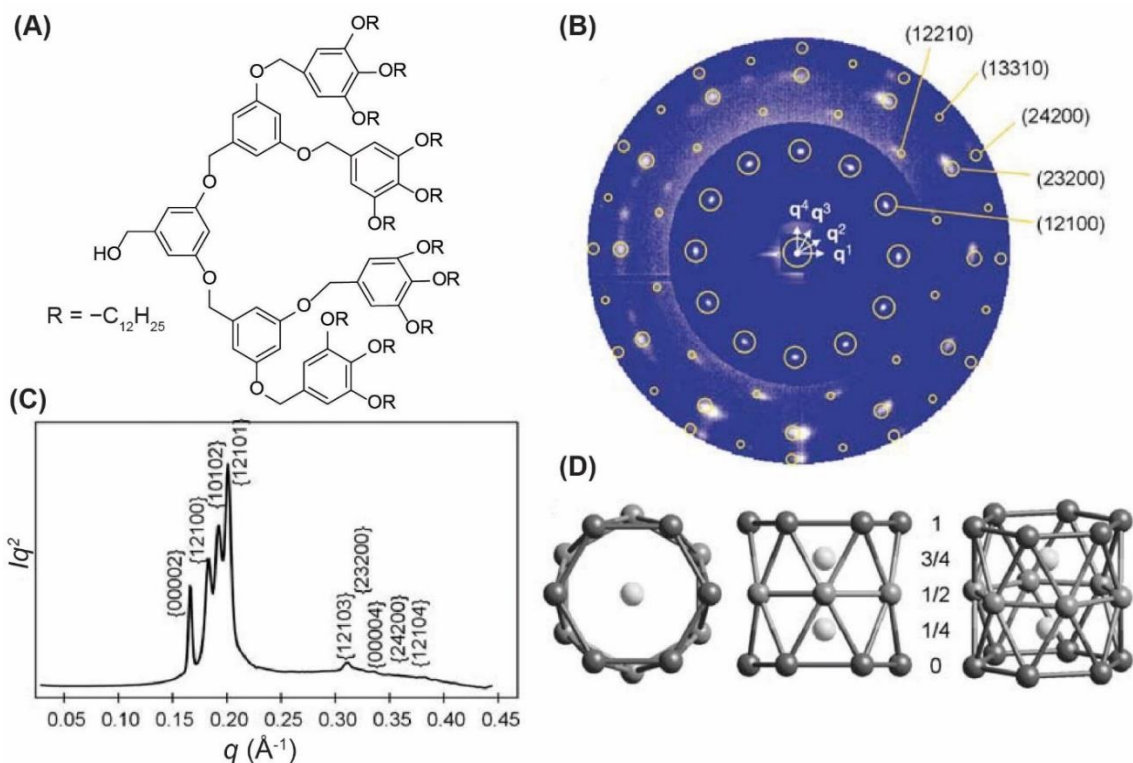


Figure 1.21. (A) Molecular structure of third generation dendron that forms a DDQC. (B) 2D-SAXS pattern normal to the quasicrystalline layers clearly showing the 12-fold rotational symmetry. The open circles indicate calculated reflections for a monodomain of the DDQC. (C) Azimuthally-integrated SAXS trace obtained from a polycrystalline sample of the QC. (D) Arrangement of micelles in a hexagonal antiprism motif of the 3D DDQC structure. The 2D layers of the QC are constructed using the three tiling elements shown in Figure 1.20. Reprinted by permission from Springer Nature Customer Service Centre GmbH: Nature - Zeng, X.; Ungar, G.; Liu, Y.; Percec, V.; Dulcey, A. E.; Hobbs, J. K., Supramolecular dendritic liquid quasicrystals. *Nature* **2004**, 428 (6979), 157-160. Copyright 2004.

Soon after, Hayashida et al. reported the formation of a DDQC in blends of ABC star terpolymers containing PI, PS, and poly(2-vinylpyridine) blocks tethered to one junction point blended with PS homopolymer.²⁴⁰ TEM micrographs revealed the square-triangle tiling consistent with dodecagonal ordering of cylindrical micelles on a 2D plane. The ratio of the number of triangles to squares was found to be ~ 2.309 , which is typical of a DDQC. Pseudo-single domain

scattering analyses also showed the expected 12-fold rotational symmetry. Surprisingly, eight reflections of the pattern displayed higher scattering intensities than the remaining four, in contrast to the oriented pattern obtained by Zeng et al. shown in Figure 1.21B. The origins for the formation of quasiperiodic order in this terpolymer blend are not well understood.²⁴⁰

The discovery of quasiperiodic order in the simpler diblock polymers followed discoveries of the σ phase in the self-assembly of di-^{36,113} and tetrablock polymers.^{36,152} In 2012, a DDQC was confirmed using TEM and SAXS analyses in melt self-assembly of SISO tetrablocks. Note that the block polymer had a comparable molecular weight (~ 23 kg/mol) but lower S (35% by volume) and higher I content (56% by volume) as compared to tetrablocks probed by Lee et al., which formed the σ phase.³⁶ The samples were preannealed at 120 °C for 24 h to yield the HEX_s morphology.¹⁵³ Heating the polymer to $T = 175 - 190$ °C led to the development of a SAXS trace distinct from HEX_s or σ phases. TEM micrographs obtained from the specimen showed regions of periodic 3².4.3.4 tiling consistent with the σ phase. However, large areas of the image lacked translational periodicity in the 2D plane. Fourier analyses of these regions produced a 12-fold rotationally symmetric pattern, strongly suggesting the formation of a DDQC in block polymer self-assembly. The co-existence of the QC with the approximant is preceded in the formation of all classes of QCs in intermetallics.^{150,241} Heating the polymeric DDQC induced a transition to a pure σ phase, which ultimately disordered at 215 °C. Interestingly, the QC reformed upon cooling the disordered state to $T = 175 - 190$ °C, which calls into question the equilibrium nature of the structure.

Following the observation of DDQCs in block polymer melts, Gillard et al. sought to gain fundamental insights into the thermodynamic stability and kinetics of phase transformation of the complex micellar structures in diblock polymers.²⁴² A PI-PLA diblock with $M_n = 4.6$ kg/mol and $f_{\text{PLA}} = 18\%$ was quenched to different temperatures from the disordered state (Lee et al. found the

σ phase in PI-PLA with $M_n = 3.9$ kg/mol, $f_{\text{PLA}} = 28\%$). Quenching to 45 °C triggered the formation of a BCC structure, which was stable upon extended annealing at the quench T . Deeper quenches to 35 °C and 25 °C initially led to the development of peaks consistent with a DDQC. Isothermal annealing of the sample at 35 °C induced a subsequent DDQC \rightarrow σ transition, consistent with observations of Zhang and Bates.²⁴³ The kinetics of this transformation were probed using DMA, where the increase in loss modulus was used as an indicator for phase growth. The resulting time-temperature transformation (TTT) diagram shows that the QC is metastable against the periodic σ phase in diblock melts (Figure 1.22).¹⁶⁵ Remarkably, no thermodynamically stable DDQC has been definitively discovered in intermetallic alloys.^{227,244}

The authors suggest that the DDQC originates from a non-ergodic liquid-like packing (LLP) state of micelles with a distribution of sizes formed upon quenching the disordered state to below the ergodicity temperature (T_{erg}). Metal alloys forming DDQCs have contained at least two elements of different atomic radii. Moreover, the composition of the alloy forming the approximant only slightly differs from that forming the QC. Hence, the formation of the quasiperiodic mesophase in soft materials can be expected to include at least two micelle-sizes and a size-distribution with a narrow spread. For $T < T_{\text{erg}}$, intermicellar chain exchange is severely limited, decelerating any phase transitions in the system.²⁴⁵ The sudden quench from high temperature is argued to yield an arrested non-equilibrium micelle size distribution that is unable to form any periodic structures. Hence, extending annealing of the QC is required for micelle size reconfiguration via intermicellar chain exchange to achieve the micelle volumes required for the σ phase.

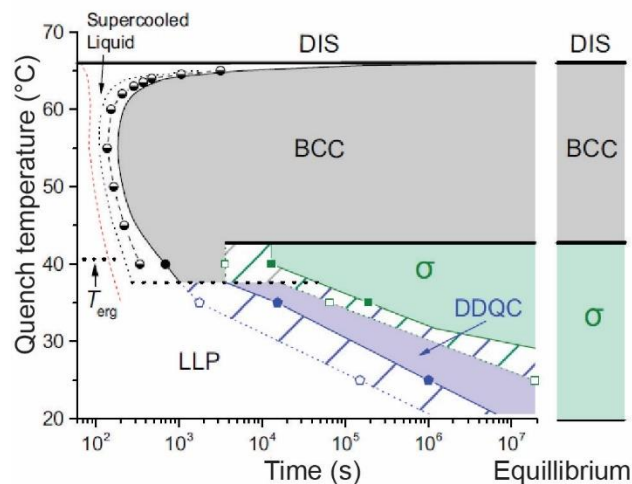


Figure 1.22. Time-temperature transformation diagram obtained for micellar phases of PI-PLA constructed using DMS and SAXS. The σ phase is the thermodynamically stable structure for $T < 40$ °C. Reprinted (adapted) from Gillard, T. M.; Lee, S.; Bates, F. S., Dodecagonal Quasicrystalline Order in a Diblock Copolymer Melt. *Proc. Natl. Acad. Sci. U.S.A.* **2016**, *113* (19), 5167-5172, with permission.

Lindsay et al. have observed an DDQC \rightarrow A15 transition in binary AB and A'B blends upon extended annealing at 180 °C.¹⁰⁹ Alternatively, Bates et al. observed a direct transition from the disordered state to the cubic A15 approximant for neat diblocks.³⁸ The A15 structure only has square tiling motifs against the square-triangle elements of the DDQC. These observations prompt questions about the nucleation and growth mechanisms of the DDQC, σ , and A15 structures. Moreover, the exact rationale leading to the formation of an intermediate DDQC morphology en route to the periodic phases from a disordered state in block polymers is poorly understood.³⁶

A DDQC was also reported by Cheng and co-workers in the self-assembly of POSS-based giant surfactants attached with three or four polystyrene chains as shown in Figure 1.10.⁴⁰ Molecules containing PS volume fractions intermediate between BCC and disorder exhibited a 1D-SAXS trace similar to those obtained for dendrons and block polymers. Quasiperiodicity of the structure was confirmed using TEM analyses. The mesophase exhibited no further phase transitions upon

extended annealing at elevated temperatures.

Quasiperiodic ordering was also obtained in the self-assembly of dendritic molecules, which contained one hydrophilic POSS cage attached to three hydrophobic POSS cages at one junction point.¹¹⁷ In a manner similar to Gillard et al., samples were heated to disorder and quenched to multiple temperatures to study the isothermal growth kinetics of the various phases. Quenching to $T = 110$ °C leads to the nucleation and growth of a DDQC that remains stable upon extended annealing. At a quench temperature of 125 °C, disorder \rightarrow σ transition is observed, with no evidence of quasiperiodic order within the time resolution of the SAXS experiment. Avrami analyses of the growth of the scattering maxima yielded an exponent of 1.15, which differs drastically from 2.5 reported for σ phase formation in block polymers.³⁶ The latter exponent was obtained using evolution of the loss modulus in DMA. The origins of this discrepancy are unclear but suggest a difference in the nucleation and growth mechanisms for the tetragonal structure in the two soft material systems. Upon quenching the disordered state to $T = 118$ °C, a QC phase initially forms, which slowly transforms to a σ phase at long annealing times. The σ phase is retained upon cooling to 110 °C indicating the metastability of quasiperiodic order in these systems. The intensities of the (002) and (00002) peaks of the σ and DDQC morphologies were investigated as a function of time to construct a TTT for these dendronized surfactants. Analogous to diblock polymers, these molecules exhibit a T_{erg} below which phase formation is completely arrested due to diffusion limitations. Probing the kinetics of these transformations will provide insight into mechanisms of phase transitions between soft quasicrystals and their periodic approximants.

Soft materials have exclusively formed 12-fold rotationally symmetric quasicrystals, which have only been found in phase space vicinity to the periodic approximants, FK A15 and σ phases. Fischer et al. presented the only exception to this observation, by obtaining 12- and 18-fold symmetric structures in the self-assembly of hydrated PI-PEO under shear. In the absence of a

mechanical field, the block polymer LLCs containing 15 wt% amphiphile form the FCC structure at 25 °C. The closest-packed mesophase was shear-oriented and cooled under oscillatory shear to yield 2D-SAXS patterns exhibiting 12- and 18-fold rotational symmetry for $15 < T < 20$ °C and $T = 10$ °C respectively. The 12-fold symmetry emerged from the 6-fold symmetric pattern of FCC implying that the (00002) quasiperiodic plane of the DDQC is parallel to the closest packed (111) planes of the cubic structure. Remarkably, 18-fold symmetry was later discovered in the molecular simulations of spherical particles with varying long-range interaction lengthscales.²⁴⁶ The calculations also illustrated the formation of 10-fold and 24-fold rotationally symmetric structures, which have not yet been experimentally realized in soft materials.

Despite the discoveries of DDQCs across various soft materials classes, some questions remain unanswered. The origins of the stability of soft quasicrystals are unclear and the complete lack of icosahedral quasiperiodic ordering in soft materials is surprising given its ubiquity in intermetallic alloys. Lifshitz & Diamant suggested that three-body interactions at two length-scales are required for the formation of soft QCs.²⁴⁷ Soft micelles formed by amphiphiles involve a length-scale associated with the volume exclusion of the core and a longer, more diffusive length scale associated with inter-coronal interactions. Simulations show the formation of 12-fold rotationally symmetric quasicrystalline order of deformable cores with varying interaction corona potentials, lending support to the hypothesis.^{97,248-250} However, in the case of diblock polymers and hydrated LLCs, the micelles also readily reconfigure their sizes by chain exchange to achieve a distribution conducive for the formation of a QC. The chain-exchange mediated mechanism of complex phase formation and stabilization in soft materials has been scarcely explored in theoretical simulations.²¹⁰ Molecular design criteria informed by simulations will augment the dependence on serendipitous discoveries of new complex morphologies.

The formation of large-length scale quasicrystals will provide opportunities for their

applications as wave guides and photonic crystals.²⁵¹⁻²⁵² However, the exact structure of DDQCs formed by soft materials has not yet been definitively determined.²³⁴ High quality scattering data in conjunction with real space imaging will be essential to unambiguously determine micelles positions in the mesophase. Additionally, the principles governing the nucleation and growth of the QC are poorly understood. Information about the critical nuclei shape and size, epitaxial pathways for phase formation, and lattice defect formation mechanisms are also imperative to control the kinetically-limited phase behavior of soft materials.²⁵³

1.10 Conclusions and Outlook

Over the last two decades, the universality in the formation of complex micellar morphologies in soft materials has been well-established. Low-symmetry packings result from a strong preference for maximizing local particle symmetry while filling space at constant density. Amphiphile design principles to access new mesophases have been extensively investigated in neat, neutral amphiphiles including dendritic molecules, POSS-based shape surfactants, and block polymers. Quasiperiodic orderings of micelles have also been identified as long-lived metastable states in these systems. Self-assembly of solvated amphiphiles has yielded the FK σ and A15 structures as well as the Laves C14 and C15 phases. However, design rules for molecular motifs that induce FK phase formation in Type I LLCs are lacking. The σ phase has only been observed in hydrated ionic amphiphiles, whereas the closely related A15 structure is prevalent across all amphiphile classes. Moreover, despite the observation of the periodic approximants, no lyotropic QCs have been reported. Insights into phase formation and stability across soft material classes will pave the way for utilizing these mesophases for real-world applications.^{231,251} This thesis aims to establish molecular design criteria for ionic and non-ionic surfactants to enable access to complex morphologies and tune their relative thermodynamic and compositional stabilities.

Chapter 2 details the investigations into the molecular design of anionic surfactants to access the FK σ phase in aqueous LLCs. The stability of the micellar morphologies is assessed as a function of the headgroup, associated counterions, and length of the alkyl tail. Electron density reconstructions are utilized to ‘locate’ the counterions in the hydrated matrix and correlate their positions with the observed phase behavior. The extent of headgroup-counterion association is argued to drive phase formation by modifying the local micelle curvature.

Chapter 3 reports the discovery of a lyotropic dodecagonal quasicrystal formed by *n*-decane swollen micelles of bis(tetramethylammonium) alkyl phosphonate. The well-ordered aperiodic structure showed over 10 sharp scattering maxima, which allowed the assignment of a 5D space group for the morphology. The thermodynamic stability of quasiperiodic order is investigated by different sample preparation protocols, indicating the inherent complexity in lyotropic phase formation and the metastability of this soft aperiodic crystal.

Chapters 4 and 5 are aimed at understanding the micellar phase formation in non-ionic amphiphiles. The temperature- and concentration-dependent phase behavior of short polyethylene-*block*-poly(ethylene oxide) is explored. Thermal processing of an A15 forming LLC yielded a metastable FK σ phase. The parameters affecting the stability of the tetragonal structure are investigated and a mechanism to explain the apparent metastability is suggested. In Chapter 4, the hydroxy endgroup of the diblock oligomer is synthetically transformed into a carboxylic acid, ionic sodium sulfonate or ammonium chloride group. The LLC phase behavior of the end-group modified amphiphiles is thoroughly investigated using SAXS. The different molecular interactions induced changes in the relative thermodynamic stabilities and composition windows for all the micellar morphologies including the FK σ and A15, and the canonical BCC and FCC structures. Moreover, a DDQC is obtained in the self-assembly of the trimethylammonium chloride-terminated amphiphile.

Chapter 2.

Counterion-Dependent Access to Low-Symmetry Lyotropic Sphere Packings of Ionic Surfactant Micelles

Reprinted from Jayaraman A. & Mahanthappa M. K., *Langmuir* **2018**, *34*, 2290-2301.

<https://pubs.acs.org/doi/abs/10.1021/acscentsci.8b00903>

©American Chemical Society, 2018

2.1 Introduction

Amphiphilic molecules, comprising polar headgroups covalently linked to nonpolar hydrocarbon tails, self-assemble in water to minimize unfavorable hydrophobic/water contacts while optimizing headgroup hydration.³ The myriad of useful properties of these hydrated materials stems from the specific morphologies of their supramolecular assemblies, which include spherical and wormlike micelles and bilayer vesicles.²⁵⁴ Aqueous dispersions of wormlike micelles find widespread applications as rheological modifiers in diverse contexts, including enhanced oil recovery and personal care product formulations due to their viscoelastic properties.²⁵⁵⁻²⁵⁷ Spherical micelles and vesicular structures also find applications as stabilizers and encapsulation agents in therapeutic delivery applications.^{20,258-260} The noncovalent assemblies formed by hydrated surfactants delicately balance the interfacial tension between the hydrophilic and hydrophobic domains against steric and electrostatic repulsions between the hydrophilic headgroups.^{5,11,261-262}

The self-assembled structures formed by ionic surfactants depend sensitively on the structures of their hydrophobic tails, the counterion-headgroup pair chemistries, and the extent of their hydration.^{5,8,12,261} Highly dissociated surfactant counterions induce electrostatic repulsions between adjacent headgroups situated at the hydrophobic/hydrophilic interface, leading to the formation of high-curvature spherical micelles.²¹⁵ On the other hand, counterion association with the interfacial headgroups mitigates such electrostatic repulsions and enables the formation of flatter-curvature

aggregates such as cylindrical micelles, bilayers (lamellae), and vesicles.²⁶³⁻²⁶⁴ However, the hydrated headgroup arrangements must also allow packing of the surfactant hydrocarbon tails at nearly constant density while minimizing their unfavorable interactions with water.^{8,12} At low hydrations when the surfactant counterion and headgroup are closely associated, the interfacial tension between the salty aqueous and hydrophobic domains is high. Thus, the surfactant tails stretch away from the interface in a manner that leads to tight intermolecular packings into low mean-curvature aggregates. If instead the counterion and headgroup are highly dissociated, then the interfacial tension between the hydrophobic and hydrophilic domains is lower and highly curved spherical micelles form.^{4,265} Thus, judicious pairing of headgroup-counterion chemistry with hydrocarbon tail structure offers opportunities for subtly tuning the preferred interfacial curvatures of these supramolecular structures and their consequent properties.⁸

At low surfactant concentrations in water above the critical micelle concentration, dielectric screening of interactions between micelles results in the absence of long-range intermicellar correlations. Dehydrating these micellar dispersions beyond a critical concentration leads the counterion clouds around the micelles to impinge and to induce cohesion, resulting in the formation of lyotropic liquid crystals (LLCs). LLCs are supramolecular assemblies that exhibit periodic nanoscale order, the morphologies of which depend upon the concentration, temperature, and pressure at which they form.^{18,266-268} Well-known LLC morphologies include lamellae (L_α), bicontinuous network phases (N), hexagonally packed cylinders (H), and spherical micelle packings (I). In a manner similar to the dilute solution-phase behavior of ionic amphiphiles, the self-assembled structures of LLCs primarily reflect the chemical structure of the surfactant, the degree of its solvation, and the temperature. LLCs are classified by the curvature of their hydrophobic domains: type I LLCs exhibit convex hydrophobic interfaces, whereas the hydrophobic domains are concave in type II structures.²⁶⁹ The hydrophilic/ hydrophobic domain

interfaces in these nanostructured assemblies are lined with the surfactant headgroups and their counterions, which endow them with unique properties. H- and N-phase LLCs have found applications as water-purification membranes,^{22,270} structured ion-conducting electrolytes,^{23,271} templates for mesoporous materials syntheses,^{24,272-274} and therapeutic delivery vehicles.^{20,259-260,275}

A recent review by Shearman et al. cataloged the bewildering array of LLC sphere packings observed to date.³² By analogy to colloidal hard sphere packings and metallic crystals,⁴⁹ micelles can self-assemble into high-symmetry body-centered cubic (BCC), high-packing-fraction face-centered cubic (FCC), and hexagonally closest-packed (HCP) LLC sphere phases. However, the deformability of soft spheres also enables deviations from their preferred spherical particle symmetries, which facilitate their packing into complex, low-symmetry phases.^{111,162} For example, Balmbra et al. first reported a type I cubic micellar LLC packing with $Pm\bar{3}n$ symmetry.¹⁸⁹ Vargas et al. later elucidated the structure of this complex type I phase²⁷⁶ as a tetrahedral close packing of two spherical and six platelet micelles into a cubic unit cell, which mimics that of the Cr_3Si intermetallic A15 structure.⁴⁹ In type I LLCs, A15, FCC, BCC, and HCP sphere packings are well documented.³² Pioneering work by Seddon and co-workers has also established that certain natural lipids form type II aqueous LLCs with $Fd\bar{3}m$ symmetry.²⁷⁷⁻²⁷⁸ The latter structure has eight reverse micelles situated at the positions of a cubic diamond lattice, wherein the remaining tetrahedral interstitial sites are filled with tetrahedral groupings of smaller reverse micelles. This so-called C15 phase mimics the $MgCu_2$ intermetallic structure.⁴⁹ We note that the $Fd\bar{3}m$ structure is ubiquitous in type II LLCs, with only relatively recent reports of inverse FCC,¹⁸⁰ HCP,¹⁸⁸ and A15¹⁹⁰ phases. Notable common features of both of the A15 and C15 LLC sphere packings include the formation of giant, low-symmetry unit cells containing ≥ 8 micelles of different and discrete volumes.

The aforementioned micellar LLC sphere packings belong to a broader class of tetrahedrally

close-packed structures known as Frank–Kasper (FK) phases, which were first identified over 50 years ago in metals and their alloys.⁵³ A defining feature of these complex, low-symmetry phases is that their lattice sites exhibit either 12-, 14-, 15-, or 16-fold coordination.⁵⁸ Thus, the aforementioned A15 and C15 LLCs represent the first examples of FK phases observed in soft materials, and until recently, these were the only FK LLC phases known. Over the last 15 years, FK phases have been observed in amphiphilic systems in the absence of solvents, including thermotropic liquid crystals based on wedge-type dendrons,^{35,91,279} in giant shape amphiphiles,^{40,148} and in linear diblock and multiblock polymers.^{36-37,96,152} Percec, Ungar, and co-workers have elucidated the detailed structures of the FK phases formed by families of wedge-type dendrons using electron microscopy and X-ray diffraction.^{34,73,75,84,280-282} These phases are recognized as periodic 3D approximants of quasicrystals.^{150,224} Quasicrystals exhibit local rotational symmetry, yet they are devoid of long-range translational order.²¹⁷ By virtue of these structural relationships, dodecagonal QCs have been observed in these amphiphilic self-assembled materials^{40,152,235,242-243} and in micellar solutions of nonionic diblock polymers.¹⁷⁶

Kim et al. only very recently reported that the hydration of bis(tetramethylammonium) decylphosphonate (DPA-TMA₂) drives the formation of an exceptionally well-ordered and previously unknown type I FK σ LLC phase with P4₂/mnm symmetry (Figure 2.1).³¹ The lyotropic σ mesophase exhibits a large, low-symmetry unit cell containing 30 quasispherical micelles, which belong to five different symmetry-equivalent classes each with discrete aggregation numbers. This unusual structure, which mimics that of β -tantalum, β -uranium, and Fe₄₆Cr₅₄ alloys,⁴⁹ represents the LLC analog of previously reported thermotropic dendron and block polymer phases.³⁵⁻³⁶ The formation of FK σ phases in wedge-type dendrons block polymers, and conceptually related type II C15 LLCs has been argued to stem from filling space with uniform density while maximizing

the spherical symmetry of the inverse micelles.^{113,196} In other words, these amphiphilic materials adopt structures that minimize differential molecular stretching known as packing frustration (or lipid tail frustration) within the ⁷⁴⁻⁷⁷ hydrocarbon matrix phase.^{196,283-285} In type II LLCs, it is known that the addition of hydrophobic additives can relieve packing frustration and enable access to other phases.¹⁸⁰ However, such arguments do not apply to type I LLCs, in which the normal micelles surrounded by water make no van der Waals contacts. Kim et al. instead rationalized the formation of type I FK A15 and σ phases as maximizing electrostatic cohesion between the micelles while minimizing variations in surfactant counterion- headgroup hydration.³¹ Since only one example of an FK LLC σ phase has been reported to date, amphiphile design criteria that facilitate reliable access to these structurally complex packings are unknown.

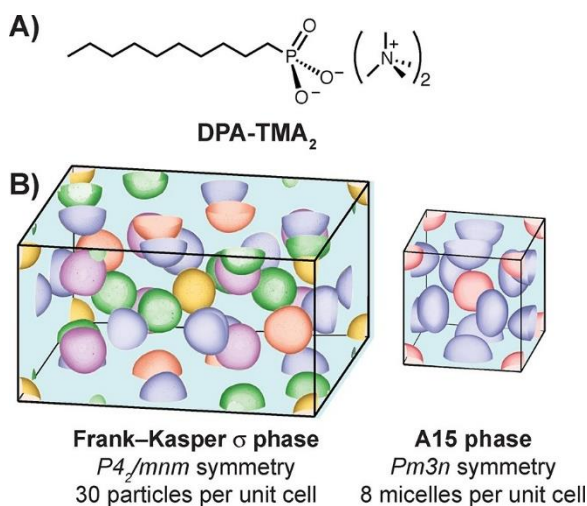


Figure 2.1 (A) Chemical structure of dianionic surfactant DPA-TMA₂, which (B) forms tetrahedrally close-packed aqueous lyotropic Frank-Kasper σ and A15 mesophases. In the low-symmetry σ phase unit cell that contains 30 particles, 5 discrete micelle sizes spontaneously form to maximize electrostatic cohesion in the LLC while minimizing variations in surfactant hydration.

In this report, we investigate the synthesis and aqueous LLC phase behaviors of dianionic

surfactants in order to identify molecular motifs that drive the formation of complex FK mesophases. Our studies focus on homologous 2-alkylmalonate surfactants ($C_n\text{Mal-M}_2$) in which the dicarboxylate headgroups carry charge-compensating counterions $M = K^+$, Cs^+ , or $(CH_3)_4N^+$ (TMA⁺). By mapping the water concentration dependent LLC phase behaviors of these amphiphiles using temperature-dependent X-ray scattering, we demonstrate that access to the FK σ phase crucially depends on the nature of the counterion and the degree of its dissociation from the dianionic surfactant headgroups. Soft and highly dissociated counterions enable σ -phase formation, while more closely associated ion pairs instead favor surfactant self-assembly into FK A15 phases. The length of the alkyl chain exerts a weaker influence over the preferred LLC structures, although shorter alkyl surfactant tails also favor σ -phase formation. Thus, these studies provide new insights into amphiphile structures that stabilize FK σ phase LLCs.

2.2 Experimental Section

Materials. All reagent-grade solvents and chemicals were purchased from the Sigma–Aldrich Chemical Co. (Milwaukee, WI) and were used as received unless otherwise noted. Lauric acid was obtained from Acros Organics (Geel, Belgium) and used as received. Anhydrous, anaerobic tetrahydrofuran (THF) was obtained by sparging analytical-grade solvent with $N_2(g)$ for 30 min, followed by repetitive circulation through a column of activated molecular sieves over 12 h in a Vacuum Atmospheres Co. (Hawthorne, CA) solvent purification system. Hexamethylphosphoramide (HMPA) and diisopropylamine (iPr_2NH) were distilled from CaH_2 and stored under nitrogen. n-Butyllithium (2.154 M in hexanes) was titrated using $Ph_2CHCOOH$ in anhydrous and anaerobic THF prior to use. $(CH_3)_4NOH(aq)$ was titrated against a standardized solution of 1 N $HCl(aq)$ and thus was determined to have a concentration of 0.9912 M aqueous base.

Molecular Characterization. ^1H and ^{13}C nuclear magnetic resonance (NMR) spectra were recorded on a Bruker Avance III HD 400 MHz spectrometer with Smartprobe or a Bruker Avance III HD 500 MHz spectrometer with a TCI cryoprobe. All spectra were obtained in and were referenced relative to the residual proton shift in CD_3OD (δ 3.31 ppm) or DMSO-d_6 (δ 2.50 ppm). Carbon/hydrogen/ nitrogen (C/H/N) combustion elemental analyses were performed by Atlantic Microlab, Inc. (Norcross, GA, USA).

Representative Synthesis of 2-Octylmalonic Acid (C_8Mal). This synthesis protocol was adapted from that of Weber and Mahanthappa.²⁸⁶ A 500 mL two-necked round-bottomed flask fitted with an addition funnel and equipped with a stir bar was charged with $i\text{Pr}_2\text{NH}$ (16.73 mL, 119.0 mmol) and THF (30 mL) under a nitrogen atmosphere. This solution was cooled to $-40\text{ }^\circ\text{C}$ in an $\text{EtOH}/\text{H}_2\text{O}/\text{CO}_2(\text{s})$ bath, and $n\text{-BuLi}$ (44.8 mL, 116 mmol) was added dropwise via addition funnel, whereupon the solution turned pale yellow. After stirring this reaction mixture for 30 min, a solution of decanoic acid (9.998 g, 58.04 mmol) in THF (60 mL) was added dropwise via an addition funnel. HMPA (10.0 mL, 57.5 mmol) was subsequently added, and the stirred reaction mixture was warmed to $22\text{ }^\circ\text{C}$ and stirred for 30 min. The resulting enolate solution was again cooled to $-40\text{ }^\circ\text{C}$ and transferred batchwise via cannula to a 500 mL two-necked round-bottomed flask containing excess $\text{CO}_2(\text{s})$ ($>255\text{ g}$, $>5.79\text{ mol}$) under a nitrogen atmosphere over 45 min. The reaction mixture was then allowed to warm slowly to $22\text{ }^\circ\text{C}$ over 12 h, leading to soft gel formation. This gelatinous reaction mixture was quenched by the addition of 2.0 M HCl (60 mL), which yielded two distinct layers. The layers were separated, and the aqueous (lower) layer was washed with diethyl ether ($3 \times 50\text{ mL}$). The combined organic layers were washed with 2.0 M HCl ($3 \times 25\text{ mL}$) followed by saturated $\text{NaCl}(\text{aq})$ ($2 \times 25\text{ mL}$). The ether layer was then dried using $\text{MgSO}_4(\text{s})$ and concentrated under vacuum to yield a white solid. The crude product was purified by recrystallization from heptane (100 mL), and the resulting crystals were azeotropically freeze-dried

from C₆H₆ prior to further use. Yield 8.29 g (66.0%). ¹H NMR (500 MHz, DMSO-d₆, 22 °C) δ (ppm): 12.61 (COOH, s, 2H), 3.17 (CH, t, 1H), 1.70 (CH-CH₂-CH₂, q, 2H), 1.24 (CH₂, m, 12H), 0.86 (CH₃-CH₂, t, 3H). ¹³C NMR (126 MHz, DMSO-d₆, 22 °C) δ (ppm): 171.35 (C=O), 52.05 (CH), 31.71 (CH₂), 29.23 (CH₂), 29.20 (CH₂), 29.06 (CH₂), 28.83 (CH₂), 22.55 (CH₂), 14.37 (CH₃).

2-Decylmalonic Acid (C₁₀Mal). This compound was synthesized from lauric acid and CO₂(s) per the procedure for C₈Mal. Yield 9.63 g (78.9%). ¹H NMR (500 MHz, DMSO-d₆, 22 °C) δ (ppm): 12.61 (COOH, s, 2H), 3.18 (CH, t, 1H), 1.70 (CH-CH₂-CH₂, q, 2H), 1.24 (CH₂, m, 16H), 0.86 (CH₃, t, 3H). ¹³C NMR (126 MHz, DMSO-d₆, 22 °C) δ (ppm): 171.35 (C=O), 52.05 (CH), 31.77 (CH₂), 29.45 (CH₂), 29.42 (CH₂), 29.29 (CH₂), 29.21 (CH₂), 29.19 (CH₂), 28.84 (CH₂), 27.27 (CH₂), 22.57 (CH₂), 14.38 (CH₃).

Representative Synthesis of Tetramethylammonium 2-octylmalonate (C₈Mal-TMA₂). 2-octylmalonic acid (1.00 g, 4.63 mmol) and (CH₃)₄NOH(aq) (9.50 mL of 0.9912 M solution, 9.42 mmol) were suspended in CH₃OH at a concentration of 0.15 M and stirred for 12 h. The reaction mixture was filtered through a fine glass frit, and the filtrate was concentrated in vacuo to furnish a quantitative yield of a white solid. Hygroscopic solids thus obtained were freeze-dried three times from C₆H₆ and stored in a glovebox under an argon atmosphere to avoid adventitious atmospheric moisture uptake. ¹H NMR (400 MHz, CD₃OD, 22 °C) δ (ppm): 3.21 (N-CH₃, s, 24H), 3.11 (CH, t, 1H), 1.85 (CH-CH₂-CH₂, m, 2H), 1.31 (CH₂, m, 12H), 0.91 (CH₃-CH₂, t, 3H). ¹³C NMR (101 MHz, CD₃OD, 22 °C) δ (ppm): 180.07 (C=O), 60.80 (CH), 55.99 (N-CH₃, t), 33.09 (CH₂), 32.58 (CH₂), 31.13 (CH₂), 30.89 (CH₂), 30.52 (CH₂), 30.02 (CH₂), 23.74 (CH₂), 14.48 (CH₃). Anal. Calc. for C₁₉H₄₂O₄N₂ · 0.88H₂O: C, 60.29; H, 11.68; N, 7.40. Found: C, 60.29; H, 11.85; N, 7.29.

Potassium 2-Octylmalonate (C₈Mal-K₂). This compound was synthesized from 2-octylmalonic acid and K₂CO₃(s) in place of (CH₃)₄NOH per the above protocol. ¹H NMR (400

MHz, CD₃OD, 22 °C) δ (ppm): 3.09 (CH, t, 1H), 1.82 (CH-CH₂-CH₂, m, 2H), 1.31 (CH₂, m, 12H), 0.91(CH₃-CH₂, t, 3H). ¹³C NMR (101 MHz, CD₃OD, 22 °C) δ (ppm): 181.08 (C=O), 60.52 (CH), 33.08 (CH₂), 32.32 (CH₂), 31.01 (CH₂), 30.82 (CH₂), 30.49 (CH₂), 29.91 (CH₂), 23.72 (CH₂), 14.45 (CH₃). Anal Calc. for C₁₁H₁₈O₄K₂·0.28H₂O: C, 44.39; H, 6.30. Found: C, 44.39; H, 6.26.

Cesium 2-Octylmalonate (C₈Mal-Cs₂). This compound was synthesized from 2-octylmalonic acid and Cs₂CO₃(s) in place of (CH₃)₄NOH per the above protocol. ¹H NMR (400 MHz, CD₃OD, 22 °C) δ (ppm): 3.08 (CH, t, 1H), 1.82 (CH-CH₂-CH₂, m, 2H), 1.31 (CH₂, m, 12H), 0.91(CH₃-CH₂, t, 3H). ¹³C NMR (101 MHz, CD₃OD, 22 °C) δ (ppm): 180.70 (C=O), 60.37 (CH), 33.09 (CH₂), 32.25 (CH₂), 31.02 (CH₂), 30.83 (CH₂), 30.50 (CH₂), 29.89 (CH₂), 23.74 (CH₂), 14.45 (CH₃). Anal Calc. for C₁₁H₁₈O₄Cs₂·0.46H₂O: C, 27.05; H, 3.91. Found: C, 27.05; H, 4.25.

Tetramethylammonium 2-Decylmalonate (C₁₀Mal-TMA₂). ¹H NMR (400 MHz, CD₃OD, 22 °C) δ (ppm): 3.12 (N-CH₃, s, 24H), 3.1 (CH, t, 1H), 1.85 (CH-CH₂-CH₂, m, 2H), 1.31 (CH₂, m, 16H), 0.91 (CH₃-CH₂, t, 3H). ¹³C NMR (101 MHz, DMSO-d₆, 22 °C) δ (ppm): 180.10 (C=O), 60.82 (CH), 55.98 (N-CH₃, t), 33.07 (CH₂), 31.13 (CH₂), 30.93 (CH₂), 30.86 (CH₂), 30.79 (CH₂), 30.48 (CH₂), 30.02 (CH₂), 23.74 (CH₂), 14.47 (CH₃). Anal Calc. for C₂₁H₄₆O₄N₂·0.89H₂O: C, 62.00; H, 11.86; N, 6.89. Found: C, 62.00; H, 12.07; N, 7.00.

Cesium 2-Decylmalonate (C₁₀Mal-Cs₂). ¹H NMR (400 MHz, CD₃OD, 22 °C) δ (ppm): 3.09 (CH, t, 1H), 1.82 (CH-CH₂-CH₂, m, 2H), 1.31 (CH₂, m, 12H), 0.91(CH₃-CH₂, t, 3H). ¹³C NMR (101 MHz, DMSO-d₆, 22 °C) δ (ppm): 180.66 (C=O), 60.28 (CH), 33.08 (CH₂), 32.25 (CH₂), 31.01 (CH₂), 30.86 (CH₂), 30.83 (CH₂), 30.78 (CH₂), 30.48 (CH₂), 29.97 (CH₂), 23.74 (CH₂), 14.46 (CH₃). Anal Calc. for C₁₃H₂₂O₄Cs₂·1.18H₂O: C, 29.49; H, 4.65. Found: C, 29.49; H, 4.52.

Lyotropic Liquid Crystal (LLC) Sample Preparation. LLC samples were prepared by placing desired amounts of surfactant into 1 dram vials, followed by the addition of ultrapure water (18 M Ω ·cm). These mixtures were homogenized to yield clear gel-like solids by three cycles of

centrifugation (4950g for 10 min) and hand mixing. Sample vials were capped and sealed with Parafilm to prevent any loss of water. Binary surfactant/H₂O LLC compositions are reported in terms of $w_{0s} = (\text{total moles of H}_2\text{O})/(\text{moles of surfactant})$, wherein the numerator in this quotient accounts for both the added water and that arising from the surfactant hydrate.

Small- and Wide-Angle X-ray Scattering (SWAXS). LLC sample morphologies were investigated using synchrotron SWAXS analyses. Using an incident beam energy of 13.3 keV ($\lambda = 0.932 \text{ \AA}$) and a 2.027 m sample-to-detector distance at the 12-ID-B beamline of the Advanced Photon Source (Argonne, IL), synchrotron 2D-SWAXS patterns were recorded on a Pilatus 2 M (25.4 cm \times 28.9 cm rectangular area) detector with 1475 \times 1679 pixel resolution (172 $\mu\text{m} \times$ 172 μm pixel size). The scattering wavevector (q) scale in these patterns was calibrated using a silver behenate standard ($d = 58.38 \text{ \AA}$). LLC samples were hermetically sealed in alodined aluminum DSC pans (TA Instruments, Newcastle, DE), which were equilibrated at the desired temperature using a home-built multiarray sample stage for at least 5 min prior to SWAXS analysis (typical exposure times $\leq 0.1 \text{ s}$). SWAXS patterns were obtained in the first heating cycle of the LLC samples as prepared, with additional patterns acquired at 25 $^\circ\text{C}$ upon completion of the temperature sweep to assess potential phase metastability. Unless otherwise noted in the text, the initial and final LLC phases were identical upon thermal cycling. The resulting 2D patterns were azimuthally integrated to obtain one-dimensional scattering intensity $I(q)$ versus q plots using the DataSqueeze software package (<http://www.datasqueezesoftware.com/>).

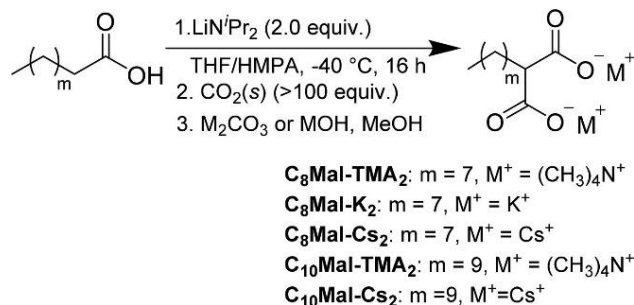
Using JANA2006 crystallographic computing system software,²⁸⁷ Le Bail refinement of selected SWAXS data sets was used to extract the structure factor intensities for each scattering maximum. These data were used as inputs for the charge-flipping algorithms within the SUPERFLIP software package²⁸⁸ to reconstruct the electron density maps for various observed LLC phases. The resulting electron density contour maps (typically 90% isosurfaces) were

visualized using the VESTA software package,⁶⁷ from which electron density line profiles along selected crystallographic directions were obtained. Details of these analyses along with the SUPERFLIP input files (in which the static structure factor intensities are listed) are provided in the Supporting Information.

2.3 Results and Analysis

Given the recent discovery of an aqueous LLC σ mesophase in the dianionic surfactant DPA-TMA₂,³¹ we sought to identify amphiphile design criteria that enable robust access to this and other low-symmetry lyotropic packings of ionic micelles. On the basis of the structure of DPA-TMA₂, we initially sought to assess whether a dianionic surfactant headgroup was an essential ingredient for σ phase formation and whether its chemical identity influences the stability of this complex packing. Additionally, we aimed to probe the extent to which the charge-compensating counterions guide LLC phase selection. Consequently, we synthesized a series of analytically pure 2-alkylmalonate surfactants with n-octyl and n-decyl tails by the method of Weber et al.²⁸⁶ (Scheme 1) in which the carboxylate headgroups bear either K⁺, Cs⁺, or (CH₃)₄N⁺ (TMA⁺) counterions. Hereafter, we designate these surfactants C_nMal-M₂, where n is the total number of carbons in the alkyl chain appended to the 2-position of the malonate headgroup and M⁺ = TMA⁺, Cs⁺, and K⁺ is the surfactant counterion. Note that there are always two monovalent counterions (M⁺) associated with each malonate headgroup to maintain charge neutrality. We restricted our attention to monovalent counterions to avoid potential surfactant precipitation through the formation of bridging interactions between headgroups fostered by divalent counterions.²⁸⁹ Note that Hagslaett et al. previously studied the aqueous LLC phase behavior of related dipotassium dodecylmalonate surfactants; however, the quality of their SAXS data were insufficient to conclusively identify the observed morphologies.²¹⁵

Scheme 2.1 Synthesis of 2-Alkylmalonates Surfactants



The aqueous LLC phase behavior of **C₁₀Mal-TMA₂** was investigated by SWAXS analyses of a series of samples with surfactant headgroup hydrations ranging from $w_{0s} = (\text{total moles of H}_2\text{O})/(\text{moles of surfactant}) = 3\text{--}40$ (Figure 2.2). All SWAXS patterns were acquired during the first heating cycle of the as-prepared LLC samples, and patterns were obtained upon cooling to 25 °C to assess the potential metastability of the observed phases. Samples with $w_{0s} > 40$ form free-flowing solutions of disordered micelles. In the headgroup hydration range of $24 \leq w_{0s} \leq 37$, we observe an ordered LLC phase with an ambient temperature SWAXS signature comprising at least 12 peaks corresponding to hexagonally closest-packed (HCP) spherical micelles. A representative azimuthally integrated SWAXS intensity profile for this HCP LLC obtained at 25 °C with $w_{0s} = 25.9$ (Figure 2.2A) exhibits unit cell parameters of $a \approx 3.94$ nm and $c \approx 6.42$ nm. The observed $c/a = 1.629$ deviates modestly from the ideal value of 1.635, which is geometrically predicted for HCP hard spheres. The scattering signature for this sample, including the slightly diminished intensity of the (002) scattering peak ($q = 0.1958 \text{ \AA}^{-1}$), is similar to that reported by Liu and Warr for LLCs of cationic 4^o ammonium surfactants with strongly hydrated counterions.¹⁸⁷ Upon heating this sample to 60 °C, we observe a transition to a body-centered cubic (BCC) sphere packing, as evidenced by the observation of up to six SWAXS maxima at relative positions of $q/q^* = \sqrt{2}, \sqrt{4}$,

$\sqrt{6}$, $\sqrt{10}$, $\sqrt{12}$, and $\sqrt{14}$ ($q^* = 0.2057 \text{ \AA}^{-1}$). These peaks correspond to the (110), (200), (211), (310), (222), and (321) Miller planes of a supramolecular BCC structure, with a (220) peak extinction. When $T > 80 \text{ }^\circ\text{C}$, the sharp peaks for the ordered BCC LLCs melt into the broad intermicellar correlation scattering associated with a disordered dispersion of micelles. In the hydration window $w_{0s} = 38\text{--}40$, we observe the formation of an ordered BCC micelle packing that coexists with disordered micelles. The occurrence of a BCC phase near the lyotropic order–disorder transition hydration ($w_{0s,ODT}$) is anticipated by the entropic arguments of Alexander and McTague regarding liquid–solid phase transitions: the configurational entropy loss upon symmetry breaking of the liquid state to form an ordered LLC is minimized by the formation of a BCC phase due to site symmetry equivalence within this lattice.¹³² Across the window $w_{0s} = 24\text{--}40$, the thermal order–disorder transition temperature (T_{ODT}) monotonically decreases with increasing w_{0s} .

In the headgroup hydration range of $w_{0s} = 20\text{--}24$, **C₁₀Mal-TMA₂** forms a LLC characterized by the appearance of at least 40 instrument-resolution-limited SWAXS peaks (Figure 2.2A). This distinctive scattering signature conforms to that previously reported for FK σ phases ($P4_2/mnm$ symmetry) in LLCs and block polymers.^{31,36} Detailed analyses of a SWAXS pattern obtained at $w_{0s} = 22.2$ at $25 \text{ }^\circ\text{C}$ demonstrate the formation of a giant tetragonal unit cell with $a = 13.3 \text{ nm}$ and $c = 6.99 \text{ nm}$ ($c/a = 0.526$), constituting only the second report of a LLC FK σ phase. (See Figure A1.1 for fully indexed pattern and Table A1.1 for a complete listing of peak positions and residuals.) On the basis of the observation of various high-index peaks (e.g., (730)) in conjunction with the unit cell parameter, we estimate that the coherent grain radii for these LLCs comprising sub-2-nm micelles exceed $\sim 90 \text{ nm}$. As in the case of the LLC FK σ phase derived from DPA-TMA₂, this LLC structure is characterized by exceptional long-range translational order at length scales that are somewhat unusual in lyotropic mesophases.^{31,290} We note that the unit cell parameters for the σ phase based on **C₁₀Mal-TMA₂** are comparable to those reported for the same phase derived from

10-carbon surfactant DPA-TMA₂, suggesting similarities in their packings and mechanisms of complex phase formation.

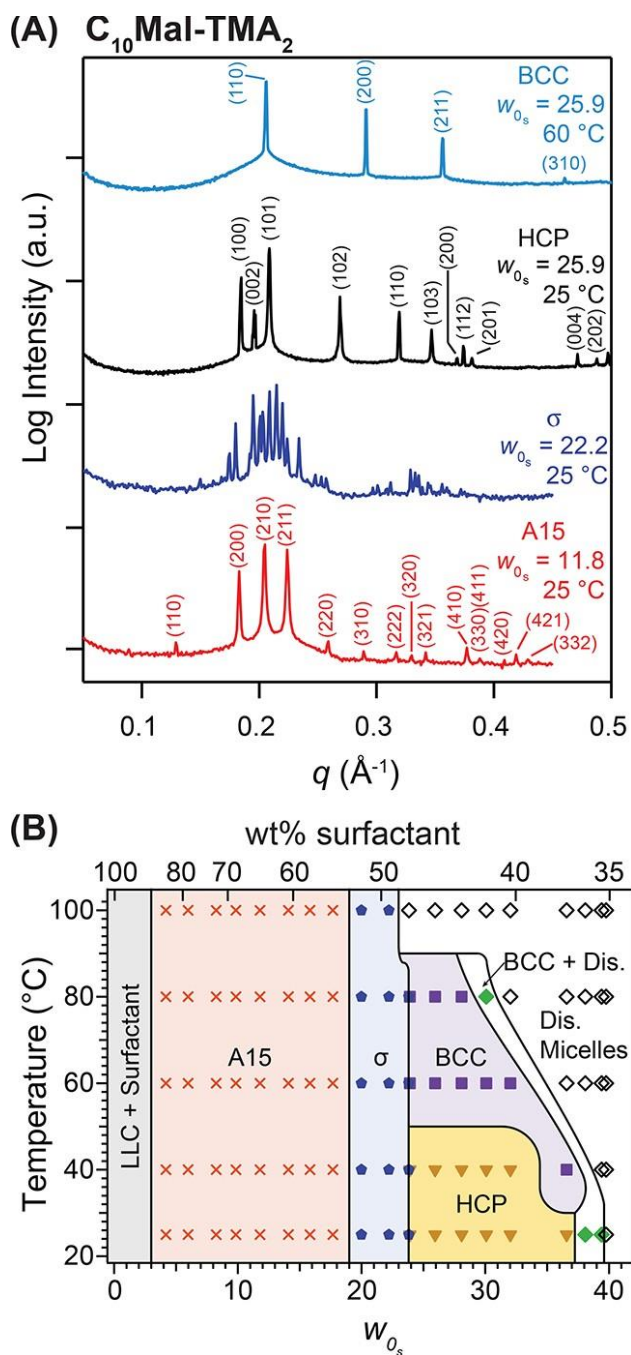


Figure 2.2 Aqueous lyotropic liquid crystalline phase behavior for C₁₀Mal-TMA₂. (A) Synchrotron SWAXS powder patterns illustrating the formation of A15, σ , HCP, and BCC ordered phases at various headgroup

hydration numbers w_{0s} . (B) Temperature versus w_{0s} phase diagram depicting the lyotropic mesophase progression of ordered phases to disordered micellar solutions with increasing w_{0s} .

At the lower hydrations $w_{0s} = 3-19$, we found that **C₁₀Mal-TMA₂** forms aqueous LLCs exhibiting much simpler scattering patterns with up to 14 SWAXS peaks located at $q/q^* = \sqrt{2}, \sqrt{4}, \sqrt{5}, \sqrt{6}$...etc. (Figure 2.2A). These peak positions are consistent with a FK A15 phase with cubic $Pm\bar{3}(-)n$ space group symmetry, which has been previously observed in other ionic surfactant LLCs.^{187,190,276} The A15 phase formed at $w_{0s} = 8.25$ exhibits a unit cell parameter $a \approx 6.91$ nm. The value of a in the A15 phase depends weakly on w_{0s} and T in the range 22– 100 °C: it monotonically increases from $a = 6.81$ to 6.92 nm with increasing w_{0s} and it decreases by less than 3% (~ 0.2 nm) upon heating to 100 °C. In contrast to the LLCs formed at higher hydrations, the FK σ and A15 phases of **C₁₀Mal-TMA₂** remain thermally stable up to 100 °C. A temperature versus water content LLC phase diagram for **C₁₀Mal-TMA₂** is given in Figure 2.2B. Although windows of two-phase coexistence are anticipated at intermediate compositions and temperatures between each pure LLC phase window according to Gibbs phase rule,^{254,291} our phase mapping methodology employed a resolution specified by the headgroup hydration increment $\Delta w_{0s} = 1-1.5$ and temperature increment $\Delta T = 20$ °C. Thus, the absence of some of these expected two-phase windows in this phase map suggests that they are sufficiently narrow that we did not directly observe them in the investigated LLC compositions unless noted. Note that a high level of surfactant crystallinity when $w_{0s} < 4$ prevents the formation of homogeneous ordered phases, and we instead observe the coexistence of crystalline surfactant with a LLC phase. Thus, we do not observe the hexagonally-packed cylinder (H₁) LLCs that arise from minimal hydration of the previously reported dianionic surfactant DPA-TMA₂.⁷²

Decreasing the alkyl chain length of the malonate surfactant significantly impacts the observed LLC phase behavior, as assessed by SWAXS characterization of the water-concentration-

dependent mesophase morphologies of **C₈Mal-TMA₂** (Figure 2.3). The lyotropic order–disorder transition hydration below which ordered LLC phases form considerably decreases from $w_{0s,ODT} = 40$ for **C₁₀Mal-TMA₂** to $w_{0s,ODT} = 18$ in **C₈Mal-TMA₂**. In proximity to this ordering transition at $w_{0s} = 16–18$, we observe phase coexistence of an ordered BCC LLC with a fluid isotropic dispersion of micelles as evidenced by the broadened base of the primary SWAXS peak (Figure 2.3A). Notably, the HCP sphere phase of **C₁₀Mal-TMA₂** does not form in this shorter-tail malonate amphiphile analog. We observe the formation of FK σ phases upon further reduction of the LLC water content to $11 \leq w_{0s} \leq 16$, with weakly w_{0s} -dependent unit cell parameters of $a = 11.4$ nm and $c = 5.99$ nm ($c/a = 0.525$). (See Figure A1.2 for the fully indexed pattern and Table A1.2 for a complete listing of peak positions and residuals.) Given that the micelles of **C₈Mal-TMA₂** are expected to be smaller than those of the **C₁₀** analog, the unit cell parameters for this σ phase are noted to be $\sim 15\%$ smaller. We also find that reducing the surfactant tail length from **C₁₀** to **C₈** renders the lattice order–disorder transition temperatures for FK σ phases accessible with $T_{ODT} \leq 70$ °C, and T_{ODT} decreases monotonically with increasing w_{0s} . Finally, A15 phases formed from samples with $w_{0s} = 4–8.25$ display cubic unit cell parameters $a = 5.82$ nm and accessible $T_{ODT} \leq 90$ °C. (See Figure A1.3 for the fully indexed pattern.) Figure 2.3B depicts a temperature versus composition phase diagram for **C₈Mal-TMA₂** LLCs; again, not all of the expected two-phase coexistence windows² were observed given the headgroup hydration increment resolution of our phase map $\Delta w_{0s} = 1–1.5$ and the temperature increment $\Delta T = 20$ °C. An inspection of these data reveals that LLCs based on the **C₁₀** surfactant display higher T_{ODT} 's than do those of the **C₈** homologue at comparable values of w_{0s} .

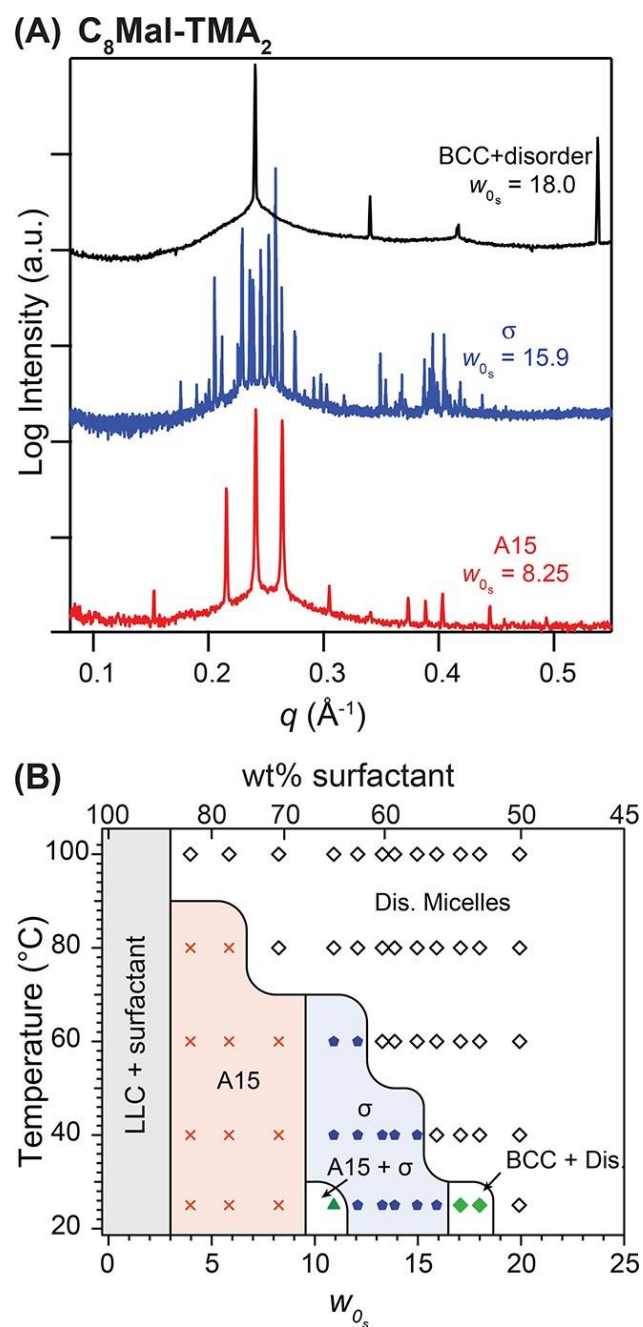


Figure 2.3 (A) Synchrotron SWAXS powder patterns for aqueous LLCs derived from **C₈Mal-TMA₂**, illustrating the formation of A15 and σ ordered phases and the coexistence of BCC and disordered micelles at 25 °C. (B) Temperature versus surfactant hydration number w_{0s} phase diagram showing the lyotropic phase

progression: disordered micelles \rightarrow BCC + disordered micelles \rightarrow σ \rightarrow A15 with decreasing w_{0s} .

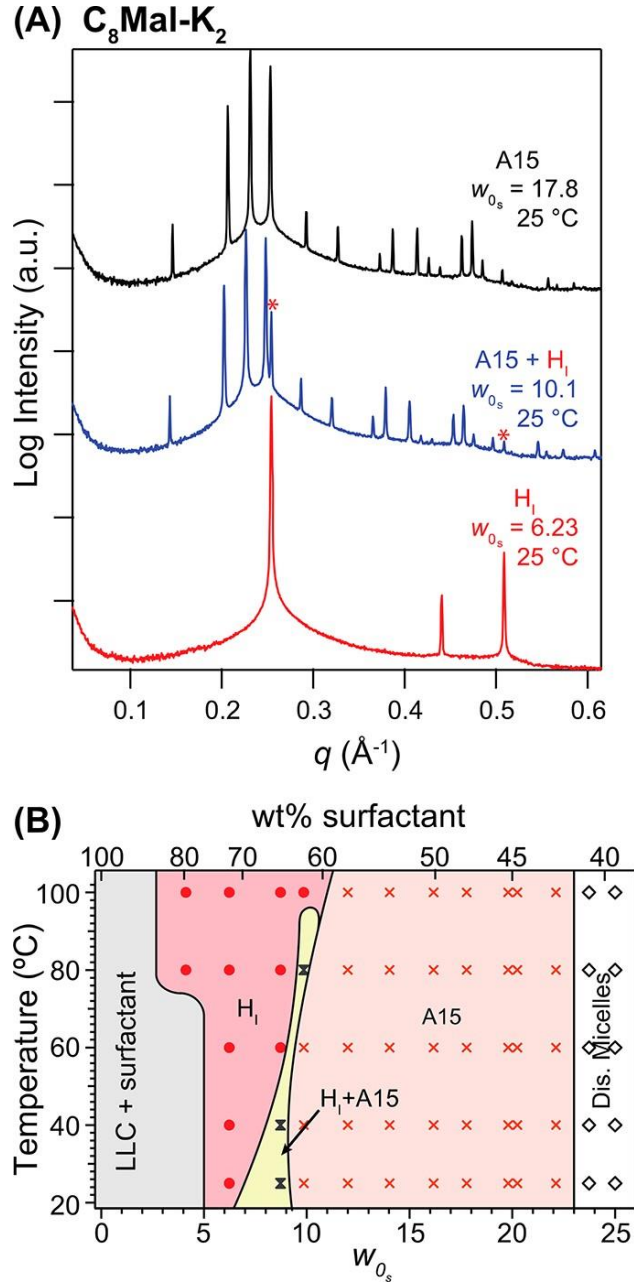


Figure 2.4 (A) Synchrotron SWAXS powder patterns for C_8Mal-K_2 LLCs illustrating the formation of hexagonally packed cylinders (H_I), $H_I/A15$ two-phase coexistence (* demarcates peaks corresponding to the H_I phase), and pure A15 sphere packing phases. (B) Temperature versus w_{0s} phase diagram, which notably lacks an FK σ phase.

Changing the identity of the counterion in **C₈Mal-TMA₂** from TMA⁺ to K⁺, as in **C₈Mal-K₂**, dramatically alters the observed LLC phase behavior (Figure 2.4). First, we observe an increase in $w_{0s,ODT} = 23$ for the potassium-containing LLCs. We also find no evidence of a BCC phase proximal to the lyotropic order–disorder transition hydration $w_{0s,ODT}$ within the resolution of our LLC phase map. The presence of the alkali counterion also eliminates the σ mesophase window in favor of an enlarged A15 phase that forms when $w_{0s} = 9–22$ with no accessible T_{ODT} (>100 °C) by SWAXS analyses (Figure 2.4A). The lattice parameters for the A15 LLCs decrease monotonically from $a = 6.28$ to 5.99 nm with increasing w_{0s} . This unit cell shrinkage with increasing w_{0s} is quite different from the monotonic increase in A15 and the σ phase unit cell dimensions for the TMA⁺-based surfactants. Also noteworthy is the fact that the A15 unit cells of **C₈Mal-K₂** are generally larger than those of **C₈Mal-TMA₂** at comparable w_{0s} values. For example, $a = 6.28$ nm at $w_{0s} = 9.84$ for **C₈Mal-K₂**, whereas $a = 5.82$ nm when $w_{0s} = 8.25$ for **C₈Mal-TMA₂**. Finally, we found that the A15 phase gives way to a thermally stable H_I phase at low hydration $w_{0s} = 5–7$ in **C₈Mal-K₂**, with a narrow intervening window of H_I/A15 two-phase coexistence (Figure 2.4A,B). Within the headgroup hydration- and temperature-resolution increments of our experiment, we observe no other two-phase coexistence windows. SWAXS patterns for the latter coexisting phases appear as direct superpositions of the adjacent pure-phase LLCs. On the basis of these counterion-dependent differences in the LLC phase behaviors of the C₈- and C₁₀alkylmalonate surfactants, we hypothesized that the highly dissociated nature of the soft, polarizable, and slightly hydrophobic TMA⁺ counterion was essential for LLC FK σ phase formation.

In order to test this last hypothesis regarding the role of counterion identity in LLC phase selection, we examined the phase behaviors of alkylmalonate surfactants bearing polarizable and slightly hydrophobic Cs⁺ counterions. We synthesized samples of **C_nMal-Cs₂** ($n = 8$ and 10) by deprotonation of the parent malonic acids with Cs₂CO₃. Figure 2.5A summarizes the aqueous LLC

phase behavior of **C₈Mal-Cs₂**, which displays hybrid behavior between that of amphiphiles with either TMA⁺ or K⁺ counterions. (See Figure A1.4A for representative 1D SWAXS intensity profiles on which these phase diagrams are based.) We explicitly found that $w_{0s,ODT} \approx 26$ is somewhat higher for **C₈Mal-Cs₂** than for **C₈Mal-K₂** and that the Cs surfactant forms a modestly stable BCC LLC near this lyotropic ODT with $T_{ODT} < 60$ °C. In the hydration range $w_{0s} = 8-24.5$, as-formed LLCs exhibit A15 morphologies that are thermally stable up to $T > 100$ °C with one notable exception. At $w_{0s} = 22.8$, the LLC obtained from iterative cycles of high-speed centrifugation and hand-mixing exhibits A15/σ two-phase coexistence (Figure A1.4A). Upon heating this sample to 40 °C, we observe a thermally-induced transition to a pure A15 phase that remains stable up to 100 °C. Since cooling this specific LLC composition back to 22 °C does not recover the coexisting phases, we suggest that the complex σ phase is metastable with respect to the A15 structure in **C₈Mal-Cs₂** LLCs. SWAXS reveals that the A15 unit cell parameter for **C₈Mal-Cs₂** is $a \approx 6.17$ nm at $w_{0s} = 8.00$, which is ~6% greater than that of a comparably hydrated **C₈Mal-TMA₂** A15 LLC. The unit cell parameters for **C₈Mal-Cs₂** are comparable to those for **C₈Mal-K₂**, and they show only weak temperature dependence as with the other counterions. The unit cell parameter also decreases with increasing w_{0s} , similar to that for **C₈Mal-K₂**, although the dependence on headgroup hydration is much weaker. As with the potassium-based surfactants, **C₈Mal-Cs₂** forms a H_I morphology at headgroup hydrations lower than that of the A15 phase. In the case of **C₁₀Mal-Cs₂**, we observe a similar water-concentration-dependent phase progression, BCC + Iso → HCP → A15/σ → A15 → H_I/A15 → H_I, with decreasing w_{0s} at ambient temperature (Figure 2.5B). Although the Gibbs phase rule again anticipates a pure σ phase and a σ/HCP (or σ/BCC) two-phase coexistence window at high hydrations of **C₁₀Mal-Cs₂**, the limited resolution of our phase map ($\Delta w_{0s} = 1-2$ and $\Delta T = 20$ °C) did not permit their observation. Representative SWAXS data for **C₁₀Mal-Cs₂** are given in Figure A1.4B. We note that most of these phases are thermally stable, with the exception of the

HCP LLC that exhibits a thermoreversible transition to a BCC phase at $T \geq 80$ °C. Notably, lengthening the surfactant tail stabilizes the coexisting A15 and σ phases and does not lead to the apparent σ phase metastability observed in the corresponding C_8 surfactant.

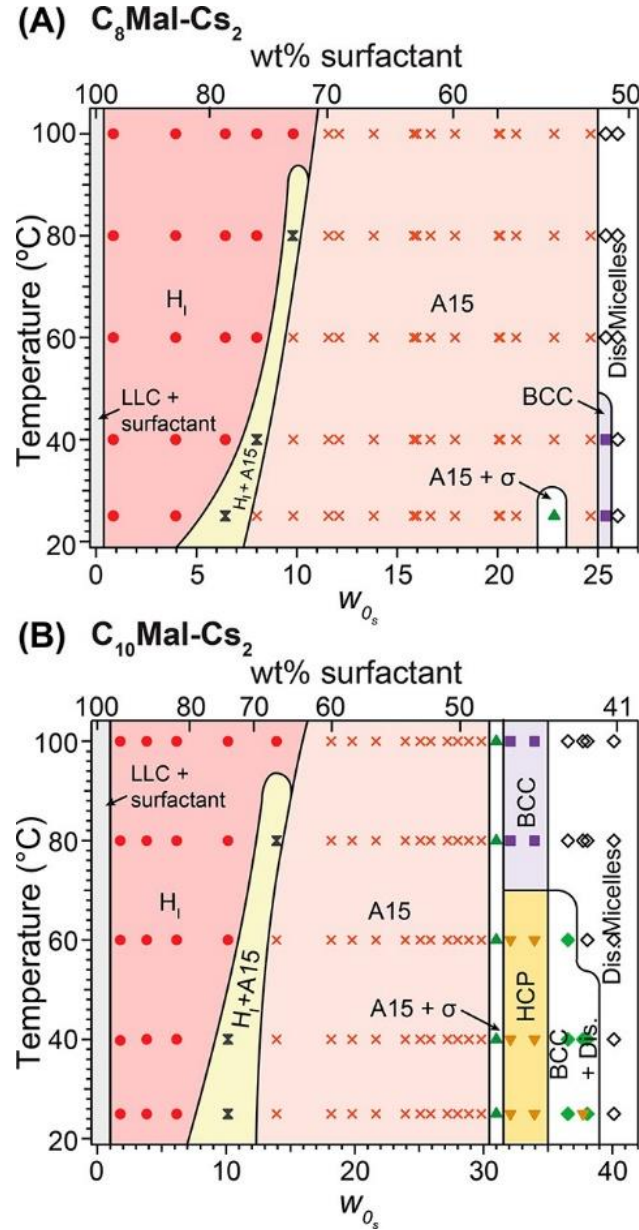


Figure 2.5 Temperature versus surfactant hydration number w_{0s} phase diagram for aqueous LLCs of (A) $C_8\text{Mal-Cs}_2$ and (B) $C_{10}\text{Mal-Cs}_2$, which shows that the soft and somewhat hydrophobic Cs^+ counterions allow σ phase formation in narrow composition windows.

2.4 Discussion

Kim et al. rationalized the DPA-TMA₂ lyotropic phase sequence $BCC \rightarrow \sigma \rightarrow A15 \rightarrow H_I$ with decreasing w_0 , in terms of a frustrated force balance within these supramolecular assemblies.³¹ Molecular dynamics (MD) simulations revealed that the water-solvated TMA⁺ counterions in the aqueous domains of these LLCs mediate electrostatic cohesion between the quasispherical alkylphosphonate (anionic) micelles. The lowest free-energy counterion configuration in these ordered LLCs localizes them near the midplanes bisecting line segments that connect the centers of neighboring micelles. Geometrically, the counterions are thus concentrated along the polyhedral interfaces of the Voronoi (or Wigner-Seitz) cells associated with each site in the ordered lattice. Electrostatic correlations between the counterions and the surfactant headgroups consequently drive soft faceting of the micelles. However, the formation of a polyhedral counterion cloud around each faceted micelle is unfavorable, since the ions and surfactant headgroups situated at the edges and vertices of the polyhedra are differentially hydrated as compared to those sitting on the faces. Each micelle instead tends toward ionic sphericity, that is, the formation of a spherically symmetric particle (with constant mean curvature) wherein the counterions are isotropically distributed around the core. At a given w_0 , the LLC assembly must optimize intermicellar cohesion while also maximizing the average ionic sphericity of its constituent micelles. As the micelles become more concentrated within a BCC LLC (decreasing w_0), the counterion clouds deviate significantly from the preferred ionic sphericity due to decreased nearest neighbor distances in the ordered lattice. Beyond a critical reduction in w_0 , the LLC reconfigures by interparticle chain exchange of surfactants and their counterions to generate a new configuration that optimizes both ionic sphericity and ensemble electrostatic cohesion. The lattice sites in the new LLC morphology have a greater number of nearest neighbors (average coordination numbers $CN > 12$) to induce greater

faceting of the counterion clouds, which renders them more spherical. However, the higher average lattice site CN results in lower overall lattice symmetry. Furthermore, the micelles in this new phase are not all of the same size or volume: the adoption of a lower packing symmetry induces the formation of a discrete distribution of particle sizes with specific aggregation numbers.

The sphericity of a polyhedron may be quantified through the isoperimetric quotient, $IQ = 36\pi S^3/V^2$ such that $IQ = 1$ for a perfect sphere.³⁸ On this basis, the number-average IQ calculated from the constituent Voronoi cell IQs in an ordered lattice quantifies the overall sphericity of that packing symmetry. On this basis, one calculates that $IQ(\sigma) > IQ(A15) > IQ(BCC) > IQ(HCP)$.^{113,196} Thus, the balance of ionic sphericity and interparticle cohesion leads DPA-TMA₂ micelles to form FK σ phases across the range $w_{0s} = 21-31$ and A15 phases when $w_{0s} = 10-18$. We note that the initial formation of BCC just below $w_{0s,ODT} = 44$ probably arises for entropic reasons,¹³² in spite of the obvious deviation from maximal sphericity.

While the ionic sphericity concept should apply to all aqueous lyotropic packings of ionic spherical micelles, our studies reveal that access to the FK σ phase depends on the nature of the surfactant headgroup. We first note that the phase diagrams given in Figures 1.2B and 1.3B establish that single-tailed dianionic surfactants bearing TMA⁺ counterions generally appear to self-assemble into FK σ -phase LLCs. However, **C₁₀Mal-TMA₂** surfactants display a relatively smaller FK σ phase window width ($\Delta w_{0s} = 4$) as compared to DPA-TMA₂ ($\Delta w_{0s} = 10$), in spite of their both having C₁₀-alkyl tails. In aqueous **C₁₀Mal-TMA₂** LLCs at 22 °C, the phase sequence HCP \rightarrow σ \rightarrow A15 with a relatively small σ -phase window suggests that this surfactant does not enforce ionic sphericity as strictly as does DPA-TMA₂. In other words, the alkylmalonate derived micelles are softer and more deformable than the alkylphosphonate micelles. Thus, greater deviations from ionic sphericity are allowed in the former case. The origins of this enhanced particle deformability probably lie in the

relative strengths of the counterion–headgroup correlations, which are directly related to the surfactant headgroup chemistries. DPATMA₂ forms high-curvature micelles that are relatively rigid due to strong Coulombic repulsions between adjacent dianionic headgroups situated at the water/hydrophobic interface, with only partial screening by the highly dissociated TMA⁺ counterions. While the malonate headgroup of **C₁₀Mal-TMA₂** is nominally dianionic, the close spatial proximity of the two anionic carboxylate headgroups linked through a one-carbon bridge leads the counterions to sit closer to the micelle surface to screen both intramolecular and interheadgroup electrostatic repulsions. The lower degree of counterion dissociation leads the decylmalonate surfactant to form larger micelles with interfaces that are more deformable. Enhanced micelle deformability probably also enables the formation of the lower-sphericity HCP packing at high hydrations and low temperatures near $w_{0s,ODT}$.

Naturally, the question arises as to why the σ phase window width Δw_{0s} for **C₁₀Mal-TMA₂** is smaller than that for **C₈Mal-TMA₂**. Alkylmalonates with shorter *n*-alkyl tails form micelles with smaller radii, with more tightly packed anionic headgroups lining their surfaces. The enhanced electrostatic repulsions among these ionic headgroups and the short alkyl tail length likely rigidify these spherical particles, leading to a stronger preference for ionic sphericity. The larger C₁₀ micelles have a decreased surface area-to-volume ratio leading to a smaller effective headgroup area per surfactant. Thus, the counterions are more closely associated with the micelle surface²⁹² and the more deformable interface enables the formation of lower sphericity morphologies.

Upon changing the surfactant counterion from TMA⁺ to K⁺ with C₈Mal, we observe that the σ phase window closes at the expense of widening that of the A15 morphology. The inaccessibility of the σ phase in K-based surfactant LLCs likely reflects a higher degree of potassium carboxylate association,²⁹³ which enables the formation of larger and more deformable micelles that pack into lower-sphericity LLCs by the above mechanism. Note that the intermediate level of Cs⁺–

carboxylate association²⁶³ in **C₈Mal-Cs₂** allows the formation of a metastable σ phase at low temperatures, which irreversibly converts to an aqueous A15 LLC. This behavior probably reflects subtle differences in alkali-carboxylate ion pair dissociation that are only discernible by virtue of the cooperative nature of lyotropic self-assembly, in which the morphology serves as a macroscopic reporter for microscopic interactions.

We can also explain the expansion of the A15 unit cell parameters upon exchanging the TMA⁺ counterions for K⁺ in the C₈Mal LLCs, by considering the specific counterion distributions between the micelles in the aqueous domains. Recall that the counterions in each LLC sphere packing localize along the Voronoi cell boundaries of each lattice site in order to maximize interparticle cohesion. The breadth of the counterion distribution along these Voronoi boundaries depends on the relative strengths of their pairwise electrostatic repulsions. Soft and polarizable TMA⁺ cations, in which the positive charge is delocalized across the four methyl groups, can more densely concentrate along the Voronoi cell boundaries as compared to the more point-like K⁺ ions that are correlated over much larger distances.²⁹⁴ To experimentally support this notion, we used our established methodology to reconstruct the electron density maps for A15 LLCs based on **C₈Mal-K₂** and **C₈Mal-TMA₂** at $w_{0s} = 9.85$ and 8.25 , respectively (Figure 2.6A; see Supporting Information for electron density map reconstruction details). Figure 2.6B depicts the normalized electron density variation in the $z = 0$ plane along vectors parallel to the [010] direction connecting the centers of the platelet micelles (6f Wyckoff positions) and to the [100] direction along the unit cell edge, as a function of the dimensionless fractional lattice parameter for A15 phases with K⁺ and TMA⁺ counterions. The electron density was normalized by the linear density along this vector (area under the raw linear plot), wherein we arbitrarily assigned the highest-density regions to be the cores of the micelles. We specifically use the dimensionless fractional distance to compare these two phases at slightly different hydrations, since they have different unit cell parameters. By our

convention, the maxima in this plot correspond to the micelle cores, and the broad minimum stems from the counterion distributions between the surfaces of neighboring micelles. Qualitative inspection of the plots in Figure 2.6B reveals that the trough for the TMA⁺ counterions is narrower and deeper than that for the K⁺ ions, indicating denser localization of TMA⁺ along the Voronoi cell boundaries as expected. On the other hand, the shallower and broader troughs corresponding to the K⁺ counterions in the aqueous nanodomains imply their more diffuse counterion clouds. The counterion distributions deduced from the experimental SWAXS data are consistent with the notion that the K⁺ ions are more closely associated with the carboxylate headgroups than the TMA⁺ ions in these C₈Mal A15 LLCs at comparable hydrations. Consequently, the unit cell dimensions are larger for the surfactant LLCs with K⁺ counterions due to electrostatic repulsions between the correlated point-like charges, in a manner consistent with expectations based on theory by Jho et al.²⁹⁵

Finally, we note that the values of $w_{0s,ODT}$ are generally higher for surfactants with alkali counterions as opposed to those with TMA⁺ counterions. Since the alkali counterions are electrostatically correlated over longer distances by virtue of their point-like charge distributions,²⁹⁴ we surmise that larger amounts of water are required in order to effectively screen all of the pairwise interactions between the micelles and induce lattice disordering. However, the more diffuse and polarizable nature of the TMA⁺ counterion lends to its effective screening by smaller amounts of water. Therefore, cohesion between the micelles is lost at relatively lower hydrations for the TMA-based surfactants.

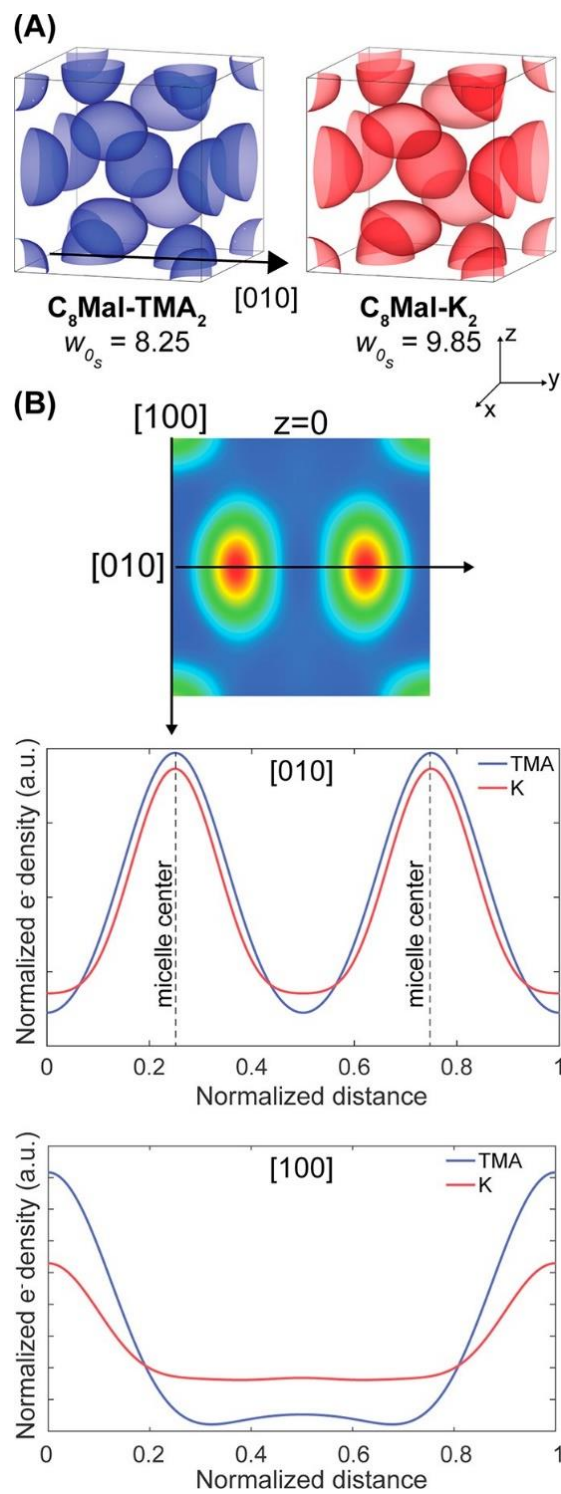


Figure 2.6. (A) 90% isosurface electron density reconstructions of the A15 phase unit cells for $C_8\text{Mal-TMA}_2$ and $C_8\text{Mal-K}_2$ at $w_{0s} = 8.25$ and 9.85 , respectively. (B) Normalized linear electron density profile in the $z =$

0 plane along the [010] direction passing through the centers of the platelet micelles and in the [100] direction along the unit cell edge. The peaks correspond to the micelle cores, and the troughs correspond to the counterion distribution between neighboring micelles. The relative depth and breadth of the troughs in the [010] and [100] directions indicate that the counterions are more localized along the Voronoi cell boundaries in the case of TMA⁺ (blue) than with K⁺ (red).

2.5 Conclusions

Detailed studies of the water concentration-dependent lyotropic mesophase behaviors of a homologous series of 2alkylmalonate ionic surfactants revealed their propensities to form four possible spherical micelle packings, the exact symmetries of which depend sensitively on their associated counterions. The soft, polarizable TMA⁺ ion leads to the formation of micelles that strongly prefer a local spherical particle symmetry, since the high degree of counterion–headgroup dissociation fosters significant electrostatic repulsions between adjacent surfactant headgroups within each micelle. This preference for ionic sphericity while maximizing micellar cohesion drives a spontaneous lowering of the global lattice symmetry to form a complex FK σ phase, the unit cell of which contains 30 quasispherical particles with five different volumes. Reducing the water content of these LLCs drives the formation of the structurally related FK A15 phase. However, replacing the soft TMA⁺ counterion with a more point-like K⁺ counterion completely destabilizes the σ phase in favor of the A15 phase. This change in packing symmetry originates from the reduced preference for spherical particle symmetry, which arises from closer counterion–headgroup association in the latter case. These findings generally suggest that controlling both counterion–headgroup and counterion–counterion correlations in normal LLC phases furnishes new means for self-assembling hydrated surfactants into unusual mesostructured supramolecular assemblies with tunable unit cell sizes.

Chapter 3.

Quasiperiodic Ordering of Oil-Swollen Ionic Surfactant Micelles

3.1 Introduction

The 1984 discovery of Al-Mn alloys that form quasicrystals (QCs),²¹⁷ which display local rotational symmetry yet no long-range translational order, forced the redefinition of crystals to include both periodic and aperiodic structures that yield discrete X-ray diffraction patterns.²¹⁶ Metal alloys are now known to form polygonal QCs comprising periodic layers of 2D aperiodic particle arrangements with 5-, 8-, 10-, or 12-fold symmetries, as well as 3D aperiodic icosahedral QCs.²²³ A harbinger of the emergence of metallic quasicrystallinity is the observation of tetrahedrally close-packed approximants, known as Frank-Kasper (FK) phases, which exhibit gigantic low-symmetry unit cells with average lattice site coordination numbers $CN_{\text{avg}} > 13$.⁵²⁻⁵³

Self-assembled soft dodecagonal quasicrystals (DDQCs) also form in charge-neutral thermotropic liquid crystalline dendrons,²³⁵ block polymer melts^{37,152,240,242-243} and their aqueous dispersions,¹⁷⁶ and giant shape amphiphiles.⁴⁰ In a manner analogous to metal alloys,²²⁵ these discoveries were preceded by observations of soft matter FK A15 and σ approximants in adjacent regions of phase space.^{40,109,115,235,242-243} Access to soft DDQCs generally requires elaborate syntheses^{40,235,240} or complex materials-specific processing protocols,^{37,176,242} which hampers their detailed structural characterization and obscures insights into the origins their aperiodic order. Whether or not soft DDQCs are thermodynamic equilibrium or metastable states also remains a topic of some debate.^{37,117,227,235,242,244}

Hydration of selected molecular amphiphiles induces their mesoscale self-assembly into high-symmetry micellar body-centered cubic (BCC), face-centered cubic (FCC), and hexagonally closest-packed (HCP) lyotropic liquid crystals (LLCs).¹⁸ Two recent reports established that

minimally hydrated dianionic surfactants also form complex Frank-Kasper (FK) A15 and σ phases,^{31,95} the latter of which exhibits a tetragonal unit cell with 30 ionic micelles of five discrete volumes. Recent models^{31,38,111-112} rationalize the parallel self-assembly behaviors of both charge-neutral and ionic micellar materials in terms of frustrated energy minimization at two different structural length scales. While these universal structure directing principles suggest that DDQCs should form in LLCs of small molecule amphiphiles, such lyotropic mesophases have yet to be reported.

Herein, we describe the straightforward preparation of self-assembled lyotropic DDQCs by hydration of mixtures of bis(tetramethylammonium) dodecylphosphonate ($C_{12}PA-TMA_2$) with *n*-decane. Small-angle X-ray scattering (SAXS) analyses reveal the formation of DDQCs of oil-swollen ionic micelles with high degrees of aperiodic order, which facilitate definitive identification of their underlying space group symmetry. We further document the markedly path-dependent formation of these QCs and demonstrate their non-equilibrium nature. The discovery of a lyotropic DDQC mesophase thus establishes the universality of 12-fold aperiodic order in soft micellar materials.

3.2 Experimental section

Materials. All materials and reagents were purchased from Sigma-Aldrich Chemical Co. (Milwaukee, WI) and used as received unless other noted. $(CH_3)_4NOH$ (1.0065 M in H_2O) was titrated using standardized 1.0 N $HCl(aq)$. Ultra-pure water ($18 M\Omega\bullet cm$) obtained from Thermo ScientificTM BarnsteadTM Smart2Pure 3 UV/UF water purification system was degassed by sparging $N_2(g)$ for at least 30 min.

Molecular Characterization. 1H and ^{13}C nuclear magnetic resonance (NMR) spectra were recorded on a Bruker Avance 400 MHz spectrometer with Smartprobe. Spectra referenced relative

to the residual proton shift in CD₃OD-*d*₄ (δ 3.31 ppm). Combustion analysis (C, H, and N) was performed by Atlantic Microlab, Inc. (Norcross, GA, USA).

Synthesis of Bis(tetramethylammonium) Dodecylphosphonate (C₁₂PA-TMA₂). A suspension of dodecylphosphonic acid (3.03 g, 12.10 mmol) in MeOH (50 mL) was stoichiometrically deprotonated with an aqueous solution of (CH₃)₄NOH (24.05 mL, 1.0065 M in H₂O, 24.20 mmol) in a 250 mL round-bottom flask equipped with a stir bar. This mixture was stirred at 22 °C for an additional 2 h after it became homogeneous to ensure reaction completion, after which the volatile solvents were removed under vacuum. The resulting hygroscopic solid was freeze-dried two times by suspending the solids in C₆H₆ (20 mL), freezing the suspension in N₂(l), and subliming the frozen solvent at reduced pressure.

¹H NMR (400.18 MHz, CD₃OD, 24 °C): δ (ppm) 3.23 (N-CH₃, s, 24H), 1.70–1.64 (P-CH₂, m, 2H), 1.51–1.42 (CH₂-CH₂, m, 2H), 1.36–1.30 (CH₂, m, 18H), 0.93–0.90 (CH₂-CH₃, t, 3H).

¹³C NMR (100.62 MHz, CD₃OD, 24 °C): δ (ppm) 54.59 (N(CH₃)₄), 32.14 (CH₂), 31.96 (CH₂), 31.96 (CH₂), 31.68 (CH₂), 31.41 (CH₂), 30.11 (CH₂), 29.54 (CH₂), 29.43 (CH₂), 29.10 (CH₂), 24.83 (CH₂), 22.35 (CH₂), 13.06 (CH₃).

Anal. calc for C₂₀H₄₉PN₂O₃·5.07 H₂O: C, 49.22; H, 12.24; N, 5.74. Found: C, 49.22; H, 12.29; N, 5.62.

LLC sample preparation.

Normal order of addition: Desired masses of surfactant were weighed into 1 dram vials with 10 wt% decane and mixed via three cycles of centrifugation (4950×*g* for 10 min) and hand-mixing. LLC samples were then prepared by addition of ultrapure water and subsequent homogenization by an additional three cycles of centrifugation and hand-mixing, and isothermal annealing at 50 °C for 30 min.

Inverse order of addition: Appropriate masses of surfactant and ultrapure water were weighed

into 1 dram vials and homogenized by three cycles of centrifugation (4950×g for 10 min) and hand-mixing to yield transparent LLC samples. Decane (10 wt% with respect to surfactant) was added and mixed by three more cycles of centrifugation and hand-mixing. In order to ensure complete oil uptake by the LLC, samples thus prepared were isothermally annealed for 30 min at 50 °C.

The extent of hydration of each LLC sample is quantified using:

$$w_0 = \frac{\text{total moles of H}_2\text{O}}{\text{moles of C}_{12}\text{PA-TMA}_2}$$

Small-angle X-ray Scattering (SAXS). LLC samples were quiescently equilibrated at 22 °C for at least 24 h to allow for stress relaxation induced by sample preparation prior to morphological analyses by synchrotron SAXS.

Using an incident beam energy of either 13.3 or 14.0 keV ($\lambda = 0.932$ or 0.886 Å) and a 2.011 m sample-to-detector distance at the 12-ID-B beamline of the Advanced Photon Source (Argonne, IL), synchrotron 2D-SAXS patterns were recorded on a Pilatus 2M detector (25.4 cm × 28.9 cm rectangular area) with 1475×1679 pixel resolution. The scattering wavevector ($q = (4\pi \sin \theta)/\lambda$) scale in these patterns was calibrated using a silver behenate standard ($d = 58.38$ Å). LLC samples were hermetically sealed in alodined aluminum DSC pans (TA Instruments, Newcastle, DE), which were equilibrated at the desired temperature on a custom-built multiple-sample array stage for at least 10 min prior to data collection (typical exposure times ~ 0.1 s). In order to assess sample homogeneity, SAXS data were acquired at a minimum of three different positions in each DSC pan.

Lab-source SAXS measurements were made using a SAXSLAB Ganesha 300XL instrument in the University of Minnesota College of Science & Engineering Characterization Facility. Cu K_α X-rays ($\lambda = 1.54$ Å) generated by a Xenocs Geni3DX source were collimated through two sets of motorized 4-bladed slits (JJ X-ray, A/S). 2D-SAXS patterns were acquired using a Dectris EIGER

R 1M detector (7.72 cm \times 7.99 cm rectangular area) with 1030 \times 1065 pixels at a 46.8 cm sample-to-detector distance. Samples were sealed in home-built sandwich sample holders equipped with Kapton windows. They were mounted on a Linkam hot-stage and equilibrated at the desired temperature for \sim 20 min prior to data acquisition (typical exposure times \sim 10 min) within an evacuated sample and X-ray flight path environment. All 2D-SAXS patterns were azimuthally-integrated to obtain one-dimensional scattered intensity $I(q)$ versus q plots, using the DataSqueeze software package (<http://www.physics.upenn.edu/~heiney/datasqueeze/index.html>). The 1D scattering intensity profiles were analyzed using customized Igor Pro procedure files developed internally by our group.

3.3 Results and Discussion

LLCs were prepared as transparent solids by controlled hydration of mixtures of C₁₂PA-TMA₂ with 10 wt% *n*-decane relative to amphiphile (**C₁₂PA-Dec10**) by three successive iterations of hand-mixing and centrifugation (4950 \times *g* for 10 min) followed by annealing at 50 °C for 30 min. Attempts to prepare LLCs with higher *n*-decane loadings led to sample macrophase separation. This contrasts with LLCs containing monoanionic tetramethyl ammonium decanoates, which allowed for addition of 40 wt% decane before phase separation was observed. {Baez-Cotto, 2018 #207} Soft carboxylate headgroups yield flexible micelles, which tolerate large perturbations in micelle curvature caused by the addition of 40 wt% decane. {Jayaraman, 2018 #170} The hard dianionic phosphonate headgroups resists extensive micelle deformations limiting the total decane incorporated into the sample. LLC water contents are hereafter specified in terms of $w_0 =$ (total moles of H₂O)/(moles of C₁₂PA-TMA₂). Temperature-dependent SAXS analyses of LLC samples contained in hermetically-sealed, alodined, differential scanning calorimetry (DSC) pans were conducted at the Advanced Photon Source at Argonne National Laboratory (see Section 3.2 for

experimental details).

Figure 3.1 depicts SAXS data acquired from aqueous **C₁₂PA-Dec10** LLCs with $w_0 = 5-70$. LLCs with $w_0 \geq 70$ are free-flowing liquids that exhibit only one broad SAXS correlation, indicative of disordered micellar solutions. Decreasing the hydration to $w_0 = 61-67$ gives rise to structured solids with the sharp SAXS maxima at $(q/q^*)^2 = 1, 4/3, 8/3, 11/3, 4, 19/3, \text{ and } 20/3$ ($q^* = 0.1681 \text{ \AA}^{-1}$ at $w_0 = 66.1$ and $25 \text{ }^\circ\text{C}$), which correspond to an FCC micelle packing with unit cell parameter $a = 6.47 \text{ nm}$. In the range $40 \leq w_0 \leq 45$, the oil-swollen ionic micelles form a HCP packing. A SAXS pattern obtained from one such LLC with $w_0 = 42.1$ at $60 \text{ }^\circ\text{C}$ exhibits 15 sharp peaks consistent with the $P6_3/mmc$ symmetry and lattice constant $a = 4.41 \text{ nm}$ and nearly ideal $c/a = 1.629$. In concurrence with Gibbs' phase rule, the pure FCC and HCP phases are separated by a window of their two-phase coexistence when $46 \leq w_0 \leq 61$ (Figure A2.1). Heating these samples drives thermoreversible transitions to micellar BCC phases, with (110), (200), (211), (220), (310), (222) and (321) SAXS reflections ($a = 4.89 \text{ nm}$ for $w_0 = 42.1$ at $80 \text{ }^\circ\text{C}$). Note that the FCC/HCP \rightarrow BCC order-to-order transition temperature (T_{OOT}) decreases from $80 \text{ }^\circ\text{C}$ to $40 \text{ }^\circ\text{C}$ on increasing w_0 (Figure 3.1B), and the BCC LLCs with $w_0 = 52-61$ reversibly melt into disordered solutions at $100 \text{ }^\circ\text{C}$.

The distinctive SAXS signatures of exceptionally well-ordered lyotropic FK σ mesophases with ≥ 50 synchrotron resolution-limited peaks are observed at the lower water contents $w_0 = 32-35$ between $25-100 \text{ }^\circ\text{C}$. Consistent with an earlier report on σ LLCs of structurally homologous ionic phosphonate amphiphiles in the absence of alkane additives,³¹ the σ phase formed here at $w_0 = 35.2$ has lattice constants $a = 15.24 \text{ nm}$ and $c = 8.01 \text{ nm}$, with the expected $c/a = 0.526$ (see Figure A2.2 for an enlarged X-ray pattern and Table A2.1 for peak positions and residuals). A narrow σ /HCP two-phase coexistence window is located in the range $w_0 = 35-40$ at $25 \text{ }^\circ\text{C}$ (Figure A2.1), however, these samples irreversibly transform into σ LLCs on heating to $60 \text{ }^\circ\text{C}$, which are retained upon

subsequent cooling to 25 °C. The last observation suggests that the high-symmetry HCP phases are metastable with respect to the lower symmetry σ phase in this hydration range.

The brittle solid LLCs in the composition window $26 \leq w_0 \leq 31$ displayed unique SAXS signatures between 25–100 °C that do not correspond to any known periodic crystal phase in metal alloys or soft materials (Figure 3.2). These SAXS patterns exhibit four closely spaced yet broad low q peaks with multiple high q maxima that are much less well-defined. The qualitative resemblance of these patterns to those obtained from DDQCs of charge-neutral, self-assembled soft materials,^{37,40,152,235,242} coupled with the sample composition proximity to that of the σ phase strongly suggests the emergence of dodecagonal quasicrystalline order in this ionic micelle packing.

In spite of the polycrystalline nature of this LLC that precludes direct observation of the expected 12-fold rotational symmetry of a DDQC,^{176,235,243} the 10 well-resolved peaks in the SAXS pattern in Figure 3.2A are readily indexed using the five-dimensional reflection scheme developed by Yamamoto²⁹⁶ and validated by Ishimasa *et al.* in Mn-Cr-Ni-Si alloys.^{241,244} The observed peaks conform to the reflection condition $(h_1h_2h_10h_5)$, $[h_5 = 2n: n \geq 0, n \in Z]$ (see Table A2.2 for peak positions and residuals), which firmly establishes that this DDQC exhibits the non-symmorphic 5D space group symmetry $P12_6/mmc$.²⁹⁶ This structural assignment concurs with the prediction by Lifshitz and Diamant regarding the generic structure of soft quasicrystals.²⁴⁷

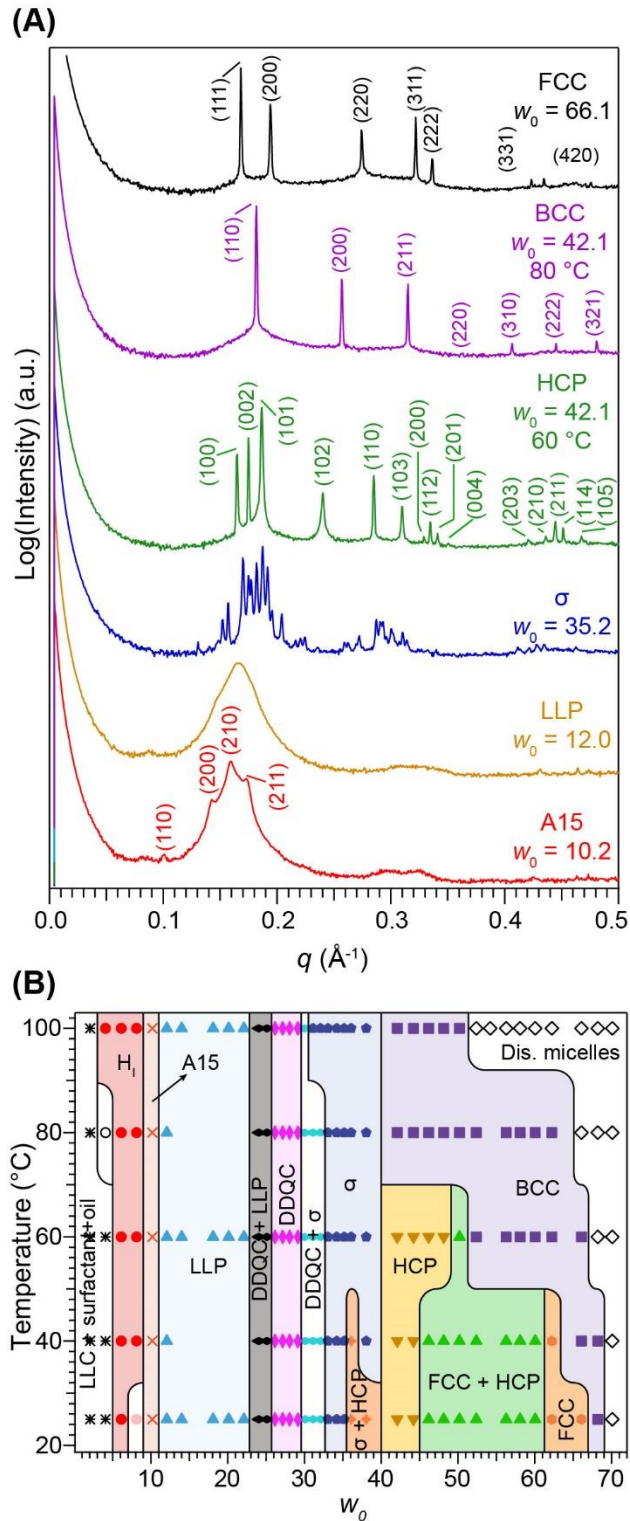


Figure 3.1. (A) Synchrotron 1D-SAXS intensity profiles for aqueous LLCs prepared by **C₁₂PA-Dec10**,

illustrating formation of canonical FCC, HCP, and BCC micellar cubic packings, tetrahedrally close-packed σ and A15 phases, as well as a glassy LLP state. All data were acquired at 25 °C, except where indicated. (B) Temperature versus amphiphile hydration number (w_0) phase diagram from aqueous LLCs of **C₁₂PA-Dec10**, derived by SAXS analyses of samples on their first heating. Solid lines indicate approximate phase boundary locations.

This lyotropic DDQC is comprised of periodic layers, in which ionic micelles are aperiodically arranged at the vertices of a square-triangle tiling that displays local 12-fold rotational symmetry. A random Stampfli tiling representing the aperiodic in-plane order for an ideal, defect-free DDQC is given in Figure 3.2B,²³⁴ where the ratio of the number of triangles to squares is $4/\sqrt{3}$.²⁹⁷ From the SAXS pattern in Figure 3.2 and peak positions given in Table A2.2, we deduce that the interlayer spacing is $c = 8.02$ nm and the in-plane intermicellar distance is $a = 7.91$ nm (edge length in Figure 3.2B). The obtained $c/a = 1.01$ compares well with those obtained in less well-ordered diblock polymers and giant shape amphiphiles DDQCs,^{40,242} as well as those of quaternary metal alloys.²⁴¹ Note that the periodic FK σ approximant may also be conceptualized as a specific, periodic square-triangle tiling.²³⁵

Consistent with the latter structural relationship, we find that as-prepared LLC samples with $31 \leq w_0 < 33$ exhibit σ /DDQC phase coexistence at 25 °C, evidenced by shoulders observed on the four prominent low- q SAXS peaks of the quasicrystal (Figure 3.3). Heating these samples to 100 °C triggers their irreversible rearrangement into pure σ phases with no further evolution on cooling to 25 °C. Analyses of different sample regions demonstrate the complete loss of aperiodic order in favor of the periodic 3D σ phase. Notably, the location of the (002) peak of the σ phase thus obtained coincides with that of the (00002) DDQC reflection. The interlayer spacings in the 12-fold quasicrystal and its periodic approximant are thus identical, in a manner reminiscent of diblock polymer DDQCs.²⁴² The irreversibility of the DDQC + $\sigma \rightarrow \sigma$ transition provokes questions

regarding the equilibrium nature of the DDQC LLC.

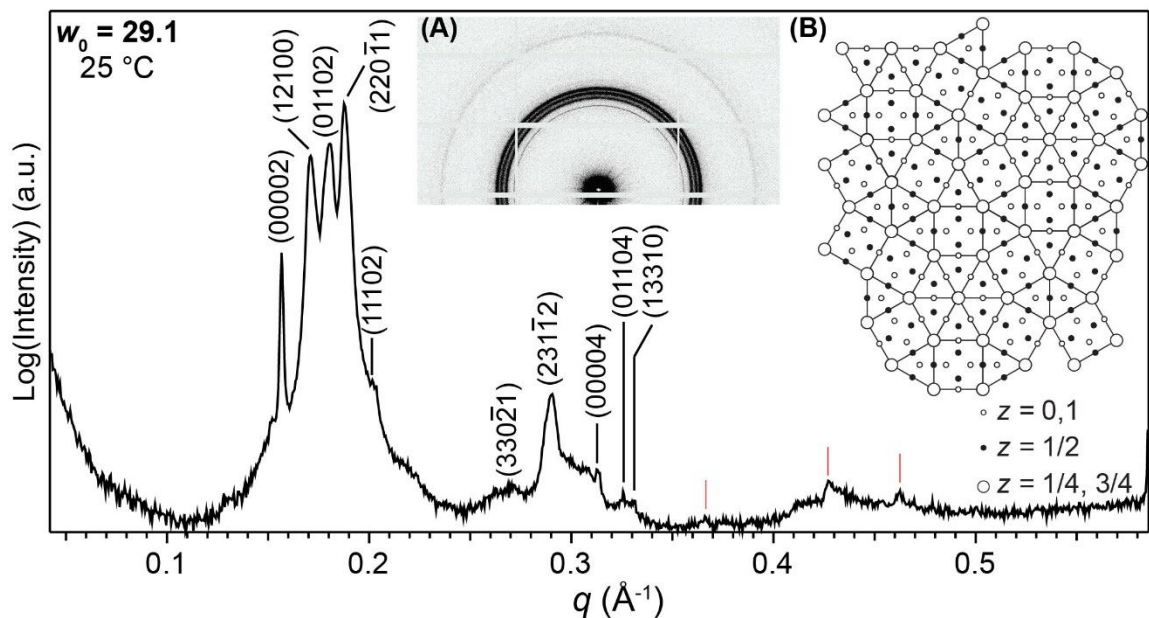


Figure 3.2. (A) SAXS pattern obtained by $\text{C}_{12}\text{PA-Dec10}$ hydrated to $w_0 = 29.1$ at $25\text{ }^\circ\text{C}$ corresponding to a well-ordered DDQC with interlayer spacing $c = 8.02\text{ nm}$ and in-plane intermicellar distance $a = 7.91\text{ nm}$. Miller indices for the first ten peaks corresponding to the 5D space group symmetry $P12_6/mmc$ are provided (red tick marks correspond to peaks that could not be unambiguously assigned). (B) Schematic Stampfli tiling depiction of the in-plane, aperiodic order of the oil-laden micelles of an ideal, defect-free DDQC.

X-ray scattering patterns for LLCs with $w_0 = 11\text{--}23$ are devoid of sharp peaks (Figure 3.1A). They are instead characterized by broad, low-intensity correlations at $q = 0.07\text{--}0.09\text{ \AA}^{-1}$ and $0.28\text{--}0.35\text{ \AA}^{-1}$, with an intervening broad peak at $q = 0.17\text{ \AA}^{-1}$. Some of these samples exhibit SAXS patterns with a low- q shoulder on the highest intensity broad peak, which apparently coincides with the (00002) peak of the DDQC (Figure A2.3). The lack of Bragg scattering suggests the absence of order in these solid samples, consistent with a dynamically arrested, super-cooled micelle liquid. Bates and co-workers identified similarly correlated block polymer melt states as non-ergodic, liquid-like packings (LLP).^{37,242} The lyotropic LLP persists on heating to $100\text{ }^\circ\text{C}$, consistent with

the dynamic arrest of a glassy state. The composition window bounded by the LLP and DDQC states between $23 \leq w_0 \leq 26$ is populated by LLCs that exhibit two-phase coexistence (Figure A2.3). Further reduction in LLC hydration to $w_0 = 10.2$ yields SAXS patterns with four scattering maxima superposed on a broad correlation peak. Since the sharp SAXS maxima are located at $q/q^* = \sqrt{2}$, $\sqrt{4}$, $\sqrt{5}$, and $\sqrt{6}$ ($q^* = 0.1024 \text{ \AA}^{-1}$ at $25 \text{ }^\circ\text{C}$), we tentatively assign this LLC as a poorly ordered FK A15 phase ($Pm\bar{3}n$ symmetry) possibly coexisting with the glassy LLP. Qualitatively, the SAXS peaks breadths indicate that the average A15 phase grain size is small. Su et al. observed a similar SAXS trace for an intermediate structure while transitioning from A15 to Z phase in the self-assembly of giant-shape amphiphiles.⁴¹ We are currently exploring the implications of this surprising similarity. Finally, LLCs with $w_0 = 6.1$ form hexagonally-packed cylindrical micelles (H₁) (Figure A2.4).

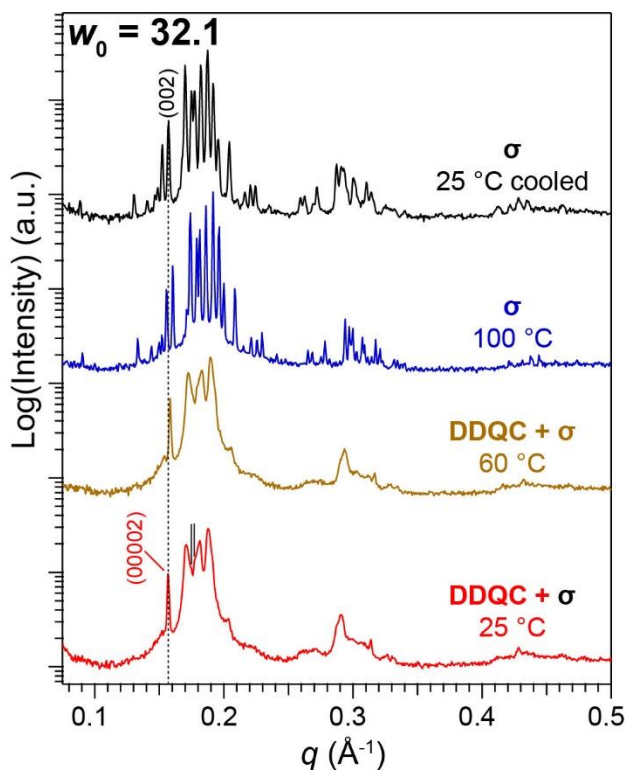


Figure 3.3. Synchrotron SAXS data for as-prepared **C₁₂PA-Dec10** LLCs formed at $w_0 = 32.1$ on heating,

during which samples were equilibrated at each temperature for ≥ 10 min. The as-made sample that exhibits DDQC/ σ two-phase coexistence irreversibly transforms on heating to 100 °C into a pure FK σ phase, which persists on cooling to 25 °C. The reflections corresponding to the σ phase are indicated by the tick marks in pattern in the initial obtained at 25 °C. Note the coincidence of the respective (00002) and (002) spacings of the DDQC and the σ phase (*dashed line*).

Given the occurrence of non-ergodic LLP states and irreversible thermal transformations of some lyotropic DDQCs into σ phases, we sought to assess the thermodynamic stability of the DDQC by studying how path-dependent preparation of the same final LLC composition impacts the observed morphologies and their thermal stabilities. We first premixed C₁₂PA-TMA₂ and H₂O via three cycles of centrifugation and hand-mixing to form LLCs, after which 10 wt% *n*-decane relative to C₁₂PA-TMA₂ was added by additional centrifugation and hand-mixing cycles. Isothermal sample annealing at 50 °C for 30 min subsequently effected complete oil uptake to yield clear, homogeneous samples (see Section 3.2 for details). The phase portrait in Figure 3.4 obtained for oil-laden LLCs made by this “inverse” order of component addition differs substantially from that in Figure 3.1B, which stems from the “normal” order of component addition (oil first). Inverse addition notably yields BCC order at $w_0 = 70$, whereas the normal addition order yields a disordered solution at the same composition. Therefore, the lyotropic order-disorder transition shifts to a higher w_0 -value. Inverse order of addition LLCs also form BCC phases when $w_0 = 61$ –70, instead of the FCC structure obtained on adding water to surfactant/oil mixtures (Figure 3.1B). The BCC structure thermoreversibly transitions to a disordered state when heated 60 °C, albeit with slower nucleation kinetics of the ordered structure when cooled back to 25 °C. When $w_0 = 40$ –60, closest-packed FCC and HCP phases are again observed using the inverse order of addition protocol. While hard sphere FCC packings are typically favored over HCP phases on entropic grounds,¹⁸³ the free energy differences between these phases are minute and the observed phase likely arises from

nucleation-limited growth.¹⁷⁵ These closest-packed structures again undergo thermally-induced transitions to BCC phases on heating to 60–80 °C.

In contrast to LLP and DDQC formation, inverse addition order of LLC preparation triggers the self-assembly of pure FK σ phases when $31 < w_0 < 41$ and periodic A15 structures when $w_0 = 6$ –27. SAXS traces for the A15 LLCs exhibit up to 18 peaks, indicative of high degrees of long-range translational order with large grains sizes (Figure A2.5). Thus, the DDQC is strikingly absent from this phase diagram. The preference for the σ phase over the QC on changing the order of LLC component addition coupled with the aforementioned irreversible DDQC \rightarrow σ thermal transition strongly suggests that the quasicrystalline state is metastable with respect to the 3D approximants.

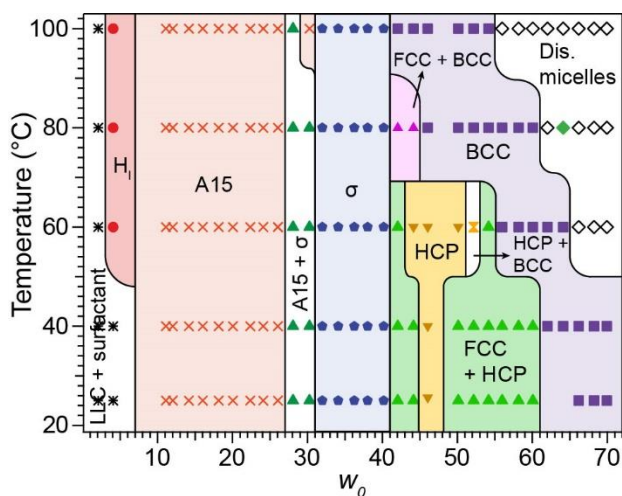


Figure 3.4. Temperature *versus* w_0 LLC phase portrait obtained from samples produced by mixing 10 wt% decane relative to amphiphile into pre-formed, $C_{12}PA$ - TMA_2 aqueous LLCs, in which the DDQC is entirely absent.

The counterion clouds of self-assembled ionic micelles mediate their electrostatic cohesion in ordered LLCs, whereby free energy minimization centers the counterion distribution equidistant from the oppositely charged interfaces of each micelle and its neighbors.^{31,95,202} Thus, the counterion clouds in ionic micellar LLCs outline the polyhedral Wigner-Seitz (W-S) cells of the

underlying lattice. However, these hydrated micelles also prefer spherical shapes that minimize the interfacial area per surfactant with minimal variations in amphiphile hydration. Thus, ordered LLC phase selection must optimize both counterion-mediated intermicellar cohesion in the lattice and the local average ionic sphericity of the micelle counterion clouds.^{31,95} The number-averaged isoperimetric quotient of the W-S cells ($IQ = 36\pi V^2/S^3$, where V is volume and S is surface area of the cell) quantifies average lattice sphericity and decreases in the order $IQ_{\sigma} > IQ_{A15} > IQ_{BCC} > IQ_{FCC} = IQ_{HCP}$ due to the higher average coordination numbers of the FK phases.¹¹²⁻¹¹³ In bis(tetramethylammonium) decylphosphonate ($C_{10}PA-TMA_2$) aqueous LLCs, Kim *et al.* demonstrated that this free energy balance drives the phase sequence $BCC \rightarrow \sigma \rightarrow A15 \rightarrow H_I$ with decreasing w_0 .³¹ Dehydrating a BCC phase with one micelle type induces deviations in ionic sphericity by reducing the intermicellar distances, which drives amphiphile chain exchange to facilitate formation of a FK σ phase with five symmetry equivalent classes of micelles of discrete sizes. Thus, local spherical particle symmetry is optimized in the σ phase at the expense of the global lattice symmetry through particle reconfiguration.

The aqueous LLC phase behavior of $C_{12}PA-TMA_2$ mirrors that of $C_{10}PA-TMA_2$, albeit with larger A15 and smaller σ phase windows (see Figure A2.6) in addition to HCP packings at high w_0 . By virtue of the longer 12-carbon tail, $C_{12}PA-TMA_2$ forms larger hydrated micelles with lower interfacial curvatures than $C_{10}PA-TMA_2$. This lower curvature requires a smaller average counterion-headgroup distance in order to screen the electrostatic repulsions between the more closely packed, dianionic headgroups. This higher degree of counterion association with the particle surface renders the micelles more deformable, reducing the penalty for ionic sphericity deviations.⁹⁵ Thus, the lower sphericity A15 lattice forms over a larger region of phase space.

The shift of the σ phase window to lower w_0 -values on addition of n -decane to $C_{12}PA-TMA_2$ (Figure 3.4) relative to the oil-free system (Figure A2.6) stems from its localization in the swollen

micelle cores.^{202,205} Micelle swelling in an A15 LLC phase of C₁₂PA-TMA₂ increases the hydrophobic volume at each lattice site, forcing the counterion cloud to more strongly conform the polyhedral W-S cell boundaries. Thus, oil addition amplifies ionic sphericity deviations and drives higher sphericity phases to form at lower w_0 -values. Note that conceptually related arguments have recently been advanced to explain the emergence of micelle packings in homopolymer-swollen sphere-forming diblock polymer melts.²⁰⁷

The path-dependent preparation of decane-swollen C₁₂PA-TMA₂ micellar LLCs indicates that method of oil introduction impacts the breadth of the micelle size distribution and consequent ordered phase nucleation. In the case of inverse order of addition, oil is introduced to an ordered LLC with a pre-determined micelle size distribution dictated by electrostatics. Therefore, particle swelling is templated so that the micelle size distribution only modestly broadens and is accompanied by relatively minor spatial rearrangements that optimize micelle sphericity and cohesion. The close structural relationship between the A15 and σ phases likely enables the observed transition from the former to the latter phase.⁶² On the other hand, normal H₂O addition to pre-mixed *n*-decane/C₁₂PA-TMA₂ most likely forces rapid and uneven decane partitioning into the micelles to yield a broader particle size distribution that cannot readily relax, due to substantial barriers for oil and amphiphile exchange in this strongly segregated system. This broader micelle size distribution fails to order, thus shifting the lyotropic disorder-to-BCC transition to a slightly lower w_0 for samples prepared by normal order of addition. Additionally, the unit cell parameter of the BCC structure formed by the “normal” order of addition are $\sim 9\%$ greater than that formed by “inverse” order of addition at comparable hydrations, further suggesting the non-equilibrium nature of the micelle-sizes in LLCs formed by hydration of surfactant/oil mixtures. At $w_0 = 32.1$, normal order of oil addition also results in σ phase unit cell volumes that are $\sim 5\%$ larger than those obtained from the inverse addition protocol. The finding that only pure σ phases form on thermal cycling

DDQC + σ ($w_0 = 31\text{--}33$), and σ + HCP ($w_0 = 36\text{--}40$) LLCs, coupled with the sole formation of pure σ phases by inverse oil addition strongly suggests that σ is the underlying equilibrium structure.

At the lowest hydrations, the formation of poorly ordered A15 phases and non-ergodic LLP states by normal order of addition contrasts the well-ordered A15 LLCs formed at the same w_0 -values under the inverse addition method of sample preparation method. This observation is in contrast with Carlos Baez-Cotto & Mahanthappa, where addition of 10 wt% decane to A15 forming LLCs of tetramethylammonium decanoate led to the formation of periodic C14 and C15 micellar arrangements.²⁰² The Laves phases exhibit a $\pm 20\%$ variation in the W-S cell volumes as compared to the modest 3% variation found in an A15 structure. We posit that the hard dianionic nature headgroup of **C₁₂PA-TMA₂** yields rigid micelles, which resist the large variation in micelle sizes and curvatures to form the Laves phases. Instead, the micelle size distribution in the A15 structure is only weakly disturbed, that decreases the extent of ordering of the A15 phase formed by **C₁₂PA-Dec10** at $w_0 = 10.2$. At higher hydrations, the competition between the micelle curvature as dictated by the electrostatics and the oil leads to complete loss of long-range order leading to the formation of the LLP state. Interestingly, the low- q correlations observed in the LLP state at $0.07 \leq q \leq 0.09 \text{ \AA}^{-1}$ coupled with the broad peak at $q = 0.17 \text{ \AA}^{-1}$ are reminiscent of scattering patterns obtained from the C15 structure formed by LLCs of TMA-decanoate.

These observations strongly suggest that the DDQC and LLP are long-lived, non-equilibrium states, which originate from the broad, non-equilibrium distribution of micelle sizes formed on water addition to a surfactant/oil mixture. By geometrical analogy to the formation of intermetallic quasicrystals,²⁹⁷ this micelle ensemble apparently exhibits a lower nucleation barrier as compared to the periodic σ phase approximant, in spite of the latter being the thermodynamic equilibrium phase. The lyotropic DDQC remains trapped at low temperatures and only partially relaxes on gaining structural mobility by heating to 100 °C, by aperiodic layer rearrangement and intermicellar

chain and oil exchange to facilitate σ phase formation. These observations mirror a report by Gillard *et al.* of a microphase separated diblock polymer DDQC, wherein the quasicrystalline state emerges from a thermally quenched LLP and only slowly transforms into a periodic σ phase on extended isothermal annealing.²⁴² In this context, the appearance of a lyotropic LLP in a region of phase space adjacent to the lyotropic DDQC suggests similarities in how these soft quasicrystals emerge from soft micellar glasses.

3.4 Conclusions

The simple, path-dependent formation of a kinetically stable, non-equilibrium lyotropic DDQC of oil-laden ionic micelles of a small molecule surfactant defies the conventional view that structural relaxations in low molecular weight amphiphilic systems are fast. Minimal hydration of the ionic surfactant headgroups of decane-swollen $C_{12}PA-TMA_2$ micelles induces a strongly segregated state, in which the free energy penalty for intermicellar alkane and amphiphile exchange slows, due to the highly incompatible nature of the hydrophobic and salty aqueous nanodomains. Water addition to an oil/surfactant mixture results in a dynamically arrested and broad particle size distribution trapped far from equilibrium, which forms both supercooled liquid-like packings of ionic micelles and DDQCs. Our findings support the notion that LLP structure intrinsically encodes the formation of periodic or aperiodic crystals with different nucleation and growth barriers per recent work by Bates and co-workers.^{37,242} The fragile order in the lyotropic DDQC is readily apparent, as attempts to prepare pseudo-single domain DDQCs for detailed structural analyses by oscillatory or steady shear processing drive sample fracture into a glassy state.

The formation of quasicrystals and their periodic approximants in lyotropic and thermotropic liquid crystals,²³⁵ diblock polymers,²⁴² and giant shape amphiphiles⁴⁰ suggests the existence of scale-invariant self-assembly principles that control access to periodic and aperiodic order in these

supramolecular materials. Understanding and harnessing this apparent universality may enable the scale up of (a)periodic order to technologically-relevant length scales toward useful hyperuniform structures²⁹⁸ with unusual photonic bandgap behaviors.^{251-252,299} The facile methodology of using additives to modify the particle size distribution in complex phases may be utilized to access previously unknown periodic and aperiodic morphologies. Our definitive identification of the lyotropic DDQC space group symmetry may also aid computational efforts that provide a window into the preferential formation of 2D QCs with 12-fold aperiodic order in soft matter,^{246,248} which starkly contrasts the preference for 3D icosahedral order in intermetallic alloys. This materials behavior dichotomy may stem from differences in the types and numbers of degrees of freedom that specify the sphere-size distributions, which beget structure formation in strongly correlated particle ensembles.

Chapter 4.

Path-Dependent Preparation of Complex Micelle Packings of a Hydrated Diblock Oligomer

Reprinted from Jayaraman A.; Zhang D. Y.; Dewing B. L.; Mahanthappa M. K. *ACS Central Science* **2019**, 5, 619-628.

© American Chemical Society, 2019

4.1 Introduction

The structures and properties of diverse classes of materials arise from their path-dependent solidification transitions from the liquid state. Crystallization of a liquid of spherical particles typically results in the formation of high packing-fraction structures such as body-centered cubic (BCC), face-centered cubic (FCC) and hexagonally closest-packed (HCP) crystals, exemplified by the ubiquity of such ordered phases in elemental metals and their alloys,⁴⁹ solidified noble gases,³⁰⁰ and hard sphere colloids.³⁰¹ In some exceptional cases, pure metals and their alloys also crystallize into low-symmetry Frank-Kasper (FK) phases, wherein multiple classes of symmetry-equivalent particles pack into giant unit cells containing ≥ 7 particles.⁵²⁻⁵³ One such exemplary packing is the FK σ phase formed by β -U,³⁰² β -Ta,³⁰³ and FeCr alloys,⁴⁹ which comprises 30 particles of five distinct, symmetry-equivalent classes arranged in a large tetragonal unit cell. While ligand-decorated nanoparticles,³⁰⁴⁻³⁰⁵ sphere-forming block polymers,^{170-171,176,306} and hydrated surfactant micelles form FCC and HCP structures,^{185,187} the less dense BCC packing is also commonly observed.^{18,32} Until recently, soft materials were long thought to adopt only these high-symmetry packings. However, recent experimental reports describe thermotropic liquid crystals,^{34-35,307} block polymers,^{36-37,152,308} giant shape amphiphiles,³⁰⁹ and functional nanoparticles³¹⁰ comprising charge-neutral building blocks that form micellar FK phases and related dodecagonal

quasicrystals.^{37,40,152,235,242-243,311} The appearance of these complex phases apparently originates from a frustrated balance between preserving the preferred local spherical particle symmetry, and filling space at constant density in order to maximize interparticle van der Waals cohesion.^{113,196}

FK A15 and σ phases have been recently recapitulated in lyotropic liquid crystals (LLCs) of minimally hydrated ionic surfactants.^{31,95} In contrast to the aforementioned solvent-free self-assembling systems, low symmetry ionic LLC sphere packings arise from maximization of counterion-mediated electrostatic cohesion amongst the micelles while minimizing energetically expensive variations in counterion-headgroup solvation.^{31,95,202} The disparate natures of the non-covalent forces and the space filling constraints underlying complex phase formation in solventless non-ionic and solvated ionic amphiphilic materials naturally beg the question: do solvated non-ionic amphiphiles form FK structures? In this connection, earlier studies of the water concentration-dependent lyotropic mesophases formed by model poly(ethylene-*block*-ethylene oxide) diblock oligomers (“ C_iE_j ” surfactants) documented the formation of BCC, FCC, and HCP spherical micelle packings, as well as FK A15 phases.^{14,169,186,312} However, the low symmetry σ phase and other FK phases are strikingly absent in these non-ionic lyotropic systems.

Herein, we describe the water concentration-dependent LLC self-assembly behavior of the non-ionic amphiphile $n\text{-C}_{16}\text{H}_{33}(\text{OCH}_2\text{CH}_2)_{20}\text{-OH}$ ($\text{C}_{16}\text{E}_{20}$, commercially available as Brij® 58). Temperature-dependent synchrotron small-angle X-ray scattering (SAXS) studies between $T = 25\text{--}100\text{ }^\circ\text{C}$ reveal that $\text{C}_{16}\text{E}_{20}$ self-assembles into FK A15 phases at LLC compositions comprising ~ 40 wt% water. Upon heating such samples, we observe an order-to-order transition (OOT) to a BCC phase, which gives way to a hexagonally-packed cylinders (H_1) morphology at higher temperatures. However, rapidly quenching this sample to $25\text{ }^\circ\text{C}$ surprisingly leads to the development of an exceptionally well-ordered FK σ phase, which only slowly transforms into the original A15 state upon extended ambient temperature annealing. Thus, we demonstrate a previously unrecognized

dependence of LLC mesophase morphology on sample thermal history for low molecular weight amphiphiles. These findings highlight analogies between the path-dependent processing of sphere-forming soft materials and metal alloys, establishing the importance of nucleation and growth kinetics in the self-assembly of spherical particles across disparate materials classes in accord with Ostwald's rule for the crystallization of solids.

4.2 Results

LLC samples were produced by mixing the block oligomer C₁₆E₂₀ with variable amounts of ultra-pure water (18 M Ω •cm), followed by sample homogenization by at least three cycles of centrifugation (4950 x g for 10 min each) and hand-mixing at 22 °C. The commercial sample of C₁₆E₂₀ (Brij® 58), which derives from ethoxylation of *n*-C₁₆H₃₃OH, was used as received without additional purification. ¹H NMR end group analyses reveal that $M_{n,NMR} = 1074$ g/mol, while size-exclusion chromatography indicates that $M_{n,SEC} = 1000$ g/mol with $\bar{D} = M_w/M_n = 1.17$ (against poly(styrene) standards). (See Figures S1 and S2 for ¹H NMR and size-exclusion chromatography traces, respectively.) The resulting LLC samples were sealed in hermetic, alodined differential scanning calorimetry (DSC) pans for synchrotron SAXS analysis at the Advanced Photon Source at Argonne National Lab. Detailed sample preparation and data acquisition protocols are provided in the Supporting Information. Previous studies of the phase behavior of C₁₆E₂₀ relied solely on optical microscopy and low resolution SAXS to identify the LLC mesophases formed, thus precluding definitive morphology assignments.^{169,313-314}

Figure 4.1 presents representative SAXS data for a series of aqueous LLCs formed by centrifugation in the concentration range 30-65 wt% C₁₆E₂₀, from which a phase map was constructed using data obtained during the first heating cycle for each composition. Figure 4.1A depicts a representative SAXS intensity profile for a sample with 32.1 wt% C₁₆E₂₀ at 25 °C, which

exhibits five scattering maxima corresponding to (111), (200), (220), (311) and (222) peaks of a micellar face-centered cubic (FCC) lattice with a unit cell parameter $a = 13.0$ nm. While FCC packing persists in the range $30 \leq [C_{16}E_{20}] \leq 38$ wt% at ambient temperature, we find that samples with $[C_{16}E_{20}] = 30\text{--}32$ wt% undergo a thermoreversible melting transition to a disordered (isotropic) micellar solution above 60 °C. In the range $[C_{16}E_{20}] = 33\text{--}38$ wt%, heating the as-formed FCC structure instead drives an order-to-order transition (OOT) to a pure body-centered cubic (BCC) morphology at $T \geq 60$ °C. In some samples, we also observe the expected intervening window of FCC/BCC two-phase coexistence anticipated by Gibbs' Phase Rule for two-component systems (Figure A3.3).³¹⁵ Further heating to $T > 70$ °C leads to a BCC \rightarrow disorder transition, again with an expected window of two-phase coexistence in some cases.

On increasing $[C_{16}E_{20}]$ to $40\text{--}54$ wt%, the as-formed LLCs yield SAXS patterns with six peaks at $q/q^* = \sqrt{2}, \sqrt{4}, \sqrt{6}, \sqrt{8}, \sqrt{12}, \sqrt{14}$ ($q^* = 0.0953 \text{ \AA}^{-1}$ at 52.4 wt%) corresponding to a BCC micelle packing with a (310) scattering peak extinction. LLCs with $[C_{16}E_{20}] = 40\text{--}45$ wt% exhibit an order-disorder transition (ODT) near $T = 80$ °C, whereas samples with $[C_{16}E_{20}] = 45\text{--}54$ wt% instead exhibit an OOT to a 2D hexagonally-packed cylinders (H_I) morphology that remains stable up to 100 °C. In the weight fraction range $46\text{--}50\%$ $C_{16}E_{20}$ at 100 °C, the H_I phase coexists with an isotropic micellar solution as evidenced by the superposition of a broad correlation scattering peak on the sharp Bragg scattering (Figure A3.4). SAXS patterns for samples comprising $[C_{16}E_{20}] = 54\text{--}59$ wt% display at least 18 sharp SAXS maxima at $q/q^* = \sqrt{2}, \sqrt{4}, \sqrt{5}, \sqrt{6}$, etc. consistent with the FK A15 phase with $Pm\bar{3}(-)n$ symmetry (space group #223). Note that A15 phases have been previously observed in aqueous LLCs of structurally homologous long-chain alcohol ethoxylates.^{14,169,186} The SAXS pattern in Figure 4.1A obtained at 57.9 wt% $C_{16}E_{20}$ is characteristic of a FK A15 phase with a unit cell parameter, $a = 14.7$ nm at 25 °C. At all compositions that form the FK A15 phase, we observe the same sequence of thermally-induced OOTs: A15 \rightarrow BCC \rightarrow H_I

(Figure 4.1B), where the OOT temperature decreases with increasing $[C_{16}E_{20}]$. When $[C_{16}E_{20}] > 62$ wt%, only a thermally stable H_I phase forms over the entire accessible range $T = 25\text{--}100$ °C with intercylinder distances $d \approx 7.29$ nm. Generally, the ordered LLC unit cell parameters only weakly depend on hydration and temperature within a given pure phase window (< 5 % variation). A complete aqueous LLC phase diagram upon first heating for $C_{16}E_{20}$ is given in Figure 4.1B. Although the Gibbs phase rule anticipates two-phase coexistence windows between each pure LLC phase,³¹⁵ the composition resolution of our phase map (~ 3 wt% increments) revealed only one such occurrence as noted.

LeBail refinement of the 1D-synchrotron SAXS profile of an A15 LLC using the *JANA2006*²⁸⁷ software package enabled quantitative extraction of the structure factor intensities, which were used as inputs for the *SUPERFLIP*²⁸⁸ charge-flipping algorithm to reconstruct a real-space electron density map for this phase. The electron density map for the A15 phase formed at 58.9 wt% $C_{16}E_{20}$ shown in Figure 4.2A represents the 90% negative electron density isosurface obtained by averaging 11 charge-flipping algorithm convergences (see Supporting Information for *SUPERFLIP* input file). Based on the LLC composition and by assuming equal mass densities of the aqueous and hydrophobic domains, we estimate that the average aggregation number for the A15 phase micelles is $N_{\text{agg}} = 127$ diblock chains. However, the electron density map clearly indicates that the A15 phase consists of two symmetry-equivalent classes of quasispherical micelles, which appear to differ in size and shape. From the 2D electron density map of the $z = 0$ and 1 planes of the A15 phase (Figure 4.2B), the micelles appear to be polyhedral, with facets and apparent sizes that mirror the shapes and volumes of the Wigner-Seitz (W-S) cells for each occupied lattice position.

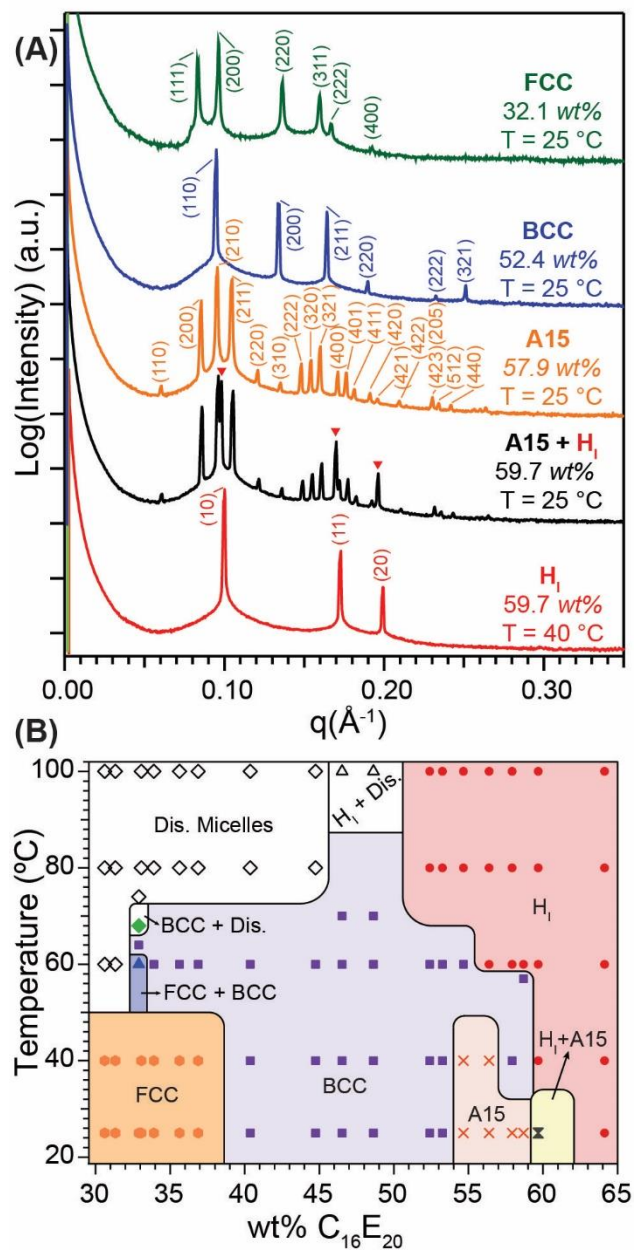


Figure 4.1. Aqueous LLC phase behavior of C₁₆E₂₀: (A) Synchrotron SAXS patterns exhibiting the formation of H₁, A15 + H₁, A15, BCC, and FCC phases at diblock oligomer concentrations ranging 30–65 wt% C₁₆E₂₀. (B) Temperature *versus* wt% C₁₆E₂₀ phase portrait depicting the composition-dependent LLC phases that form, based on synchrotron SAXS analyses of as-prepared samples at 22 °C on the first heating. The solid lines delineate the approximate locations of the phase boundaries.

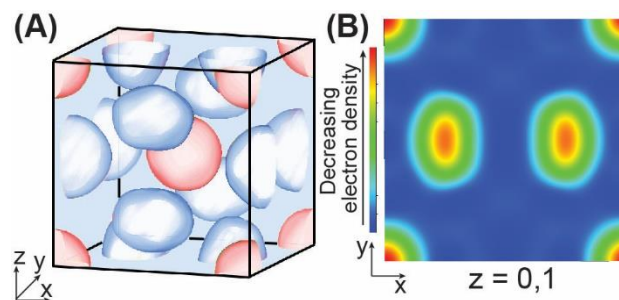


Figure 4.2. (A) Electron density map (90% isosurface) of an A15 phase reconstructed from a 1D-synchrotron SAXS pattern derived from a LLC with 58.9 wt% C₁₆E₂₀, comprising six coordination number $CN = 14$ micelles (*blue*) and two $CN = 12$ micelles (*red*). (B) 2D electron density map of the $z = 0$ and 1 planes of the A15 phase showing faceted micelles, which face each other and mimic the underlying Wigner-Seitz cell structure of each corresponding lattice position.

Similarly faceted micelles in self-assembled FK A15 and σ phases have been previously noted in X-ray data-derived electron density reconstructions for wedge-shaped dendritic liquid crystals^{35,84,307} and for lyotropic mesophases of ionic alkylphosphonate LLCs.³¹ In the latter case, molecular dynamics (MD) simulations by Kim *et al.* revealed that the negatively charged alkylphosphonate micelle facets mirror the W-S cell structures of these aqueous FK LLC phases.³¹ These MD simulations also demonstrated that the ionic micelle aggregation numbers (N_{agg}) in the σ phase vary by as much as $\pm 9\%$ around the mean volume, whereas related self-consistent mean-field theory (SCMFT) calculations for solvent-free diblock polymer A15 phases indicate a $\pm 3\%$ variation in the micelle sizes within a unit cell.³⁷ The limited resolution of the density map in Figure 4.2A precludes quantitative analyses of such differences in micelle volumes. Nonetheless, the micelles at different symmetry-equivalent positions appear to have different volumes and thus different N_{agg} values.

Thermally cycling LLCs comprising [C₁₆E₂₀] = 54–59 wt% between 25 and 70 °C unexpectedly leads to the formation of complex morphologies not observed on heating the as-prepared samples.

Heating a sample comprising 58.7 wt% C₁₆E₂₀ resulted in the sequence of phase transitions A15 (25 °C) → A15 + BCC (37 °C) → H_I (60 °C) with increasing T . However, rapidly quenching this sample from 70 °C to 25 °C by immersion in a thermostatted water bath induces its transformation from a H_I phase to a BCC morphology ($a = 9.18$ nm) with a series of low intensity SAXS peaks near the base of the (110) peak after 5 min (Figure 4.3). Isothermal annealing at 25 °C causes the latter peaks to grow in intensity at the expense of the BCC scattering maxima. After 50 min, the sample develops a remarkably complex scattering pattern with > 50 sharp SAXS peaks with the most intense peaks occurring at intermediate q -values (Figure 4.3). This distinctive scattering signature corresponds to that of a pure Frank-Kasper σ phase ($P4_2/mnm$ symmetry) with tetragonal unit cell parameters $a = 28.4$ nm and $c = 14.9$ nm ($c/a = 0.525$) (see Figure A3.5 for fully indexed pattern and Table A3.1 for complete peak listing with residuals). While similar scattering signatures have been obtained for wedge-shaped dendrons,³⁵ block polymers,^{36-37,152} and ionic surfactant LLCs,^{31,95} this unexpected discovery constitutes an unrecognized example of a lyotropic FK σ phase in non-ionic diblock oligomer LLCs.

By applying the *SUPERFLIP* charge-flipping algorithm to SAXS data for the FK σ phase obtained by quenching a LLC with 58.7 wt% C₁₆E₂₀ from 60 to 25 °C and isothermally annealing it for 2 d, we obtained the electron density reconstruction shown in Figure 4.4A (see Supporting Information for *SUPERFLIP* input file). This structure exhibits five classes of symmetry-equivalent micelles located in different environments having coordination numbers $CN = 12, 14,$ and 15 , consistent with prior reports of σ phases.^{31,52-53,113} In a manner analogous to the A15 phase, the micelles in the σ phase exhibit facets corresponding to the W-S cell (Voronoi) lattice partition. The degree of micellar faceting in the σ phase (Figure 4.4B) is apparently less pronounced than in the A15 phase (Figure 4.2B). MD simulations of ionic micelles forming the σ phase,³¹ and SCMFT calculations for σ phase-forming diblock polymers show that the micelle volumes vary by $\pm 9\%$

around the mean value,^{31,37,113} which mimics the volume the variation in the W-S cells of the lattice. Thus, the formation of the σ phase suggests the adoption of a discrete N_{agg} distribution among the micelles to enable the formation of the specific micelle sizes required by this structure.

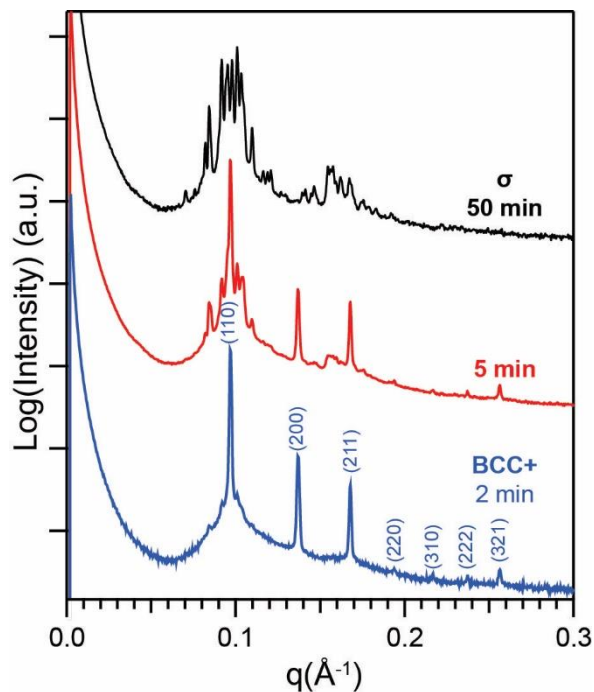


Figure 4.3. SAXS patterns obtained from a LLC having 58.7 wt% $C_{16}E_{20}$, upon quenching from 70 °C to 25 °C. The HI phase rapidly transforms into BCC, evidenced by the 7 sharp SAXS maxima recorded 2 min after quenching. The BCC phase then evolves into a well-developed FK σ phase on further isothermal annealing at 25 °C for 50 min.

Further isothermal annealing of this FK σ phase at 25 °C for 60 d leads to the development of new peaks coincident with an A15 phase (Figure 4.5). While the (002) reflection for the A15 phase is distinct from the (002) peak for the σ phase, the relatively close values are consistent with the observed epitaxial relationship between these tetrahedrally close packed FK phases.^{35,40,95,235} Over a period of 150 d of isothermal annealing at 25 °C, the sample continues to evolve and eventually transforms into a pure A15 phase (Figure 4.5). Note that the unit cell parameter for this A15 phase

is identical to that of the initially prepared LLC ($a = 14.7$ nm), indicating the apparent metastability of the σ phase with respect to the thermodynamically preferred A15 phase at 25 °C.

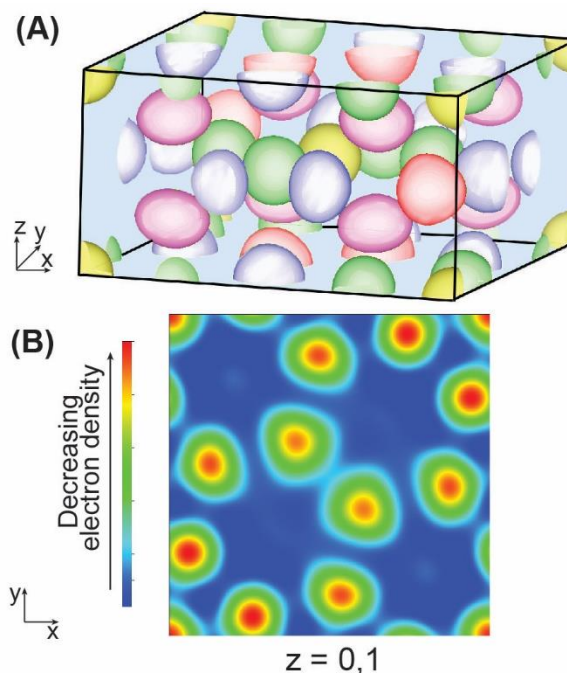


Figure 4.4. (A) Electron density reconstruction (90% isosurface) depicting the FK σ phase formed by a sample with 58.7 wt% $C_{16}E_{20}$ on quenching from 60 °C to 25 °C, followed by isothermally annealing at 25 °C for 2 d. The 30 particles within the tetragonal unit cell belong to five symmetry-equivalent classes exhibiting coordination numbers $CN = 12$ (red and blue), 14 (green and purple), and 15 (yellow). (B) 2D-electron density map of the $z = 0$ and 1 planes of the σ phase, illustrating the more modest faceting of the micelles as compared to the A15 phase in Figure 4.2B.

In view of the appearance of the FK σ phase as a long-lived, metastable liquid crystalline state, we carefully reassessed the potential accessibility of the σ phase on heating. Figure A3.6 furnishes temperature-dependent SAXS results for a LLC formed at 58.7 wt% $C_{16}E_{20}$ on heating in 2 °C increments, with a 5 min sample equilibration time at each temperature, in the window $T = 25\text{--}60$ °C. This in-depth analysis established that the phase sequence on heating is:



Within the confidence of these high-resolution and high-sensitivity synchrotron SAXS analyses, we observe no evidence for even weak peaks corresponding to any other phases. Thus, we conclude that the σ phase is only accessible upon cooling from H_I via a transient BCC phase within the temperature and time resolution of our experiments.

We subsequently examined the impact of sample cooling rate on the formation of the $C_{16}E_{20}$ LLC FK σ phase (Figure 4.6). Rapidly quenching a 58.7 wt% $C_{16}E_{20}$ LLC from 70 °C to 25 °C reproducibly forms a FK σ phase, which remains unchanged even after isothermal annealing for up to 3 d. On the other hand, cooling a sample with $[C_{16}E_{20}] = 57.9$ wt% from 70 °C to 25 °C at 0.1 °C/min (over 550 min) followed by annealing at 25°C for 2 h yields a SAXS pattern indicative of a FK σ phase with at least three additional peaks that correspond to a coexisting A15 phase. More explicitly, the additional reflections correspond to the (200), (210), (211), and (400) planes of the A15 lattice.

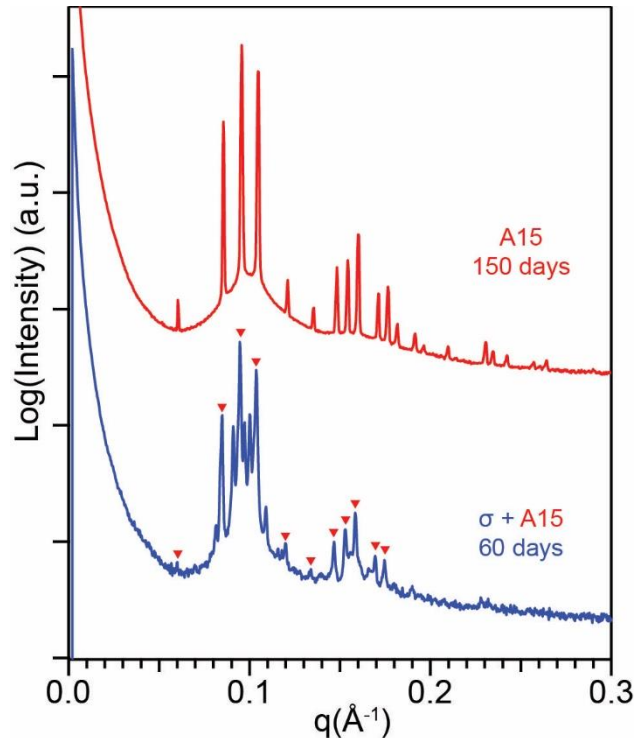


Figure 4.5. SAXS patterns of the σ phase obtained from a quenched LLC with 58.7 wt% $C_{16}E_{20}$ upon ambient

temperature annealing for 60 d shows the development of peaks which index to A15 (*red markers*). Extended annealing for 150 d reveals that the σ phase completely reverts to the original A15 phase of the as-prepared sample, indicating that the σ phase is a long-lived metastable liquid crystalline state at 25 °C.

Given the recent recognition that thermal processing sensitively impacts the observed spherical micelle morphologies of neat diblock polymers,³⁷ we probed the influence of temperature quench depth on the formation of the LLC σ phase formed at $[C_{16}E_{20}] = 58.7$ wt%. A relatively shallow quench of a H_I phase at 70 °C ($q^* = 0.0984 \text{ \AA}^{-1}$) to 50 °C led to the formation of a BCC LLC ($q^* = 0.0977 \text{ \AA}^{-1}$) that remains stable upon 50 °C annealing for ~ 10 h (Figure A3.7). We note that the SAXS peak intensities for the BCC LLC evolve even after phase nucleation during the annealing period, suggesting a relatively long timescale for micelle size equilibration even at this relatively high temperature. This size equilibration, which presumably occurs through intermicellar chain exchange of $C_{16}E_{20}$ amphiphiles, highlights the dynamic nature of these reconfigurable soft particle assemblies. Rapidly cooling a sample with the same composition from 70 °C to 40 °C (into the A15/BCC coexistence window observed on heating) initially drives formation of a BCC structure, which is followed by σ phase nucleation evidenced by the evolution of a second set of weaker intensity SAXS peaks 10 min after the quench (Figure A3.8). Annealing this LLC at 40 °C for ~ 18.5 h leads to reduced σ phase SAXS peak intensities, suggesting a preference for the BCC structure at 40 °C. Finally, quenching the sample from 70 °C to 0 °C drives a transition from the H_I to a BCC morphology exhibiting seven, somewhat broad SAXS peaks with $(q/q^*)^2 = 1, 2, 3, \dots$ etc. (Figure A3.9). Upon isothermal annealing at 0 °C over 4 d, this BCC morphology remains unchanged (*i.e.*, the SAXS peak intensities do not change) with no evidence for σ or A15 phase nucleation or growth. Since the BCC morphology comprises only one class of symmetry equivalent micelles, the formation of either of the FK A15 (two micelle types) or σ (five micelle types) phases requires both significant micelle reconfiguration through interparticle unimer exchange and

nucleation of a denser, tetrahedral close packing.^{31,113}

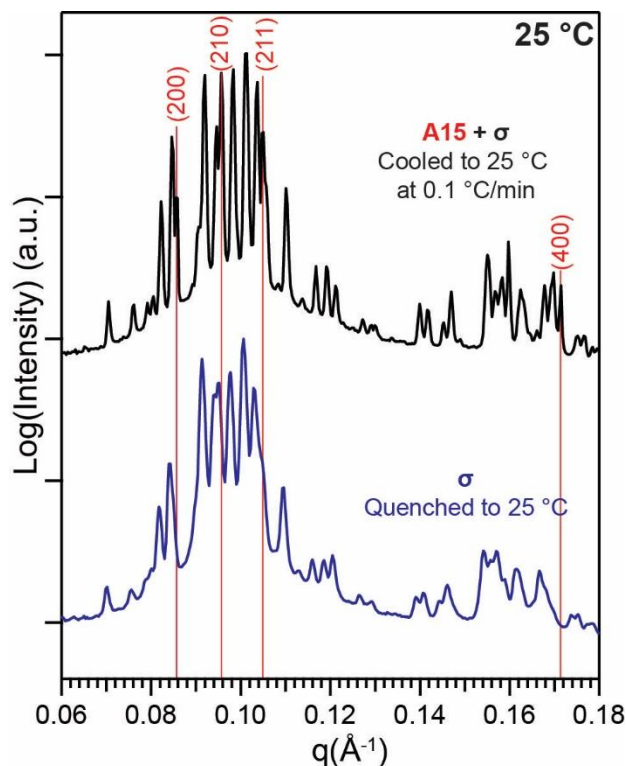


Figure 4.6. SAXS traces obtained by two different LLC sample cooling protocols from 70 °C to 25 °C: (1) quenching a sample formed at 58.7 wt% $C_{16}E_{20}$ at > 60 °C/min and isothermally annealing for > 3 days at 25 °C (blue), and (2) cooling a sample comprising 57.9 wt% $C_{16}E_{20}$ at 0.1 °C/min followed by isothermal annealing for 2 h at 25 °C (black). The rapid quench yields a pure σ phase, whereas slow cooling yields coexisting A15 and σ phases. The red lines correspond to (200), (210), (211) and (400) peak positions of A15 structure, which are present in the black trace and are absent in the blue trace.

The fact that quenching of the above LLC to 0 °C leads to a stable BCC phase is consistent with cessation of chain exchange, which retards mass exchange-dependent phase transitions. Note that SAXS patterns for these quenched samples do not exhibit any signs of crystallization of the alkyl tails, the PEO segments, or the water in the LLC. Therefore, the cessation of chain exchange must stem from an increased penalty for extraction of a hydrocarbon chain into the aqueous domain due to the increased chemical incompatibility of the alkyl core and the aqueous corona at low

temperatures.³¹⁶ A similar temperature-dependent frustration of interparticle chain exchange that delays σ phase nucleation and growth was previously reported by Gillard *et al.*, upon quenching neat diblock polymers from the disordered state to below the ergodicity temperature (T_{erg}). Below T_{erg} , long-lived non-equilibrium states comprising disordered yet non-ergodic, liquid-like micelle packings become trapped.^{36,113,242,308} The authors argued that the jammed, glassy state forms due to increased core-corona segregation at temperatures below T_{erg} that leads to the loss of relaxation modes required for equilibrium structure formation.

Rapidly quenching the 58.7 wt% $\text{C}_{16}\text{E}_{20}$ LLC from 70 °C to 30 °C followed by isothermal annealing leads to the formation of coexisting BCC and σ phases after 15 min (Figure 4.7). After 20 min of annealing at 30 °C, we also observe the splitting of the σ -phase (002) SAXS peak (*red markers*) and the appearance of a new, lower intensity peak at $q = 0.0606 \text{ \AA}^{-1}$. After further annealing this sample for 19.5 h post-quench, we observe the appearance of the (110), (200), (210), and (211) peaks of the A15 phase. However, these SAXS features do not develop upon sample quenching to 25 °C and subsequent annealing for 3 d. These findings collectively suggest that the thermally activated process of interparticle chain exchange accelerates the reversion of the metastable σ phase to the A15 phase.

The results of these various thermal processing experiments for the 58.7 wt% $\text{C}_{16}\text{E}_{20}$ aqueous LLCs are graphically summarized in Figure 8. The as-made sample produced by centrifugation of water and the diblock oligomer followed by hand-mixing at 22 °C leads to the formation of an A15 phase with $a = 14.75 \text{ nm}$. Heating the A15 phase to 70 °C drives the formation of a H_1 LLC, which undergoes the depicted time-dependent transformations upon quenching to temperatures $T \leq 50 \text{ °C}$. At all quench temperatures, we initially observe the nucleation of a BCC phase with slightly different unit cell parameters. At 50 °C, the BCC phase remains stable upon isothermal annealing at the quench temperature. Quenching the LLC sample to 40 °C initially forms a BCC phase,

followed by nucleation of a σ phase that reverts to BCC upon extended annealing at 40 °C for 18.5 h. At $T = 25$ or 30 °C, the initially formed BCC phase transforms into a σ phase that slowly reverts to the original A15 phase (same unit cell parameter).

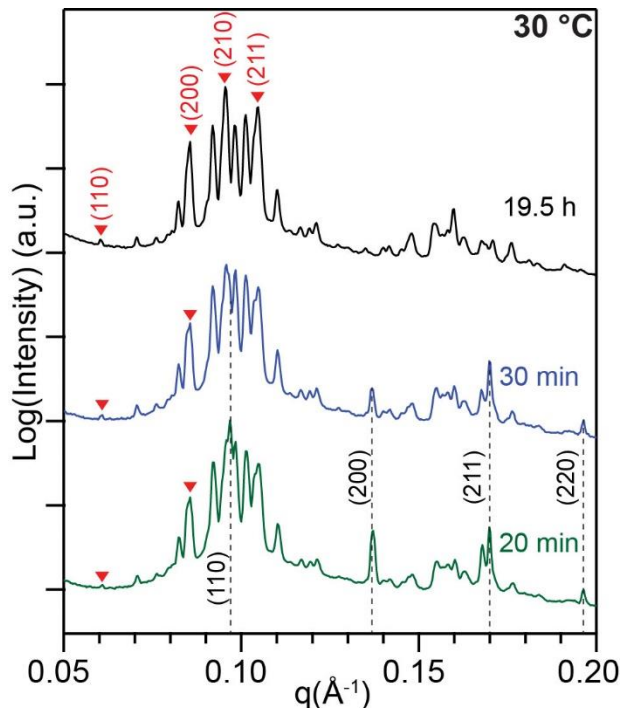


Figure 4.7 SAXS traces depicting the nucleation of the FK σ and A15 phases from a BCC morphology, upon quenching an aqueous LLC comprising 58.7 wt% $C_{16}E_{20}$ from 70 to 30 °C with subsequent isothermal annealing. BCC/ σ phase coexistence is observed after 20 min of isothermal annealing at 30 °C, after which the BCC peak intensities (*dashed lines*) decrease with concomitant growth of an A15 LLC morphology indicated by the appearance of the (110), (200), (210), and (211) SAXS peaks (*red triangles*).

4.3 Discussion

The water concentration-dependent self-assembly behavior of $C_{16}E_{20}$ into lyotropic sphere packings at 25 °C originates from a frustrated balance of minimizing water-hydrophobic contacts, while maximizing poly(ethylene oxide) (PEO) corona chain hydration and minimizing repulsive micellar packing (steric) interactions. In dilute aqueous solution (high H_2O contents), theoretical

and experimental studies have shown that the PEO coronae of $C_{12}E_8$ micelles partially dehydrate and accumulate near the interface between the hydrocarbon core and the water to mitigate energetically unfavorable contacts.¹⁷⁸⁻¹⁷⁹ The micelles consequently exhibit a core-shell-brush structure, wherein the hydrocarbon core is surrounded by a dehydrated PEO layer from which hydrated PEO chains extend. Thus, the core appears larger than anticipated by the amphiphile composition, and the spatial extent of the hydrated corona is smaller than expected. In a manner akin to hard spheres, these so-called “crew-cut micelles” pack into a closest-packed FCC lattice.^{170,174} However, maintaining this crew-cut structure as the LLC hydration decreases would drive further accumulation of ethylene oxide units at the water/hydrocarbon interface and result in unfavorable intramicellar corona chain overlap. To obviate these unfavorable steric interactions, the PEO segments of the amphiphiles become more uniformly hydrated and stretched so that the interfacial area per chain decreases.^{170,173,317-318} The resulting “hairy” micelles, comprising hydrocarbon cores decorated with stretched PEO arms, now prefer a lower packing fraction BCC structure to prevent unfavorable intermicellar corona chain overlap. Further decreasing the H_2O content in the LLC drives coronae chain stretching (reduced interfacial area per surfactant) and transforms the BCC structure into the lower packing fraction A15 phase to further alleviate interparticle coronal repulsions.^{49,163,170-171,173,319} At fixed temperature, note that N_{agg} increases with decreasing water content along the lyotropic sequence: FCC \rightarrow BCC \rightarrow A15 \rightarrow H_I.

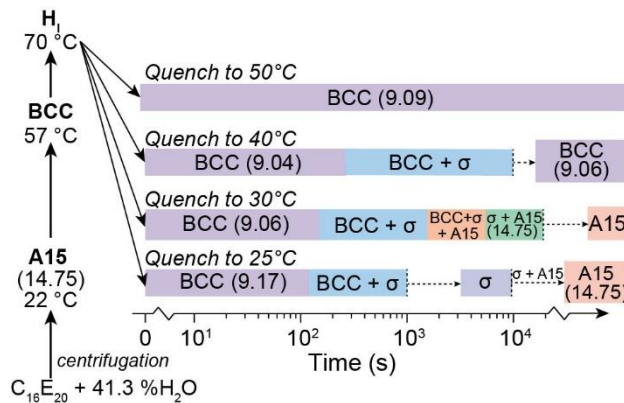


Figure 4.8. Summary of the results of various thermal processing protocols applied to an LLC with 58.7 wt% C₁₆E₂₀. The progression of phases upon quenching to 50, 40, 30, and 20 °C is depicted as a function of log(time). Dotted arrows represent time intervals where no SAXS data were obtained. Numerical values in the parentheses correspond to the unit-cell parameters (in nm) of the respective phases. The unit cell parameters of the BCC phase were obtained immediately following the quench ($t = 0$ s). The unit cell parameter of the A15 phase as-formed by centrifugation is equal to that of samples that were quenched and subsequently annealed at 25 and 30 °C for 150 d and 19.5 h, respectively.

The complex temperature-dependent phase behavior of the C₁₆E₂₀ LLCs on heating may be rationalized in terms of the temperature-dependent water solubility of PEO.³¹⁸ On heating the A15 LLC formed at 54–59 wt% C₁₆E₂₀, the PEO coronae of the hairy micelles partially dehydrate and retract toward the hydrophilic/hydrophobic interface due to reduced PEO solubility with increasing temperature. Thus, heating effectively transforms the hairy micelles into partially crew-cut micelles that prefer to pack into a BCC lattice. Further heating drives greater PEO dehydration and brings the micelles into close proximity, so that they fuse along the <111>-direction of BCC to form the cylindrical micelles of the H_I phase.^{14,320} In a manner consistent with previous reports on solvated block polymer and small molecule amphiphile dispersions,^{14,320-321} the last transition is thermoreversible. This same molecular-level mechanism also explains the somewhat counterintuitive thermal transition from a dense FCC packing to sparsely packed BCC for LLCs with [C₁₆E₂₀] < 39 wt%. Heating the crew-cut micelles of the FCC drives further accumulation of ethylene oxide segments near the water/hydrocarbon interface, as a consequence of reduced PEO solubility with increasing temperature. The resulting “dry” PEO segments near the hydrophobic/hydrophilic interface may penetrate into the hydrophobic particle core. Thus, the particle cores swell and a more loosely packed BCC phase forms in order to mitigate intermicellar corona repulsions.

The observed formation of the C₁₆E₂₀ LLC FK σ phase from a BCC phase is reminiscent of previous reports from Bates and co-workers on di- and tetra-block polymer melts.^{36,113} Since the FK σ phase comprises five distinct classes of symmetry-equivalent micelles (Figure 4) with a specific N_{agg} distribution that exhibits a $\pm 9\%$ variation around the mean value, the transition from a BCC phase (in which all micelles are symmetry-equivalent) must stem from micelle reconfiguration by interparticle amphiphile exchange.³⁰⁸ Bates and co-workers have rationalized σ phase formation in terms of maximizing the van der Waals cohesion of the particle ensemble while maximizing local spherical particle symmetry. In other words, the block polymers fill space at constant density while minimizing both interfacial area between the core and corona and energetically expensive variations in corona segment stretching.^{113,322} Similar arguments have been advanced by Rappolt *et al.* in the case of inverse micellar LLCs.¹⁹⁶ In order to maximize local particle sphericity, the micelles reconfigure into a lattice with a higher average coordination number to introduce more facets to the W-S cells to render them more spherical. According to a metric developed by Polya,³²³ the sphericity of an object with volume V and surface area S may be quantified using the dimensionless isoperimetric quotient (IQ) = $36\pi V^2/S^3$, such that $IQ_{\text{sphere}} = 1$. The number-averaged values of the IQ s for the constituent W-S cells for various phases ascend in the order: BCC (0.7534) < A15 (0.7617) < σ (0.7623). Consequently, one expects that a frustrated BCC phase may transform into a FK σ phase to maximize local particle sphericity and global lattice cohesion.

However, the geometrically predicted phase stability of σ over A15 based on the IQ formalism does not explain the observed metastability of the σ LLC with 54–59 wt% C₁₆E₂₀ in H₂O at 25–30 °C. From the electron density reconstructions given in Figures 2 and 4, we note that the polyhedral micelle cores in the C₁₆E₂₀ FK phases reflect the W-S cells (Voronoi partition) of their underlying crystal lattices. Therefore, the area of the W-S cells serves as a geometric proxy for the micellar

interfacial area in each morphology. Upon calculating the W-S cell area per diblock chain for LLCs formed with 58.7 wt% C₁₆E₂₀ at 25 °C (A_{int} in units of nm²/diblock chain) assuming a uniform interfacial tension across all interfaces, one finds that A_{int} decreases in the order BCC (1.602) > σ (1.354) > A15 (1.353). This calculation demonstrates that the equilibrium A15 phase formed at 25 °C exhibits a slightly lower interfacial area per chain as compared to the metastable σ phase. This trend in A_{int} runs counter to that for IQ , suggesting that the observed morphology reflects a complex optimization of the interfacial contact area and the entropic penalty for chain stretching to completely fill space. Grason and co-workers recently reported a general approach for predicting the phases formed by soft spherical particles in the polyhedral interface limit (PIF), which highlights the subtle thermodynamic balance underlying phase selection in these systems.^{111,322}

These geometric arguments lead to a nuanced picture of the driving forces for FK σ and A15 phase formation in C₁₆E₂₀ LLCs upon thermal quenching to 25 °C. At 70 °C, the PEO corona chains of the H_I micelles are concentrated near the hydrocarbon/water interface due to decreased water solubility of PEO at higher temperatures. Quenching this state to 25 °C drives hydration of the PEO segments, causing the cylinders to pinch off and epitaxially form discontinuous spherical micelles packed onto a BCC lattice. Rapid cooling of the H_I phase likely leads to a non-equilibrium micelle size distribution in the BCC structure. Note that the rates at which the micellar coronae of these newly formed particles approach their equilibrium hydration state and equilibrium micelle size distribution are governed by the relatively slow rate of amphiphile chain exchange between the micellar particles (see Figure A3.7; *vide supra*). As the PEO segments drive toward their equilibrium hydration, the incompatibility between the hydrophobic particle core and the hydrated corona increases. Consequently, the increased enthalpic penalty of hydrocarbon-water contacts drives the transition from the BCC phase to σ followed by A15 via intermicellar amphiphile exchange so as to minimize A_{int} . The fact that the average N_{agg} are nearly the same in the BCC

(123.2), σ (127.7), and A15 (128.2) phases formed with 58.7 wt% C₁₆E₂₀ at 25 °C suggests that micelle fission/fusion events are not operative, and that a combination of chain exchange and spatial redistribution of the micelles effect the overall transition from BCC to A15.

The observed phase sequence BCC \rightarrow σ \rightarrow A15 on quenching from 70 to 25 °C suggests that the barrier for BCC \rightarrow σ is relatively lower than that for the direct BCC \rightarrow A15 transition. Quenching the H_I phase at 70 °C to 25 °C drives a low energy, epitaxial transition to a non-equilibrium BCC phase.^{14,320-321} We speculate that the distribution of N_{agg} for the spherical micelles in this BCC structure is somewhat broad due to the rapid quench conditions. The breadth of this N_{agg} distribution more readily allows the formation of the disperse yet discrete distribution of sphere sizes requisite for σ phase formation, wherein N_{agg} varies by $\pm 9\%$ around a mean value. This transition also enables the system to lower its free energy by reducing A_{int} . As the chains approach their equilibrium hydration, the LLC undergoes a transition to the original A15 phase (formed directly from centrifugation of C₁₆E₂₀ with H₂O) to further reduce A_{int} while also narrowing the variation in N_{agg} to $\pm 3\%$ around a mean value. Given the nearly identical average N_{agg} values for the σ and A15 phases, this transition must involve a subtle spatial rearrangement of the micelles in addition to chain exchange whereby the slow kinetics imply a significant nucleation barrier. The fact that we observe a direct A15 \rightarrow BCC transition on heating from 25 to 70 °C with no intervening phases also suggests that there is a significant barrier to nucleation and growth of the σ phase from A15, possibly due to the required broadening of the micellar N_{agg} distribution. Ha *et al.* have recently reported similarly slow nucleation of FK A15 phases of phosphonate block polymer LLCs in ionic liquids upon cooling from the disordered micellar state.³²⁴ These findings highlight the competing roles of nucleation and growth kinetics that underlie complex phase formation in amphiphilic soft materials. Note that the formation of a metastable σ phase upon quenching LLCs to $T \leq 30$ °C is reminiscent of Ostwald's step rule in solid crystallization: the least stable polymorph

nucleates first upon cooling a melt or a super-saturated solution of the solid.³²⁵ In this present case, both the metastable BCC and σ structures nucleate first and only slowly convert to the equilibrium A15 phase.

Epitaxial transitions between micellar phases in aqueous LLCs of a homologous $C_{12}E_{12}$ amphiphile were previously investigated by Sakya *et al.*¹⁴ The aqueous LLC phase behaviors of $C_{12}E_{12}$ and $C_{16}E_{20}$ are similar in that both amphiphiles form FCC, BCC, A15 and H_I phases with increasing diblock oligomer concentration. Additionally, $C_{12}E_{12}$ LLCs display the temperature-dependent OOT sequence $A15 \rightarrow BCC \rightarrow H_I \rightarrow$ disordered micelles in a narrow composition range. Cooling such LLCs from high temperature while applying shear triggers an epitaxial transition from an aligned H_I to a shear-oriented BCC phase as expected. However, further cooling of this oriented BCC phase led to a complete loss of alignment and the development of SAXS patterns that could not be indexed. Based on similarities between the LLC phase behaviors of $C_{12}E_{12}$ and $C_{16}E_{20}$ and the thermal processing protocols employed, we surmise that the unreported pattern may have been a $C_{12}E_{12}$ LLC σ phase or some other tetrahedrally closest packed FK structure.

4.4 Conclusions

The aqueous LLC phase behavior of the model diblock oligomer $C_{16}E_{20}$ was investigated using temperature-dependent SAXS. In the composition range 54–59 wt% $C_{16}E_{20}$, we observe the formation of a FK A15 phase upon mixing the amphiphile with water. Upon heating this LLC, we observe temperature-dependent order-order transitions to a BCC structure, followed by formation of a H_I morphology. However, rapidly quenching the H_I phase from 70 °C to 25 °C leads to the nucleation and growth of a previously unrecognized FK σ phase, comprising 30 quasispherical micelles packed into a gigantic tetragonal unit cell. This unexpected finding establishes that the σ phase generically forms in systems comprising hydrated ionic surfactants, hydrated non-ionic

diblock oligomers, and solvent-free diblock polymers in spite of the disparate intermolecular forces stabilizing these self-assembling systems. Extended ambient temperature annealing of the LLC FK σ phase results in its remarkably slow reversion to the original A15 phase over the course of 150 days. These findings highlight the unappreciated dependence of LLC morphology on sample thermal history for low molecular weight amphiphiles, which can guide the nucleation and growth of metastable intermediate phases.

The accessibility of myriad particle packings in a given amphiphile system depends on a subtle competition between equilibrium self-assembly thermodynamics and the barriers to phase nucleation and growth. Since thermal processing of both hard and soft materials enables access to fundamentally interesting and commercially important metastable states, one may be tempted to draw parallels between their processing characteristics. For example, rapidly quenching low carbon-content austenite (FCC γ -Fe) drives its diffusionless transformation into a body-centered tetragonal martensitic steel that is metastable with respect to the α -ferrite (BCC) and cementite (Fe_3C).³²⁶ However, quasispherical particle packings observed in solvated block polymer and related amphiphile dispersions stem from diffusion-dependent, interparticle chain exchange between the micelles to reconfigure their sizes and consequent packings. The kinetics of these chain exchange events depend sensitively on the incompatibility between the core domain and the solvent and the core block mobility.^{245,327} High amphiphile concentrations and lattice ordering of their micelles are known to decelerate chain exchange by over an order of magnitude, as compared to dilute solutions.³¹⁶ Therefore, slow unimer dynamics enable the nucleation of higher energy states which become kinetically trapped, because large activation barriers inhibit fast relaxation to the equilibrium structure.^{37,306} Aside from thermal processing, we envision that unimer dynamics in the systems studied here may be tuned by variations in solution pH, addition of exogenous electrolytes, or other environmental stimuli. This conceptual framework for understanding the complex free

energy landscape underlying solvated amphiphile self-assembly suggests that subtle changes in the conditions under which they aggregate and assemble may beget access to exciting, new and undiscovered states.

Chapter 5.

End Group-Dependent Complex Micellar Self-assembly of Hydrated Diblock Oligomers

5.1 Introduction

Selective solvent addition to amphiphiles drives formation of ordered supramolecular soft materials known as lyotropic liquid crystals (LLCs), which display mesoscale ordering at length scales commensurate with their constituent small molecules,^{17,266} block oligomers,^{14,177} or block polymers.^{170-171,328} A variety of segregated morphologies emerge on solvated amphiphile self-assembly, the topologies of which depend primarily on amphiphile structure and solvent concentration, including lamellae (L_{α}), triply periodic multiply continuous networks (e.g., double gyroid and double diamond),^{167,329} hexagonally-packed cylinders (H), and spherical micelle packings.^{18,31,202} LLCs thus present enticing opportunities for bottom-up molecular design of mesostructured soft materials at tailored length scales for morphology-specific applications as selective separations membranes,³²⁹⁻³³⁰ therapeutic encapsulation and delivery vehicles,^{17,19-20} and photonic crystals.^{251,331} Modulation of the amphiphile assembly medium by changing solvent composition, aqueous pH, and the addition of exogenous electrolytes,¹⁸ furnishes alternate means for controlling LLC structure subject to the kinetics of amphiphile rearrangement and ordered morphology nucleation and growth.

Hydrated surfactant micelles typically organize into high-symmetry body-centered cubic (BCC), face-centered cubic (FCC), and hexagonally closest-packed (HCP) structures in a manner analogous to elemental metals.³² These structures form as Type I phases in which the micelle cores are hydrophobic, and Type II phases with hydrophilic micelle interiors. However, recent studies of minimally hydrated alkylphosphonate surfactant LLCs demonstrated the unexpected formation of

a complex Type I micellar Frank-Kasper σ phase with a large, low-symmetry tetragonal unit cell. Well-known in Fe-Cr alloys⁵⁵ and elemental β -U³³² and β -Ta,⁵⁷ the σ phase is an archetypal member of a class of low-symmetry structures known as Frank-Kasper (FK) phases that were geometrically formulated to rationalize the complex particle packings encountered in intermetallic alloys.⁵²⁻⁵³ Tetrahedrally close-packed FK phases exhibit 12-, 14-, 15-, and 16-fold lattice coordination environments with ≥ 7 particles of at least two discrete types packed into low-symmetry unit cells, such that the average coordination number (CN_{avg}) > 13 . More specifically, the σ phase comprises 30 micelles of five symmetry-equivalent classes that conform to a discrete aggregation number (N_{agg}) distribution that is geometrically specified by the unit cell structure. The first soft matter FK phases were observed in aqueous LLCs of hydrated lipids and their mixtures, as well-known Type I A15 ($Pm\bar{3}n$ symmetry)¹⁸⁹ and Type II Laves C15 ($Fd\bar{3}m$ symmetry)³⁰ structures. Decades after these initial discoveries, complex FK phases were observed in wedge-shaped dendrons,^{35,82} neat di- and tetrablock polymers,^{36,38} giant-shape amphiphiles,⁴⁰⁻⁴¹ ionic and non-ionic aqueous LLCs,^{31,95,177} and sugar-terminated polyolefins.¹⁶⁰⁻¹⁶¹ The magnitudes of the intermolecular forces underlying these phases span weak van der Waals interactions in the case of neutral building blocks, H-bonding involving water and sugar moieties in block oligomers, and long-range electrostatic interactions in ionic small molecule amphiphiles. The universal, scale-invariant complex micelle packing phase behaviors of these self-assembled soft materials and their intermetallic counterparts is striking.

Phase selection in self-assembled soft micellar assemblies may be directed through judicious thermal processing or by co-assembly with carefully designed additives. Thermal and shear processing of solvated and neat diblock polymers enables access to new phases, including the first reports of both C14 and C15 Laves intermetallic structure analogs in diblock polymers by Bates and co-workers.^{37,96,176-177} Swelling of hydrated alkylcarboxylate micelle cores with *n*-decane also

triggers formation of Laves C14 and C15 mesophases.²⁰² This last strategy was recently extrapolated to BCC sphere-forming diblock polymers, whereby blending of a homopolymer nearly identical to that of the particle core domain drives σ , C14, and C15 phase formation.²⁰⁷ Bates and co-workers have also demonstrated routes to A15 and σ phases and aperiodically ordered, dodecagonal quasicrystals (DDQCs) in bidisperse blends of polystyrene-*block*-poly(1,4-butadiene), wherein the constituents form only canonical BCC and hexagonally-packed cylinders (H) phases.¹⁰⁹ In a related finding, Takagi and co-workers demonstrated that the formation of complex particle packings in poly(1,4-butadiene)-*block*-poly(ϵ -caprolactone) sensitively depends on the molecular weight of the polybutadiene corona dopant.¹⁵⁸⁻¹⁵⁹ Electron density reconstructions and self-consistent field theory calculations for some of these phases indicate that self-assembled micelles in these complex phases exhibit polyhedrally warped core-corona interfaces that assume the shapes of the corresponding Wigner-Seitz (W-S) cells of the underlying lattice.^{31,37-38} The diblock foam model developed by Grason and co-workers rationalizes the experimentally observed formation of FK phases in terms of a delicate balance between the amphiphile interfacial area and chain stretching in the polyhedral surface limit.¹¹¹⁻¹¹² Within this framework, dopant addition in the matrix or core nanodomains of FK phases modulates either the micellar interfacial area or the corona chain stretching to allow access to new particle packings.

A recent report by Jayaraman *et al.* documented the rich aqueous LLC phase behavior of the hydroxyl-terminated polyethylene-*block*-poly(ethylene oxide) oligomer $C_{16}H_{33}(OCH_2CH_2)_{20}OH$ ($C_{16}E_{20}$), which exhibits the Type I phase sequence $H_1 \rightarrow A15 \rightarrow BCC \rightarrow FCC$ with increasing hydration.¹⁷⁷ Formed at 54–59 wt% $C_{16}E_{20}$ in H_2O , the A15 phases undergo thermally-induced order-to-order (OOT) transitions into H_1 morphologies at 70 °C. However, rapidly quenching these samples to 25 °C unexpectedly enables nucleation and growth of a long-lived, metastable FK σ phase that reverts to the original A15 phase after ~150 d of isothermal annealing (Figure 5.1).

Electron density reconstructions obtained from the A15 and σ phases reveal polyhedral micelle distortions, suggesting that intercorona interactions play important roles in micelle cohesion, ordered phase nucleation, and morphology stabilization. Given the documented impact of polymer end groups on their self-assembled morphologies³³³ and the inference that the $C_{16}E_{20}$ endgroups are situated near the micelle peripheries, the hydroxyl end groups may play a non-trivial role in the stabilization of the metastable σ phase and its slow reversion to the original A15 structure.

Herein, we demonstrate that end group modifications of $C_{16}E_{20}$ substantially alter the its LLC phase behavior and lead to the stabilization of complex Type I quasispherical micellar assemblies with periodic crystalline and aperiodic quasicrystalline mesoscale order. We specifically report the synthesis and phase behavior of $C_{16}E_{20}$ amphiphiles bearing carboxylic acid ($-COOH$), sodium sulfonate ($-SO_3^-Na^+$), and trimethylammonium chloride ($-NMe_3^+Cl^-$) end groups. These studies reveal that carboxylated and sulfonates amphiphiles form FK σ phases at 25 °C that thermoreversibly transition into H_I morphologies on heating. However, the trimethylammonium-terminated surfactants serendipitously self-assemble into a dodecagonal quasicrystal (DDQC). While this quasicrystalline state rapidly transforms into a H_I phase on heating, the reverse transition on cooling is slow and leads to less well-formed structure that remains indefinitely stable at 25 °C. The formation of the periodic FK phase and DDQC are rationalized within the polyhedral surface limit framework augmented by specific interactions induced by amphiphile end group identity. Thus, these studies highlight the previously unrecognized role of coronal end group interactions in complex micellar phase stabilization.

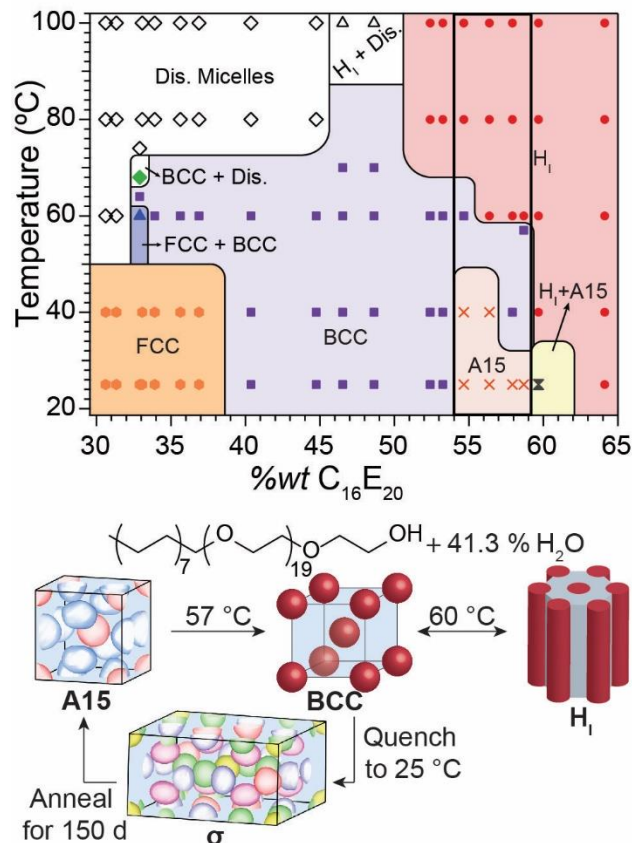


Figure 5.1. (A) Temperature *versus* amphiphile weight fraction phase portrait of hydroxyl-terminated $C_{16}E_{20}$ reported by Jayaraman et al., documenting formation of FCC, BCC, FK A15, and H_I phases on decreasing hydration. (B) Aqueous LLCs formed at 54–59 wt% $C_{16}E_{20}$ adopt A15 structures that undergo OOTs to BCC and H_I morphology at elevated temperatures, yet quenching the H_I phase to 25 °C nucleates a FK σ phase that only slowly reverts to the original A15 phase over 150 days. Reprinted (adapted) with permission from Jayaraman A.; Zhang D. Y.; Dewing B. L.; Mahanthappa M. K. Path-Dependent Preparation of Complex Micelle Packings of a Hydrated Diblock Oligomer. *ACS Central Science* **2019**, 5 (4), 619-628. Copyright 2019 American Chemical Society.

5.2 Experimental Section

Materials. All materials and reagent grade solvents were purchased from Sigma-Aldrich (Milwaukee, WI) and used as received unless other noted. NaH was used as a 60 wt% suspension

in mineral oil. 1,3 propanesultone and *p*-toluenesulfonyl chloride (TsCl) were obtained from Alfa Aesar (Will Barr, MA). 7.3 M NMe₃ in H₂O was purchased from Acros Organics (Geel, Belgium). Anhydrous NEt₃ was obtained by drying and distilling from CaH₂. Acetonitrile was dried over P₂O₅, purified via distillation and stored under a N₂ atmosphere. Anhydrous, anaerobic tetrahydrofuran (THF) and CH₂Cl₂ were obtained by sparging analytical grade solvent with nitrogen for 30 min followed by cycling through a column of activated alumina for 12 h in a Vacuum Atmospheres solvent purification system. All glassware were dried in an oven maintained at 140 °C for at least 12 h prior to use. Ultra-pure water (18 MΩ•cm) obtained from Thermo Scientific™ Barnstead™ Smart2Pure 3 UV/UF water purification system was degassed by sparging N_{2(g)} for ≥ 30 min.

Molecular characterization. ¹H and ¹³C nuclear magnetic resonance (NMR) spectra were recorded on a Bruker Avance 400 MHz with Smartprobe or Avance-500 with DCH cryoprobe. They were referenced relative to the residual proton shift in CD₃OD-*d*₄ (δ 3.31 ppm) or CDCl₃ (δ 7.26 ppm).

Synthesis of C₁₆E₂₁-C. Inside a glove box under argon, C₁₆E₂₀-OH (10.03 g, 9.34 mmol) and NaH (1.56 g, 4.27 equiv.) were weighed into 100 mL and 200 mL Schlenk flasks, respectively. The flasks were sealed using rubber septa and brought outside the glove box. Anhydrous CH₃CN (50 mL) was added to C₁₆E₂₀ under N₂ to yield a cloudy solution. An addition funnel was attached to the flask containing NaH under flowing N₂, which was subsequently cooled to 0 °C using an ice bath. The C₁₆E₂₀ solution was added to NaH over 10 min and the 100 mL flask was further washed using 20 mL CH₃CN to recover any residual C₁₆E₂₀. The ice bath was removed, and the reaction was allowed to proceed at room temperature (RT) for 1.5 h after which it was again cooled to 0 °C. A solution of 2-bromoacetic acid (2.57 g, 2.04 equiv.) in CH₃CN (10 mL) as added to the reaction flask dropwise using the addition funnel over 40 min. The flask as allowed to warm to 22 °C over

12 h. The reaction mixture was quenched by the addition of 1 M HCl (50 mL) at 0 °C. All organic volatiles were removed to yield a cloudy aqueous solution, which was diluted by addition of 50 mL CH₂Cl₂. The mixture was transferred to a separatory funnel and the layers were separated. The aqueous layer (*top*) was washed using DCM (2 × 70 mL) and the combined organic layers were washed with 1 M HCl_(aq) (1 × 50 mL), sat. NaCl_(aq) (2 × 40 mL). The organic layer was dried over anhydrous Na₂SO_{4(s)} and all volatiles were removed *in vacuo*. The white solid thus obtained was re-dissolved in DCM (15 mL) and precipitated in hexanes twice. The supernatant solution was decanted and the resulting solid was azeotropically freeze-dried from C₆H₆. Yield : 7.1 g (61.5%).
¹H NMR (400 MHz, CDCl₃, 22 °C) δ (ppm): 4.17 (O-CH₂-COOH, s, 2H) 3.66 (-OCH₂CH₂-, m, 85H), 3.46 (CH₂-CH₂-OCH₂CH₂-, t, 2H), 1.59 (CH₂-CH₂-OCH₂CH₂-, p, 2H), 1.27 (CH₂-CH₂-, m, 25H), 0.91 (CH₃-CH₂-, t, 3H).

Synthesis of C₁₆E₁₉-S. C₁₆E₂₀-OH (5.01 g, 4.66 mmol) and NaH (411.9 mg, 2.27 equiv.) was added to a 100 mL Schlenk flask under Ar atmosphere inside a glove box. The flask was sealed with a rubber septum and removed from the box followed by addition of dry CH₃CN (30 mL) under N₂ atmosphere. After stirring for 1.5 h, 1,3-propanesultone was dissolved in 10 mL CH₃CN and transferred to the reaction flask under N₂. The reaction was allowed to proceed for 12 h at RT in the inert atmosphere. The orange-tinged, heterogenous reaction mixture was quenched by the addition dH₂O (20 mL) followed by stirring for 1 h. The contents of the flask were transferred to a separatory funnel and the layers were separated. The lower aqueous layer was washed with CH₂Cl₂ (3 × 50 mL) with intermittent addition of NaCl_(s) to break any emulsions formed during these washing steps. The organic layers were combined and washed with 50 mL saturated NaCl_(aq) solution and dried over Na₂SO_{4(s)}. All volatiles are removed to yield an orange solid. The solid was dissolved in 30 mL CH₂Cl₂ and 1.05 g activated charcoal was added. After stirring for 1 h, the mixture was eluted through a silica gel column by sequential addition of 150 mL CH₂Cl₂, 150 mL

ethyl acetate, and 250 mL MeOH. The fraction containing the product was isolated and filtered to remove fine silica particulates and yield a clear and colorless solution. Removal of volatiles yielded a yellowish-white solid, which was dissolved in CH₂Cl₂ and precipitated in pentane three times. The solid thus obtained from decantation of the supernatant was azeotropically freeze-dried from C₆H₆. Yield: 3.5 g (60.9 %) ¹H NMR (400 MHz, CD₄OD, 22 °C) δ (ppm): 3.67 (–OCH₂CH₂–, m, 77H), 3.49 (CH₂–**CH**₂–OCH₂CH₂, t, 2H), 2.89 (O–CH₂–CH₂–**CH**₂–SO₃Na, m, 2H), 2.06 (O–CH₂–**CH**₂–CH₂–SO₃Na, m, 2H), 1.59 (**CH**₂–CH₂–OCH₂CH₂–, p, 2H), 1.31 (CH₂–CH₂, m, 25H), 0.92 (**CH**₃–CH₂, t, 3H).

Synthesis of C₁₆E₂₁–N. C₁₆E₂₀–OH (5.99 g, 5.58 mmol) was weighed into a 200 mL Schlenk flask under Ar_(g) inside a glove box. The flask was sealed with a rubber septum and brought out to a Schlenk line, where an addition funnel was attached under a flush of N_{2(g)}. Et₃N (4.6 mL, 5.60 equiv.) and anhydrous CH₂Cl₂ (20 mL) were sequentially added and this mixture was cooled to 0 °C. A solution of TsCl (2.00 g, 2.64 equiv.) in 10 mL anhydrous CH₂Cl₂ was added over a period of 10 min. The clear and colorless reaction was allowed to proceed for 12 h at 22 °C. The reaction mixture was then filtered through a medium frit, and the resulting white residue was washed with ethyl acetate. Volatile solvent removal from the combined filtrates yielded a yellowish-white solid. The solid was treated with EtOAc (30 mL) and 1 M HCl (40 mL) and this mixture was transferred to a separatory funnel to facilitate layer separation and isolation of the organic layer. The lower aqueous layer was then washed with EtOAc (3 × 40 mL). The combined organic layers were then washed with saturated NaHCO_{3(aq)} (2 × 40 mL) and saturated NaCl_(aq) (2 × 40 mL), followed by drying with anhydrous Na₂SO_{4(s)}. All volatiles are removed from the resulting solution to furnish the C₁₆E₂₀–OTs as a waxy white solid, which was used without further purification.

The C₁₆E₂₀–OTs solid intermediate was dissolved in CH₃CN (60 mL) in a 200 mL round bottom flask and 10 mL of N(CH₃)_{3(aq)} (>10 equiv.) was added. The reaction was stirred for 12 h and the

volatiles were removed *in vacuo* to yield a white solid, which is presumed to be an ammonium tosylate salt. MeOH (80 mL) and DOWEX® 1×4 chloride form ion chloride ion exchange resin (30.8 g) were added to the solid and stirred for 4 d at RT. This solution was filtered away from the ionic exchange resin, which was subsequently washed with MeOH (100 mL). Passage of the combined filtrates a Celite plug yielded a colorless solution. Upon removal of the volatile solvents, the resulting white solid was re-dissolved in CH₂Cl₂ and precipitated in hexanes twice. The final product was azeotropically freeze-dried from C₆H₆ to yield a white solid. Yield: 2.9 g (41.5 %). ¹H NMR (400 MHz, CD₄OD, 22 °C) δ (ppm): 3.98 (–OCH₂CH₂–N(CH₃)₃Cl, m, 2H), 3.66 (–OCH₂CH₂–, m, 82H), 3.49 (CH₂–CH₂–OCH₂CH₂, t, 2H), 3.24 (–CH₂–N(CH₃)₃Cl, s, 9H), 1.59 (CH₂–CH₂–OCH₂CH₂–, p, 2H), 1.31 (CH₂–CH₂, m, 25H), 0.92 (CH₃–CH₂, t, 3H).

Lyotropic Liquid Crystal (LLC) Sample Preparation. Desired amounts of polymer were massed into 1-dram vials inside an anhydrous glove box and requisite amount of ultra-pure water was added. The samples were homogenized by three cycles of centrifugation (4950×g, 10 min) and hand-mixing at 22 °C to yield transparent soft solids. Sample vials were sealed with Parafilm® to prevent LLC dehydration and samples remained sealed when not in use.

Small-angle X-Ray Scattering (SAXS). The samples were quiescently equilibrated at 22 °C for 24 h before their morphologies were investigated using synchrotron SAXS analyses. Using an incident beam energy of 13.3 or 14.0 keV ($\lambda = 0.932$ or 0.886 Å) and a 3.617 m sample-to-detector distance at the 12-ID-B beamline of the Advanced Photon Source (Argonne, IL), synchrotron 2D-SAXS patterns were recorded on a Pilatus 2M (25.4 cm × 28.9 cm rectangular area) detector with 1475 × 1679 pixel resolution (172 μm × 172 μm pixel size). The scattering wavevector (q) scale in these patterns was calibrated using a silver behenate standard ($d = 58.38$ Å). LLC samples were hermetically sealed in alodined aluminum DSC pans (TA Instruments, Newcastle, DE), which were equilibrated at the desired temperature in a home-built multi-sample heated array stage for at least

10 min prior to data collection (typical exposure times ~ 1 s).

Preliminary SAXS measurements were made using a SAXSLab Ganesha300XL instrument in the Characterization Facility, University of Minnesota. Cu K_α X-rays ($\lambda = 1.54 \text{ \AA}$) generated by a Xenocs Geni3DX source were collimated through 2 or 3 sets of 4-bladed motorized, “scatterless” slits. 2D-SAXS patterns were acquired using a Dectris EIGER R 1M detector (7.72 cm \times 7.99 cm rectangular area) with 1030 \times 1065 pixels (75 μm \times 75 μm pixel size) at a sample-to-detector distance of 46.8 cm. Samples were sealed in home-built sample holders with Kapton windows and equilibrated at the desired temperature on a Linkam hot stage for ~20 min within an evacuated sample environment prior to data acquisition (typical exposure times ~10 min).

The resulting 2D patterns were azimuthally-integrated to obtain one-dimensional scattered intensity $I(q)$ versus q plots, using the DataSqueeze software package (<http://www.datasqueezesoftware.com/>). The 1D scattering intensity profiles were analyzed using freely available Igor Pro procedure files developed by our group.

5.3 Results

The end groups of commercially available non-ionic amphiphile $\text{C}_{16}\text{E}_{20}$ (also known as Brij® 58) were modified by the functional group transformations outlined in Scheme 5.1 to install carboxylate, sulfonate, and trimethylammonium end groups (see section 5.2 for synthesis details). Hydroxyl-terminated $\text{C}_{16}\text{E}_{20}$ was deprotonated using NaH in anhydrous CH_3CN to form the corresponding sodium alkoxide. Treatment of this strong nucleophile with electrophilic BrCH_2COOH and 1,3-propanesultone yielded the carboxyl- and sulfonate-terminated oligomers $\text{C}_{16}\text{E}_{21}\text{-C}$ and $\text{C}_{16}\text{E}_{19}\text{-S}$, respectively. Quaternary ammonium chloride end-functionalization of this $\text{C}_{16}\text{E}_{20}$ oligomer was instead achieved by alkylation of NMe_3 with the end-tosylated parent amphiphile, followed by tosylate ion exchange to chloride over a DOWEX® resin to yield $\text{C}_{16}\text{E}_{21}\text{-}$

N. The crude oligomers were precipitated into hexanes or pentane twice and azeotropically freeze-dried from C₆H₆ before LLC sample preparation. Number averaged molar masses (M_n) of the modified C₁₆E₂₀ amphiphiles were determined by ¹H NMR spectroscopy with end group analysis (Figures A4.1-A4.3), the results of which are summarized in Table 5.1. Note that the purification the modified oligomers by non-solvent precipitation selectively fractionated these samples to yield higher M_n molecules that are sometimes slightly enriched in ethylene oxide units relative to the parent amphiphile.

Scheme 5.1. Synthetic modification of hydroxy-terminated C₁₆E₂₀ to access C₁₆E₂₁-C, C₁₆E₁₉-S, and

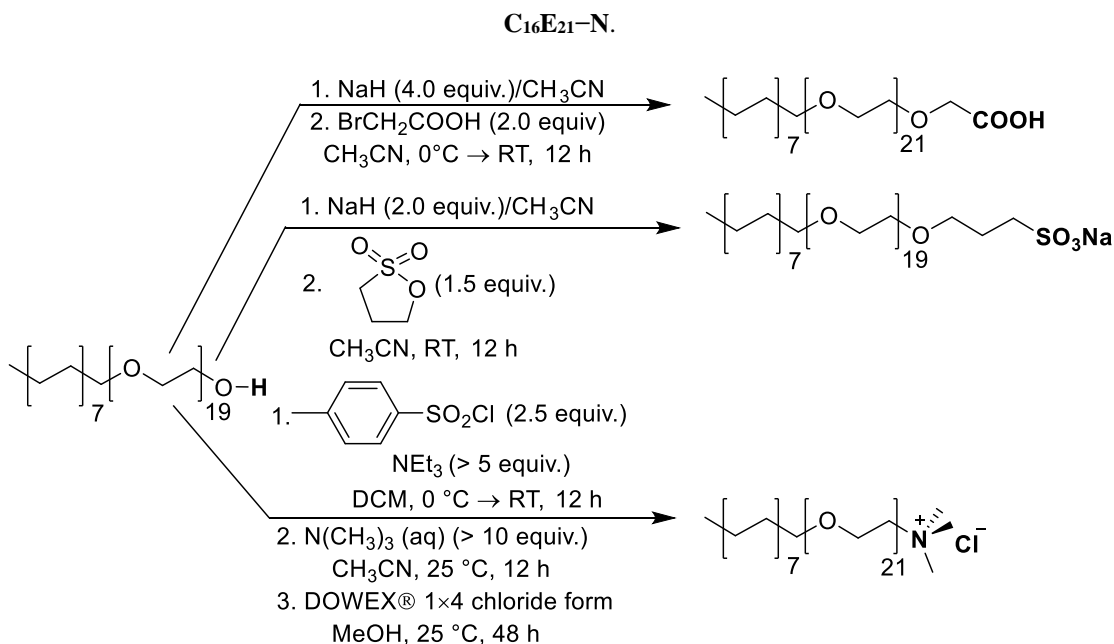
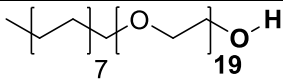
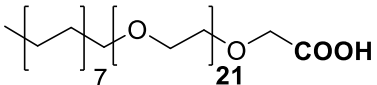
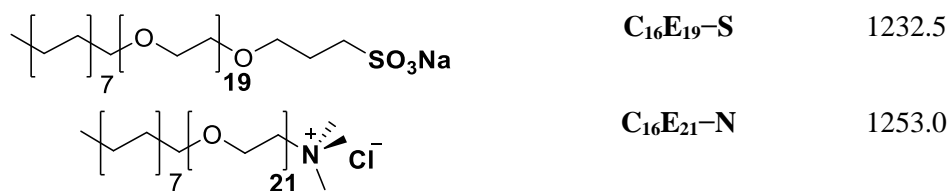


Table 5.1. Molecular characterization of the modified oligomers used in this study

Structure	Abbreviation	M_n (g/mol)
	C ₁₆ E ₂₀	1074.2*
	C ₁₆ E ₂₁ -C	1237.1



*Reported in a previous study Ref [177].

LLCs were prepared by addition of varying amounts of ultrapure water ($> 18 \text{ M}\Omega\cdot\text{cm}$) to the amphiphiles followed by homogenization by three cycles of centrifugation and hand-mixing. The samples were allowed to rest for at least 24 h prior to structure characterization by temperature-dependent synchrotron small-angle X-ray scattering analyses (SAXS; see Section 5.2 for sample preparation and synchrotron SAXS data acquisition details).

The aqueous LLC phase behavior of **C₁₆E₂₁-C** was studied over the composition range 28–70 wt% amphiphile between 25–100 °C (Figure 2). Freely flowing aqueous dispersions with $[\text{C}_{16}\text{E}_{21}\text{-C}] < 28 \text{ wt\%}$ yield SAXS patterns devoid of sharp diffraction peaks, consistent with the formation of disordered micelle solutions. Increasing the amphiphile composition fraction to 30.2 wt% drives a lyotropic disorder-to-order transition that results in self-assembly of FCC LLCs evidenced by scattering maxima located at $(q/3q^*)^2 = 1, 4, 8, 11$ and 12 ($q^* = 0.0830 \text{ \AA}^{-1}$). This closest-packed lyotropic phase undergoes a thermotropic order-to-disorder transition (ODT) to a solution of disordered micelles at 40 °C. However, the morphology obtained on cooling the disordered state to 25 °C exhibits an anisotropic spot pattern with numerous additional peaks not predicted by the $Fm\bar{3}m$ space group symmetry (Figure A4.4A), along with the notable appearance of Bragg rods in the 2D-SAXS pattern (Figure A4.4B). These scattering data suggest the formation of an FCC LLC with numerous stacking faults in the expected ABCABCA... sequence of closed packed (111) planes of micelles.⁴⁹ The presence of stacking faults in a lattice typically manifests as Bragg rods¹⁷⁵ and additional diffuse scattering maxima in the resulting SAXS patterns.³³⁴

LLCs comprising 33–64 wt% **C₁₆E₂₁-C** yield scattering patterns with maxima that stem from

the (110), (200), (211), (220), (222), and (321) reflections of a BCC micelle packing. Those samples containing $[\mathbf{C}_{16}\mathbf{E}_{21}\text{-C}] < 50$ wt% undergo ODTs on heating to 100 °C, whereas samples containing 50–64 wt% amphiphile instead exhibit order-to-order transitions (OOTs) to H_I phases at $T = 100$ °C. In the composition window spanning 64–69 wt% $\mathbf{C}_{16}\mathbf{E}_{21}\text{-C}$, we acquired striking SAXS patterns that exhibit 60 instrument resolution-limited scattering peaks with the characteristic intensity profiles of FK σ phases having $P4_2/mnm$ space group symmetry. For example, SAXS analysis of the LLC formed at 66.2 wt% $\mathbf{C}_{16}\mathbf{E}_{21}\text{-C}$ (Figure 5.2A) reveals a FK σ phase with a tetragonal unit cell parameter $a = 27.00$ nm and the expected $c/a = 0.527$ (see Figure A4.5 for fully indexed pattern and Table A4.1 for list of peaks and residuals) on the basis of previous soft matter analogs.^{31,35-36,40} The σ phase transitions to a H_I morphology on heating to 60 °C, in which the discrete spherical micelle size distribution required for FK phase formation is presumably erased by fusion into ordered cylindrical micelles. The fact that this last transition is reversible on cooling with no hysteresis nor any apparent intermediate states implies that the specific micelle size distribution required for σ phase formation reflects the thermodynamic equilibrium state at 25 °C. We note that the unit cell parameters of the σ phase formed by $\mathbf{C}_{16}\mathbf{E}_{21}\text{-C}$ are ~5% smaller than those of that formed by $\mathbf{C}_{16}\mathbf{E}_{20}$, probably as a consequence of the lower H_2O content at which this phase forms in the carboxy-terminated amphiphile. Within the ~2 wt% resolution increments of the phase diagram given in Figure 5.2B, $\mathbf{C}_{16}\mathbf{E}_{21}\text{-C}$ does not form any FK A15 phases. Thus, these observations starkly contrast the phase behavior of unmodified $\mathbf{C}_{16}\mathbf{E}_{20}$ for which A15 is the equilibrium phase with a long-lived, metastable σ state is achieved only on cooling from the high temperature H_I phase.¹⁷⁷

LLCs with $[\mathbf{C}_{16}\mathbf{E}_{21}\text{-C}] > 69$ wt% form coexisting σ and H_I phases in a narrow composition window (Figure A4.6). The samples transition to a cylindrical micelle packing at $T = 40$ °C, which upon cooling to 25 °C, forms coexisting σ and BCC phases. Isothermal sample annealing for 6 h at

22 °C leads to its reversion to the original $H_I + \sigma$ coexistence observed in the as-made sample, illustrating the slow dynamics of the phase transitions in these strongly segregated LLC systems. For completeness, we note that the resolution of the phase map in Figure 5.2B precludes the observation of all phase coexistence windows, as anticipated by the Gibbs phase rule.

Stimulated by the dramatic changes in LLC phase behavior afforded by carboxylic acid end-group modification of the parent $C_{16}E_{20}$ amphiphile, we investigated the LLCs formed by $C_{16}E_{19}-S$ with a sodium sulfonate terminus. A temperature *versus* amphiphile weight fraction LLC phase diagram constructed by SAXS phase mapping is given in Figure 5.3 for this amphiphile. The lyotropic ordering transition into coexisting BCC/FCC phases for this sulfonated amphiphile (Figure A4.7) occurs at a much lower composition of 20 wt% amphiphile as compared to the carboxylated surfactant (Figure 5.2B), and the former BCC LLCs remain thermally stable up to 100 °C. Since this phase diagram was mapped with a lower resolution (larger wt% increments) with a focus on FK phase formation, the expected pure FCC LLC window was not documented. LLCs with $[C_{16}E_{19}-S] = 57-64$ wt% form FK σ phases at 25 °C (see Figure A4.8 for illustrative SAXS pattern and Table A4.2 for list of peaks and residuals). Quantitative comparisons of the unit cells of these σ phases reveal that $C_{16}E_{19}-S$ lattice constants are ~5% larger than those for $C_{16}E_{21}-C$ at nearly identical water contents. Moreover, the sulfonated amphiphile stabilizes the σ phase over a wider composition window than its carboxylated counterpart. As-formed σ phase LLCs of $C_{16}E_{19}-S$ also transition to the H_I phase upon heating to 60 °C, again with an intervening temperature window of H_I and σ phase co-existence observed for samples with lower water contents. Cooling the H_I morphology to 25 °C again triggers a transition to coexisting BCC and σ phases that revert to the pure, as-made σ phase over 2 months. This transformation pathway and timescale to the initial structure compares well with the slow $H_I \rightarrow BCC \rightarrow \sigma \rightarrow A15$ transformation at $T = 25$ °C previously reported for hydroxy-terminated $C_{16}E_{20}$ LLCs. From this

observation, we deduce that the presence of the ionic sulfonate end group does not appreciably alter the phase transformation mechanism by intermicellar chain exchange and micelle rearrangements. In the concentration window 64–67 wt% $\text{C}_{16}\text{E}_{19}\text{-S}$, as-formed LLCs exhibit coexisting A15 + σ + H_1 phases (Figure A4.9). While the A15 phase is typically expected at lower hydrations than the σ morphology by analogy to ionic small molecule surfactant LLCs,^{31,95} the Gibbs phase rule disallows three-phase coexistence at equilibrium. Thermally cycling these samples from 25 °C to 100 °C leads to σ + H_1 coexistence, and thus we conclude that the as-formed A15 LLC is metastable. This behavior contrasts that of $\text{C}_{16}\text{E}_{20}$ that forms an equilibrium A15 phase and a metastable σ LLC.¹⁷⁷

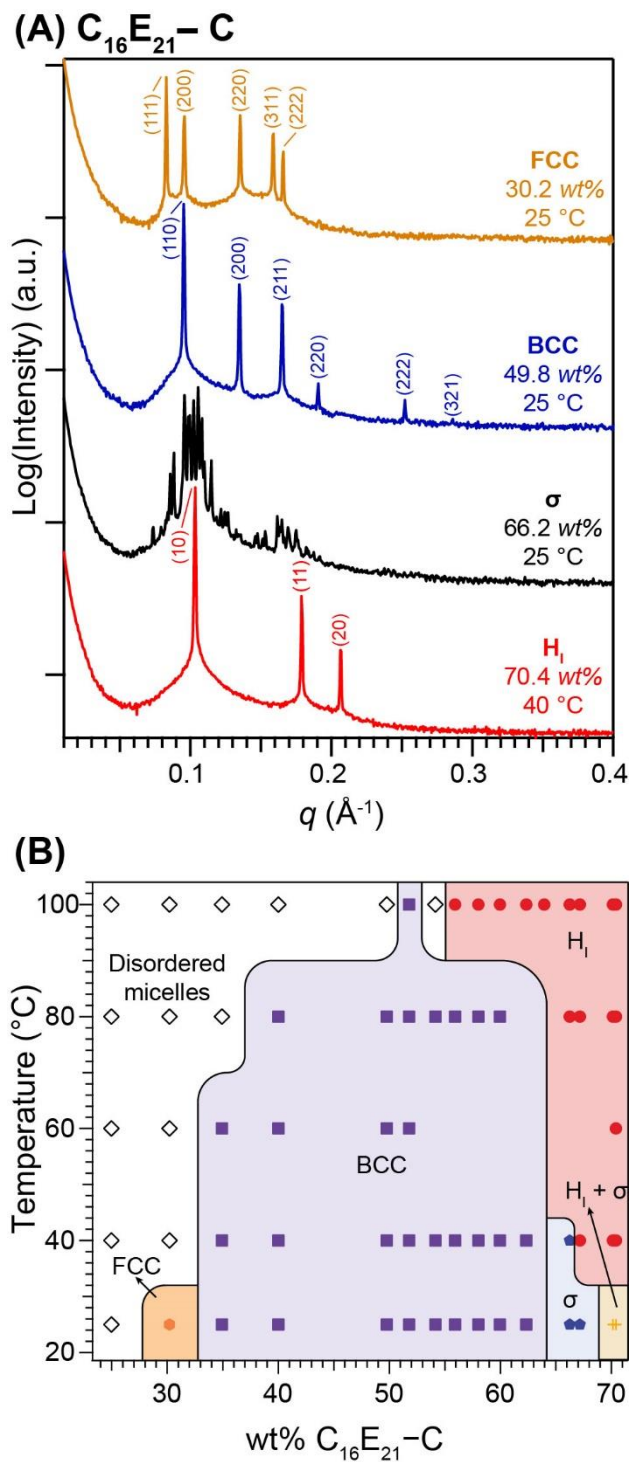


Figure 5.2. (A) Representative synchrotron small-angle scattering intensity profiles obtained from $C_{16}E_{21}-C$ aqueous LLCs at the specified compositions, annotated with Miller indices for the

corresponding diffraction peaks for the FCC, BCC, and H_I phases; see Figure A4.5 for a fully indexed σ phase pattern. (B) Phase diagram depicting the LLC morphology progression of $C_{16}E_{21}-C$ as a function of hydration and temperature, which demonstrates the formation of disordered micelles, FCC, BCC, σ and H_I phases with increasing amphiphile content in LLCs. Solid black lines indicate approximate phase boundary locations within the ~ 2 wt% phase mapping protocol.

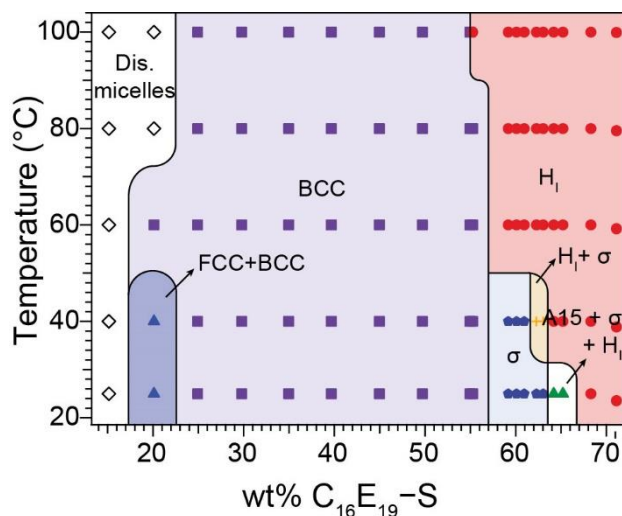


Figure 5.3. Temperature *versus* wt% $C_{16}E_{19}-S$ morphology diagram derived from temperature-dependent synchrotron SAXS phase mapping on the first heating cycle from 25 to 100 °C. As-made σ phase samples exhibit thermoreversible OOTs to H_I phases, and all samples exhibit greater thermal stabilities (higher ODTs) than aqueous LLCs of $C_{16}E_{21}-C$

The intermolecular interaction strength of the end-groups in water decreases as follows: $-\text{SO}_3\text{Na} > -\text{COOH} \gg -\text{OH}$, ranging from a highly dissociated ion pair to a H-bonding and weakly acidic moiety to a nonionic H-bond donor-acceptor. In order to probe the generality with which the ionic end group modification of $C_{16}E_{20}$ stabilizes an equilibrium σ LLC at the expense of the A15 phase, we synthesized the quaternary trimethylammonium chloride-terminated $C_{16}E_{21}$. LLCs with $17 < [C_{16}E_{21}-N] < 58$ wt% self-assemble into a BCC structure at 25 °C with unit cell

parameters $a = 9.57 - 12.01$ nm, intermediate to those obtained for $\mathbf{C}_{16}\mathbf{E}_{19}\text{-S}$ and $\mathbf{C}_{16}\mathbf{E}_{21}\text{-C}$. BCC-forming LLC samples in the concentration range 49–52 wt% transition to coexisting H_1 and σ phases at $T = 100$ °C. While the FK phase is retained upon cooling to 25 °C, subsequent annealing led to the growth of an additional peak at $q = 0.130 \text{ \AA}^{-1}$ that does not belong to the σ phase (Figure A4.10). Comparing the position of the peak to the SAXS trace obtained from the as-made sample suggests that it corresponds to the (200) reflection of a BCC lattice. LLCs with $53 < [\mathbf{C}_{16}\mathbf{E}_{21}\text{-N}] < 58$ wt% exhibit an additional broad scattering feature superimposed on the (110) reflection of the BCC structure. At $[\mathbf{C}_{16}\mathbf{E}_{21}\text{-N}] = 60.0$ wt% and 25 °C, we obtained the SAXS trace shown in Figure 5.4A (*red curve*) with four sharp SAXS maxima and numerous broad high- q reflections. This unusual SAXS signature is reminiscent of scattering patterns obtained from self-assembled wedge-shaped dendrons,²³⁵ di- and tetra-block polymers,^{37,152,242-243} giant-shaped amphiphiles,⁴⁰ and hydrated oil-swollen ionic surfactant micelles (see Figure 3.2). In-depth analysis of the peak positions in this 1D-SAXS intensity profile reveals that they conform to the five-dimensional indexing scheme of a dodecagonal quasicrystal (DDQC) with $P12_6/mmc$ symmetry with a micelle center-to-center distance $a = 15.1$ nm with $c/a = 1.02$; see Table A4.3 for full peak position listing and residuals. This DDQC comprises periodically stacked layers of quasiperiodically arranged micelles situated at the vertices of a square-triangle tiling framework,^{224,235,242} so that the ensemble exhibits 12-fold rotational symmetry with no long-range translational periodicity. This finding suggests that the two broad scattering features observed in the BCC-forming LLCs comprising 53–58 wt% $\mathbf{C}_{16}\mathbf{E}_{21}\text{-N}$ arise from two-phase coexistence with a DDQC. This hypothesis is confirmed by fact that heating one of these two-phase LLCs to 60 °C leads to a pure DDQC phase, confirming our inference based on the Gibbs phase rule (Figure A4.11). Further support for the DDQC phase assignment arises from the fact that the σ phase is a periodic DDQC approximant wherein the (002) peak of the σ phase is expected to coincide with the (00002) reflection of the

quasicrystal.²⁴² The observation of the σ phase at $49 < [\text{C}_{16}\text{E}_{21}\text{-N}] < 52$ wt% and 100 °C with the expected peak coincidence further corroborates our discovery of a lyotropic DDQC formed by $\text{C}_{16}\text{E}_{21}\text{-N}$.

DDQCs observed in other self-assembled soft materials typically transition to FK σ phases at elevated temperatures.^{235,242-243} Moreover, the quasiperiodic structure has been found to be metastable relative to this periodic approximant in both neat diblock polymer melts^{152,242} and oil-swollen alkylphosphonate surfactants (see Chapter 3). However, the DDQC formed by 60.0 wt% $\text{C}_{16}\text{E}_{21}\text{-N}$ in H_2O apparently transforms directly into a pure H_1 morphology on heating to 60 °C with no intervening σ phase temperature window. To confirm the absence of any intermediate periodic sphere-packing, we heated the DDQC in 2 °C increments from 25 to 37 °C with 5 min equilibration at each temperature. Within the limits of this high-resolution synchrotron SAXS experiment, we observed the transformation sequence $\text{DDQC} \rightarrow \text{H}_1 + \text{DDQC}$ and confirmed the absence of the σ phase upon heating (Figure A4.12). Cooling the H_1 phase from 100 to 25 °C yields a poorly ordered DDQC (Figure 5.4A, *green curve*). The sample nanostructure remains arrested for up to 3 months with no change in scattering signature, suggesting that kinetic limitations that arrest further phase transformation. LLCs containing $60 < [\text{C}_{16}\text{E}_{21}\text{-N}] < 63$ wt% coexist as H_1 and DDQC phases, as a broad scattering maxima is superimposed on the (10) peak of the cylindrical phase (Figure 5.4A, *black curve*) along with a low- q shoulder corresponding to the DDQC (00002) peak. The reformation of aperiodic order upon cooling the H_1 phase for LLCs with $[\text{C}_{16}\text{E}_{21}\text{-N}] = 60.0$ wt% in conjunction with the observation of composition windows exhibiting coexisting BCC/DDQC and H_1 /DDQC phases insinuate the equilibrium nature of the micellar DDQC formed by aqueous LLCs of $\text{C}_{16}\text{E}_{21}\text{-N}$.

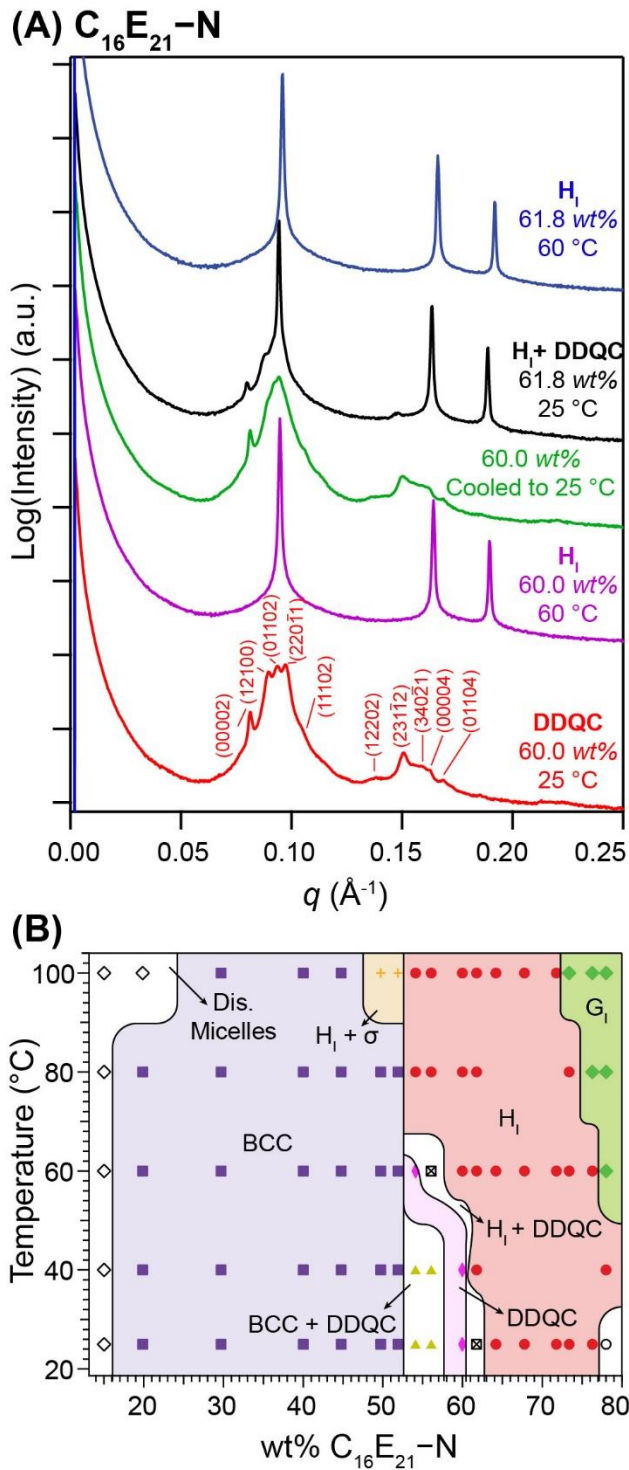


Figure 5.4. (A) SAXS traces obtained from LLCs formed by $C_{16}E_{21}-N$. Dispersions containing 60.0 wt% $C_{16}E_{21}-N$ self-assemble into DDQCs, which transform to H_1 phases at elevated temperatures. However,

cooling the mesophase to 25 °C leads to the hysteretic formation of a poorly ordered DDQC that coexists with the H_I . LLCs containing 61.8 wt% amphiphile coexist as H_I /DDQC phases and transition into a pure H_I at 60 °C. (B) LLC phase portrait obtained for $C_{16}E_{21}-N$ obtained on the first heating cycle, which reveals a narrow composition window of 12-fold aperiodic ordering of micelles in the vicinity of the periodic FK σ phase approximant.

Decreasing the oligomer concentration to 63–73 wt% leads to the formation of a pure H_I morphology, which remains thermally stable up to 100 °C. Finally, the cylindrical phase formed with $[C_{16}E_{21}-N] = 73 - 80$ wt% transitions to a double gyroid structure (G_I) (Figure A4.13) at 100 °C. The G_I phase is a triply periodic network structure comprising two continuous, enantiomeric lipidic channels derived from enchaining 3-fold connectors with a 70.5° dihedral angle in a water matrix.³²⁹ The complete concentration- and temperature-dependent phase behavior of $C_{16}E_{21}-N$ observed on the first heating cycle is summarized in Figure 5.4B. The isothermal lyotropic phase behavior of $C_{16}E_{21}-N$ at 100 °C: $BCC \rightarrow H_I + \sigma \rightarrow H_I$ is reminiscent of the lyotropic phase behavior of $C_{16}E_{19}-S$ and $C_{16}E_{21}-C$ at 25 °C, suggesting similar mechanisms of LLC phase formation of the end-group modified amphiphiles. Additionally, the above phase diagrams clearly indicate that ionic end-group modification generally drives up the T_{ODTS} for dispersions at similar hydrations as compared to the charge-neutral analogs.

The isolation of end-group modified amphiphiles involved purification by two-fold precipitation of the functional oligomer in hexanes, which drives sample enrichment in amphiphiles with a slightly larger number of ethylene oxide (EO) units per chain that is reflected in the increase in M_n (Table 5.1). This enrichment in EO units is most relevant in the cases of $C_{16}E_{21}-C$ and $C_{16}E_{21}-N$, as opposed to $C_{16}E_{19}-S$ which has the same number of EO units as the parent amphiphile. To address the slight composition discrepancy, we conducted a control experiment in which we precipitated the commercially available $C_{16}E_{20}$ in hexanes two times to obtain a hydroxyl-

terminated amphiphile enriched in EO units. This procedure yielded a non-ionic $C_{16}E_{23}$ amphiphile according to 1H NMR end group analysis (Figure A4.14). Temperature-dependent SAXS analyses LLCs of $C_{16}E_{23}$ reveal the formation of only the canonical FCC, BCC, and H_1 morphologies with the complete absence of any micellar FK phases between 25–100 °C (Figure A4.15). The significantly different phase behavior of unpurified $C_{16}E_{20}$ suggests that amphiphiles with higher EO contents generally exhibit smaller or nonexistent lyotropic FK phase windows.¹⁷⁷

5.4 Discussion

Ionic end group installation at the terminus of $C_{16}E_{20}$ diblock oligomers significantly alters their lyotropic mesophase self-assembly behavior, by increasing the thermal stabilities of the ordered LLCs at low hydrations and effectively extinguishing the equilibrium FK A15 phase at intermediate hydrations. While such end group-driven morphology changes in diblock oligomer and block polymer self-assembly may initially appear surprising, a recent review highlights numerous examples of such effects in polymer melt and solution phase behavior.³³³ Specifically, Park and co-workers documented lamellar-to-network OOTs induced by systematic end group variations in low molecular weight diblock polymers of nearly constant compositions, with important implications for ion transport by the resulting assemblies.³³⁵⁻³³⁸ Related effects in canonical lamellar,³³⁹⁻³⁴⁰ cylindrical,³⁴¹ and BCC phases of self-assembled block polymers have also been observed in diblock polymer self-assembly.³⁴² However, the impact of such end group modifications on complex particle packings remain poorly explored.

The preferential formation of FCC and BCC micelle packings in $C_{16}E_{20}$ and its end group-modified homologs $C_{16}E_{21}-C$, $C_{16}E_{19}-S$, and $C_{16}E_{21}-N$ at high hydrations adjacent to the lyotropic ODT likely stem from similar physical phenomena. Jayaraman et al. previously reasoned that $C_{16}E_{20}$ micelles formed at high water contents adopt “crew-cut” structures, wherein the large

interfacial area per amphiphile drives PEO corona collapse to protect the hydrophobic core domain from energetically expensive contacts with H₂O. This collapse effectively enlarges the core domain volume while shortening the coronas, which leads to high packing fraction FCC phases by analogy to hard-sphere colloids. At slightly lower water contents, the lower interfacial area per amphiphile allows the PEO corona chains to unfurl and fully hydrate to form “hairy micelles” that assemble into lower packing fraction BCC phases.^{170-171,177} The thermally-induced FCC → BCC OOTs at high hydrations may be understood in terms of the decreasing water solubility of the PEO chains on heating,¹⁷⁷ wherein the dehydration and collapse of the PEO coronae of the crew-cut micelles leads to chain overlap. The constrained corona chains are thus forced to stretch to mitigate these unfavorable steric interactions, thus driving a BCC phase to form. Note that ionic end groups apparently do not alter these transitions.

The installation of ionic functionalities at the PEO chain ends of **C₁₆E₂₀** results in increases in the ODT temperatures of assemblies with comparable H₂O contents in the order **C₁₆E₂₀-OH** < **C₁₆E₂₁-C** < **C₁₆E₂₁-N** < **C₁₆E₁₉-S**. In other words, strongly H-bonding carboxylic acid, and ionic ammonium and sulfonate moieties with their charge compensating counterions mediate stronger electrostatic cohesion between the micelles than the parent hydroxyl-terminated oligomer. This greater cohesive energy density reinforces the microphase separated morphology and raises the *T*_{ODT}. The moderate level of carboxylic acid dissociation in water due to its weakly acidic character is the likely root of its placement toward the bottom of this series, as compared to well-dissociated quaternary ammonium chloride and sodium sulfonate hydrated ion pairs. The presence of hydrogen-bonding and ionic end groups in self-assembled, non-polar diblock polymers has similarly been shown to increase the *T*_{ODTs} of their microphase separated morphologies.³⁴²

The complete extinction of the FK A15 phase window in favor of the ordered σ or aperiodically ordered DDQC phases in ionically modified **C₁₆E₂₀** probably stems from the high degree of

intramicellar counterion correlations that impact the preferred interfacial curvatures of the aggregates and their consequent packings. Sodium alkylsulfonate ion pairs are highly dissociated in water,³⁴³⁻³⁴⁵ which drives the formation of high curvature, spherical aggregates in which the distances between the point-like charges of the sodium cations are maximized. These intramicellar coronal repulsions rigidify the micelles and disallow deformations away from their preferred spherical shapes, a concept known as “ionic sphericity.”^{31,95} However, the packing of the micelles to fill volume at constant density drives distortion of the micelles to conform to the Wigner-Seitz (W-S) cell structure of the underlying periodic lattice, in order to maximize space filling. Additionally, the counterions associated with the ionic chain ends are expected to localize along planes that perpendicularly bisect each micelle nearest neighbor center-to-center vector to maximize the electrostatic cohesion, as previously demonstrated by Kim et al. in LLCs of ionic small molecule surfactants.³¹ In other words, the counterions also outline the W-S cells of the lattice. In order to maximize local micellar sphericity and global lattice cohesion with minimal interfacial area per amphiphile, the micelles reconfigure into a distribution of discrete sizes that enable formation of complex FK phases in which the W-S cells vary in volume. Using the surface areas (S) and volumes (V) of the W-S cells of a lattice, Polyá’s isoperimetric quotient³²³ $IQ = 36\pi S^3/V^2$ enables the calculation of the number-average sphericity of the structure. On the basis of this geometric analysis, Bates and co-workers found that $IQ(\sigma) > IQ(A15) > IQ(BCC)$.¹¹³ Thus, **C₁₆E₁₉-S** exhibits a very strong preference for the formation of the high sphericity σ phase at hydrations lower than the parent amphiphile, which instead forms more deformable micelles that can pack into the lower sphericity A15 phases. The strongly directional interactions of the partially dissociated carboxylic acid and carboxylates of **C₁₆E₂₁-C** also enforce the formation of high sphericity σ phases, more so than **C₁₆E₂₁-N** for which the electrostatic correlations are weaker due to the relatively more polarizable nature of both the quaternary ammonium and chloride ions. This

analysis based on levels of counterion correlation is further supported by the fact that the σ phase window width decreases in the order $\mathbf{C}_{16}\mathbf{E}_{19}\text{-S} > \mathbf{C}_{16}\mathbf{E}_{21}\text{-C}$ with no σ phase observed in LLCs of $\mathbf{C}_{16}\mathbf{E}_{21}\text{-N}$, and the observation that the unit cells of $\mathbf{C}_{16}\mathbf{E}_{19}\text{-S}$ are ~5% greater than those of $\mathbf{C}_{16}\mathbf{E}_{21}\text{-C}$ at comparable H_2O contents.

The formation of a DDQC in $\mathbf{C}_{16}\mathbf{E}_{21}\text{-N}$ as opposed to the σ phase of $\mathbf{C}_{16}\mathbf{E}_{19}\text{-S}$ may also be rationalized within this framework of counterion correlations. We first note that the $\mathbf{C}_{16}\mathbf{E}_{19}\text{-S}$ oligomer has a slightly shorter PEO segment than $\mathbf{C}_{16}\mathbf{E}_{21}\text{-N}$, which would lead to the expectation that $\mathbf{C}_{16}\mathbf{E}_{21}\text{-N}$ would form higher curvature micelles that assemble into either FCC or BCC packings by analogy to other known aqueous LLCs.¹⁶⁹ This expectation is supported by the parallel observation that the parent $\mathbf{C}_{16}\mathbf{E}_{20}$ forms FCC, BCC, A15, and H_1 aqueous LLCs, whereas $\mathbf{C}_{16}\mathbf{E}_{23}$ forms only FCC, BCC, and H_1 and no FK lyotropic mesophases with increasing water contents. In other words, the greater PEO content of $\mathbf{C}_{16}\mathbf{E}_{23}$ leads to the formation of higher curvature aggregates with a greater interfacial area per chain (A_{int}) compared to the as-received oligomer at similar hydrations.^{5,18} Thus, the A15 phase does not form in amphiphiles with higher EO contents. However, the $\mathbf{C}_{16}\mathbf{E}_{21}\text{-N}$ forms a DDQC at 25 °C that is adjacent in phase space to a FK σ phase that forms at higher water contents at 100 °C. Based on prior reports of soft matter DDQCs (see Chapter 3), we surmise that the mean interfacial curvatures of DDQCs are generally intermediate between the A15 and σ phases. The formation of $\mathbf{C}_{16}\mathbf{E}_{21}\text{-N}$ micelles having lower mean curvatures than those of $\mathbf{C}_{16}\mathbf{E}_{19}\text{-S}$ at similar water contents suggests that the ionic sphericity enforced by $\mathbf{C}_{16}\mathbf{E}_{21}\text{-N}$ is lower than that of the sodium sulfonate homologue.

The discovery of a lyotropic 12-fold quasicrystalline state in LLCs containing $\mathbf{C}_{16}\mathbf{E}_{21}\text{-N}$ was serendipitous, yet not entirely unexpected given similar discoveries of aperiodic dodecagonal quasicrystalline order in other soft materials systems in phase space adjacent to FK A15 and σ approximants. While DDQCs have been observed in self-assembly of dendrons,²³⁵ block

polymers,^{152,176,242} giant-shaped amphiphiles,⁴⁰ and hydrated oil-swollen micelles of ionic surfactants (see Chapter 3), the underlying free energy balance that guides nucleation and growth of these aperiodically ordered structures remain poorly understood. One surprising feature of the DDQCs formed by aqueous dispersions of $C_{16}E_{21}-N$ is that they undergo OOTs to H_I phases at elevated temperatures apparently with no intermediate discontinuous micellar phases. In the parent $C_{16}E_{20}$ amphiphile, a thermally induced $A15 \rightarrow BCC \rightarrow H_I$ phase transition sequence was rationalized in terms of the decreased solubility of the micellar PEO coronae on heating that results in their partial collapse and triggers a transition to a higher packing fraction BCC phase. Further heating results in additional corona collapse with concomitant aggregate fusion along the $\langle 111 \rangle$ -direction of the BCC lattice to epitaxially form a H_I phase.^{14,320,346} Thus, the 4° ammonium chloride end group enforces the sphericity of the aperiodic DDQC state at elevated temperatures, until the corona chain collapse triggers an abrupt transition to a H_I phase with no intermediate BCC structure.

The mechanisms of DDQC formation in these LLCs qualitatively differ from similar findings in neat diblock polymer self-assembly. Cooling the H_I phase formed by $C_{16}E_{21}-N$ to 25 °C leads to the rapid reappearance of the (0002) layer spacing peak (Figure 5.4A) along with some broad high- q correlations. We attribute this observation to the kinetically-limited reversibility of the DDQC $\rightarrow H_I$ transition. In sphere-forming diblock polymers, a DDQC is observed to nucleate and grow from a micellar liquid-like packing (LLP) state obtained from rapid quenching of the disordered state. This microphase separated diblock quasicrystal then slowly transforms into an equilibrium σ approximant on isothermal annealing for ~ 250 days at 25 °C, indicative of slow chain exchange and micelle rearrangements.²⁴² In the case of recently discovered, aqueous lyotropic DDQC mesophases of oil-swollen alkylphosphonate micelles, rapid hydration of oil/amphiphile mixtures that results in a broad sphere size distribution leading to emergence of quasicrystalline order. Studies of the path-dependent formation of this DDQC reveal that it is also metastable with

respect to the periodic FK σ and A15 phases. However, the aqueous lyotropic DDQC of $C_{16}E_{21}-N$ apparently reforms directly from the H_I phase upon cooling with no intermediate LLP or BCC states. As in the case of the metastable σ phase formed by $C_{16}E_{20}$ surfactants on rapidly quenching a H_I phase at 70 °C to a 25 °C that induces formation of a metastable BCC structure from which a σ phase nucleates and grows, cooling the $C_{16}E_{21}-N$ H_I phase results in the micelles pinching off to form a broad sphere size distribution that apparently enables nucleation and growth of a DDQC. This reasoning suggests that production of the requisite broad micelle size distribution for DDQC formation can occur either from a disordered or an ordered state in a manner not previously recognized.

5.5 Conclusions

We described the effect of ionic end groups modifications of non-ionic $C_{16}E_{20}$ amphiphiles on their aqueous lyotropic self-assembly behaviors. The parent, hydroxyl-terminated amphiphile forms an equilibrium A15 lyotropic phase with rapid OOTs to BCC and H_I phases at elevated temperatures, while quenching the cylindrical phase back to ambient temperature results in the time-dependent transformation sequence: $H_I \rightarrow BCC \rightarrow \sigma \rightarrow A15$ with the last transformation taking ~ 5 months. Installation of either an ionic sodium sulfonate and a carboxylic acid end group at the terminus of $C_{16}E_{20}$ completely extinguishes the A15 equilibrium phase window and a FK σ phase is instead stabilized at 25 °C as the apparent equilibrium structure. We rationalize this difference in phase behavior in terms of the ionic sphericity of the micelles, by which they prefer local spherical particle symmetry to minimize unfavorable electrostatic correlations amongst the charge-compensating counterions. In the case of the highly hydrated and well-dissociated quaternary ammonium chloride end group, the greater polarizability of the solvated ion pair enforces a slightly lower degree of ionic sphericity that allows for micelle deformation and their

unexpected packing into an aperiodically ordered DDQC. The exact origins of aperiodic DDQC order in $C_{16}E_{20}$ -N aqueous LLCs remain unresolved, especially, how the underlying broad spherical micelle size distribution is generated to enable nucleation and growth of the aperiodic mesophase. Nonetheless, these studies illustrate that the subtle chemical modifications of block oligomers and diblock polymers can profoundly alter the free energy balance underlying both periodic and aperiodic structure formation in soft materials and present exciting opportunities to access hitherto unreported structures.

Chapter 6. Conclusions

Micelles formed by hydrated-amphiphiles pack on high-symmetry lattices such as body-centered cubic, face-centered cubic, and hexagonally closest-packed structures. Our group discovered the formation of a complex lyotropic σ mesophase in the self-assembly of bis(tetramethylammonium) alkyl phosphonates in water. This low-symmetry structure comprises 30 micelles of five different sizes packed on a giant tetragonal unit cell. The formation of the mesophase was argued to stem from maximizing counterion-mediated intermicellar cohesion while minimizing local variations in headgroup-counterion solvation. The σ phase has also been observed in neat self-assembled soft materials including wedge-shaped dendrons, giant-shape surfactants, and block polymers. The tetragonal structure belongs to a class of complex particle packings called Frank-Kasper (FK) phases, which contain 12-, 14-, 15-, and 16-fold coordination environments. These periodic lattices are approximants to quasicrystals (QCs), structures that exhibit rotational symmetry yet lack translational periodicity. In soft materials, dodecagonal quasicrystals (DDQC), which possess 12-fold rotational symmetry, have been observed in the self-assembly of the neat amphiphiles in phase space vicinity to the σ and A15 phases. Chapter 1 reviews the formation of these low-symmetry micellar structures in the different soft materials and presents analogies among them. Despite the observation of a σ phase, the molecular design criteria directing complex phase formation in hydrated amphiphiles were unknown. This thesis aimed to establish the amphiphile structural motifs required to access FK and related structures and to investigate methodologies to tune their thermodynamic phase behavior.

Chapter 2 investigated the design of small-molecule ionic surfactants to access the FK σ and A15 phases in hydrated dispersions. Bis(tetramethylammonium) alkyl malonate surfactants were designed as chemically different dianionic surfactant analogs of alkylphosphonates, which formed

the lyotropic σ phase. We found that the tetramethylammonium carboxylate analog does form the tetragonal structure with tunable thermodynamic and composition stabilities. Changing the counterion to K^+ led to complete disappearance of the σ phase, and only the A15 structure was observed. Real-space electron density reconstructions revealed that the counterion cloud is localized at the midpoint between two micelles. The K^+ ions were less well localized due to greater counterion correlations for the smaller ion as compared to the large tetramethylammonium counterion. Hence, K^+ ions remain more associated with the headgroups, forming more deformable micelles that tolerate the lower ionic sphericity in the A15 structure.

Chapter 3 reported the discovery of a self-assembled lyotropic DDQC of bis(tetramethylammonium) dodecylphosphonate micelles swollen with 10 wt% decane (relative to surfactant). Observed at hydrations intermediate to the A15 and σ phases, the DDQC exhibited sufficient long-range order that allowed the assignment of the 5D space group symmetry $P12_1/mmc$ to the mesophase. Heating the quasiperiodic structure from 25 to 100 °C induces an irreversible transition to the σ phase. Additionally, modifying the sample preparation protocol, by adding oil to premixed surfactant-water lyotropic phases, does not yield a DDQC. Thus, the QC is assessed to be metastable with respect to its periodic approximant σ phase, analogous to observations in dendronized shape amphiphiles and diblock polymers. Hydration of surfactant-oil mixtures is argued to yield a broad, non-equilibrium micelle size distribution due to uneven partitioning of the decane in the micellar cores. The resulting nucleation barrier for this ensemble of particle sizes is hypothesized to be lower for the QC as compared to the periodic FK phases. Accelerating intermicellar chain exchange by increasing the temperature allows the system to modify the particle-size distribution to rearrange into the expected distribution for the equilibrium σ phase.

Chapter 4 explored the LLC phase behavior of hydrated non-ionic poly(ethylene-*block*-poly(ethylene oxide)). The oligomer displays the FCC, BCC, A15, and H_I structures with decreasing

hydration at 22 °C. Heating the A15 structure to 70 °C triggered a transformation to the H₁ morphology. However, quenching the sample to 25 °C led to the nucleation and growth of a σ phase, which reverted to the original A15 lattice upon extended annealing. The metastability of the σ phase was probed a function of quench depth and rate of cooling from the H₁ phase. The formation of the complex structure was rationalized based on a non-equilibrium sphere-size distribution obtained due to the rapid quench, which provides a decreased nucleation barrier to form the σ phase as it contains greater dispersity in its micelle sizes. Facilitated by intermicellar chain exchange, the σ phase isothermally transitions to the A15 structure, which involves only a $\pm 3\%$ variation of overall particle volumes about the mean. The transformation is argued to be driven by the minimization of interfacial area per chain.

Finally, the endgroup on the poly(ethylene oxide) block of the oligomer was modified to examine the effect of inter- and intra-coronal interactions on complex phase formation. Carboxylic acid, sodium sulfonate, and trimethyl ammonium chloride groups were chosen to span a range of intermolecular forces. The carboxylic acid and sodium sulfonate-terminated amphiphiles form a thermodynamically stable σ phase, demonstrating that the ionic endgroup leads to a wider window of compositional stability for the structure as compared to the neutral hydroxyl group. The formation of the σ phase is rationalized based on the greater ionic sphericity preference for micelles bearing solvated ionic endgroups and counterions. Amphiphiles containing the trimethyl ammonium chloride endgroup serendipitously form a DDQC, which transformed into a H₁ morphology on heating. The thermodynamic stability of the structure is unclear, as a poorly ordered structure is obtained upon cooling the QC, which remains arrested at 25 °C. The origins for the formation of quasicrystalline order in these LLCs are ill-understood.

These investigations of complex micellar morphologies in minimally hydrated amphiphiles illustrate the subtle free energy balance governing the formation of these structures. Sample

preparation protocols and minute changes in the molecular interaction parameters were shown to represent new tools to access otherwise hidden morphologies. While this thesis explored the thermodynamics of micellar LLCs, questions about the kinetics of phase formation and phase transformations remain open. Quantitative investigations of dynamics of the phase transitions will provide insights into pathways involved in effecting those transformations and may enable access to new long-lived metastable states. The exclusive formation of 12-fold rotational symmetric aperiodic order in soft materials contrasts the larger library of icosahedral ordering in intermetallic alloys. The lack of harmony in QC formation in hard and soft matter possibly stems from the differing natures of the melt disordered states, which will dictate the mechanism of phase formation. Foams with quasiperiodic symmetry in 3D have been shown to rival the Weaire-Phelan solution to the Kelvin problem,³⁴⁷ suggesting their eminent discovery in soft materials.

While realizations of the technological applications of these structures may be far in the future, they may offer opportunities to design and to engineering materials with useful optical properties, especially as photonic band-gap materials and wave guides.

While such properties have been observed in structures with larger unit cells (≥ 100 nm) derived from colloidal particles,^{305,348-349} fabrication of these structures from such building blocks requires tight control of particle size dispersity and coupled with intricate processing protocols that are kinetically limited and lead to defect-ridden structures.^{301,304} Thus, the scalable fabrication of these materials at larger length scales is curtailed. Self-assembly of single- or two-component systems comprising neat or solvated amphiphiles of well-defined structures presents a more robust strategy for achieving these structures, if the design principles identified in this thesis can be scaled up to molecules that assemble at length scales 10 times larger. Furthermore, these assemblies will likely be amenable to thermal, chemical, and mechanical processing strategies that give rise to well-ordered, defect-free materials. Alternatively, cooperative self-assembly of colloidal materials with

structure-directing amphiphiles by inclusion of particles as core or matrix domain additives,³⁵⁰ or by covalent tethering the amphiphiles to the particle surfaces may open drive robust access to technological relevant low-symmetry particle-packings.^{106,351}

References

- (1) Gibbs, F. W., The History of the Manufacture of Soap. *Annals of Science* **1939**, *4*, 169-190.
- (2) Holmberg, K., Surfactants. In *Ullmann's Encyclopedia of Industrial Chemistry*, 2020; pp 1-56.
- (3) Chandler, D., Interfaces and the Driving Force of Hydrophobic Assembly. *Nature* **2005**, *437*, 640-647.
- (4) Hiemenz, P. C.; Rajagopalan, R., *Principle of Colloid and Surface Chemistry*. 3rd ed.; CRC Press: Boca Raton, 1997.
- (5) Israelachvili, J. N., *Intermolecular and Surface Forces*. 3rd ed.; Academic Press: London, 2011.
- (6) Gruner, S. M., Stability of Lyotropic Phases with Curved Interfaces. *J. Phys. Chem.* **1989**, *93*, 7562-7570.
- (7) Tanford, C., Theory of Micelle Formation in Aqueous Solutions. *J. Phys. Chem.* **1974**, *78*, 2469-2479.
- (8) Nagarajan, R., One Hundred Years of Micelles: Evolution of the Theory of Micellization. In *Surfactant Science and Technology*, Romsted, L. S., Ed. CRC Press: Boca Raton, 2014.
- (9) Shearman, G. C.; Ces, O.; Templer, R. H.; Seddon, J. M., Inverse Lyotropic Phases of Lipids and Membrane Curvature. *J. Phys.: Condens. Matter* **2006**, *18*, 1105-1124.
- (10) Elizabeth, G. K.; Paul, D. B.; Michihiro, N., Collective Dynamics in Model Biological Membranes Measured by Neutron Spin Echo Spectroscopy. In *Characterization of Biological Membranes*, De Gruyter: Berlin, Boston, 2019; pp 131-176.
- (11) Israelachvili, J. N.; Mitchell, J. D.; Ninham, B. W., Theory of Self-Assembly of Lipid Bilayers and Vesicles. *Biochim. Biophys. Acta* **1977**, *470*, 185-201.
- (12) Nagarajan, R., Molecular Packing Parameter and Surfactant Self-Assembly: The Neglected Role of the Surfactant Tail. *Langmuir* **2002**, *18*, 31-38.
- (13) Paolo, M.; Lia, Q. A.; Letizia, S.; Hervé, D., Hexagonal-Cubic Phase Transitions in Lipid Containing Systems : Epitaxial Relationships and Cylinder Growth. *J. Phys. II France* **1994**, *4*, 1393-1416.
- (14) Sakya, P.; Seddon, J. M.; Templer, R. H.; Mirkin, R. J.; Tiddy, G. J. T., Micellar Cubic Phases and Their Structural Relationships: The Nonionic Surfactant System C12eo12/Water. *Langmuir* **1997**, *13*, 3706-3714.
- (15) Floudas, G.; Ulrich, R.; Wiesner, U., Microphase Separation in Poly(Isoprene-B-Ethylene Oxide) Diblock Copolymer Melts. I. Phase State and Kinetics of the Order-to-Order Transitions. *J. Chem. Phys.* **1998**, *110*, 652-663.
- (16) Wang, C.-Y.; Lodge, T. P., Kinetics and Mechanisms for the Cylinder-to-Gyroid Transition in a Block Copolymer Solution. *Macromolecules* **2002**, *35*, 6997-7006.
- (17) Mezzenga, R.; Seddon, J. M.; Drummond, C. J.; Boyd, B. J.; Schröder-Turk, G. E.; Sagalowicz, L., Nature-Inspired Design and Application of Lipidic Lyotropic Liquid Crystals. *Adv. Mater.* **2019**, *31*, 1900818.
- (18) Hyde, S. T., Chapter 16: Identification of Lyotropic Liquid Crystalline Mesophases. In *Handbook of Applied Surface and Colloid Chemistry*, Holmberg, K., Ed. John Wiley & Sons, Ltd.: New York, 2001; Vol. 2, pp 299-332.
- (19) Porras-Gomez, M.; Leal, C., Lipid-Based Liquid Crystalline Films and Solutions for the Delivery of Cargo to Cells. *Liq. Cryst. Rev.* **2019**, *7*, 167-182.
- (20) Kim, H.; Leal, C., Cuboplexes: Topologically Active Sirna Delivery. *ACS Nano* **2015**, *9*, 10214-10226.
- (21) Kim, H.; Song, Z.; Leal, C., Super-Swelled Lyotropic Single Crystals. *Proc. Natl. Acad. Sci. U.S.A.* **2017**, *114*, 10834-10839.

- (22) Werber, J. R.; Osuji, C. O.; Elimelech, M., Materials for Next-Generation Desalination and Water Purification Membranes. *Nature Rev. Mater.* **2016**, *1*, 16018.
- (23) Jackson, G. L.; Perroni, D. V.; Mahanthappa, M. K., Roles of Chemical Functionality and Pore Curvature in the Design of Nanoporous Proton Conductors. *J. Phys. Chem. B* **2017**, *121*, 9429-9436.
- (24) Han, L.; Che, S., Anionic Surfactant Templated Mesoporous Silicas (Amss). *Chem. Soc. Rev.* **2013**, *42*, 3740-3752.
- (25) Huo, Q.; Margolese, D. I.; Stucky, G. D., Surfactant Control of Phases in the Synthesis of Mesoporous Silica-Based Materials. *Chem. Mater.* **1996**, *8*, 1147-1160.
- (26) Attard, G. S.; Glyde, J. C.; Göltner, C. G., Liquid-Crystalline Phases as Templates for the Synthesis of Mesoporous Silica. *Nature* **1995**, *378*, 366-368.
- (27) Kruk, M., Ordered Mesoporous Materials. In *Handbook of Solid State Chemistry*, Dronskowski, R.; Kikkawa, S.; Stein, A., Eds. Wiley-VCH Verlag GmbH & Co. KGaA: 2017; pp 121-140.
- (28) Bates, F. S.; Fredrickson, G. H., Block Copolymers-Designer Soft Materials. *Phys. Today* **1999**, *52*, 32-38.
- (29) Vargas, R.; Mariani, P.; Gulik, A.; Luzzati, V., Cubic Phases of Lipid-Containing Systems: The Structure of Phase Q223 (Space Group Pm3n). An X-Ray Scattering Study. *J. Mol. Biol.* **1992**, *225*, 137-145.
- (30) Luzzati, V.; Vargas, R.; Gulik, A.; Mariani, P.; Seddon, J. M.; Rivas, E., Lipid Polymorphism: A Correction. The Structure of the Cubic Phase of Extinction Symbol Fd $\bar{3}$ m Consists of Two Types of Disjointed Reverse Micelles Embedded in a Three-Dimensional Hydrocarbon Matrix. *Biochemistry* **1992**, *31*, 279-285.
- (31) Kim, S. A.; Jeong, K.-J.; Yethiraj, A.; Mahanthappa, M. K., Low-Symmetry Sphere Packings of Simple Surfactant Micelles Induced by Ionic Sphericity. *Proc. Natl. Acad. Sci. U.S.A.* **2017**, *114*, 4072-4077.
- (32) Shearman, G. C.; Tyler, A. I. I.; Brooks, N. J.; Templer, R. H.; Ces, O.; Law, R. V.; Seddon, J. M., Ordered Micellar and Inverse Micellar Lyotropic Phases. *Liq. Cryst.* **2010**, *37*, 679-694.
- (33) Yaghmur, A.; Rappolt, M., Chapter Five - the Micellar Cubic Fd $\bar{3}$ m Phase: Recent Advances in the Structural Characterization and Potential Applications. In *Advances in Planar Lipid Bilayers and Liposomes*, Iglič, A.; Kulkarni, C. V., Eds. Academic Press: 2013; Vol. 18, pp 111-145.
- (34) Balagurusamy, V. S. K.; Ungar, G.; Percec, V.; Johansson, G., Rational Design of the First Spherical Supramolecular Dendrimers Self-Organized in a Novel Thermotropic Cubic Liquid-Crystalline Phase and the Determination of Their Shape by X-Ray Analysis. *J. Am. Chem. Soc.* **1997**, *119*, 1539-1555.
- (35) Ungar, G.; Liu, Y.; Zeng, X.; Percec, V.; Cho, W. D., Giant Supramolecular Liquid Crystal Lattice. *Science* **2003**, *299*, 1208-11.
- (36) Lee, S.; Bluemle, M. J.; Bates, F. S., Discovery of a Frank-Kasper σ Phase in Sphere-Forming Block Copolymer Melts. *Science* **2010**, *330*, 349-353.
- (37) Kim, K.; Schulze, M. W.; Arora, A.; Lewis, R. M.; Hillmyer, M. A.; Dorfman, K. D.; Bates, F. S., Thermal Processing of Diblock Copolymer Melts Mimics Metallurgy. *Science* **2017**, *356*, 520-523.
- (38) Bates, M. W.; Lequeieu, J.; Barbon, S. M.; Lewis, R. M.; Delaney, K. T.; Anastasaki, A.; Hawker, C. J.; Fredrickson, G. H.; Bates, C. M., Stability of the A15 Phase in Diblock Copolymer Melts. *Proc. Natl. Acad. Sci. U.S.A.* **2019**, *116*, 13194-13199.
- (39) Huang, M.; Hsu, C. H.; Wang, J.; Mei, S.; Dong, X.; Li, Y.; Li, M.; Liu, H.; Zhang, W.; Aida, T.; Zhang, W. B.; Yue, K.; Cheng, S. Z., Selective Assemblies of Giant Tetrahedra Via Precisely Controlled Positional Interactions. *Science* **2015**, *348*, 424-428.

- (40) Yue, K.; Huang, M.; Marson, R. L.; He, J.; Huang, J.; Zhou, Z.; Wang, J.; Liu, C.; Yan, X.; Wu, K.; Guo, Z.; Liu, H.; Zhang, W.; Ni, P.; Wesdemiotis, C.; Zhang, W.-B.; Glotzer, S. C.; Cheng, S. Z. D., Geometry Induced Sequence of Nanoscale Frank–Kasper and Quasicrystal Mesophases in Giant Surfactants. *Proc. Natl. Acad. Sci. U.S.A.* **2016**, *113*, 14195-14200.
- (41) Su, Z.; Hsu, C.-H.; Gong, Z.; Feng, X.; Huang, J.; Zhang, R.; Wang, Y.; Mao, J.; Wesdemiotis, C.; Li, T.; Seifert, S.; Zhang, W.; Aida, T.; Huang, M.; Cheng, S. Z. D., Identification of a Frank–Kasper Z Phase from Shape Amphiphile Self-Assembly. *Nat. Chem.* **2019**, *11*, 899-905.
- (42) Hales, T. C., A Proof of the Kepler Conjecture. *Ann. Math.* **2005**, *162*, 1065-1185.
- (43) Hales, T.; Adams, M.; Bauer, G.; Dang, T. D.; Harrison, J.; Hoang, L. T.; Kaliszyk, C.; Magron, V.; McLaughlin, S.; Nguyen, Tat T.; Nguyen, Q. T.; Nipkow, T.; Obua, S.; Pleso, J.; Rute, J.; Solovyyev, A.; Ta, T. H. A.; Tran, N. T.; Trieu, T. D.; Urban, J.; Vu, K. Y.; Zumkeller, R., A Formal Proof of the Keplet Conjecture. *Forum Math. Pi* **2017**, *5*, e2.
- (44) Torquato, S., Perspective: Basic Understanding of Condensed Phases of Matter Via Packing Models. *J. Chem. Phys.* **2018**, *149*, 020901.
- (45) De Laat, D.; De Oliveira Filho, F. M.; Vallentin, F., Upper Bounds for Packings of Spheres of Several Radii. *Forum Math. Sigma* **2014**, *2*, e23.
- (46) Hales, T. C., The Honeycomb Conjecture. *Discrete Comput. Geom.* **2001**, *25*, 1-22.
- (47) Thomson, W., Lxiii. On the Division of Space with Minimum Partitional Area. *The London, Edinburgh, and Dublin Philosophical Magazine and Journal of Science* **1887**, *24*, 503-514.
- (48) Weaire, D.; Phelan, R., A Counter-Example to Kelvin's Conjecture on Minimal Surfaces. *Philos. Mag. Lett.* **1994**, *69*, 107-110.
- (49) De Graef, M.; McHenry, M. E., *Structure of Materials: An Introduction to Crystallography, Diffraction and Symmetry*. Cambridge University Press: Cambridge, 2012.
- (50) Steurer, W.; Dshemuchadse, J., Intermetallics : Structures, Properties, and Statistics. **2016**.
- (51) Sinha, A. K., Topologically Close-Packed Structures of Transition Metal Alloys. *Prog. Mater Sci.* **1972**, *15*, 81-185.
- (52) Frank, F. C.; Kasper, J. S., Complex Alloy Structures Regarded as Sphere Packings. I. Definitions and Basic Principles. *Acta Cryst.* **1958**, *11*, 184-190.
- (53) Frank, F. C.; Kasper, J. S., Complex Alloy Structures Regarded as Sphere Packings. II. Analysis and Classification of Representative Structures. *Acta Cryst.* **1959**, *12*, 483-499.
- (54) Dutour Sikiric, M.; Delgado-Friedrichs, O.; Deza, M., Space Fullerenes: A Computer Search for New Frank-Kasper Structures. *Acta Cryst. A* **2010**, *66*, 602-615.
- (55) Bergman, B. G.; Shoemaker, D. P., The Space Group of the Σ -FeCr Crystal Structure. *J. Chem. Phys.* **1951**, *19*, 515-515.
- (56) Tucker, C., The Crystal Structure of the [Beta] Phase of Uranium. *Acta Cryst.* **1951**, *4*, 425-431.
- (57) Moseley, P. T.; Seabrook, C. J., The Crystal Structure of [Beta]-Tantalum. *Acta Cryst. B* **1973**, *29*, 1170-1171.
- (58) Rivier, N., Kelvin's Conjecture on Minimal Froths and the Counter-Example of Weaire and Phelan. *Philos. Mag. Lett.* **1994**, *69*, 297-303.
- (59) Hall, E. O.; Algie, S. H., The Sigma Phase. *Metall. Rev.* **1966**, *11*, 61-88.
- (60) Nowotny, H.; Machenschalk, R.; Kieffer, R.; Benesovsky, F., Untersuchungen an Silizidsystemen. *Monatshefte für Chemie und verwandte Teile anderer Wissenschaften* **1954**, *85*, 241-244.
- (61) Wilson, C. G.; Thomas, D. K.; Spooner, F. J., The Crystal Structure of Zr_4Al_3 . *Acta Cryst.* **1960**, *13*, 56-57.
- (62) Andersson, S., Structures Related to the B-Tungsten or Cr_3Si Structure Type. *J. Solid State Chem.* **1978**, *23*, 191-204.

- (63) Berry, R. L.; Raynor, G. V., The Crystal Chemistry of the Laves Phases. *Acta Cryst.* **1953**, *6*, 178-186.
- (64) Thoma, D. J., Intermetallics: Laves Phases. In *Encyclopedia of Materials: Science and Technology*, Buschow, K. H. J.; Cahn, R. W.; Flemings, M. C.; Ilshner, B.; Kramer, E. J.; Mahajan, S.; Veyssière, P., Eds. Elsevier: Oxford, 2001; pp 4205-4213.
- (65) Mehl, M. J.; Hicks, D.; Toher, C.; Levy, O.; Hanson, R. M.; Hart, G.; Curtarolo, S., The Aflow Library of Crystallographic Prototypes: Part 1. *Comput. Mater. Sci.* **2017**, *136*, S1-S828.
- (66) Hicks, D.; Mehl, M. J.; Gossett, E.; Toher, C.; Levy, O.; Hanson, R. M.; Hart, G.; Curtarolo, S., The Aflow Library of Crystallographic Prototypes: Part 2. *Comput. Mater. Sci.* **2019**, *161*, S1-S1011.
- (67) Momma, K.; Izumi, F., Vesta 3 for Three-Dimensional Visualization of Crystal, Volumetric and Morphology Data. *J. Appl. Crystallogr.* **2011**, *44*, 1272-1276.
- (68) Huang, M.; Yue, K.; Wang, J.; Hsu, C.-H.; Wang, L.; Cheng, S. Z. D., Frank-Kasper and Related Quasicrystal Spherical Phases in Macromolecules. *Sci. China Chem.* **2018**, *61*, 33-45.
- (69) Matsumoto, M.; Tanaka, H., On the Structure Selectivity of Clathrate Hydrates. *J. Phys. Chem. B* **2011**, *115*, 8257-8265.
- (70) Sullivan, J. M., *The Geometry of Bubble and Foams*. NATO Advanced Science Institute Series E: Applied Sciences: Kluwer, 1998; Vol. 354.
- (71) Gabbriellini, R., A New Counter-Example to Kelvin's Conjecture on Minimal Surfaces. *Philos. Mag. Lett.* **2009**, *89*, 483-491.
- (72) Sun, H.-J.; Zhang, S.; Percec, V., From Structure to Function Via Complex Supramolecular Dendrimer Systems. *Chem. Soc. Rev.* **2015**, *44*, 3900-3923.
- (73) Rosen, B. M.; Wilson, C. J.; Wilson, D. A.; Peterca, M.; Imam, M. R.; Percec, V., Dendron-Mediated Self-Assembly, Disassembly, and Self-Organization of Complex Systems. *Chem. Rev.* **2009**, *109*, 6275-6540.
- (74) Percec, V.; Cho, W.-D.; Ungar, G., Increasing the Diameter of Cylindrical and Spherical Supramolecular Dendrimers by Decreasing the Solid Angle of Their Monodendrons Via Periphery Functionalization. *J. Am. Chem. Soc.* **2000**, *122*, 10273-10281.
- (75) Yeardley, D. J. P.; Ungar, G.; Percec, V.; Holerca, M. N.; Johansson, G., Spherical Supramolecular Minidendrimers Self-Organized in an "Inverse Micellar"-Like Thermotropic Body-Centered Cubic Liquid Crystalline Phase. *J. Am. Chem. Soc.* **2000**, *122*, 1684-1689.
- (76) Lee, E.; Ryu, J.-H.; Park, M.-H.; Lee, M.; Han, K.-H.; Chung, Y.-W.; Cho, B.-K., Observation of an Unprecedented Body Centered Cubic Micellar Mesophase from Rod-Coil Molecules. *Chem. Commun.* **2007**, 2920-2922.
- (77) Lee, M.; Cho, B.-K.; Jang, Y.-G.; Zin, W.-C., Spontaneous Organization of Supramolecular Rod-Bundles into a Body-Centered Tetragonal Assembly in Coil-Rod-Coil Molecules. *J. Am. Chem. Soc.* **2000**, *122*, 7449-7455.
- (78) Cho, B.-K.; Jain, A.; Gruner, S. M.; Wiesner, U., Mesophase Structure-Mechanical and Ionic Transport Correlations in Extended Amphiphilic Dendrons. *Science* **2004**, *305*, 1598-1601.
- (79) Zeng, X.; Poppe, S.; Lehmann, A.; Prehm, M.; Chen, C.; Liu, F.; Lu, H.; Ungar, G.; Tschierske, C., A Self-Assembled Bicontinuous Cubic Phase with a Single-Diamond Network. *Angew. Chem. Int. Ed.* **2019**, *58*, 7375-7379.
- (80) Percec, V.; Cho, W.-D.; Ungar, G.; Yeardley, D. J. P., Synthesis and Structural Analysis of Two Constitutional Isomeric Libraries of Ab₂-Based Monodendrons and Supramolecular Dendrimers. *J. Am. Chem. Soc.* **2001**, *123*, 1302-1315.
- (81) Sahoo, D.; Imam, M. R.; Peterca, M.; Partridge, B. E.; Wilson, D. A.; Zeng, X.; Ungar, G.; Heiney, P. A.; Percec, V., Hierarchical Self-Organization of Chiral Columns from Chiral Supramolecular Spheres. *J. Am. Chem. Soc.* **2018**, *140*, 13478-13487.

- (82) Percec, V.; Ahn, C. H.; Ungar, G.; Yeardley, D. J. P.; Möller, M.; Sheiko, S. S., Controlling Polymer Shape through the Self-Assembly of Dendritic Side- Groups. *Nature* **1998**, *391*, 161-164.
- (83) Borisch, K.; Diele, S.; Göring, P.; Tschierske, C., Molecular Design of Amphitropic Liquid Crystalline Carbohydrates–Amphiphilic N-Methyl-Glucamides Exhibiting Lamellar, Columnar or Cubic Mesophases. *Chem. Commun.* **1996**, 237-238.
- (84) Hudson, S. D.; Jung, H.-T.; Percec, V.; Cho, W.-D.; Johansson, G.; Ungar, G.; Balagurusamy, V. S. K., Direct Visualization of Individual Cylindrical and Spherical Supramolecular Dendrimers. *Science* **1997**, *278*, 449-452.
- (85) Dukeson, D. R.; Ungar, G.; Balagurusamy, V. S. K.; Percec, V.; Johansson, G. A.; Glodde, M., Application of Isomorphous Replacement in the Structure Determination of a Cubic Liquid Crystal Phase and Location of Counterions. *J. Am. Chem. Soc.* **2003**, *125*, 15974-15980.
- (86) Hudson, S. D.; Jung, H. T.; Kewsuwan, P.; Percec, V.; Cho, W. D., Grain Boundaries and Stacking Faults in a Pm3n Cubic Mesophase. *Liq. Cryst.* **1999**, *26*, 1493-1499.
- (87) Borisch, K.; Diele, S.; Göring, P.; Kresse, H.; Tschierske, C., Design of Thermotropic Liquid Crystals with Micellar Cubic Mesophases: Amphiphilic N-(2,3-Dihydroxypropyl)Benzamides. *Angew. Chem. Int. Ed.* **1997**, *36*, 2087-2089.
- (88) Borisch, K.; Diele, S.; Göring, P.; Kresse, H.; Tschierske, C., Tailoring Thermotropic Cubic Mesophases: Amphiphilic Polyhydroxy Derivatives. *J. Mater. Chem.* **1998**, *8*, 529-543.
- (89) Fuchs, P.; Tschierske, C.; Raith, K.; Das, K.; Diele, S., A Thermotropic Mesophase Comprised of Closed Micellar Aggregates of the Normal Type. *Angew. Chem. Int. Ed.* **2002**, *41*, 628-631.
- (90) Tschierske, C., Development of Structural Complexity by Liquid-Crystal Self-Assembly. *Angew. Chem. Int. Ed.* **2013**, *52*, 8828-8878.
- (91) Percec, V.; Peterca, M.; Tsuda, Y.; Rosen, B. M.; Uchida, S.; Imam, M. R.; Ungar, G.; Heiney, P. A., Elucidating the Structure of the Pm $\bar{3}$ N Cubic Phase of Supramolecular Dendrimers through the Modification of Their Aliphatic to Aromatic Volume Ratio. *Chem. Eur. J.* **2009**, *15*, 8994-9004.
- (92) Percec, V.; Holerca, M. N.; Uchida, S.; Cho, W.-D.; Ungar, G.; Lee, Y.; Yeardley, D. J. P., Exploring and Expanding the Three-Dimensional Structural Diversity of Supramolecular Dendrimers with the Aid of Libraries of Alkali Metals of Their AB₃ Minidendritic Carboxylates. *Chem. Eur. J.* **2002**, *8*, 1106-1117.
- (93) Coco, S.; Cordovilla, C.; Donnio, B.; Espinet, P.; García-Casas, M. J.; Guillon, D., Self-Organization of Dendritic Supermolecules, Based on Isocyanide–Gold(I), –Copper(I), –Palladium(II), and –Platinum(II) Complexes, into Micellar Cubic Mesophases. *Chem. Eur. J.* **2008**, *14*, 3544-3552.
- (94) Kim, D.; Jon, S.; Lee, H.-K.; Baek, K.; Oh, N.-K.; Zin, W.-C.; Kim, K., Anion-Directed Self-Organization of Thermotropic Liquid Crystalline Materials Containing a Guanidinium Moiety. *Chem. Commun.* **2005**, 5509-5511.
- (95) Jayaraman, A.; Mahanthappa, M. K., Counterion-Dependent Access to Low-Symmetry Lyotropic Sphere Packings of Ionic Surfactant Micelles. *Langmuir* **2018**, *34*, 2290-2301.
- (96) Schulze, M. W.; Lewis III, R. M.; Lettow, J. H.; Hickey, R. J.; Gillard, T. M.; Hillmyer, M. A.; Bates, F. S., Conformational Asymmetry and Quasicrystal Approximants in Linear Diblock Copolymers. *Phys. Rev. Lett.* **2017**, *118*, 207801.
- (97) Iacovella, C. R.; Keys, A. S.; Glotzer, S. C., Self-Assembly of Soft-Matter Quasicrystals and Their Approximants. *Proc. Natl. Acad. Sci. U.S.A.* **2011**, *108*, 20935-20940.
- (98) Yao, X.; Cseh, L.; Zeng, X.; Xue, M.; Liu, Y.; Ungar, G., Body-Centred Cubic Packing of Spheres – the Ultimate Thermotropic Assembly Mode for Highly Divergent Dendrons. *Nanoscale Horiz.* **2017**, *2*, 43-49.

- (99) Percec, V.; Cho, W.-D.; Möller, M.; Prokhorova, S. A.; Ungar, G.; Yeardley, D. J. P., Design and Structural Analysis of the First Spherical Monodendron Self-Organizable in a Cubic Lattice. *J. Am. Chem. Soc.* **2000**, *122*, 4249-4250.
- (100) Holerca, M. N.; Sahoo, D.; Partridge, B. E.; Peterca, M.; Zeng, X.; Ungar, G.; Percec, V., Dendronized Poly(2-Oxazoline) Displays within Only Five Monomer Repeat Units Liquid Quasicrystal, A15 and σ Frank–Kasper Phases. *J. Am. Chem. Soc.* **2018**, *140*, 16941-16947.
- (101) Percec, V.; Imam, M. R.; Peterca, M.; Wilson, D. A.; Heiney, P. A., Self-Assembly of Dendritic Crowns into Chiral Supramolecular Spheres. *J. Am. Chem. Soc.* **2009**, *131*, 1294-1304.
- (102) Wilson, D. A.; Andreopoulou, K. A.; Peterca, M.; Leowanawat, P.; Sahoo, D.; Partridge, B. E.; Xiao, Q.; Huang, N.; Heiney, P. A.; Percec, V., Supramolecular Spheres Self-Assembled from Conical Dendrons Are Chiral. *J. Am. Chem. Soc.* **2019**, *141*, 6162-6166.
- (103) Sahoo, D.; Peterca, M.; Aqad, E.; Partridge, B. E.; Heiney, P. A.; Graf, R.; Spiess, H. W.; Zeng, X.; Percec, V., Tetrahedral Arrangements of Perylene Bisimide Columns Via Supramolecular Orientational Memory. *ACS Nano* **2017**, *11*, 983-991.
- (104) Peterca, M.; Imam, M. R.; Hudson, S. D.; Partridge, B. E.; Sahoo, D.; Heiney, P. A.; Klein, M. L.; Percec, V., Complex Arrangement of Orthogonal Nanoscale Columns Via a Supramolecular Orientational Memory Effect. *ACS Nano* **2016**, *10*, 10480-10488.
- (105) Huang, N.; Imam, M. R.; Sienkowska, M. J.; Peterca, M.; Holerca, M. N.; Wilson, D. A.; Rosen, B. M.; Partridge, B. E.; Xiao, Q.; Percec, V., Supramolecular Spheres Assembled from Covalent and Supramolecular Dendritic Crowns Dictate the Supramolecular Orientational Memory Effect Mediated by Frank–Kasper Phases. *Giant* **2020**, *1*, 100001.
- (106) Matsubara, M.; Stevenson, W.; Yabuki, J.; Zeng, X.; Dong, H.; Kojima, K.; Chichibu, S. F.; Tamada, K.; Muramatsu, A.; Ungar, G.; Kanie, K., A Low-Symmetry Cubic Mesophase of Dendronized Cds Nanoparticles and Their Structure-Dependent Photoluminescence. *Chem.* **2017**, *2*, 860-876.
- (107) Haji-Akbari, A.; Engel, M.; Keys, A. S.; Zheng, X.; Petschek, R. G.; Palfy-Muhoray, P.; Glotzer, S. C., Disordered, Quasicrystalline and Crystalline Phases of Densely Packed Tetrahedra. *Nature* **2009**, *462*, 773-777.
- (108) Damasceno, P. F.; Engel, M.; Glotzer, S. C., Predictive Self-Assembly of Polyhedra into Complex Structures. *Science* **2012**, *337*, 453-457.
- (109) Lindsay, A. P.; Lewis, R. M.; Lee, B.; Peterson, A. J.; Lodge, T. P.; Bates, F. S., A15, Σ , and a Quasicrystal: Access to Complex Particle Packings Via Bidisperse Diblock Copolymer Blends. *ACS Macro Lett.* **2020**, *9*, 197-203.
- (110) Zhang, W.; Huang, M.; Su, H.; Zhang, S.; Yue, K.; Dong, X.-H.; Li, X.; Liu, H.; Zhang, S.; Wesdemiotis, C.; Lotz, B.; Zhang, W.-B.; Li, Y.; Cheng, S. Z. D., Toward Controlled Hierarchical Heterogeneities in Giant Molecules with Precisely Arranged Nano Building Blocks. *ACS Cent. Sci.* **2016**, *2*, 48-54.
- (111) Grason, G. M., The Packing of Soft Materials: Molecular Asymmetry, Geometric Frustration and Optimal Lattices in Block Copolymer Melts. *Phys. Rep.* **2006**, *433*, 1-64.
- (112) Reddy, A.; Buckley, M. B.; Arora, A.; Bates, F. S.; Dorfman, K. D.; Grason, G. M., Stable Frank–Kasper Phases of Self-Assembled, Soft Matter Spheres. *Proc. Natl. Acad. Sci. U.S.A.* **2018**, *115*, 10233-10238.
- (113) Lee, S.; Leighton, C.; Bates, F. S., Sphericity and Symmetry Breaking in the Formation of Frank-Kasper Phases from One Component Materials. *Proc. Natl. Acad. Sci. U.S.A.* **2014**, *111*, 17723-17731.
- (114) Zhang, W.; Lu, X.; Mao, J.; Hsu, C.-H.; Mu, G.; Huang, M.; Guo, Q.; Liu, H.; Wesdemiotis, C.; Li, T.; Zhang, W.-B.; Li, Y.; Cheng, S. Z. D., Sequence-Mandated, Distinct Assembly of Giant Molecules. *Angew. Chem. Int. Ed.* **2017**, *56*, 15014-15019.

- (115) Feng, X.; Zhang, R.; Li, Y.; Hong, Y.-l.; Guo, D.; Lang, K.; Wu, K.-Y.; Huang, M.; Mao, J.; Wesdemiotis, C.; Nishiyama, Y.; Zhang, W.; Zhang, W.; Miyoshi, T.; Li, T.; Cheng, S. Z. D., Hierarchical Self-Organization of Abn Dendron-Like Molecules into a Supramolecular Lattice Sequence. *ACS Cent. Sci.* **2017**, *3*, 860-867.
- (116) Ni, B.; Qu, H.; Mao, J.; Bai, R.; Zhang, S.; Feng, X.; Wesdemiotis, C.; Dong, X.-H.; Cheng, S. Z. D., Facile Synthesis and Linker Guided Self-Assembly of Dendron-Like Amphiphiles. *Polymer* **2019**, *167*, 118-121.
- (117) Feng, X.; Liu, G.; Guo, D.; Lang, K.; Zhang, R.; Huang, J.; Su, Z.; Li, Y.; Huang, M.; Li, T.; Cheng, S. Z. D., Transition Kinetics of Self-Assembled Supramolecular Dodecagonal Quasicrystal and Frank–Kasper Σ Phases in Abn Dendron-Like Giant Molecules. *ACS Macro Lett.* **2019**, *8*, 875-881.
- (118) Liu, Y.; Liu, G.; Zhang, W.; Du, C.; Wesdemiotis, C.; Cheng, S. Z. D., Cooperative Soft-Cluster Glass in Giant Molecular Clusters. *Macromolecules* **2019**, *52*, 4341-4348.
- (119) Hsu, C.-H.; Cheng, S. Z. D., The Deconstruction of Supramolecular Structures Based on Modular Precise Macromolecules. *Macromol. Chem. Phys.* **2018**, *219*, 1700390.
- (120) Bates, C. M.; Bates, F. S., 50th Anniversary Perspective: Block Polymers—Pure Potential. *Macromolecules* **2017**, *50*, 3-22.
- (121) Bates, F. S.; Hillmyer, M. A.; Lodge, T. P.; Bates, C. M.; Delaney, K. T.; Fredrickson, G. H., Multiblock Polymers: Panacea or Pandora's Box? *Science* **2012**, *336*, 434-40.
- (122) Leibler, L., Theory of Microphase Separation in Block Copolymers. *Macromolecules* **1980**, *13*, 1602-1617.
- (123) Matsen, M. W.; Bates, F. S., Origins of Complex Self-Assembly in Block Copolymers. *Macromolecules* **1996**, *29*, 7641-7644.
- (124) Matsen, M. W.; Bates, F. S., Unifying Weak- and Strong-Segregation Block Copolymer Theories. *Macromolecules* **1996**, *29*, 1091-1098.
- (125) Dormidontova, E. E.; Lodge, T. P., The Order–Disorder Transition and the Disordered Micelle Regime in Sphere-Forming Block Copolymer Melts. *Macromolecules* **2001**, *34*, 9143-9155.
- (126) Bates, F. S.; Cohen, R. E.; Berney, C. V., Small-Angle Neutron Scattering Determination of Macrolattice Structure in a Polystyrene-Polybutadiene Diblock Copolymer. *Macromolecules* **1982**, *15*, 589-592.
- (127) Huang, Y.-Y.; Hsu, J.-Y.; Chen, H.-L.; Hashimoto, T., Existence of Fcc-Packed Spherical Micelles in Diblock Copolymer Melt. *Macromolecules* **2007**, *40*, 406-409.
- (128) McCreedy, K.; Keskkula, H., Effect of Thermal Crosslinking on Decomposition of Polybutadiene. *Polymer* **1979**, *20*, 1155-1159.
- (129) Huang, Y.-Y.; Chen, H.-L.; Hashimoto, T., Face-Centered Cubic Lattice of Spherical Micelles in Block Copolymer/Homopolymer Blends. *Macromolecules* **2003**, *36*, 764-770.
- (130) Chen, L.-T.; Chen, C.-Y.; Chen, H.-L., Fcc or Hcp: The Stable Close-Packed Lattice of Crystallographically Equivalent Spherical Micelles in Block Copolymer/Homopolymer Blend. *Polymer* **2019**, *169*, 131-137.
- (131) Lee, S. Structure and Dynamics of Block Copolymer Based Soft Materials. University of Minnesota, 2011.
- (132) Alexander, S.; McTague, J., Should All Crystals Be Bcc? Landau Theory of Solidification and Crystal Nucleation. *Phys. Rev. Lett.* **1978**, *41*, 702-705.
- (133) Thomas, E. L.; Kinning, D. J.; Alward, D. B.; Henkee, C. S., Ordered Packing Arrangements of Spherical Micelles of Diblock Copolymers in Two and Three Dimensions. *Macromolecules* **1987**, *20*, 2934-2939.

- (134) Lewis, R. M.; Beech, H. K.; Jackson, G. L.; Maher, M. J.; Kim, K.; Narayanan, S.; Lodge, T. P.; Mahanthappa, M. K.; Bates, F. S., Dynamics of a Supercooled Disordered Sphere-Forming Diblock Copolymer as Determined by X-Ray Photon Correlation and Dynamic Mechanical Spectroscopies. *ACS Macro Lett.* **2018**, *7*, 1486-1491.
- (135) Xie, N.; Li, W.; Qiu, F.; Shi, A.-C., σ Phase Formed in Conformationally Asymmetric Ab-Type Block Copolymers. *ACS Macro Lett.* **2014**, *3*, 906-910.
- (136) Matsen, M. W.; Bates, F. S., Conformationally Asymmetric Block Copolymers. *J. Polym. Sci., Part B: Polym. Phys.* **1997**, *35*, 945-952.
- (137) Bates, F. S.; Schulz, M. F.; Khandpur, A. K.; Förster, S.; Rosedale, J. H.; Almdal, K.; Mortensen, K., Fluctuations, Conformational Asymmetry and Block Copolymer Phase Behaviour. *Faraday Discuss.* **1994**, *98*, 7-18.
- (138) Hiemenz, P. C.; Lodge, T., *Polymer Chemistry*. Second ed.; CRC Press: Boca Raton, 2007.
- (139) Fredrickson, G. H.; Helfand, E., Fluctuation Effects in the Theory of Microphase Separation in Block Copolymers. *J. Chem. Phys.* **1987**, *87*, 697-705.
- (140) Qin, J.; Morse, D. C., Fluctuations in Symmetric Diblock Copolymers: Testing Theories Old and New. *Phys. Rev. Lett.* **2012**, *108*, 238301.
- (141) Lewis, R. M.; Arora, A.; Beech, H. K.; Lee, B.; Lindsay, A. P.; Lodge, T. P.; Dorfman, K. D.; Bates, F. S., Role of Chain Length in the Formation of Frank-Kasper Phases in Diblock Copolymers. *Phys. Rev. Lett.* **2018**, *121*, 208002.
- (142) Cavicchi, K. A.; Lodge, T. P., Self-Diffusion and Tracer Diffusion in Sphere-Forming Block Copolymers. *Macromolecules* **2003**, *36*, 7158-7164.
- (143) Johnston, R. L.; Hoffmann, R., Structure-Bonding Relationships in the Laves Phases. *Z. Anorg. Allg. Chem.* **1992**, *616*, 105-120.
- (144) Stein, F.; Palm, M.; Sauthoff, G., Structure and Stability of Laves Phases. Part I. Critical Assessment of Factors Controlling Laves Phase Stability. *Intermetallics* **2004**, *12*, 713-720.
- (145) Stein, F.; Palm, M.; Sauthoff, G., Structure and Stability of Laves Phases Part II. Structure Type Variations in Binary and Ternary Systems. *Intermetallics* **2005**, *13*, 1056-1074.
- (146) Meli, L.; Lodge, T. P., Equilibrium vs Metastability: High-Temperature Annealing of Spherical Block Copolymer Micelles in an Ionic Liquid. *Macromolecules* **2009**, *42*, 580-583.
- (147) Dormidontova, E. E., Micellization Kinetics in Block Copolymer Solutions: Scaling Model. *Macromolecules* **1999**, *32*, 7630-7644.
- (148) Liu, M.; Qiang, Y.; Li, W.; Qiu, F.; Shi, A.-C., Stabilizing the Frank-Kasper Phases Via Binary Blends of Ab Diblock Copolymers. *ACS Macro Lett.* **2016**, *5*, 1167-1171.
- (149) Kim, K.; Arora, A.; Lewis, R. M.; Liu, M.; Li, W.; Shi, A.-C.; Dorfman, K. D.; Bates, F. S., Origins of Low-Symmetry Phases in Asymmetric Diblock Copolymer Melts. *Proc. Natl. Acad. Sci. U.S.A.* **2018**, *115*, 847-854.
- (150) Steurer, W.; Deloudi, S., *Crystallography of Quasicrystals: Concepts, Methods, and Structures*. Springer-Verlag: Berlin, 2009; Vol. 126.
- (151) Klatt, M. A.; Lovrić, J.; Chen, D.; Kapfer, S. C.; Schaller, F. M.; Schönhöfer, P. W. A.; Gardiner, B. S.; Smith, A.-S.; Schröder-Turk, G. E.; Torquato, S., Universal Hidden Order in Amorphous Cellular Geometries. *Nat. Commun.* **2019**, *10*, 811.
- (152) Chanpuriya, S.; Kim, K.; Zhang, J.; Lee, S.; Arora, A.; Dorfman, K. D.; Delaney, K. T.; Fredrickson, G. H.; Bates, F. S., Cornucopia of Nanoscale Ordered Phases in Sphere-Forming Tetrablock Terpolymers. *ACS Nano* **2016**, *10*, 4961-4972.
- (153) Zhang, J.; Sides, S.; Bates, F. S., Ordering of Sphere Forming SISO Tetrablock Terpolymers on a Simple Hexagonal Lattice. *Macromolecules* **2012**, *45*, 256-265.
- (154) Liu, M.; Li, W.; Qiu, F.; Shi, A.-C., Stability of the Frank-Kasper σ -Phase in BABC Linear Tetrablock Terpolymers. *Soft Matter* **2016**, *12*, 6412-6421.

- (155) Jeon, S.; Jun, T.; Jo, S.; Ahn, H.; Lee, S.; Lee, B.; Ryu, D. Y., Frank–Kasper Phases Identified in Pdms-B-Ptfea Copolymers with High Conformational Asymmetry. *Macromol. Rapid Commun.* **2019**, *40*, 1900259.
- (156) Li, W.; Duan, C.; Shi, A.-C., Nonclassical Spherical Packing Phases Self-Assembled from Ab-Type Block Copolymers. *ACS Macro Lett.* **2017**, *6*, 1257-1262.
- (157) Bates, M. W.; Barbon, S. M.; Levi, A. E.; Lewis, R. M.; Beech, H. K.; Vonk, K. M.; Zhang, C.; Fredrickson, G. H.; Hawker, C. J.; Bates, C. M., Synthesis and Self-Assembly of Abn Miktoarm Star Polymers. *ACS Macro Lett.* **2020**, 396-403.
- (158) Takagi, H.; Hashimoto, R.; Igarashi, N.; Kishimoto, S.; Yamamoto, K., Frank–Kasper σ Phase in Polybutadiene-Poly(E-Caprolactone) Diblock Copolymer/Polybutadiene Blends. *J. Phys.: Condens. Matter* **2017**, *29*, 204002.
- (159) Takagi, H.; Yamamoto, K., Phase Boundary of Frank–Kasper σ Phase in Phase Diagrams of Binary Mixtures of Block Copolymers and Homopolymers. *Macromolecules* **2019**, *52*, 2007-2014.
- (160) Lachmayr, K. K.; Wentz, C. M.; Sita, L. R., An Exceptionally Stable and Scalable Sugar–Polyolefin Frank–Kasper A15 Phase. *Angew. Chem. Int. Ed.* **2020**, *59*, 1521-1526.
- (161) Lachmayr, K. K.; Sita, L. R., Small-Molecule Modulation of Soft-Matter Frank–Kasper Phases: A Method for Adding Function to Form. *Angew. Chem. Int. Ed.* **2020**, *59*, 3563-3567.
- (162) Zihlerl, P.; Kamien, R. D., Soap Froths and Crystal Structures. *Phys. Rev. Lett.* **2000**, *85*, 3528-3531.
- (163) Zihlerl, P.; Kamien, R. D., Maximizing Entropy by Minimizing Area: Towards a New Principle of Self-Organization. *J. Phys. Chem. B* **2001**, *105*, 10147-10158.
- (164) Gao, Y.; Deng, H.; Li, W.; Qiu, F.; Shi, A.-C., Formation of Nonclassical Ordered Phases of A_nB_m-Type Multiarm Block Copolymers. *Phys. Rev. Lett.* **2016**, *116*, 068304.
- (165) Duan, C.; Zhao, M.; Qiang, Y.; Chen, L.; Li, W.; Qiu, F.; Shi, A.-C., Stability of Two-Dimensional Dodecagonal Quasicrystalline Phase of Block Copolymers. *Macromolecules* **2018**, *51*, 7713-7721.
- (166) Han, L.; Che, S., An Overview of Materials with Triply Periodic Minimal Surfaces and Related Geometry: From Biological Structures to Self-Assembled Systems. *Adv. Mater.* **2018**, *30*, 1705708.
- (167) Schröder-Turk, G. E.; de Campo, L.; Evans, M. E.; Saba, M.; Kapfer, S. C.; Varslot, T.; Grosse-Brauckmann, K.; Ramsden, S.; Hyde, S. T., Polycontinuous Geometries for Inverse Lipid Phases with More Than Two Aqueous Network Domains. *Faraday Discuss.* **2013**, *161*, 215-247.
- (168) Mitchell, D. J.; Tiddy, G. J. T.; Waring, L.; Bostock, T.; McDonald, M. P., Phase Behaviour of Polyoxyethylene Surfactants with Water. Mesophase Structures and Partial Miscibility (Cloud Points). *J. Chem. Soc., Faraday Trans. 1* **1983**, *79*, 975-1000.
- (169) Kunieda, H.; Shigeta, K.; Ozawa, K.; Suzuki, M., Self-Organizing Structures in Poly(Oxyethylene) Oleyl Ether–Water System. *J. Phys. Chem. B* **1997**, *101*, 7952-7957.
- (170) McConnell, G. A.; Gast, A. P.; Huang, J. S.; Smith, S. D., Disorder-Order Transitions in Soft Sphere Polymer Micelles. *Phys. Rev. Lett.* **1993**, *71*, 2102-2105.
- (171) Lodge, T. P.; Pudil, B.; Hanley, K. J., The Full Phase Behavior for Block Copolymers in Solvents of Varying Selectivity. *Macromolecules* **2002**, *35*, 4707-4717.
- (172) Dong, R.; Hao, J., Complex Fluids of Poly(Oxyethylene) Monoalkyl Ether Nonionic Surfactants. *Chem. Rev.* **2010**, *110*, 4978-5022.
- (173) Lodge, T. P.; Bang, J.; Park, M. J.; Char, K., Origin of the Thermoreversible Fcc-Bcc Transition in Block Copolymer Solutions. *Phys. Rev. Lett.* **2004**, *92*, 145501.
- (174) Hamley, I. W.; Pople, J. A.; Diat, O., A Thermally Induced Transition from a Body-Centred to a Face-Centred Cubic Lattice in a Diblock Copolymer Gel. *Colloid. Polym. Sci.* **1998**, *276*, 446-450.

- (175) Chen, L.; Lee, H. S.; Lee, S., Close-Packed Block Copolymer Micelles Induced by Temperature Quenching. *Proc. Natl. Acad. Sci. U.S.A.* **2018**, *115*, 7218-7223.
- (176) Fischer, S.; Exner, A.; Zielske, K.; Perlich, J.; Deloudi, S.; Steurer, W.; Lindner, P.; Förster, S., Colloidal Quasicrystals with 12-Fold and 18-Fold Diffraction Symmetry. *Proc. Natl. Acad. Sci. U.S.A.* **2011**, *108*, 1810-1814.
- (177) Jayaraman, A.; Zhang, D. Y.; Dewing, B. L.; Mahanthappa, M. K., Path-Dependent Preparation of Complex Micelle Packings of a Hydrated Diblock Oligomer. *ACS Cent. Sci.* **2019**, *5*, 619-628.
- (178) Carlström Göran, H. G., The State of Water in Non-Ionic Surfactant Solutions and Lyotropic Phases. Oxygen-17 Magnetic Relaxation Study. *J. Chem. Soc., Faraday Trans. 1* **1989**, *85*, 1049-1063.
- (179) Bjoerling, M.; Linse, P.; Karlstroem, G., Distribution of Segments for Terminally Attached Poly(Ethylene Oxide) Chains. *J. Phys. Chem.* **1990**, *94*, 471-481.
- (180) Martiel, I.; Sagalowicz, L.; Mezzenga, R., A Reverse Micellar Mesophase of Face-Centered Cubic Fm3m Symmetry in Phosphatidylcholine/Water/Organic Solvent Ternary Systems. *Langmuir* **2013**, *29*, 15805-15812.
- (181) Deng, S.-l.; Zhao, J.-x.; Wen, Z.-x., Self-Assembly of Quaternary Ammonium Gemini Surfactants in Cyclohexane Upon Reinforcement by Simple Counterions. *RSC Advances* **2018**, *8*, 18880-18888.
- (182) Deng, S.; Zhao, J., Self-Assembly of Cationic Gemini Surfactants, Alkanediyl-Bis-(Dimethyldodecyl-Ammonium Bromide), in Cyclohexane: Effects of Spacer Length on Their Association into Reverse Lyotropic Liquid Crystalline or Reverse Vesicles. *Soft Matter* **2018**, *14*, 734-741.
- (183) Woodcock, L. V., Entropy Difference between the Face-Centred Cubic and Hexagonal Close-Packed Crystal Structures. *Nature* **1997**, *385*, 141-143.
- (184) Marianne, C., A New Symmetry for the Packing of Amphiphilic Direct Micelles. *J. Phys. II France* **1996**, *6*, 961-968.
- (185) Zeng, X.; Liu, Y.; Impérator-Clerc, M., Hexagonal Close Packing of Nonionic Surfactant Micelles in Water. *J. Phys. Chem. B* **2007**, *111*, 5174-5179.
- (186) Imai, M.; Yoshida, I.; Iwaki, T.; Nakaya, K., Static and Dynamic Structures of Spherical Nonionic Surfactant Micelles During the Disorder-Order Transition. *J. Chem. Phys.* **2005**, *122*, 044906.
- (187) Liu, C. K.; Warr, G. G., Hexagonal Closest-Packed Spheres Liquid Crystalline Phases Stabilised by Strongly Hydrated Counterions. *Soft Matter* **2014**, *10*, 83-87.
- (188) Shearman, G. C.; Tyler, A. I. I.; Brooks, N. J.; Templer, R. H.; Ces, O.; Law, R. V.; Seddon, J. M., A 3-D Hexagonal Inverse Micellar Lyotropic Phase. *J. Am. Chem. Soc.* **2009**, *131*, 1678-1679.
- (189) Balmbra, R. R.; Clunie, J. S.; Goodman, J. F., Cubic Mesomorphic Phases. *Nature* **1969**, *222*, 1159-1160.
- (190) Perroni, D. V.; Mahanthappa, M. K., Inverse Pm3(-)N Cubic Micellar Lyotropic Phases from Zwitterionic Triazolium Gemini Surfactants. *Soft Matter* **2013**, *9*, 7919-7922.
- (191) Conn, C. E.; Seddon, J. M., Nonlamellar Lipid Aggregates. In *Liposomes, Lipid Bilayers and Model Membranes*, 1st ed.; Pabst, G.; Kucerka, N.; Nieh, M. P.; Katsaras, J., Eds. CRC Press: Boca Raton, 2014.
- (192) van 't Hag, L.; Gras, S. L.; Conn, C. E.; Drummond, C. J., Lyotropic Liquid Crystal Engineering Moving Beyond Binary Compositional Space - Ordered Nanostructured Amphiphile Self-Assembly Materials by Design. *Chem. Soc. Rev.* **2017**, *46*, 2705-2731.

- (193) Kulkarni, C. V.; Wachter, W.; Iglesias-Salto, G.; Engelskirchen, S.; Ahualli, S., Monoolein: A Magic Lipid? *Phys. Chem. Chem. Phys.* **2011**, *13*, 3004-3021.
- (194) Minamikawa, H.; Hato, M., Reverse Micellar Cubic Phase in a Phytanyl-Chained Glucolipid/Water System. *Langmuir* **1998**, *14*, 4503-4509.
- (195) Fong, C.; Weerawardena, A.; Sagnella, S. M.; Mulet, X.; Waddington, L.; Krodkiewska, I.; Drummond, C. J., Monodisperse Nonionic Phytanyl Ethylene Oxide Surfactants: High Throughput Lyotropic Liquid Crystalline Phase Determination and the Formation of Liposomes, Hexosomes and Cubosomes. *Soft Matter* **2010**, *6*, 4727-4741.
- (196) Rappolt, M.; Cacho-Nerin, F.; Morello, C.; Yaghamur, A., How the Chain Configuration Governs the Packing of Inverted Micelles in the Cubic Fd3m-Phase. *Soft Matter* **2013**, *9*, 6291-6300.
- (197) Yaghamur, A.; de Campo, L.; Salentinig, S.; Sagalowicz, L.; Leser, M. E.; Glatter, O., Oil-Loaded Monolinolein-Based Particles with Confined Inverse Discontinuous Cubic Structure (Fd3m). *Langmuir* **2006**, *22*, 517-521.
- (198) Kumar, M.; Patil, N. G.; Choudhury, C. K.; Roy, S.; Ambade, A. V.; Kumaraswamy, G., Compact Polar Moieties Induce Lipid-Water Systems to Form Discontinuous Reverse Micellar Phase. *Soft Matter* **2015**, *11*, 5417-5424.
- (199) Seddon, J. M.; Zeb, N.; Templer, R. H.; McElhaney, R. N.; Mannock, D. A., An Fd3m Lyotropic Cubic Phase in a Binary Glycolipid/Water System. *Langmuir* **1996**, *12*, 5250-5253.
- (200) Reichelt, H.; Faunce, C. A.; Paradies, H. H., The Phase Diagram of Charged Colloidal Lipid a-Diphosphate Dispersions. *J. Phys. Chem. B* **2008**, *112*, 3290-3293.
- (201) Wang, Z.; Diao, Z.; Liu, F.; Li, G.; Zhang, G., Microstructure and Rheological Properties of Liquid Crystallines Formed in Brij 97/Water/Ipm System. *J. Colloid Interface Sci.* **2006**, *297*, 813-818.
- (202) Baez-Cotto, C. M.; Mahanthappa, M. K., Micellar Mimicry of Intermetallic C14 and C15 Laves Phases by Aqueous Lyotropic Self-Assembly. *ACS Nano* **2018**, *12*, 3226-3234.
- (203) Baez-Cotto, C. M.; Jackson, G. L.; Mahanthappa, M. K., Aqueous Lyotropic Mesophase Behavior of Gemini Dicarboxylate Surfactants Swollen with N-Decane. *Langmuir* **2020**, *36*, 2307-2321.
- (204) Stein, F., Consequences of Crystal Structure Differences between C14, C15, and C36 Laves Phase Polytypes for Their Coexistence in Transition-Metal-Based Systems. *MRS Proceedings* **2011**, *1295*, mrsf10-1295-n06-01.
- (205) Kunieda, H.; Ozawa, K.; Huang, K.-L., Effect of Oil on the Surfactant Molecular Curvatures in Liquid Crystals. *J. Phys. Chem. B* **1998**, *102*, 831-838.
- (206) Kunieda, H.; Umizu, G.; Aramaki, K., Effect of Mixing Oils on the Hexagonal Liquid Crystalline Structures. *J. Phys. Chem. B* **2000**, *104*, 2005-2011.
- (207) Mueller, A. J.; Lindsay, A. P.; Jayaraman, A.; Lodge, T. P.; Mahanthappa, M. K.; Bates, F. S., Emergence of a C15 Laves Phase in Diblock Polymer/Homopolymer Blends. *ACS Macro Lett.* **2020**, 576-582.
- (208) Uddin, M. H.; Rodriguez, C.; López-Quintela, A.; Leisner, D.; Solans, C.; Esquena, J.; Kunieda, H., Phase Behavior and Microstructure of Poly(Oxyethylene)-Poly(Dimethylsiloxane) Copolymer Melt. *Macromolecules* **2003**, *36*, 1261-1271.
- (209) Lindquist, B. A.; Jadrich, R. B.; Truskett, T. M., Communication: From Close-Packed to Topologically Close-Packed: Formation of Laves Phases in Moderately Polydisperse Hard-Sphere Mixtures. *J. Chem. Phys.* **2018**, *148*, 191101.
- (210) Bommineni, P. K.; Varela-Rosales, N. R.; Klement, M.; Engel, M., Complex Crystals from Size-Disperse Spheres. *Phys. Rev. Lett.* **2019**, *122*, 128005.

- (211) Abbas, S.; Lodge, T. P., Superlattice Formation in Binary Mixtures of Block Copolymer Micelles. *Langmuir* **2008**, *24*, 6247-6253.
- (212) Abbas, S.; Lodge, T. P., Superlattice Formation in a Binary Mixture of Block Copolymer Micelles. *Phys. Rev. Lett.* **2006**, *97*, 097803.
- (213) Hagslätt, H.; Fontell, K., Divalent Surfactants—the Influence of Headgroup Charge on the Phase Behavior of an Alkyldiamine Surfactant/Water System. *J. Colloid Interface Sci.* **1994**, *165*, 431-444.
- (214) Kaneko, D.; Olsson, U.; Sakamoto, K., Self-Assembly in Some N-Lauroyl-L-Glutamate/Water Systems. *Langmuir* **2002**, *18*, 4699-4703.
- (215) Hagslätt, H.; Soederman, O.; Joensson, B., Divalent Surfactants. Experimental Results and Theoretical Modeling of Surfactant/Water Phase Equilibria. *Langmuir* **1994**, *10*, 2177-2187.
- (216) Authier, A.; Chapuis, G., *A Little Dictionary of Crystallography*. Second ed.; International Union of Crystallography: 2017.
- (217) Shechtman, D.; Blech, I.; Gratias, D.; Cahn, J. W., Metallic Phase with Long-Range Orientational Order and No Translational Symmetry. *Phys. Rev. Lett.* **1984**, *53*, 1951-1953.
- (218) Grimm, U.; Kramer, P. Quasicrystals *arXiv e-prints* [Online], 2019, p. arXiv:1906.10392. <https://ui.adsabs.harvard.edu/abs/2019arXiv190610392G> (accessed June 01, 2019).
- (219) Levine, D.; Steinhardt, P. J., Quasicrystals: A New Class of Ordered Structures. *Phys. Rev. Lett.* **1984**, *53*, 2477-2480.
- (220) Goldman, A. I.; Kelton, R. F., Quasicrystals and Crystalline Approximants. *Rev. Mod. Phys.* **1993**, *65*, 213-230.
- (221) Walter, S., Twenty Years of Structure Research on Quasicrystals. Part I. Pentagonal, Octagonal, Decagonal and Dodecagonal Quasicrystals. *Z. Kristallogr. Cryst. Mater.* **2004**, *219*, 391-446.
- (222) Steurer, W., Why Are Quasicrystals Quasiperiodic? *Chem. Soc. Rev.* **2012**, *41*, 6719-6729.
- (223) Steurer, W., Quasicrystals: What Do We Know? What Do We Want to Know? What Can We Know? *Acta Cryst. A* **2018**, *74*, 1-11.
- (224) Janot, C., Quasicrystals—a Primer (Monographs on the Physics and Chemistry of Materials). Oxford: Oxford University Press: 1994.
- (225) Lidin, S., Quasicrystal Approximants. *Handbook of Solid State Chemistry* **2017**, 73-92.
- (226) Ishimasa, T.; Nissen, H. U.; Fukano, Y., New Ordered State between Crystalline and Amorphous in Ni-Cr Particles. *Phys. Rev. Lett.* **1985**, *55*, 511-513.
- (227) Conrad, M.; Krumeich, F.; Harbrecht, B., A Dodecagonal Quasicrystalline Chalcogenide. *Angew. Chem. Int. Ed.* **1998**, *37*, 1383-1386.
- (228) Yadav, T. P.; Mukhopadhyay, N. K., Quasicrystal: A Low-Frictional Novel Material. *Curr. Opin. Chem. Eng.* **2018**, *19*, 163-169.
- (229) Louzguine-Luzgin, D. V.; Inoue, A., Formation and Properties of Quasicrystals. *Annu. Rev. Mater. Res.* **2008**, *38*, 403-423.
- (230) Dubois, J.-M., Properties- and Applications of Quasicrystals and Complex Metallic Alloys. *Chem. Soc. Rev.* **2012**, *41*, 6760-6777.
- (231) Lifshitz, R. In *Nanotechnology and Quasicrystals: From Self-Assembly to Photonic Applications*, Silicon Versus Carbon, Dordrecht, 2009//; Magarshak, Y.; Kozyrev, S.; Vaseashta, A. K., Eds. Springer Netherlands: Dordrecht, 2009; pp 119-136.
- (232) Gähler, F. Quasicrystal Structures from the Crystallographic Viewpoint. ETH Zürich, 1988.
- (233) Niizeki, N.; Mitani, H., Two-Dimensional Dodecagonal Quasilattices. *J. Phys. A: Math. Gen.* **1987**, *20*, L405-L410.

- (234) Zhang, R.; Zeng, X.; Ungar, G., Direct Afm Observation of Individual Micelles, Tile Decorations and Tiling Rules of a Dodecagonal Liquid Quasicrystal. *J. Phys.: Condens. Matter* **2017**, *29*, 414001.
- (235) Zeng, X.; Ungar, G.; Liu, Y.; Percec, V.; Dulcey, A. E.; Hobbs, J. K., Supramolecular Dendritic Liquid Quasicrystals. *Nature* **2004**, *428*, 157-160.
- (236) Ungar, G.; Percec, V.; Zeng, X.; Leowanawat, P., Liquid Quasicrystals. *Isr. J. Chem.* **2011**, *51*, 1206-1215.
- (237) Keys, A. S.; Glotzer, S. C., How Do Quasicrystals Grow? *Phys. Rev. Lett.* **2007**, *99*, 235503.
- (238) Dzugutov, M., Formation of a Dodecagonal Quasicrystalline Phase in a Simple Monatomic Liquid. *Phys. Rev. Lett.* **1993**, *70*, 2924-2927.
- (239) Ungar, G.; Zeng, X., Frank-Kasper, Quasicrystalline and Related Phases in Liquid Crystals. *Soft Matter* **2005**, *1*, 95-106.
- (240) Hayashida, K.; Dotera, T.; Takano, A.; Matsushita, Y., Polymeric Quasicrystal: Mesoscopic Quasicrystalline Tiling in \$Abc\$ Star Polymers. *Phys. Rev. Lett.* **2007**, *98*, 195502.
- (241) Iwami, S.; Ishimasa, T., Dodecagonal Quasicrystal in Mn-Based Quaternary Alloys Containing Cr, Ni and Si. *Philos. Mag. Lett.* **2015**, *95*, 229-236.
- (242) Gillard, T. M.; Lee, S.; Bates, F. S., Dodecagonal Quasicrystalline Order in a Diblock Copolymer Melt. *Proc. Natl. Acad. Sci. U.S.A.* **2016**, *113*, 5167-5172.
- (243) Zhang, J.; Bates, F. S., Dodecagonal Quasicrystalline Morphology in a Poly(Styrene-B-Isoprene-B-Styrene-B-Ethylene Oxide) Tetrablock Terpolymer. *J. Am. Chem. Soc.* **2012**, *134*, 7636-7639.
- (244) Ishimasa, T.; Iwami, S.; Sakaguchi, N.; Oota, R.; Mihalkovič, M., Phason Space Analysis and Structure Modelling of 100 Å-Scale Dodecagonal Quasicrystal in Mn-Based Alloy. *Philos. Mag.* **2015**, *95*, 3745-3767.
- (245) Jain, S.; Bates, F. S., Consequences of Nonergodicity in Aqueous Binary Peo-Pb Micellar Dispersions. *Macromolecules* **2004**, *37*, 1511-1523.
- (246) Dotera, T.; Oshiro, T.; Zihler, P., Mosaic Two-Lengthscale Quasicrystals. *Nature* **2014**, *506*, 208-211.
- (247) Lifshitz, R.; Diamant, H., Soft Quasicrystals—Why Are They Stable? *Philos. Mag.* **2007**, *87*, 3021-3030.
- (248) Pattabhiraman, H.; Dijkstra, M., Phase Behaviour of Quasicrystal Forming Systems of Core-Corona Particles. *J. Chem. Phys.* **2017**, *146*, 114901.
- (249) Schoberth, H. G.; Emmerich, H.; Holzinger, M.; Dulle, M.; Förster, S.; Gruhn, T., Molecular Dynamics Study of Colloidal Quasicrystals. *Soft Matter* **2016**, *12*, 7644-7654.
- (250) Lindquist, B. A.; Jadrich, R. B.; Piñeros, W. D.; Truskett, T. M., Inverse Design of Self-Assembling Frank-Kasper Phases and Insights into Emergent Quasicrystals. *J. Phys. Chem. B* **2018**, *122*, 5547-5556.
- (251) Hynninen, A.-P.; Thijssen, J. H. J.; Vermolen, E. C. M.; Dijkstra, M.; van Blaaderen, A., Self-Assembly Route for Photonic Crystals with a Bandgap in the Visible Region. *Nat. Mater.* **2007**, *6*, 202-205.
- (252) Klatt, M. A.; Steinhardt, P. J.; Torquato, S., Phoamtonic Designs Yield Sizeable 3d Photonic Band Gaps. *Proc. Natl. Acad. Sci. U.S.A.* **2019**, *116*, 23480.
- (253) Barkan, K.; Engel, M.; Lifshitz, R., Controlled Self-Assembly of Periodic and Aperiodic Cluster Crystals. *Phys. Rev. Lett.* **2014**, *113*, 098304.
- (254) Laughlin, R. G., *The Aqueous Phase Behavior of Surfactants*. Academic Press: London; San Diego, 1994.
- (255) Dreiss, C. A., Wormlike Micelles: Where Do We Stand? Recent Developments, Linear Rheology and Scattering Techniques. *Soft Matter* **2007**, *3*, 956-970.

- (256) Raghavan, S. R.; Feng, Y., Chapter 2 Wormlike Micelles: Solutions, Gels, or Both? In *Wormlike Micelles: Advances in Systems, Characterisation and Applications*, Dreiss, C. A.; Feng, Y., Eds. The Royal Society of Chemistry: 2017; pp 9-30.
- (257) Walker, L. M., Rheology and Structure of Worm-Like Micelles. *Curr. Opin. Colloid Interface Sci.* **2001**, *6*, 451-456.
- (258) Leal, C.; Bouxsein, N. F.; Ewert, K. K.; Safinya, C. R., Highly Efficient Gene Silencing Activity of Sirna Embedded in a Nanostructured Gyroid Cubic Lipid Matrix. *J. Am. Chem. Soc.* **2010**, *132*, 16841-16847.
- (259) Mulet, X.; Boyd, B. J.; Drummond, C. J., Advances in Drug Delivery and Medical Imaging Using Colloidal Lyotropic Liquid Crystalline Dispersions. *J. Colloid Interface Sci.* **2013**, *393*, 1-20.
- (260) Negrini, R.; Mezzenga, R., Diffusion, Molecular Separation, and Drug Delivery from Lipid Mesophases with Tunable Water Channels. *Langmuir* **2012**, *28*, 16455-16462.
- (261) Tanford, C., Micelle Shape and Size. *J. Phys. Chem.* **1972**, *76*, 3020-3024.
- (262) Tanford, C., *The Hydrophobic Effect: Formation of Micelles and Biological Membranes*. 2nd ed.; John Wiley & Sons Limited: Sussex, England, 1980.
- (263) Vlachy, N.; Drechsler, M.; Verbavatz, J.-M.; Touraud, D.; Kunz, W., Role of the Surfactant Headgroup on the Counterion Specificity in the Micelle-to-Vesicle Transition through Salt Addition. *J. Colloid Interface Sci.* **2008**, *319*, 542-548.
- (264) Mondal, J.; Mahanthappa, M.; Yethiraj, A., Self-Assembly of Gemini Surfactants: A Computer Simulation Study. *J. Phys. Chem. B* **2013**, *117*, 4254-4262.
- (265) Berg, J. C., *An Introduction to Interfaces and Colloids*. World Scientific: 2009; p 804.
- (266) Mezzenga, R., Physics of Self-Assembly of Lyotropic Liquid Crystals. In *Self-Assembled Supramolecular Architectures: Lyotropic Liquid Crystals*, Garti, N.; Somasundaran, P.; Mezzenga, R., Eds. John Wiley & Sons, Inc.: Hoboken, NJ, 2012; pp 1-20.
- (267) Kato, T.; Mizoshita, N.; Kishimoto, K., Functional Liquid-Crystalline Assemblies: Self-Organized Soft Materials. *Angew. Chem. Int. Ed.* **2005**, *45*, 38-68.
- (268) Seddon, J. M., Structure of the Inverted Hexagonal (Hii) Phase, and Non-Lamellar Phase Transitions of Lipids. *Biochim. Biophys. Acta* **1990**, *1031*, 1-69.
- (269) Seddon, J. M.; Templer, R. H.; Lipowsky, R.; Sackmann, E., Chapter 3: Polymorphism of Lipid-Water Systems. In *Handbook of Biological Physics*, North Holland (Elsevier): New York, 1995; Vol. Volume 1, Part 1, pp 97-160.
- (270) Zhou, M.; Nemade, P. R.; Lu, X.; Zeng, X.; Hatakeyama, E. S.; Noble, R. D.; Gin, D. L., New Type of Membrane Material for Water Desalination Based on a Cross-Linked Bicontinuous Cubic Lyotropic Liquid Crystal Assembly. *J. Am. Chem. Soc.* **2007**, *129*, 9574-9575.
- (271) Kerr, R. L.; Miller, S. A.; Shoemaker, R. K.; Elliott, B. J.; Gin, D. L., New Type of Li Ion Conductor with 3d Interconnected Nanopores Via Polymerization of a Liquid Organic Electrolyte-Filled Lyotropic Liquid-Crystal Assembly. *J. Am. Chem. Soc.* **2009**, *131*, 15972-15973.
- (272) Clapper, J. D.; Sievens-Figueroa, L.; Guymon, C. A., Photopolymerization in Polymer Templating. *Chem. Mater.* **2008**, *20*, 768-781.
- (273) Davis, M. E., Ordered Porous Materials for Emerging Applications. *Nature* **2002**, *417*, 813-821.
- (274) Wan, Y.; Zhao, D., On the Controllable Soft-Templating Approach to Mesoporous Silicates. *Chem. Rev.* **2007**, *107*, 2821-2860.
- (275) Yaghmur, A.; Glatter, O., Characterization and Potential Applications of Nanostructured Aqueous Dispersions. *Adv. Colloid Interface Sci.* **2009**, *147-148*, 333-342.
- (276) Vargas, R.; Mariani, P.; Gulik, A.; Luzzati, V., Cubic Phases of Lipid-Containing Systems. *J. Mol. Biol.* **1992**, *225*, 137-145.

- (277) Luzzati V, V. R. G. A. M. P. S. J. M.; Rivas, E., Lipid Polymorphism: A Correction. The Structure of the Cubic Phase of Extinction Symbol Fd-Consists of Two Types of Disjointed Reverse Micelles Embedded in a Three-Dimensional Hydrocarbon Matrix. *Biochemistry* **1992**, *31*, 279.
- (278) Seddon, J. M.; Robins, J.; Gulik-Krzywicki, T.; Delacroix, H., Inverse Micellar Phases of Phospholipids and Glycolipids. *Phys. Chem. Chem. Phys.* **2000**, *2*, 4485-4493.
- (279) Percec, V.; Mitchell, C. M.; Cho, W. D.; Uchida, S.; Glodde, M.; Ungar, G.; Zeng, X.; Liu, Y.; Balagurusamy, V. S.; Heiney, P. A., Designing Libraries of First Generation Ab₃ and Ab₂ Self-Assembling Dendrons Via the Primary Structure Generated from Combinations of (Ab)_(Y)-Ab₃ and (Ab)_(Y)-Ab₂ Building Blocks. *J. Am. Chem. Soc.* **2004**, *126*, 6078-94.
- (280) Holerca, M. N.; Sahoo, D.; Peterca, M.; Partridge, B. E.; Heiney, P. A.; Percec, V., A Tetragonal Phase Self-Organized from Unimolecular Spheres Assembled from a Substituted Poly(2-Oxazoline). *Macromolecules* **2017**, *50*, 375-385.
- (281) Percec, V.; Ahn, C. H.; Ungar, G.; Yeardley, D. J. P.; Möller, M.; Sheiko, S. S., Controlling Polymer Shape through the Self-Assembly of Dendritic Side-Groups. *Nature* **1998**, *391*, 161-164.
- (282) Rosen, B. M.; Wilson, D. A.; Wilson, C. J.; Peterca, M.; Won, B. C.; Huang, C.; Lipski, L. R.; Zeng, X.; Ungar, G.; Heiney, P. A.; Percec, V., Predicting the Structure of Supramolecular Dendrimers Via the Analysis of Libraries of Ab₃ and Constitutional Isomeric Ab₂ Biphenylpropyl Ether Self-Assembling Dendrons. *J. Am. Chem. Soc.* **2009**, *131*, 17500-17521.
- (283) Turner, D. C.; Gruner, S. M., X-Ray Diffraction Reconstruction of the Inverted Hexagonal (Hii) Phase in Lipid-Water Systems. *Biochemistry* **1992**, *31*, 1340-1355.
- (284) Anderson, D. M.; Gruner, S. M.; Leibler, S., Geometrical Aspects of the Frustration in the Cubic Phases of Lyotropic Liquid Crystals. *Proc. Natl. Acad. Sci. U.S.A.* **1988**, *85*, 5364.
- (285) Chen, Z.; Rand, R. P., Comparative Study of the Effects of Several N-Alkanes on Phospholipid Hexagonal Phases. *Biophys. J.* **1998**, *74*, 944-952.
- (286) Weber, R. L.; Mahanthappa, M. K., Thiol-Ene Synthesis and Characterization of Lithium Bis(Malonato)Borate Single-Ion Conducting Gel Polymer Electrolytes. *Soft Matter* **2017**, *13*, 7633-7643.
- (287) Petříček, V.; Dušek, M.; Palatinus, L., Crystallographic Computing System Jana2006: General Features. *Z. Kristallogr. Cryst. Mater.* **2014**, *229*, 345-352.
- (288) Palatinus, L.; Chapuis, G., Superflip - a Computer Program for the Solution of Crystal Structures by Charge Flipping in Arbitrary Dimensions. *J. Appl. Crystallogr.* **2007**, *40*, 786-790.
- (289) Sobeck, D. C.; Higgins, M. J., Examination of Three Theories for Mechanisms of Cation-Induced Bioflocculation. *Water Res.* **2002**, *36*, 527-538.
- (290) Barauskas, J.; Cervin, C.; Tiberg, F.; Johnsson, M., Structure of Lyotropic Self-Assembled Lipid Nonlamellar Liquid Crystals and Their Nanoparticles in Mixtures of Phosphatidyl Choline and [Small Alpha]-Tocopherol (Vitamin E). *Phys. Chem. Chem. Phys.* **2008**, *10*, 6483-6485.
- (291) Gibbs, W. J., On the Equilibrium of Heterogeneous Substances. *Transactions of the Connecticut Academy* **1875-78**, *3*, 108-248, 343-524.
- (292) Feinsein, M. E.; Rosano, H. L., The Determination of the Apparent Binding of Counterions to Micelles by Electromotive Force Measurements. *J. Colloid Interface Sci.* **1967**, *24*, 73-79.
- (293) Brun, T. S.; Hoiland, H.; Vikingstad, E., The Fraction of Associated Counterion and Singly Dispersed Amphiphiles in Micellar Systems from Ion Exchange Membrane Electrode Measurements. *J. Colloid Interface Sci.* **1978**, *63*, 590-592.
- (294) Pettitt, B. M.; Rosky, P. J., Alkali Halides in Water: Ion-Solvent Correlations and Ion-Ion Potentials of Mean Force at Infinite Dilution. *J. Chem. Phys.* **1986**, *84*, 5836-5844.
- (295) Jho, Y. S.; Kanduč, M.; Naji, A.; Podgornik, R.; Kim, M. W.; Pincus, P. A., Strong-Coupling Electrostatics in the Presence of Dielectric Inhomogeneities. *Phys. Rev. Lett.* **2008**, *101*, 188101.

- (296) Yamamoto, A., Crystallography of Quasiperiodic Crystals. *Acta Cryst. A* **1996**, *52*, 509-560.
- (297) Ishimasa, T., Dodecagonal Quasicrystals Still in Progress. *Isr. J. Chem.* **2011**, *51*, 1216-1225.
- (298) Torquato, S., Hyperuniform States of Matter. *Phys. Rep.* **2018**, *745*, 1-95.
- (299) Ricouvier, J.; Tabeling, P.; Yazhgur, P., Foam as a Self-Assembling Amorphous Photonic Band Gap Material. *Proc. Natl. Acad. Sci. U.S.A.* **2019**, *116*, 9202-9207.
- (300) Wittlinger, J.; Fischer, R.; Werner, S.; Schneider, J.; Schulz, H., High-Pressure Study of H.C.P.-Argon. *Acta Cryst. B* **1997**, *53*, 745-749.
- (301) Manoharan, V. N., Colloidal Matter: Packing, Geometry, and Entropy. *Science* **2015**, *349*, 1253751.
- (302) Lawson, A. C.; Olsen, C. E.; Richardson, J. J. W.; Mueller, M. H.; Lander, G. H., Structure of B-Uranium. *Acta Cryst. B* **1988**, *44*, 89-96.
- (303) Moseley, P. T.; Seabrook, C. J., The Crystal Structure of B-Tantalum. *Acta Cryst. B* **1973**, *29*, 1170-1171.
- (304) Boles, M. A.; Engel, M.; Talapin, D. V., Self-Assembly of Colloidal Nanocrystals: From Intricate Structures to Functional Materials. *Chem. Rev.* **2016**, *116*, 11220-11289.
- (305) Goodfellow, B. W.; Rasch, M. R.; Hessel, C. M.; Patel, R. N.; Smilgies, D.-M.; Korgel, B. A., Ordered Structure Rearrangements in Heated Gold Nanocrystal Superlattices. *Nano Lett.* **2013**, *13*, 5710-5714.
- (306) Chen, L.; Lee, H. S.; Lee, S., Close-Packed Block Copolymer Micelles Induced by Temperature Quenching. *Proc. Natl. Acad. Sci. U.S.A.* **2018**, *115*, 7218-7223.
- (307) Percec, V.; Peterca, M.; Tsuda, Y.; Rosen, B. M.; Uchida, S.; Imam, M. R.; Ungar, G.; Heiney, P. A., Elucidating the Structure of the Pm3(-)N Cubic Phase of Supramolecular Dendrimers through the Modification of Their Aliphatic to Aromatic Volume Ratio. *Chem. Eur. J.* **2009**, *15*, 8994-9004.
- (308) Kim, K.; Arora, A.; Lewis, R. M.; Liu, M.; Li, W.; Shi, A.-C.; Dorfman, K. D.; Bates, F. S., Origins of Low-Symmetry Phases in Asymmetric Diblock Copolymer Melts. *Proc. Natl. Acad. Sci. U.S.A.* **2018**, *115*, 847-854.
- (309) Huang, M.; Hsu, C.-H.; Wang, J.; Mei, S.; Dong, X.; Li, Y.; Li, M.; Liu, H.; Zhang, W.; Aida, T.; Zhang, W.-B.; Yue, K.; Cheng, S. Z. D., Selective Assemblies of Giant Tetrahedra Via Precisely Controlled Positional Interactions. *Science* **2015**, *348*, 424-428.
- (310) Hajiw, S.; Pansu, B.; Sadoc, J.-F., Evidence for a C14 Frank-Kasper Phase in One-Size Gold Nanoparticle Superlattices. *ACS Nano* **2015**, *9*, 8116-8121.
- (311) Talapin, D. V.; Shevchenko, E. V.; Bodnarchuk, M. I.; Ye, X.; Chen, J.; Murray, C. B., Quasicrystalline Order in Self-Assembled Binary Nanoparticle Superlattices. *Nature* **2009**, *461*, 964-967.
- (312) Clerc, M., A New Symmetry for the Packing of Amphiphilic Direct Micelles. *J. Phys. II* **1996**, *6*, 961-968.
- (313) Fall, S.; Pattier, B.; Benyayia, L.; Gibaud, A., Binary Phase Diagram of Water/Brij58 Studied by Saxs. *Acta Phys. Pol., A* **2012**, *121*, 388-396.
- (314) L Tan, A.; Che Rose, L.; Suhaimi, H.; Ng, D., Association Behavior of Polyoxyethylene (20) Cetyl Ether (Brij 58) and Polyoxyethylene (20) Sorbitan Monooleate (Tween 80) with Polyoxyethylene (4) Lauryl Ether (Brij 30). *J. Sci. Technol.* **2009**, *1*, 1-12.
- (315) Sandler, S. I., *Chemical and Engineering Thermodynamics*. 3 ed.; John Wiley & Sons: Hoboken, 1999.
- (316) Choi, S.-H.; Bates, F. S.; Lodge, T. P., Molecular Exchange in Ordered Diblock Copolymer Micelles. *Macromolecules* **2011**, *44*, 3594-3604.
- (317) Milner, S. T., Polymer Brushes. *Science* **1991**, *251*, 905-914.

- (318) Dormidontova, E. E., Role of Competitive Peo–Water and Water–Water Hydrogen Bonding in Aqueous Solution Peo Behavior. *Macromolecules* **2002**, *35*, 987-1001.
- (319) Mai, Y.; Eisenberg, A., Self-Assembly of Block Copolymers. *Chem. Soc. Rev.* **2012**, *41*, 5969-5985.
- (320) Park, M. J.; Bang, J.; Harada, T.; Char, K.; Lodge, T. P., Epitaxial Transitions among Fcc, Hcp, Bcc, and Cylinder Phases in a Block Copolymer Solution. *Macromolecules* **2004**, *37*, 9064-9075.
- (321) Mariani, P.; Amaral, L., Q. ; Saturni, L.; Delacroix, H., Hexagonal-Cubic Phase Transitions in Lipid Containing Systems : Epitaxial Relationships and Cylinder Growth. *J. Phys. II* **1994**, *4*, 1393-1416.
- (322) Reddy, A.; Buckley, M. B.; Arora, A.; Bates, F. S.; Dorfman, K. D.; Grason, G. M., Stable Frank–Kasper Phases of Self-Assembled, Soft Matter Spheres. *Proc. Natl. Acad. Sci. U.S.A.* **2018**.
- (323) Polya, G., Induction and Analogy in Mathematics. In *Mathematics and Plausible Reasoning*, Princeton University Press: Princeton, 1954; Vol. I, pp 168-189.
- (324) Jung, H. Y.; Kim, O.; Park, M. J., Ion Transport in Nanostructured Phosphonated Block Copolymers Containing Ionic Liquids. *Macromol. Rapid Commun.* **2016**, *37*, 1116-1123.
- (325) Threlfall, T., Structural and Thermodynamic Explanations of Ostwald's Rule. *Org. Process Res. Dev.* **2003**, *7*, 1017-1027.
- (326) Callister, W. D.; Rethwisch, D. G., *Materials Science and Engineering: An Introduction*. 7th ed.; John Wiley & Sons: Quebecor, 2007.
- (327) Choi, S.-H.; Lodge, T. P.; Bates, F. S., Mechanism of Molecular Exchange in Diblock Copolymer Micelles: Hypersensitivity to Core Chain Length. *Phys. Rev. Lett.* **2010**, *104*, 047802.
- (328) Hamley, I. W., Concentrated Solutions. In *Block Copolymers in Solution: Fundamentals and Applications*, First ed.; John Wiley & Sons, Ltd: 2012; pp 105-172.
- (329) Sorenson, G. P.; Coppage, K. L.; Mahanthappa, M. K., Unusually Stable Aqueous Lyotropic Gyroid Phases from Gemini Dicarboxylate Surfactants. *J. Am. Chem. Soc.* **2011**, *133*, 14928-14931.
- (330) Gin, D. L.; Bara, J. E.; Noble, R. D.; Elliott, B. J., Polymerized Lyotropic Liquid Crystal Assemblies for Membrane Applications. *Macromol. Rapid Commun.* **2008**, *29*, 367-389.
- (331) Boyle, B. M.; French, T. A.; Pearson, R. M.; McCarthy, B. G.; Miyake, G. M., Structural Color for Additive Manufacturing: 3d-Printed Photonic Crystals from Block Copolymers. *ACS Nano* **2017**, *11*, 3052-3058.
- (332) Lawson, A. C.; Olsen, C. E.; Richardson, J. W., Jnr; Mueller, M. H.; Lander, G. H., Structure of [Beta]-Uranium. *Acta Cryst. B* **1988**, *44*, 89-96.
- (333) Kim, J.; Jung, H. Y.; Park, M. J., End-Group Chemistry and Junction Chemistry in Polymer Science: Past, Present, and Future. *Macromolecules* **2020**, *53*, 746-763.
- (334) Pujar, V. V.; Cawley, J. D., Effect of Stacking Faults on the X-Ray Diffraction Profiles of B-Sic Powders. *J. Am. Ceram. Soc.* **1995**, *78*, 774-782.
- (335) Jo, G.; Ahn, H.; Park, M. J., Simple Route for Tuning the Morphology and Conductivity of Polymer Electrolytes: One End Functional Group Is Enough. *ACS Macro Lett.* **2013**, *2*, 990-995.
- (336) Jung, H. Y.; Mandal, P.; Jo, G.; Kim, O.; Kim, M.; Kwak, K.; Park, M. J., Modulating Ion Transport and Self-Assembly of Polymer Electrolytes Via End-Group Chemistry. *Macromolecules* **2017**, *50*, 3224-3233.
- (337) Jung Ha, Y.; Kim, O.; Park Moon, J., Ion Transport in Nanostructured Phosphonated Block Copolymers Containing Ionic Liquids. *Macromol. Rapid Commun.* **2016**, *37*, 1116-1123.
- (338) Ito, K.; Nishina, N.; Ohno, H., High Lithium Ionic Conductivity of Poly(Ethylene Oxide)S Having Sulfonate Groups on Their Chain Ends. *J. Mater. Chem.* **1997**, *7*, 1357-1362.

- (339) Schädler, V.; Wiesner, U., Salt-Controlled Lamellar Spacing in Ionically End-Capped Symmetric Diblock Copolymers. *Macromolecules* **1997**, *30*, 6698-6701.
- (340) Schädler, V.; Kniese, V.; Thurn-Albrecht, T.; Wiesner, U.; Spiess, H. W., Self-Assembly of Ionically End-Capped Diblock Copolymers. *Macromolecules* **1998**, *31*, 4828-4837.
- (341) Yoshida, K.; Tanaka, S.; Yamamoto, T.; Tajima, K.; Borsali, R.; Isono, T.; Satoh, T., Chain-End Functionalization with a Saccharide for 10 Nm Microphase Separation: "Classical" Ps-B-Pmma Versus Ps-B-Pmma-Saccharide. *Macromolecules* **2018**, *51*, 8870-8877.
- (342) Jeong, U.; Ryu, D. Y.; Kim, J. K., Phase Behavior of Polystyrene-Block-Poly(N-Butyl Methacrylate) Copolymers with Various End-Functional Groups. *Macromolecules* **2003**, *36*, 8913-8918.
- (343) Jeong, K.-J.; Yethiraj, A., The Driving Force for the Association of Gemini Surfactants. *J. Phys. Chem. B* **2018**, *122*, 3259-3265.
- (344) Lebedeva, N. V.; Shahine, A.; Bales, B. L., Aggregation Number-Based Degrees of Counterion Dissociation in Sodium N-Alkyl Sulfate Micelles. *J. Phys. Chem. B* **2005**, *109*, 19806-19816.
- (345) Jackson, G. L.; Kim, S. A.; Jayaraman, A.; Diallo, S. O.; Mahanthappa, M. K., Consequences of Convex Nanopore Chemistry on Confined Water Dynamics. *J. Phys. Chem. B* **2020**, *124*, 1495-1508.
- (346) Koppi, K. A.; Tirrell, M.; Bates, F. S.; Almdal, K.; Mortensen, K., Epitaxial Growth and Shearing of the Body Centered Cubic Phase in Diblock Copolymer Melts. *J. Rheol.* **1994**, *38*, 999-1027.
- (347) Cox, S. J.; Graner, F.; Mosseri, R.; Sadoc, J. F., Quasicrystalline Three-Dimensional Foams. *J. Phys.: Condens. Matter* **2017**, *29*, 114001.
- (348) Shevchenko, E. V.; Talapin, D. V.; Kotov, N. A.; O'Brien, S.; Murray, C. B., Structural Diversity in Binary Nanoparticle Superlattices. *Nature* **2006**, *439*, 55-59.
- (349) Talapin, D. V.; Shevchenko, E. V.; Bodnarchuk, M. I.; Ye, X.; Chen, J.; Murray, C. B., Quasicrystalline Order in Self-Assembled Binary Nanoparticle Superlattices. *Nature* **2009**, *461*, 964-967.
- (350) Yeh, S.-W.; Wei, K.-H.; Sun, Y.-S.; Jeng, U. S.; Liang, K. S., Morphological Transformation of Ps-B-PeO Diblock Copolymer by Selectively Dispersed Colloidal Cds Quantum Dots. *Macromolecules* **2003**, *36*, 7903-7907.
- (351) Bockstaller, M.; Kolb, R.; Thomas, E. L., Metallodielectric Photonic Crystals Based on Diblock Copolymers. *Adv. Mater.* **2001**, *13*, 1783-1786.

Appendix 1.
Supporting Information for Chapter 2: Counterion-Dependent Access to Low-Symmetry Lyotropic Sphere Packings of Ionic Surfactant Micelles

Reprinted from Jayaraman A. & Mahanthappa M. K., *Langmuir* **2018**, *34*, 2290-2301.

©American Chemical Society, 2018

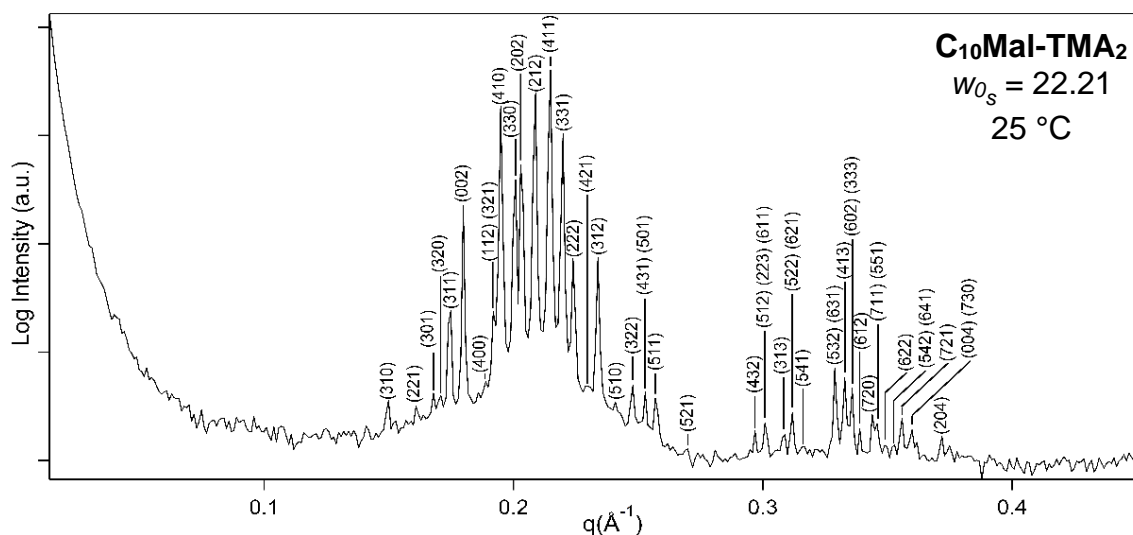


Figure A1.1 Fully indexed lyotropic s phase formed by C₁₀Mal-TMA₂ with $w_{0s} = 22.21$ at 25 °C shown in Figure 3.2A. The complete assignment of the Miller indices for the observed reflections are explicitly tabulated in Table A1.1.

Table A1.1. List of the observed and calculated peak positions for Frank-Kasper σ phase of **C₁₀Mal-TMA₂** with $w_{0_s} = 22.21$ at 25 °C using the tetragonal space group symmetry $P4_2/mnm$ (#136) and unit cell parameters $a = 13.30$ nm and $c = 6.99$ nm.

For a tetragonal lattice, the scattering wavevector modulus is given by:

$$q^2 = (2\pi)^2 \left(\frac{h^2 + k^2}{a^2} + \frac{l^2}{c^2} \right)$$

Miller Indices			%Residual		
(h	k	l)	q_{calc} (1/Å)	q_{obs} (1/Å)	$(\Delta q/q_{\text{calc}} \times 100)$
3	1	0	0.1494	0.1499	-0.41
2	2	1	0.1610	0.1609	0.07
3	0	1	0.1678	0.1679	-0.09
3	2	0	0.1703	0.1709	-0.46
3	1	1	0.1743	0.1749	-0.45
0	0	2	0.1797	0.1799	-0.14
4	0	0	0.1889	0.1889	0.01
1	1	2	0.1917	0.1919	-0.13
3	2	1	0.1925	0.1919	0.48
4	1	0	0.1947	0.1949	-0.13
3	3	0	0.2004	0.2009	-0.39
2	0	2	0.2030	0.2029	0.10
2	1	2	0.2085	0.2089	-0.34
4	1	1	0.2145	0.2149	-0.33
3	3	1	0.2196	0.2199	-0.22
2	2	2	0.2239	0.2239	0.02
4	2	1	0.2295	0.2294	0.10
3	1	2	0.2337	0.2339	-0.17
5	1	0	0.2408	0.2409	-0.06
3	2	2	0.2476	0.2479	-0.24
4	3	1	0.2527	0.2529	-0.18
5	0	1	0.2527	0.2529	-0.18
5	1	1	0.2570	0.2569	0.10
5	2	1	0.2697	0.2699	-0.12
4	3	2	0.2968	0.2969	-0.11
5	1	2	0.3005	0.3009	-0.31
2	2	3	0.3009	0.3009	-0.03
6	1	1	0.3010	0.3009	0.08
3	1	3	0.3082	0.3089	-0.53

5	2	2	0.3114	0.3119	-0.36
6	2	1	0.3119	0.3119	0.02
5	4	1	0.3155	0.3159	-0.31
6	3	0	0.3168	-	-
5	3	2	0.3288	0.3289	-0.04
6	3	1	0.3293	0.3289	0.31
4	1	3	0.3326	0.3329	-0.26
7	1	0	0.3340	-	-
5	5	0	0.3340	-	-
6	0	2	0.3356	0.3359	-0.26
3	3	3	0.3359	0.3359	-0.01
6	1	2	0.3389	0.3389	-0.03
7	2	0	0.3438	0.3439	-0.05
7	1	1	0.3458	0.3459	-0.05
5	5	1	0.3458	0.3459	-0.05
6	2	2	0.3486	0.3489	-0.22
5	4	2	0.3518	0.3519	-0.09
6	4	1	0.3522	0.3519	0.25
7	2	1	0.3554	0.3559	-0.39
0	0	4	0.3594	0.3599	-0.35
7	3	0	0.3597	0.3599	-0.16
5	1	3	0.3615	-	-
2	0	4	0.3716	0.3719	-0.19

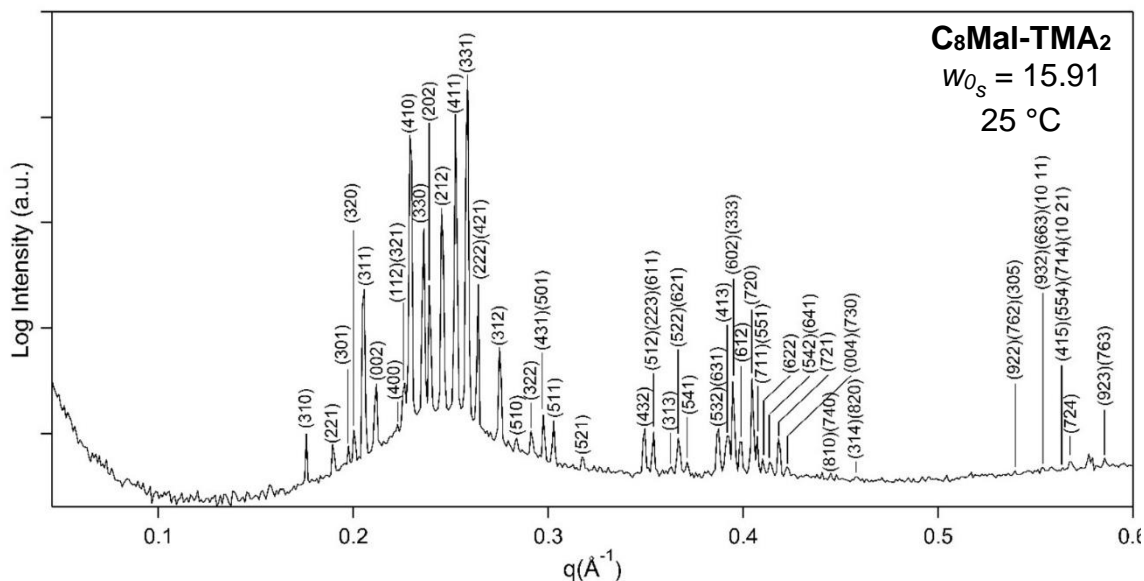


Figure A1.2 An enlarged and fully indexed SWAXS pattern for the σ phase formed by **C₈Mal-TMA₂** with $w_{0s} = 15.91$ at 25 °C shown in Figure 3A. The complete assignment of the Miller indices for the observed reflections are explicitly tabulated in Table A1.2.

Table A1.2. List of the observed and calculated peak positions for Frank-Kasper σ phase of **C₈Mal-TMA₂** with $w_{0s} = 15.91$ at 25 °C using the tetragonal space group symmetry $P4_2/mnm$ (#136) and unit cell parameters $a = 11.41$ nm and $c = 5.99$ nm.

For a tetragonal lattice, the scattering wavevector modulus is given by:

$$q^2 = (2\pi)^2 \left(\frac{h^2 + k^2}{a^2} + \frac{l^2}{c^2} \right)$$

Miller Indices					% Residual
(h	k	l)	q_{calc} (1/Å)	q_{obs} (1/Å)	($\Delta q/q_{\text{calc}} \times 100$)
3	1	0	0.1741	0.1743	-0.11
2	2	1	0.1878	0.1875	0.13
3	0	1	0.1957	0.1953	0.18
3	2	0	0.1986	0.1983	0.13

3	1	1	0.2033	0.2031	0.09
0	0	2	0.2097	0.2097	0.00
4	0	0	0.2203	0.2205	-0.10
1	1	2	0.2237	0.2235	0.10
3	2	1	0.2245	0.2247	-0.08
4	1	0	0.2271	0.2271	0.00
3	3	0	0.2336	0.2336	0.00
2	0	2	0.2368	0.2366	0.09
2	1	2	0.2432	0.2432	-0.03
4	1	1	0.2501	0.2498	0.11
3	3	1	0.2561	0.2558	0.11
2	2	2	0.2612	0.2612	0.00
4	2	1	0.2677	0.2678	-0.05
3	1	2	0.2726	0.2726	-0.01
5	1	0	0.2808	0.2810	-0.06
3	2	2	0.2888	0.2888	0.00
4	3	1	0.2946	0.2947	-0.04
5	0	1	0.2946	0.2947	-0.04
5	1	1	0.2997	0.2995	0.06
5	2	1	0.3145	0.3145	0.01
4	3	2	0.3461	0.3463	-0.05
5	1	2	0.3504	0.3505	-0.01
2	2	3	0.3510	0.3505	0.15
6	1	1	0.3510	0.3505	0.15
3	1	3	0.3595	0.3594	0.02
5	2	2	0.3632	0.3630	0.04
6	2	1	0.3637	0.3630	0.19
5	4	1	0.3679	0.3678	0.01
6	3	0	0.3694	-	-
5	3	2	0.3835	0.3834	0.02
6	3	1	0.3840	0.3834	0.15
4	1	3	0.3879	0.3876	0.08
7	1	0	0.3894	0.3894	0.00
5	5	0	0.3894	0.3894	0.00
6	0	2	0.3913	0.3912	0.03
3	3	3	0.3918	0.3912	0.15
6	1	2	0.3952	0.3948	0.10
7	2	0	0.4009	0.4014	-0.12
7	1	1	0.4033	0.4032	0.02
5	5	1	0.4033	0.4032	0.02
6	2	2	0.4065	0.4068	-0.06
5	4	2	0.4102	0.4104	-0.03

6	4	1	0.4107	0.4104	0.08
7	2	1	0.4144	0.4146	-0.04
0	0	4	0.4194	0.4194	-0.01
7	3	0	0.4194	0.4194	-0.01
5	1	3	0.4216	-	-
2	0	4	0.4336	-	-
2	1	4	0.4371	-	-
8	1	0	0.4440	0.4439	0.01
7	4	0	0.4440	0.4439	0.01
3	1	4	0.4541	0.4541	-0.01
8	2	0	0.4541	0.4541	0.00
9	2	2	0.5493	0.5494	-0.01
7	6	2	0.5493	0.5494	-0.01
3	0	5	0.5496	0.5494	0.05
3	1	5	0.5524	-	-
8	2	3	0.5524	-	-
9	4	1	0.5524	-	-
9	3	2	0.5629	0.5631	-0.04
6	6	3	0.5633	0.5631	0.02
10	1	1	0.5633	0.5631	0.02
4	1	5	0.5713	0.5721	-0.15
10	2	1	0.5713	0.5721	-0.15
7	1	4	0.5723	0.5721	0.02
5	5	4	0.5723	0.5721	0.02
7	2	4	0.5802	0.5799	0.04
9	2	3	0.5972	0.5973	-0.01
7	6	3	0.5972	0.5973	-0.01
8	2	4	0.6181	-	-

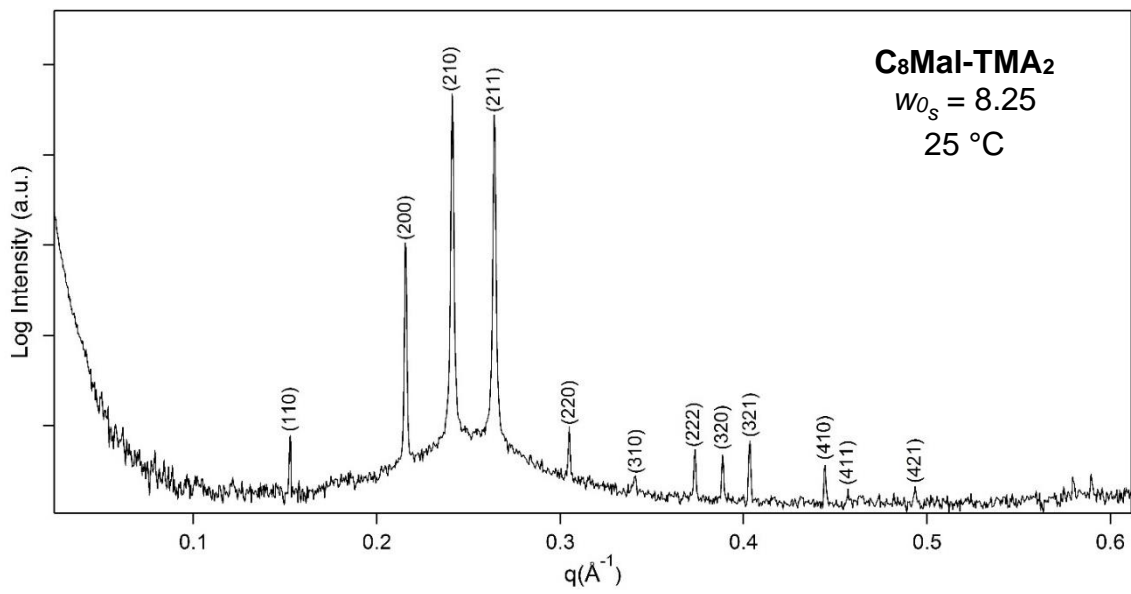


Figure A1.3. An enlarged and indexed SWAXS pattern for the A15 phase ($Pm\bar{3}(-)n$ symmetry) formed by **C₈Mal-TMA₂** with $w_{0s} = 8.25$ at 25 °C shown in Figure 2.3A.

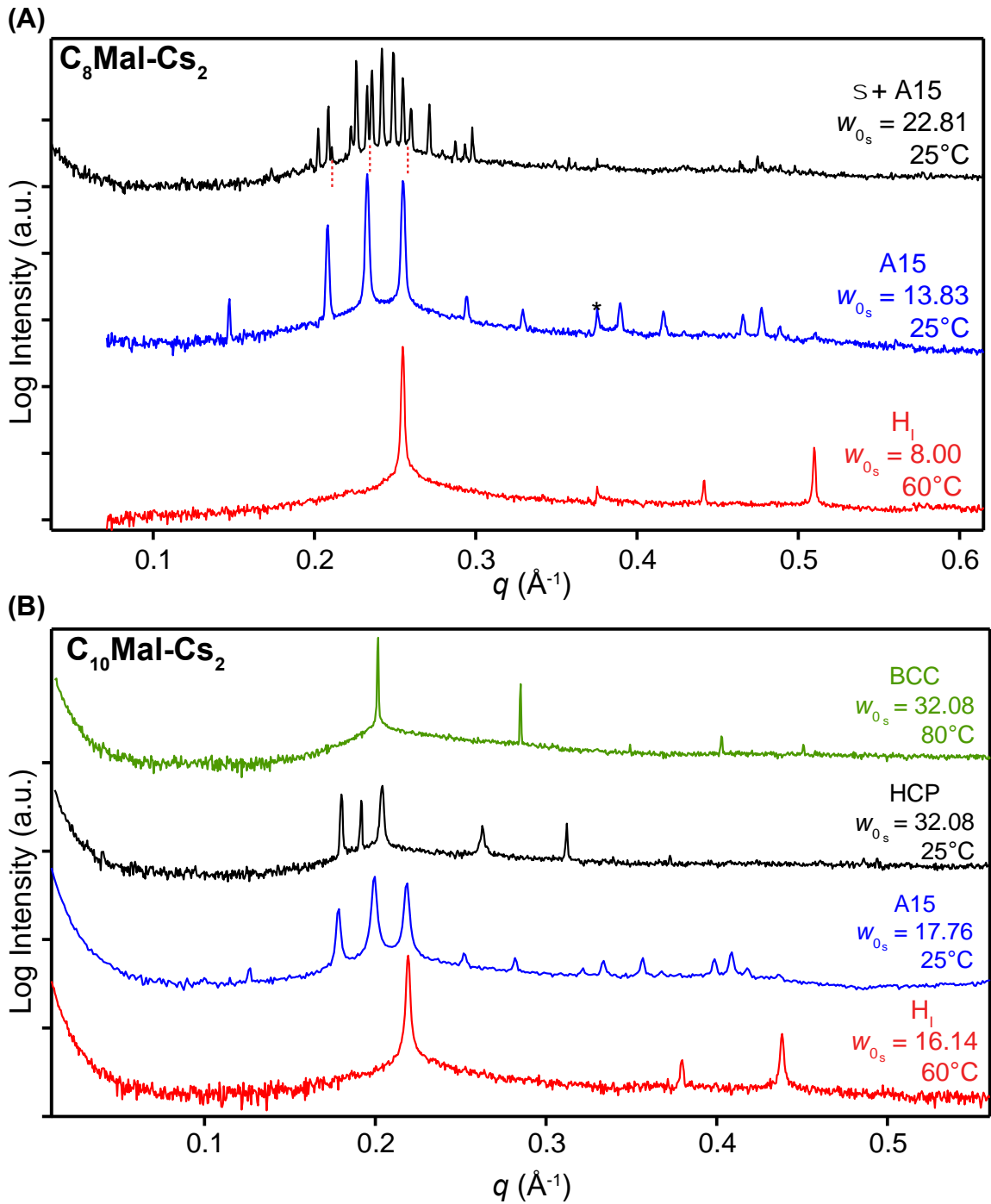


Figure A1.4 (A) Synchrotron SWAXS powder patterns illustrating the formation of the H₁, A15 and σ /A15 coexisting phases for C₈Mal-Cs₂. The red dashed lines indicate the peaks corresponding to the A15 phase that coexists with the σ phase observed at $w_{0s} = 22.81$. (B) Synchrotron SWAXS

powder patterns illustrating the formation of the H_i, A15, HCP and BCC phases for C₁₀Mal-Cs₂. (* marks a detector artifact arising from an errant pixel)

***SUPERFLIP* Input File for C₈Mal-TMA₂ A15 Phase ($w_{\theta_s} = 8.25$) Charge-Flipping Electron**

Density Reconstruction

The one-dimensional SAXS intensity $I(q)$ versus scattering wavevector q profile for the A15 phase with $w_{\theta_s} = 8.25$ (Fig. 2.3A) was scaled by multiplying the q values by 2, to halve the size of the unit cell to expedite the calculation and rendering of the electron density map with limited computing resources. Le Bail refinement of the scaled SAXS data with a fifth-order polynomial fit for the X-ray background using the *JANA2006* crystallographic computing software package²⁸⁷ enabled extraction of the static structure factor intensities for each peak in the pattern in the range $q = 0.275\text{--}0.987 \text{ \AA}^{-1}$ (in the scaled pattern), the Miller indices of which were assigned using the *Pm3(-)n* space group symmetry with a scaled cubic unit cell parameter $a = 2.915 \text{ nm}$. The structure factor intensities associated with each indexed SAXS peak are given in the text file below. Application of the *SUPERFLIP* charge-flipping algorithm²⁸⁸ using the input file below in 7000 trials yielded 141 converged electron density maps with excellent figures of merit $fm = 2$, starting from randomized initial conditions. The 141 converged maps were averaged and rendered using the VESTA software package⁶⁷ to yield the 90% isosurface electron density maps shown in Figure 2.6A.

```
*****start_file*****
*****
title SAJ58_8_25C_00437_Superflip
perform CF
outputfile "SAJ58_8_25C_00437_Superflip.m81"
"SAJ58_8_25C_00437_Superflip.m80"
outputformat jana
dimension 3
```

```

cell      29.1532   29.1532   29.1532   90.00   90.00   90.00
spacegroup Pm-3n
centro yes
centers
  0.000000  0.000000  0.000000
endcenters
symmetry
  x1      x2      x3
  -x1     -x2     x3
  -x1     x2      -x3
  x1      -x2     -x3
  x3      x1      x2
  x3      -x1     -x2
  -x3     -x1     x2
  -x3     x1      -x2
  x2      x3      x1
  -x2     x3      -x1
  x2      -x3     -x1
  -x2     -x3     x1
  x2+1/2  x1+1/2  -x3+1/2
  -x2+1/2 -x1+1/2  -x3+1/2
  x2+1/2  -x1+1/2  x3+1/2
  -x2+1/2  x1+1/2  x3+1/2
  x1+1/2  x3+1/2  -x2+1/2
  -x1+1/2  x3+1/2  x2+1/2
  -x1+1/2 -x3+1/2  -x2+1/2
  x1+1/2  -x3+1/2  x2+1/2
  x3+1/2  x2+1/2  -x1+1/2
  x3+1/2  -x2+1/2  x1+1/2
  -x3+1/2  x2+1/2  x1+1/2
  -x3+1/2 -x2+1/2  -x1+1/2
  -x1     -x2     -x3
  x1      x2     -x3
  x1     -x2     x3
  -x1     x2     x3
  -x3     -x1     -x2
  -x3     x1     x2
  x3      x1     -x2
  x3     -x1     x2
  -x2     -x3     -x1
  x2     -x3     x1
  -x2     x3     x1
  x2      x3     -x1
  -x2+1/2 -x1+1/2  x3+1/2
  x2+1/2  x1+1/2  x3+1/2
  -x2+1/2  x1+1/2  -x3+1/2
  x2+1/2  -x1+1/2  -x3+1/2
  -x1+1/2 -x3+1/2  x2+1/2

```

```

    x1+1/2 -x3+1/2 -x2+1/2
    x1+1/2  x3+1/2  x2+1/2
-x1+1/2  x3+1/2 -x2+1/2
-x3+1/2 -x2+1/2  x1+1/2
-x3+1/2  x2+1/2 -x1+1/2
  x3+1/2 -x2+1/2 -x1+1/2
  x3+1/2  x2+1/2  x1+1/2
endsymmetry
composition C779 H1722 N82 O164

# Keywords for charge flipping
repeatmode 7000 sumgood
bestdensities 1 symmetry
polish yes
maxcycles 2000
delta AUTO
weakratio 0.000
Biso 0.000
randomseed AUTO
searchsymmetry average
derivesymmetry no
# End of keywords for charge flipping
# EDMA-specific keywords
inputfile SAJ58_8_25C_00437_Superflip.m81
outputbase SAJ58_8_25C_00437_Superflip
m40forjana yes
writem40 SAJ58_8_25C_00437_Superflip_tmp.m40
maxima all
fullcell no
scale fractional
plimit 0.3000 sigma
numberofatoms composition
centerofcharge yes
chlimit 0.2500
chlimlist 0.0375 relative
# End of EDMA-specific keywords
electrons 0.0000
dataitemwidths 4 15 15
dataformat intensity fwhm
fbegin
  1 0 1 48.1023 0.0119
  0 0 2 4416.5166 0.0139
  1 0 2 10000.0020 0.0149
  1 1 2 7548.6899 0.0158
  2 0 2 237.9617 0.0177
  1 0 3 33.1641 0.0194
  2 2 2 343.9158 0.0211
  2 0 3 125.9443 0.0219

```


2	1	3	99.1154	0.0227
0	0	4	67.2860	0.0242
1	0	4	129.3323	0.0249
1	1	4	18.0229	0.0256
3	0	3	18.0229	0.0256
2	0	4	6.1415	0.0270

endf

***SUPERFLIP* Input File for C₈Mal-K₂ A15 Phase ($w_{\theta_s} = 9.85$) Charge-Flipping Electron**

Density Reconstruction

The one-dimensional SAXS intensity $I(q)$ versus scattering wavevector q profile for the A15 phase with $w_{\theta_s} = 9.85$ (Fig. 2.4A) was scaled by multiplying the q values by 2, to halve the size of the unit cell to expedite the calculation and rendering of the electron density map with limited computing resources. Le Bail refinement of the scaled SAXS data with a fifth-order polynomial fit for the X-ray background using the *JANA2006* crystallographic computing software package²⁸⁷ enabled extraction of the static structure factor intensities for each peak in the pattern in the range $q = 0.252\text{--}0.980 \text{ \AA}^{-1}$ (in the scaled pattern), the Miller indices of which were assigned using the *Pm3(-)n* space group symmetry with a scaled cubic unit cell parameter $a = 3.140 \text{ nm}$. The structure factor intensities associated with each indexed SAXS peak are given in the text file below. Application of the *SUPERFLIP* charge-flipping algorithm²⁸⁸ using the input file below in 10000 trials yielded one (1) converged electron density map with excellent figure of merit $fm = 2$, starting from randomized initial conditions. Upon conducting independent trials to validate this convergence, 10 independent convergences yielded the same electron density map and linear electron density profile shown in Figure 6A. The electron density map was rendered using the *VESTA*⁶⁷ software package to yield the 90% isosurface electron density map shown in Figure 2.6A.

```
*****startfile*****
*****
title SAJ_KE_1_01195_Superflip
```

```

perform CF
outputfile "SAJ_KE_1_01195_Superflip.m81"
"SAJ_KE_1_01195_Superflip.m80"
outputformat jana
dimension 3
cell 31.4045 31.4045 31.4045 90.00 90.00 90.00
spacegroup Pm-3n
centro yes
centers
0.000000 0.000000 0.000000
endcenters
symmetry
x1 x2 x3
-x1 -x2 x3
-x1 x2 -x3
x1 -x2 -x3
x3 x1 x2
x3 -x1 -x2
-x3 -x1 x2
-x3 x1 -x2
x2 x3 x1
-x2 x3 -x1
x2 -x3 -x1
-x2 -x3 x1
x2+1/2 x1+1/2 -x3+1/2
-x2+1/2 -x1+1/2 -x3+1/2
x2+1/2 -x1+1/2 x3+1/2
-x2+1/2 x1+1/2 x3+1/2
x1+1/2 x3+1/2 -x2+1/2
-x1+1/2 x3+1/2 x2+1/2
-x1+1/2 -x3+1/2 -x2+1/2
x1+1/2 -x3+1/2 x2+1/2
x3+1/2 x2+1/2 -x1+1/2
x3+1/2 -x2+1/2 x1+1/2
-x3+1/2 x2+1/2 x1+1/2
-x3+1/2 -x2+1/2 -x1+1/2
-x1 -x2 -x3
x1 x2 -x3
x1 -x2 x3
-x1 x2 x3
-x3 -x1 -x2
-x3 x1 x2
x3 x1 -x2
x3 -x1 x2
-x2 -x3 -x1
x2 -x3 x1
-x2 x3 x1
x2 x3 -x1

```

```

-x2+1/2 -x1+1/2  x3+1/2
  x2+1/2  x1+1/2  x3+1/2
-x2+1/2  x1+1/2 -x3+1/2
  x2+1/2 -x1+1/2 -x3+1/2
-x1+1/2 -x3+1/2  x2+1/2
  x1+1/2 -x3+1/2 -x2+1/2
  x1+1/2  x3+1/2  x2+1/2
-x1+1/2  x3+1/2 -x2+1/2
-x3+1/2 -x2+1/2  x1+1/2
-x3+1/2  x2+1/2 -x1+1/2
  x3+1/2 -x2+1/2 -x1+1/2
  x3+1/2  x2+1/2  x1+1/2
endsymmetry
composition C704 H1152 O256 K128

# Keywords for charge flipping
repeatmode 10000 sumgood
bestdensities 1 symmetry
polish yes
maxcycles 500
delta AUTO
weakratio 0.000
Biso 0.000
randomseed AUTO
searchsymmetry average
derivesymmetry no
# End of keywords for charge flipping

# EDMA-specific keywords
inputfile SAJ_KE_1_01195_Superflip.m81
outputbase SAJ_KE_1_01195_Superflip
m40forjana yes
writem40 SAJ_KE_1_01195_Superflip_tmp.m40
maxima all
fullcell no
scale fractional
plimit 0.3000 sigma
numberofatoms composition
centerofcharge yes
chlimit 0.2500
chlimlist 0.0158 relative
# End of EDMA-specific keywords

electrons 0.0000
dataitemwidths 4 15 15
dataformat intensity fwhm
fbegin
  1 0 1 59.3664 0.0213

```

```

0 0 2 5784.4746 0.0221
1 0 2 10000.0010 0.0222
1 1 2 8186.2866 0.0222
2 0 2 282.2911 0.0219
1 0 3 122.5843 0.0212
2 2 2 22.9429 0.0199
2 0 3 69.2863 0.0191
2 1 3 102.5215 0.0180
0 0 4 729.6169 0.0212
1 0 4 39.7383 0.0235
3 0 3 20.7672 0.0255
1 1 4 20.7672 0.0255
2 0 4 152.1584 0.0291
2 1 4 142.6972 0.0307
3 2 3 60.6409 0.0322
endf

```

***SUPERFLIP* Input File for C₁₀Mal-TMA₂ σ Phase ($w_{0_s} = 22.21$) Charge-Flipping Electron**

Density Reconstruction

The one-dimensional SAXS intensity $I(q)$ versus scattering wavevector q profile for the σ phase with $w_{0_s} = 22.21$ (Fig. 2.2A) was scaled by multiplying the q values by 2, to halve the size of the unit cell to expedite the calculation and rendering of the electron density map with limited computing resources. Le Bail refinement of the scaled SAXS data with a fifth-order polynomial fit for the X-ray background using the *JANA2006* crystallographic computing software package²⁸⁷ enabled extraction of the static structure factor intensities for each peak in the pattern in the range $q = 0.238\text{--}0.770 \text{ \AA}^{-1}$ (in the scaled pattern), the Miller indices of which were assigned using the *P4₂/mnm* space group symmetry with a scaled cubic unit cell parameter $a = 6.652 \text{ nm}$ and $c = 3.496 \text{ nm}$. The structure factor intensities associated with each indexed SAXS peak are given in the text file below. Application of the *SUPERFLIP* charge-flipping algorithm²⁸⁸ using the input file below in 4000 trials yielded 292 converged electron density maps with excellent figures of merit $fm = 2$, starting from randomized initial conditions. The 292 converged maps were averaged and rendered

using the VESTA⁶⁷ software package to yield the 90% isosurface electron density maps shown in Figure A1.4B.

```
*****start_file*****
*****

title SAJ-TMA10-8_Superflip
perform CF
outputfile "SAJ-TMA10-8_Superflip.m81" "SAJ-TMA10-
8_Superflip.m80"
outputformat jana
dimension 3
cell 66.5184 66.5184 34.9611 90.00 90.00 90.00
spacegroup P42/mnm
centro yes
centers
0.000000 0.000000 0.000000
endcenters
symmetry
x1 x2 x3
-x1 -x2 x3
-x2+1/2 x1+1/2 x3+1/2
x2+1/2 -x1+1/2 x3+1/2
-x1+1/2 x2+1/2 -x3+1/2
x1+1/2 -x2+1/2 -x3+1/2
x2 x1 -x3
-x2 -x1 -x3
-x1 -x2 -x3
x1 x2 -x3
x2+1/2 -x1+1/2 -x3+1/2
-x2+1/2 x1+1/2 -x3+1/2
x1+1/2 -x2+1/2 x3+1/2
-x1+1/2 x2+1/2 x3+1/2
-x2 -x1 x3
x2 x1 x3
endsymmetry
composition C4998 H10948 N476 O952

# Keywords for charge flipping
repeatmode 4000 sumgood
bestdensities 1 symmetry
polish yes
maxcycles 4000
delta AUTO
weakratio 0.000
Biso 0.000
randomseed AUTO
```

```

searchsymmetry average
derivesymmetry no
# End of keywords for charge flipping

# EDMA-specific keywords
inputfile SAJ-TMA10-8_Superflip.m81
outputbase SAJ-TMA10-8_Superflip
m40forjana yes
writem40 SAJ-TMA10-8_Superflip_tmp.m40
maxima all
fullcell no
scale fractional
plimit 0.3000 sigma
numberofatoms composition
centerofcharge yes
chlimit 0.2500
chlimlist 0.0375 relative
# End of EDMA-specific keywords

electrons 0.0000
dataitemwidths 4 15 15
dataformat intensity fwhm
fbegin
  1 1 1 0.2038 0.0115
  2 2 0 7.2878 0.0121
  2 1 1 0.4176 0.0123
  3 1 0 71.1353 0.0127
  2 2 1 53.2817 0.0131
  3 0 1 55.4726 0.0134
  3 2 0 75.5366 0.0135
  3 1 1 358.2316 0.0137
  0 0 2 7450.0386 0.0139
  4 0 0 80.5563 0.0143
  1 1 2 380.1219 0.0144
  3 2 1 69.3071 0.0144
  4 1 0 9417.1016 0.0145
  3 3 0 10000.0000 0.0147
  2 0 2 6228.9229 0.0148
  2 1 2 6366.2324 0.0151
  4 2 0 16.6715 0.0152
  4 1 1 9578.5303 0.0153
  3 3 1 8885.5273 0.0155
  2 2 2 2150.8499 0.0157
  4 2 1 37.7356 0.0159
  3 1 2 1141.1854 0.0161
  4 3 0 24.9408 0.0162
  5 1 0 86.9278 0.0164
  3 2 2 150.7694 0.0167

```

5	0	1	116.0103	0.0169
4	3	1	116.0103	0.0169
5	2	0	0.1008	0.0169
5	1	1	181.6794	0.0171
4	0	2	0.0027	0.0172
4	1	2	0.0000	0.0174
4	4	0	0.0222	0.0175
3	3	2	2.5171	0.0176
5	2	1	24.2033	0.0176
1	0	3	15.4855	0.0177
5	3	0	6.6311	0.0178
4	2	2	5.4700	0.0179
1	1	3	0.0270	0.0179
4	4	1	40.2550	0.0181
6	0	0	0.8251	0.0181
6	1	0	58.3693	0.0183
2	1	3	29.4041	0.0184
5	3	1	7.9099	0.0184
4	3	2	164.7052	0.0187
6	2	0	10.0104	0.0188
5	1	2	154.2364	0.0188
2	2	3	33.4495	0.0188
6	1	1	16.3573	0.0189
5	4	0	6.5387	0.0189
3	0	3	22.3432	0.0190
3	1	3	110.3277	0.0191
5	2	2	232.6027	0.0193
6	2	1	34.5979	0.0193
5	4	1	49.0660	0.0194
6	3	0	48.1068	0.0195
3	2	3	2.6499	0.0196
4	4	2	62.4661	0.0197
5	3	2	715.7497	0.0200
6	3	1	31.5648	0.0200
4	1	3	516.6017	0.0202
7	1	0	128.9243	0.0202
5	5	0	128.9243	0.0202
6	0	2	482.6320	0.0203
3	3	3	531.9822	0.0203
6	1	2	162.3444	0.0204
6	4	0	90.2840	0.0205
4	2	3	18.3578	0.0206
7	0	1	20.9235	0.0206
7	2	0	748.3356	0.0206
7	1	1	186.7782	0.0207
5	5	1	186.7782	0.0207
6	2	2	159.6813	0.0208
5	4	2	101.7562	0.0210

6	4	1	70.8621	0.0210
7	2	1	452.5534	0.0211
5	0	3	51.0302	0.0213
4	3	3	51.0302	0.0213
0	0	4	846.3994	0.0213
7	3	0	313.5696	0.0213
5	1	3	137.1255	0.0214
6	3	2	46.4817	0.0215
1	1	4	132.2244	0.0216
6	5	0	61.2339	0.0217
5	2	3	26.7104	0.0218
7	3	1	20.2528	0.0218
2	0	4	252.4507	0.0218
2	1	4	88.1103	0.0222
8	0	0	256.4077	0.0226
7	1	2	0.0376	0.0227
5	5	2	0.0376	0.0227
4	4	3	0.0438	0.0228
6	5	1	0.0661	0.0228
8	1	0	49.1880	0.0229
7	4	0	49.1880	0.0229
2	2	4	105.7682	0.0233
6	4	2	3.7378	0.0235
5	3	3	63.0263	0.0235
7	2	2	95.0882	0.0238

endf

***SUPERFLIP* Input File for C₈Mal-TMA₂ σ Phase ($w_{0_s} = 15.91$) Charge-Flipping Electron**

Density Reconstruction

The one-dimensional SAXS intensity $I(q)$ versus scattering wavevector q profile for the σ phase with $w_{0_s} = 15.91$ (Fig. 2.3A) was scaled by multiplying the q values by 2, to halve the size of the unit cell to expedite the calculation and rendering of the electron density map with limited computing resources. Le Bail refinement of the scaled SAXS data with a fifth-order polynomial fit for the X-ray background using the *JANA2006* crystallographic computing software package²⁸⁷ enabled extraction of the static structure factor intensities for each peak in the pattern in the range $q = 0.273\text{--}0.923 \text{ \AA}^{-1}$ (in the scaled pattern), the Miller indices of which were assigned using the $P4_2/mnm$ space group symmetry with a scaled cubic unit cell parameter $a = 5.651 \text{ nm}$ and $c = 2.971$

nm. The structure factor intensities associated with each indexed SAXS peak are given in the text file below. Application of the *SUPERFLIP* charge-flipping algorithm²⁸⁸ using the input file below in 4000 trials yielded 362 converged electron density maps with excellent figures of merit $fm = 2$, starting from randomized initial conditions. The 362 converged maps were averaged and rendered using the VESTA⁶⁷ software package to yield the 90% isosurface electron density maps shown in Figure A1.4A.

```

*****start_file*****
*****
title SAJ58_16_25C_00443_Superflip
perform CF
outputfile "SAJ58_16_25C_00443_Superflip.m81"
"SAJ58_16_25C_00443_Superflip.m80"
outputformat jana
dimension 3
cell 56.5148 56.5148 29.7102 90.00 90.00 90.00
spacegroup P42/mnm
centro yes
centers
0.000000 0.000000 0.000000
endcenters
symmetry
x1 x2 x3
-x1 -x2 x3
-x2+1/2 x1+1/2 x3+1/2
x2+1/2 -x1+1/2 x3+1/2
-x1+1/2 x2+1/2 -x3+1/2
x1+1/2 -x2+1/2 -x3+1/2
x2 x1 -x3
-x2 -x1 -x3
-x1 -x2 -x3
x1 x2 -x3
x2+1/2 -x1+1/2 -x3+1/2
-x2+1/2 x1+1/2 -x3+1/2
x1+1/2 -x2+1/2 x3+1/2
-x1+1/2 x2+1/2 x3+1/2
-x2 -x1 x3
x2 x1 x3
endsymmetry
composition C3002 H6636 O632 N316

# Keywords for charge flipping
repeatmode 4000 sumgood

```

```

bestdensities 1 symmetry
polish yes
maxcycles 2000
delta AUTO
weakratio 0.000
Biso 0.000
randomseed AUTO
searchsymmetry average
derivesymmetry no
# End of keywords for charge flipping

# EDMA-specific keywords
inputfile SAJ58_16_25C_00443_Superflip.m81
outputbase SAJ58_16_25C_00443_Superflip
m40forjana yes
writem40 SAJ58_16_25C_00443_Superflip_tmp.m40
maxima all
fullcell no
scale fractional
plimit 0.3000 sigma
numberofatoms composition
centerofcharge yes
chlimit 0.2500
chlimlist 0.0375 relative
# End of EDMA-specific keywords

electrons 0.0000
dataitemwidths 4 15 15
dataformat intensity fwhm
fbegin
  2 2 0 3.7139 0.0110
  2 1 1 3.8207 0.0109
  3 1 0 65.9991 0.0109
  2 2 1 57.7745 0.0108
  3 0 1 19.5204 0.0109
  3 2 0 105.1461 0.0109
  3 1 1 810.3314 0.0109
  0 0 2 1189.7058 0.0110
  4 0 0 28.4895 0.0118
  1 1 2 230.1801 0.0120
  3 2 1 47.0836 0.0120
  4 1 0 6846.5640 0.0122
  3 3 0 5537.5000 0.0127
  2 0 2 2355.3298 0.0129
  2 1 2 2226.9824 0.0134
  4 2 0 50.6479 0.0136
  4 1 1 5375.5039 0.0139
  3 3 1 10000.0000 0.0143

```

2	2	2	1598.3729	0.0147
4	2	1	19.7646	0.0152
3	1	2	484.0770	0.0156
4	3	0	0.0009	0.0159
5	1	0	90.5030	0.0163
3	2	2	94.3868	0.0169
4	3	1	109.5543	0.0174
5	0	1	109.5543	0.0174
5	2	0	0.4284	0.0176
5	1	1	165.3992	0.0179
4	0	2	33.5753	0.0182
4	1	2	23.1097	0.0187
4	4	0	51.3276	0.0189
3	3	2	10.3834	0.0191
5	2	1	62.1465	0.0191
1	0	3	39.0296	0.0195
5	3	0	43.4434	0.0197
4	2	2	23.8418	0.0199
1	1	3	32.7884	0.0199
4	4	1	27.4851	0.0204
6	0	0	74.9350	0.0205
6	1	0	35.5814	0.0209
2	1	3	1.9868	0.0211
5	3	1	3.6960	0.0212
4	3	2	271.3555	0.0219
6	2	0	2.7847	0.0221
5	1	2	134.5132	0.0223
2	2	3	64.0462	0.0223
6	1	1	20.4851	0.0223
5	4	0	0.3713	0.0225
3	0	3	15.4856	0.0227
3	1	3	41.9232	0.0231
5	2	2	113.6496	0.0234
6	2	1	102.6968	0.0235
5	4	1	51.0560	0.0239
6	3	0	6.0724	0.0240
3	2	3	15.1255	0.0242
4	4	2	52.5335	0.0246
5	3	2	346.0588	0.0253
6	3	1	195.8426	0.0254
4	1	3	413.4619	0.0257
5	5	0	157.1811	0.0259
7	1	0	157.1811	0.0259
6	0	2	1027.7227	0.0260
3	3	3	480.3666	0.0261
6	1	2	353.6504	0.0264
6	4	0	100.1017	0.0266
4	2	3	40.2557	0.0268

7	0	1	97.9943	0.0268
7	2	0	1479.3707	0.0269
7	1	1	191.3098	0.0271
5	5	1	191.3098	0.0271
6	2	2	166.5945	0.0274
5	4	2	112.5355	0.0278
6	4	1	60.9397	0.0278
7	2	1	329.1293	0.0282
4	3	3	61.9749	0.0285
5	0	3	61.9749	0.0285
0	0	4	97.6021	0.0286
7	3	0	89.5431	0.0286
5	1	3	67.4138	0.0288
6	3	2	35.5594	0.0291
1	1	4	8.2296	0.0293
6	5	0	0.7451	0.0297
5	2	3	12.6928	0.0298
7	3	1	7.3597	0.0299
2	0	4	55.3165	0.0299
2	1	4	4.6680	0.0303
8	0	0	14.6279	0.0306
7	1	2	3.7538	0.0308
5	5	2	3.7538	0.0308
4	4	3	2.7596	0.0308
6	5	1	3.6227	0.0308
7	4	0	82.0440	0.0310
8	1	0	82.0440	0.0310

endf

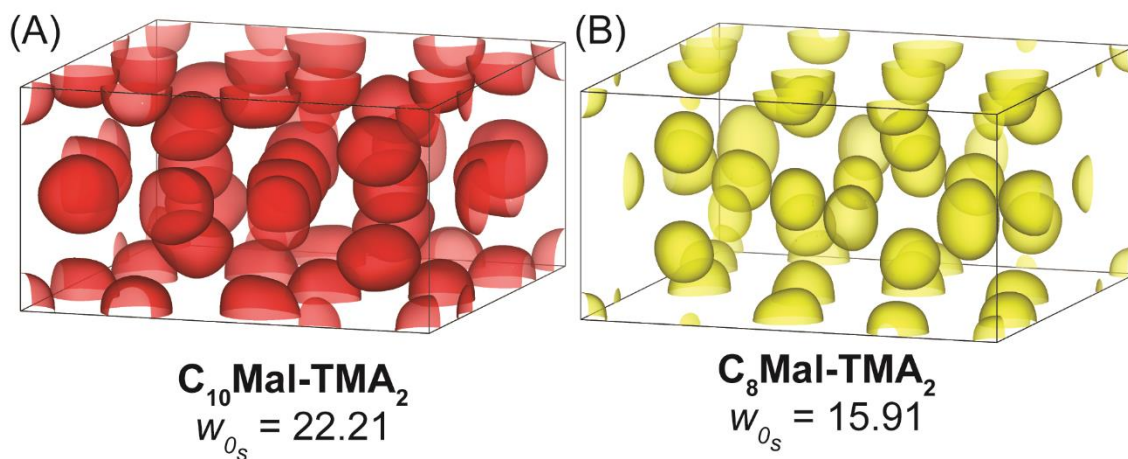


Figure A1.5. (A) 90% isosurface of the electron density reconstruction of the FK σ phase of $\text{C}_{10}\text{Mal-TMA}_2$ at $w_{0s} = 22.21$ at 25 °C. (B) 90% isosurface of the electron density reconstruction of the FK σ phase of $\text{C}_8\text{Mal-TMA}_2$ at $w_{0s} = 15.91$ at 25 °C.

Table A1.3. Key to molecules: Notebook page numbers and APS trips when data were collected

Molecules	Notebook page number	APS trips
$\text{C}_8\text{Mal-TMA}_2$	AJ1-58	August 2016
$\text{C}_8\text{Mal-K}_2$	AJ1-110_MeOH	Oct. (Sector 5ID-D), Dec. 2016
$\text{C}_8\text{Mal-Cs}_2$	AJ1-159	April 2017
$\text{C}_{10}\text{Mal-TMA}_2$	AJ1-137	April, July 2017
$\text{C}_{10}\text{Mal-Cs}_2$	AJ1-138	April 2017

Appendix 2.

Supporting information for Chapter 3: Quasiperiodic ordering of oil-swollen ionic surfactant micelles

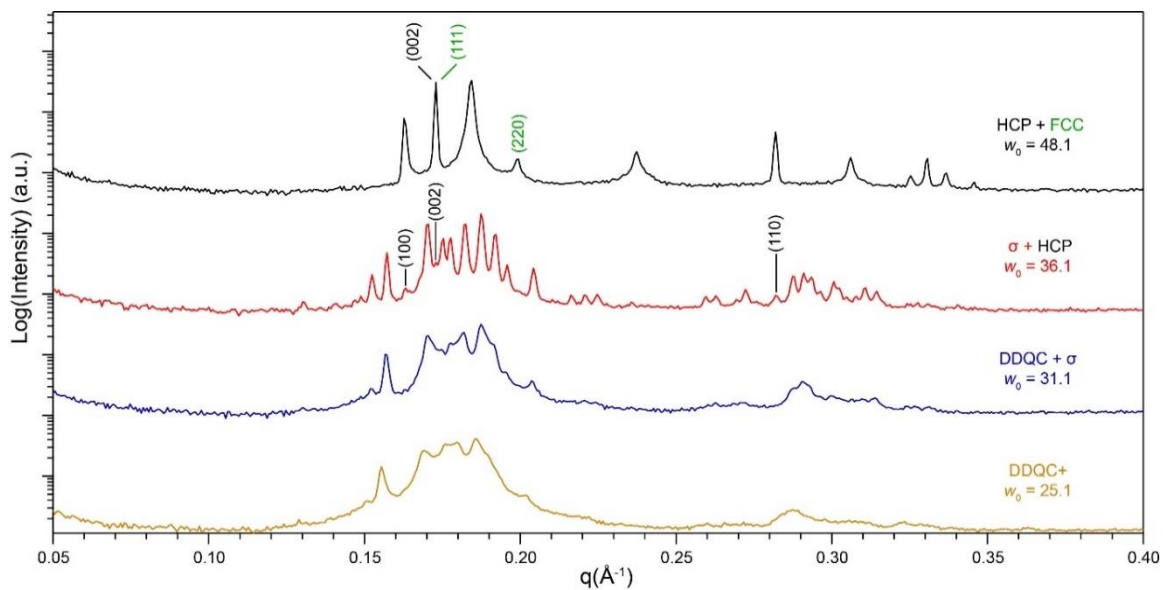


Figure A2.1. Synchrotron SAXS traces obtained from LLCs prepared by hydration of mixtures of **C₁₂PA-Dec10** at 25 °C showing the phase coexistences observed at intermediate hydrations relative to the pure phase SAXS patterns in Figure 1A. Specific indices corresponding to the reflection planes of the phases observed are color-coded with the color of the respective text.

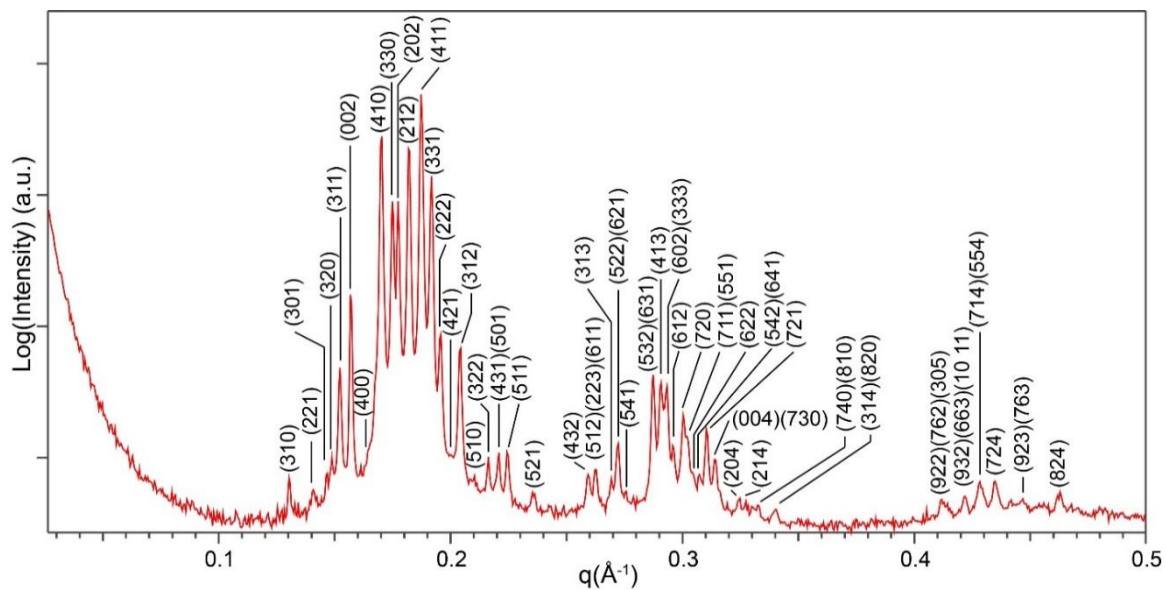


Figure A2.2. Enlarged and fully-indexed scattering pattern of the FK σ phase obtained from LLC with $w_0 = 35.2$ and $T = 25$ °C prepared by hydration of **C₁₂PA-Dec10** that exhibits > 50 synchrotron instrument resolution-limited peaks. A complete list of peak positions and residuals are given in Table A2.1.

Table A2.1. List of the observed and calculated peak positions for the Frank-Kasper σ phase formed by a LLC with $w_0 = 35.2$ at $T = 25$ °C prepared by hydration of **C₁₂PA-Dec10**. The corresponding tetragonal space group is $P4_2/mmm$ (#136) with the unit cell parameters are $a = 15.24$ nm and $c = 8.01$ nm ($c/a = 0.526$).

The scattering wavevector modulus for a tetragonal lattice is given by:

$$q^2 = (2\pi)^2 \left(\frac{h^2 + k^2}{a^2} + \frac{l^2}{c^2} \right)$$

Miller indices			%Residual		
(h	k	l)	q_{calc} (Å ⁻¹)	q_{obs} (Å ⁻¹)	$ \Delta q /q_{\text{calc}} \times 100$
1	1	0	0.0582	-	-
2	0	0	0.0823	-	-
1	0	1	0.0884	-	-
2	1	0	0.0920	-	-
1	1	1	0.0975	-	-
2	2	0	0.1163	-	-
2	1	1	0.1207	-	-
3	1	0	0.1301	0.1303	0.19
2	2	1	0.1402	0.1408	0.44
3	0	1	0.1461	0.1468	0.48
3	2	0	0.1483	0.1488	0.35
3	1	1	0.1518	0.1523	0.35
0	0	2	0.1565	0.1568	0.20
4	0	0	0.1645	0.1648	0.18
1	1	2	0.1669	-	-
3	2	1	0.1677	-	-
4	1	0	0.1696	0.1703	0.43
3	3	0	0.1745	0.1748	0.18
2	0	2	0.1768	0.1773	0.29
2	1	2	0.1815	0.1818	0.16
4	1	1	0.1867	0.1873	0.29
3	3	1	0.1912	0.1918	0.30
2	2	2	0.1950	0.1958	0.42
4	2	1	0.1999	0.1998	0.04
3	1	2	0.2035	0.2043	0.40
5	1	0	0.2097	0.2103	0.28
3	2	2	0.2156	0.2163	0.33
4	3	1	0.2200	0.2208	0.36
5	0	1	0.2200	0.2208	0.36

5	1	1	0.2238	0.2243	0.21
5	2	1	0.2349	0.2353	0.18
4	3	2	0.2584	0.2593	0.35
5	1	2	0.2617	0.2623	0.25
2	2	3	0.2620	0.2623	0.12
6	1	1	0.2621	0.2623	0.07
3	1	3	0.2684	0.2693	0.35
5	2	2	0.2712	0.2723	0.41
6	2	1	0.2716	0.2723	0.25
5	4	1	0.2747	0.2756	0.30
6	3	0	0.2759	-	-
5	3	2	0.2863	0.2873	0.33
6	3	1	0.2868	0.2873	0.19
4	1	3	0.2896	0.2908	0.42
7	1	0	0.2908	-	-
5	5	0	0.2908	-	-
6	0	2	0.2922	0.2933	0.38
3	3	3	0.2925	0.2933	0.28
6	1	2	0.2951	0.2958	0.25
7	2	0	0.2994	0.3003	0.30
7	1	1	0.3011	0.3018	0.22
5	5	1	0.3011	0.3018	0.22
6	2	2	0.3036	0.3043	0.25
5	4	2	0.3063	0.3073	0.32
6	4	1	0.3067	0.3073	0.19
7	2	1	0.3095	0.3103	0.27
0	0	4	0.3130	0.3146	0.50
7	3	0	0.3132	0.3146	0.43
5	1	3	0.3148	-	-
2	0	4	0.3236	0.3248	0.37
2	1	4	0.3262	0.3273	0.33
8	1	0	0.3316	0.3323	0.22
7	4	0	0.3316	0.3323	0.22
3	1	4	0.3389	0.3403	0.41
8	2	0	0.3391	0.3403	0.34
9	2	2	0.4102	0.4118	0.39
7	6	2	0.4102	0.4118	0.39
3	0	5	0.4102	0.4118	0.39
3	1	5	0.4123	-	-
8	2	3	0.4124	-	-
9	4	1	0.4125	-	-

9	3	2	0.4204	0.4211	0.16
6	6	3	0.4206	0.4211	0.11
10	1	1	0.4207	0.4211	0.09
4	1	5	0.4264	-	-
10	2	1	0.4266	-	-
7	1	4	0.4272	0.4283	0.25
5	5	4	0.4272	0.4283	0.25
7	2	4	0.4331	0.4346	0.33
9	2	3	0.4459	0.4468	0.19
7	6	3	0.4459	0.4468	0.19
8	2	4	0.4615	0.4628	0.28

Table A2.2. List of observed and calculated peak positions for the lyotropic dodecagonal quasicrystal formed by hydration of **C₁₂PA-Dec10** to $w_0 = 29.1$ at $T = 25$ °C. The observed Miller indices correspond to the 5D space group $P12_6/mmc$ (or $P12_6/mcm$) for the quasicrystal. The DDQC has an intermicellar distance as $a = 7.91$ nm and the interplanar distance as $c = 8.02$ nm, such that $c/a = 1.01$.

The scattering wavevector modulus for this dodecagonal quasicrystal is given by:

$$q = \sum_{n=1}^5 h_n a_n$$

$$a_n = \frac{1}{\sqrt{3}a} \left\{ i \cos \frac{(n-1)\pi}{6} + j \sin \frac{(n-1)\pi}{6} \right\} \forall n \in \{1,2,3,4\}$$

$$a_5 = \frac{c}{a}$$

$$q_{\text{obs}} = |q|$$

Miller indices					$q_{\text{calc}} (\text{Å}^{-1})$	$q_{\text{obs}} (\text{Å}^{-1})$	% Residual $\Delta q/q_{\text{calc}} \times 100$
h_1	h_2	h_3	h_4	h_5			
0	0	0	0	2	0.1566	0.1566	0.00
1	2	1	0	0	0.1711	0.1711	0.01
0	1	1	0	2	0.1799	0.1807	0.44
2	2	0	-1	1	0.1882	0.1880	-0.10
1	1	1	0	2	0.2006	0.2016	0.52
3	3	0	-2	1	0.2693	0.2706	0.49
2	3	1	-1	2	0.2882	0.2904	0.75
0	0	0	0	4	0.3133	0.3126	-0.22
0	1	1	0	4	0.3256	0.3253	-0.07
1	3	3	1	0	0.3305	0.3311	0.18

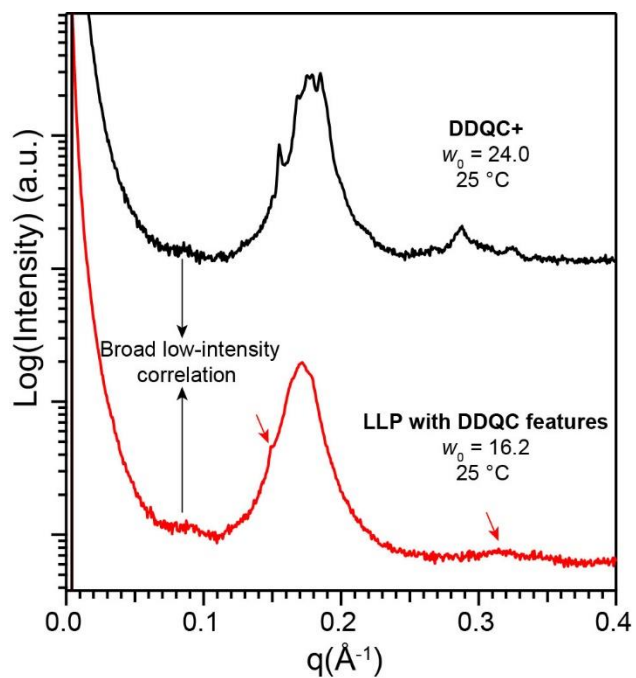


Figure A2.3. Azimuthally-integrated synchrotron SAXS patterns **C₁₂PA-Dec10** LLCs with $w_0 = 16.2$ and 24.0 at $25\text{ }^\circ\text{C}$ depicting the appearance of DDQC-like features in the LLP scattering trace, and LLP-like features in a DDQC scattering trace. The red arrows correspond to low-intensity correlations, which likely correspond to those in the DDQC.

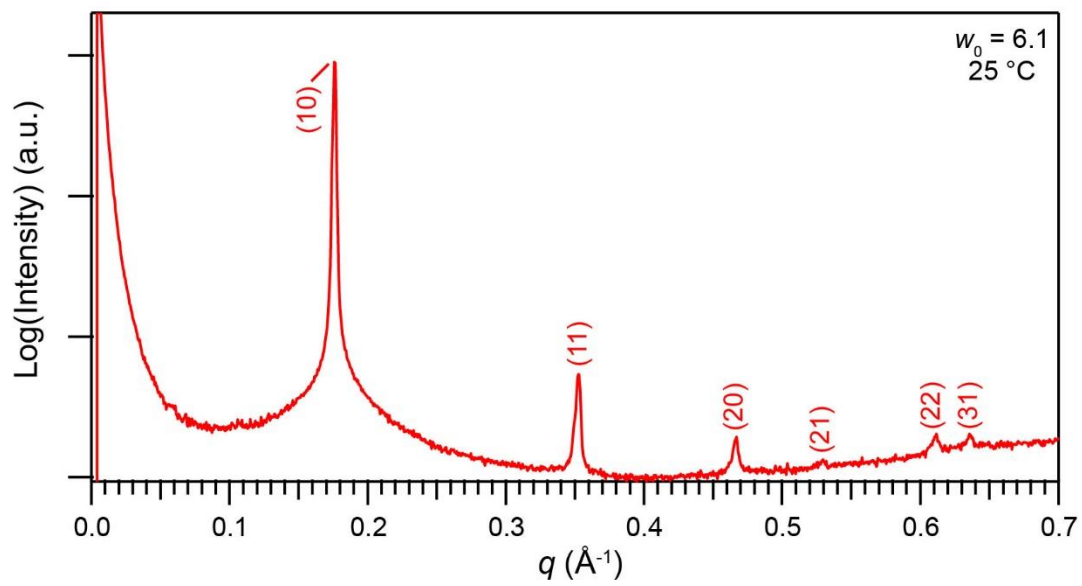


Figure A2.4. Scattering traces obtained from H_I morphology formed by LLCs of **C₁₂PA-Dec10** with $w_0 = 6.1$ at $25 \text{ }^\circ\text{C}$. The Miller indices corresponding to the 2D lattice are marked.

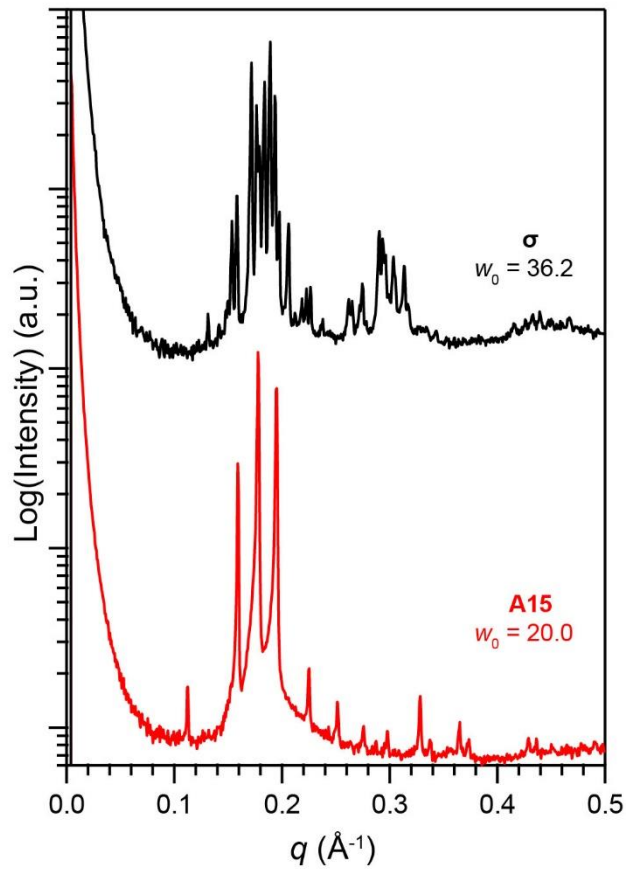


Figure A2.5. Synchrotron SAXS patterns obtained from the σ and A15 phases formed by oil addition into pre-made aqueous LLCs of C₁₂PA-TMA₂ at 25 °C.

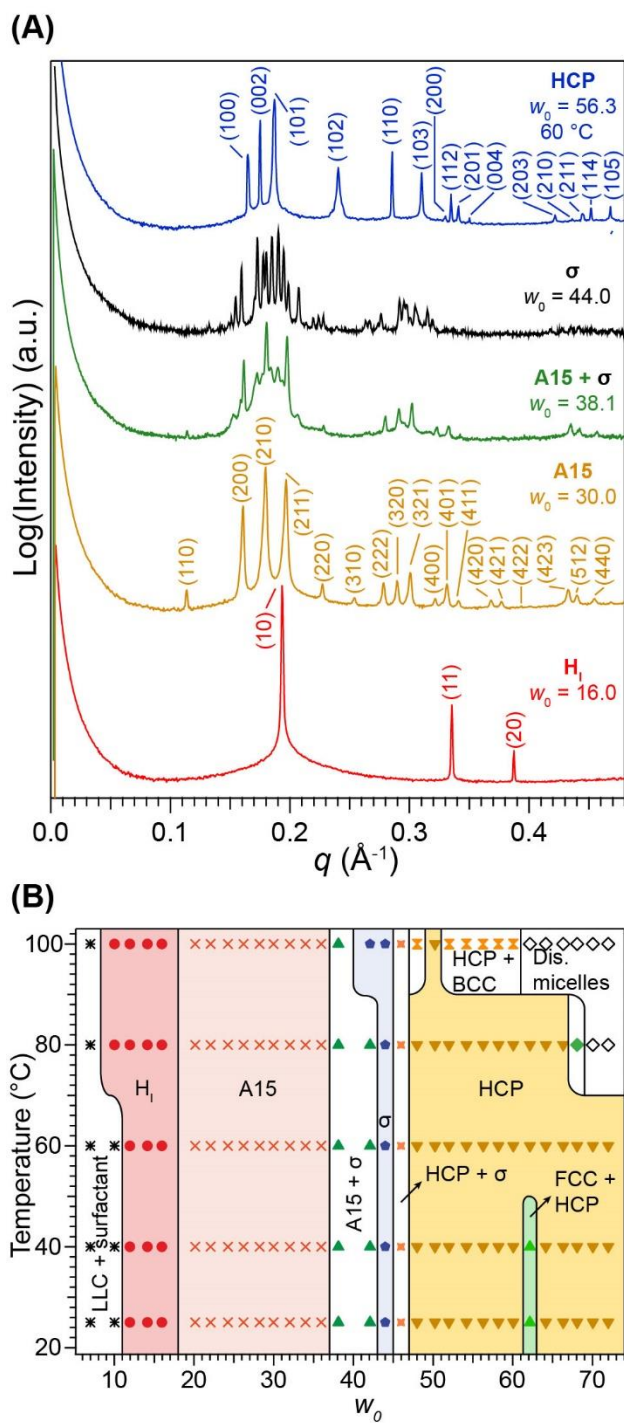


Figure A2.6. (A) Synchrotron SAXS patterns of aqueous LLCs formed by DDPA-TMA₂, in the absence of any hydrocarbon oil additive, showing the formation of H_I, A15, A15 + σ , σ , and HCP phases at 25 $^\circ\text{C}$, unless otherwise noted. All traces are vertically shifted for clarity. (B) Temperature *versus* w_0 = (moles of H₂O/moles

of surfactant) phase portrait of for DDPA-TMA₂ obtained from the synchrotron SAXS analyses of the as-prepared samples at 22 °C. Solid lines indicate the approximate locations of the phase boundaries with the resolution of the phase map, indicated by the data points.

Appendix 3.

Supporting information for Chapter 4: Path-dependent Preparation of Complex Micelle Packings of a Hydrated Diblock Oligomer

Reprinted from Jayaraman A.; Zhang D. Y.; Dewing B. L.; Mahanthappa M. K. *ACS Central*

Science **2019**, 5, 619-628.

© American Chemical Society, 2019

A3.1 Experimental Section

Materials. All reagents were purchased from the Sigma-Aldrich Chemical Co. (Milwaukee, WI) and used as received without further purification. C₁₆E₂₀ was stored in a glovebox under an anhydrous argon atmosphere to avoid adventitious atmospheric moisture uptake. Ultra-pure water (18 M Ω •cm) obtained from Thermo Scientific™ Barnstead™ Smart2Pure 3 UV/UF water purification system was degassed by sparging N_{2(g)} for at least 30 min.

¹H NMR Spectroscopy. ¹H NMR spectra were acquired in CDCl₃ in the presence of excess trifluoroacetic anhydride, using a Bruker Avance 400 MHz spectrometer with Smartprobe with a pulse repetition delay time of 20 s. All spectra were referenced relative to the residual proton shift of CDCl₃ (δ 7.26 ppm). Carbon/Hydrogen (C/H) combustion elemental analysis were performed by Atlantic Microlab, Inc. (Norcross, GA, USA). $M_n = 1074.2$ g/mol was determined by end group analysis of the trifluoroacetylated C₁₆E₂₀ (by treatment with excess trifluoroacetic anhydride in CDCl₃), based on quantitative integration of the ¹H NMR spectrum based on the methyl group in the C₁₆ hydrocarbon fragment (Figure A3.1).

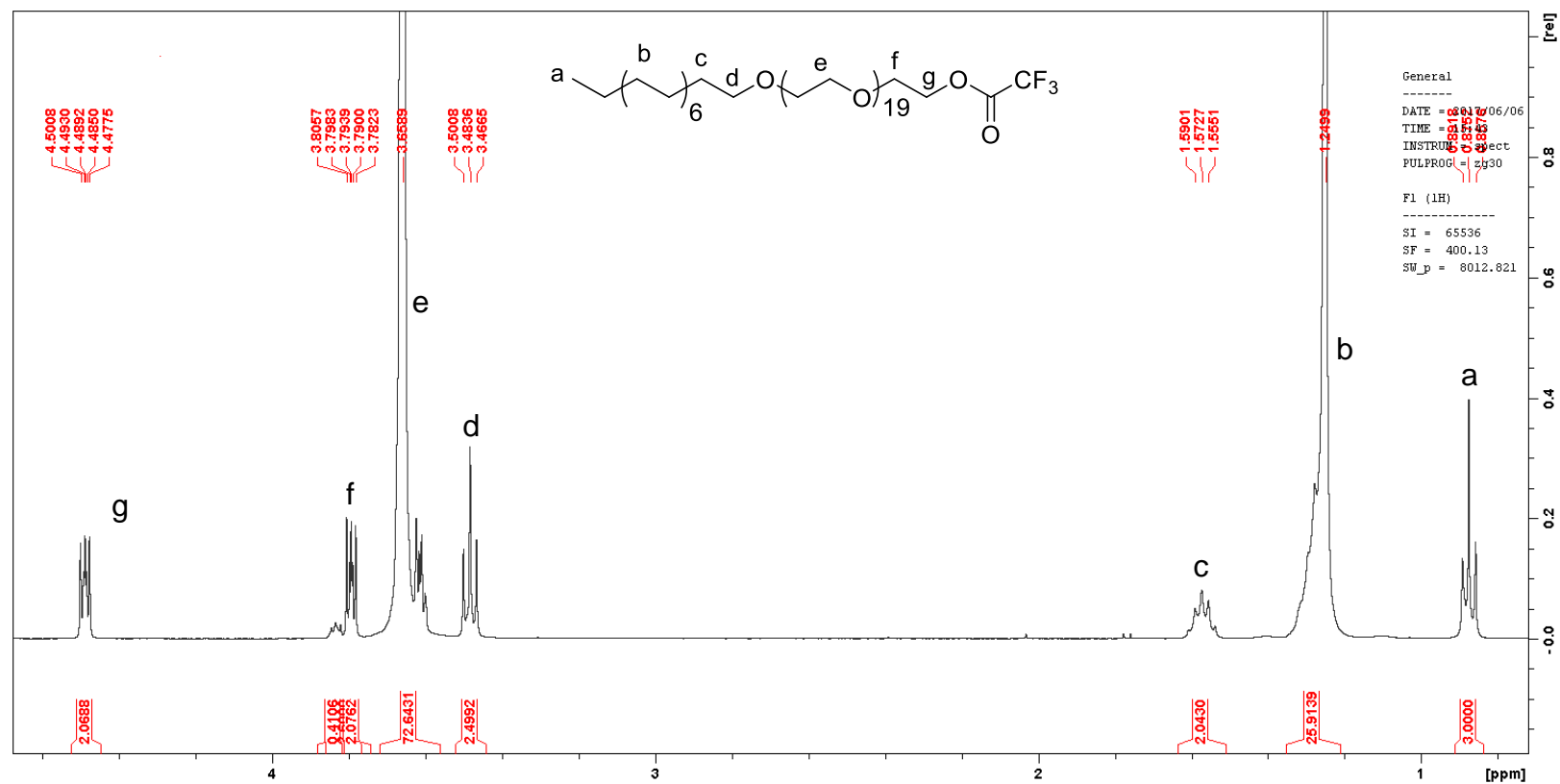


Figure A3.1. ^1H NMR of $C_{16}E_{20}$ in CDCl_3 . The spectrum is calibrated such that there are three methyl protons (a). The integration of the protons on the PEO chain (e) are used to calculate the number of EO units. The integration of the hydrocarbon fragments (a, b, c, d) is consistent with a 16 carbon alkyl chain (33 protons). M_n is calculated as the sum of masses of the hydrocarbon and PEO blocks.

Size-Exclusion Chromatography (SEC). SEC analyses in tetrahydrofuran (THF) were performed on a Viscotek GPCMax VE 2001 system equipped with three Agilent Technologies PLGel Mixed-B columns (350 mm \times 7.5 mm) and a Viscotek VE 3580 refractive index detector, using an eluent flowrate of 1 mL/min. A polystyrene molecular weight calibration curve was constructed using 10 commercially available narrow molecular weight standards with $580 \leq M_n \leq 377400$ g/mol (Polymer Laboratories, Amherst, MA). For C₁₆E₂₀ with trifluoroacetate endgroup (by reaction with excess trifluoroacetic anhydride), $M_n = 1000$ g/mol and $D = M_w/M_n = 1.17$ (against polystyrene standards without correction) (Figure A3.2).

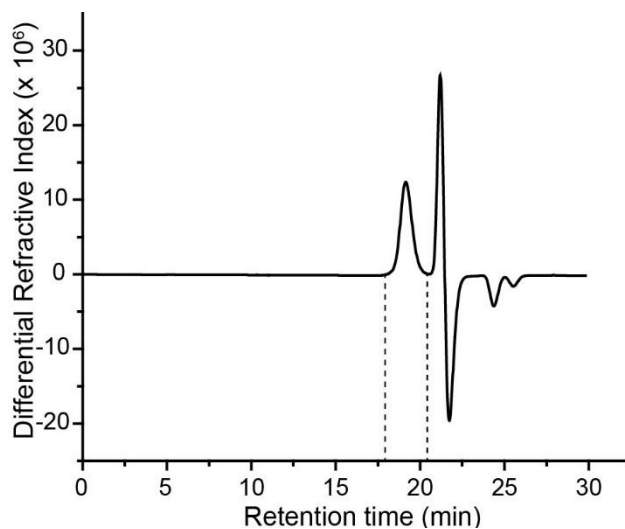


Figure A3.2. SEC trace obtained using differential refractive index detection for C₁₆E₂₀ in tetrahydrofuran. The dotted lines represent the bounds of the peak from the amphiphile.

Lyotropic Liquid Crystal (LLC) sample Preparation. LLC samples were prepared by massing desired amounts of C₁₆E₂₀ in 1 dram vials inside a glovebox under an argon atmosphere, followed by hydration using ultra-pure water (18 M Ω •cm). These mixtures were homogenized by three or more cycles of centrifugation (4950 \times g for 10 min each) and hand-mixing to yield stiff and translucent, gel-like solids. Sample vials were capped and sealed using Parafilm to prevent any

loss of water. No expected or unusually high safety hazards were encountered during sample handling or preparation.

Small-angle X-Ray Scattering (SAXS). All LLC samples were allowed to equilibrate at 22 °C for at least 24 h prior to morphological analyses by synchrotron SAXS. Using an incident beam energy of either 13.3 or 14.0 keV ($\lambda = 0.932$ or 0.886 Å) and a 3.617 m sample-to-detector distance at the 12-ID-B beamline of the Advanced Photon Source (Argonne, IL), synchrotron 2D-SAXS patterns were recorded on a Pilatus 2M detector (25.4 cm \times 28.9 cm rectangular area) with 1475×1679 pixel resolution (172 $\mu\text{m} \times 172$ μm pixel size). The scattering wavevector ($q = (4\pi\sin \theta)/\lambda$) scale in these patterns was calibrated using a silver behenate standard ($d = 58.38$ Å). LLC samples were hermetically sealed in alodined aluminum DSC pans (TA Instruments, Newcastle, DE), which were equilibrated at the desired temperature using a Linkam DSC hot-stage for at least 5 min prior to data collection (typical exposure times ~ 1 s). X-ray scattering analyses poses a significant safety hazard and all institutional radiation safety protocols were followed to mitigate exposure.

Lab source SAXS measurements were made using a SAXSLab Ganesha300XL instrument in the Characterization Facility, University of Minnesota. Cu K α X-rays ($\lambda = 1.54$ Å) generated by a Xenocs Geni3DX source were collimated through 2 or 3 sets of 4-bladed slits (JJ X-ray, A/S). 2D-SAXS patterns were acquired using a Dectris EIGER R 1M detector (7.72 cm \times 7.99 cm rectangular area) with 1030×1065 pixels (75 $\mu\text{m} \times 75$ μm pixel size) at a sample-to-detector distance of 46.8 cm. Samples were sealed in home-built sample holders with Kapton windows. They were mounted within an evacuated sample environment and equilibrated at the desired temperature on a Linkam hot-stage for ~ 20 min prior to data acquisition (typical exposure times ~ 10 min). X-ray scattering analyses poses a significant safety hazard and all institutional radiation safety protocols were followed to mitigate exposure.

All 2D-SAXS patterns were azimuthally-integrated to obtain one-dimensional scattered intensity $I(q)$ versus q plots, using the DataSqueeze software package (<http://www.physics.upenn.edu/~heiney/datasqueeze/index.html>). The 1D scattering intensity profiles were analyzed using customized Igor Pro procedure files developed by our group.

Using the *JANA2006* crystallographic computing system software,²⁸⁷ Le Bail refinement of selected SAXS data sets was used to extract the structure factor intensities for each scattering maximum. These data were used as inputs for the charge flipping algorithms within the *SUPERFLIP* software package²⁸⁸ to reconstruct the electron density maps for various observed LLC phases. The resulting electron density contour maps (typically, 90% isosurfaces) were visualized using the VESTA software package,⁶⁷ Details of these analyses along with the *SUPERFLIP* input files (in which the static structure factor intensities are listed) are provided on pages 234 and 243.

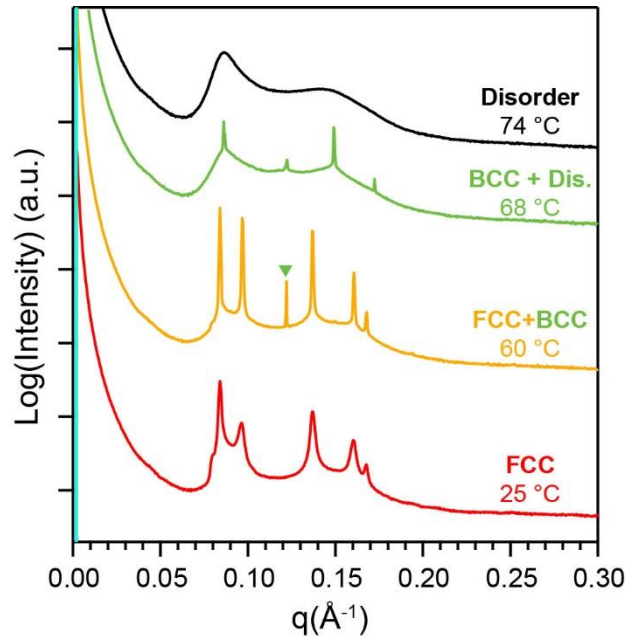


Figure A3.3. Temperature-dependent synchrotron SAXS patterns obtained from a LLC sample with 32.9 wt% C₁₆E₂₀ in water. This LLC sample transitions from an FCC micellar packing at 25 °C to BCC/FCC coexistence at 60 °C, which melts into a disordered solution of micelles at 74 °C. In the SAXS trace at 60 °C, the green marker indicates the peak corresponding to the coexisting BCC phase. At 68 °C, we observe an intervening window of two-phase coexistence between a micellar BCC phase and disordered micellar solution as expected based on Gibbs' Phase Rule.

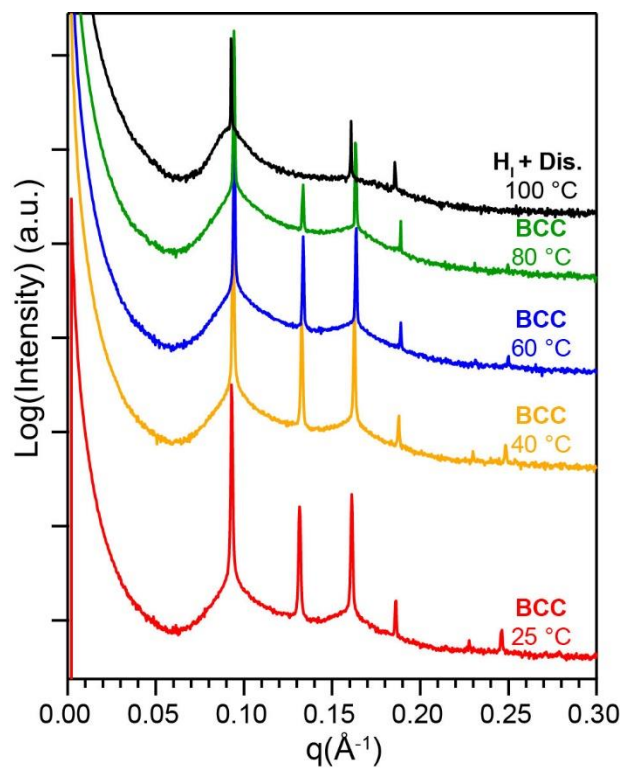


Figure A3.4. 1D-SAXS intensity profiles for the LLC formed at 46.5 wt% C₁₆E₂₀ showing the formation of a body-centered cubic (BCC) phase at $25 \leq T \leq 80$ °C, and H_I + disordered micelles at 100 °C.

***SUPERFLIP* Input File for the A15 Phase formed at 58.9 wt% C₁₆E₂₀ in H₂O Used in Charge-Flipping Electron Density Reconstruction**

The 1D-SAXS intensity $I(q)$ versus scattering wavevector q profile for the as-made A15 phase at 25 °C with 58.9 wt% C₁₆E₂₀ was scaled by multiplying the q values by 2, to halve the size of the unit cell to expedite the calculation and rendering of the electron density map with available computing resources. Le Bail refinement of the scaled SAXS data with a 10th order polynomial fit for the X-ray background using the *JANA2006* crystallographic computing software package enabled extraction of the static structure factor intensities for each peak in the pattern in the range $q = 0.053\text{--}0.255 \text{ \AA}^{-1}$ (in the original, unscaled pattern), the Miller indices of which were assigned using the *Pm3(-)n* space group symmetry with a scaled cubic unit cell parameter $a = 7.3081 \text{ nm}$. The structure factor intensities associated with each indexed SAXS peak are given in the text file below. Application of the *SUPERFLIP* charge-flipping algorithm using the input file below in 2000 trials yielded 11 converged electron density maps with excellent figures of merit (fm) < 6, starting from randomized initial conditions. The 11 converged maps were averaged and rendered using the *VESTA* software package to yield the 90% isosurface electron density maps shown in Figure 3.2A.

Details of the methodology were summarily described by Baez-Cotto *et al.*,²⁰² and more details may be found in the original papers of Palatinus and co-workers.

```
*****start_file*****
*****
title SAJB-47_00246_Try3_Superflip
perform CF
outputfile "SAJB-47_00246_Try3.xplor"
outputformat xplor
dimension 3
cell 73.0807 73.0807 73.0807 90.00 90.00 90.00
spacegroup Pm-3n
centro yes
```



```

centers
  0.000000  0.000000  0.000000
endcenters
symmetry
  x1      x2      x3
 -x1     -x2     x3
 -x1      x2     -x3
  x1     -x2     -x3
  x3      x1      x2
  x3     -x1     -x2
 -x3     -x1     x2
 -x3      x1     -x2
  x2      x3      x1
 -x2      x3     -x1
  x2     -x3     -x1
 -x2     -x3      x1
 x2+1/2  x1+1/2 -x3+1/2
-x2+1/2 -x1+1/2 -x3+1/2
 x2+1/2 -x1+1/2  x3+1/2
-x2+1/2  x1+1/2  x3+1/2
  x1+1/2  x3+1/2 -x2+1/2
-x1+1/2  x3+1/2  x2+1/2
-x1+1/2 -x3+1/2 -x2+1/2
  x1+1/2 -x3+1/2  x2+1/2
  x3+1/2  x2+1/2 -x1+1/2
  x3+1/2 -x2+1/2  x1+1/2
-x3+1/2  x2+1/2  x1+1/2
-x3+1/2 -x2+1/2 -x1+1/2
  -x1      -x2     -x3
   x1      x2     -x3
   x1     -x2     x3
  -x1      x2     x3
  -x3     -x1     -x2
  -x3      x1     x2
   x3      x1     -x2
   x3     -x1     x2
  -x2     -x3     -x1
   x2     -x3     x1
  -x2      x3     x1
   x2      x3     -x1
-x2+1/2 -x1+1/2  x3+1/2
  x2+1/2  x1+1/2  x3+1/2
-x2+1/2  x1+1/2 -x3+1/2
  x2+1/2 -x1+1/2 -x3+1/2
-x1+1/2 -x3+1/2  x2+1/2
  x1+1/2 -x3+1/2 -x2+1/2
  x1+1/2  x3+1/2  x2+1/2

```

```

-x1+1/2  x3+1/2  -x2+1/2
-x3+1/2  -x2+1/2  x1+1/2
-x3+1/2  x2+1/2  -x1+1/2
  x3+1/2  -x2+1/2  -x1+1/2
  x3+1/2  x2+1/2  x1+1/2
endsymmetry
composition C56 H114 O21

# Keywords for charge flipping
repeatmode 2000 sumgood
bestdensities 1 symmetry
polish yes
maxcycles 1000
delta AUTO
weakratio 0.000
Biso 0.000
randomseed AUTO
searchsymmetry average
derivesymmetry no
# End of keywords for charge flipping

# EDMA-specific keywords
inputfile SAJB-47_00246_Try3_Superflip.m81
outputbase SAJB-47_00246_Try3_Superflip
m40forjana yes
writem40 SAJB-47_00246_Try3_Superflip_tmp.m40
maxima all
fullcell no
scale fractional
plimit 0.3000 sigma
numberofatoms composition
centerofcharge yes
chlimit 0.2500
chlimlist 0.0375 relative
# End of EDMA-specific keywords

electrons 0.0000
dataitemwidths 4 15 15
dataformat intensity fwhm
fbegin
  1 0 1 22.0224 0.0101
  0 0 2 6987.5386 0.0110
  1 0 2 10000.0000 0.0117
  1 1 2 8136.5864 0.0125
  2 0 2 188.0041 0.0140
  1 0 3 56.9598 0.0154
  2 2 2 990.2704 0.0168

```

2	0	3	475.1289	0.0174
2	1	3	496.7450	0.0181
0	0	4	1174.6332	0.0193
1	0	4	357.6997	0.0200
3	0	3	67.6408	0.0206
1	1	4	67.6408	0.0206
2	0	4	80.2654	0.0218
2	1	4	20.9924	0.0224
3	2	3	16.7596	0.0229
2	2	4	77.5350	0.0241
3	0	4	28.4030	0.0246
3	1	4	8.7267	0.0252
1	0	5	8.7267	0.0252
2	0	5	42.3261	0.0268
3	2	4	42.3261	0.0268
2	1	5	32.1020	0.0273
4	0	4	172.2079	0.0283
3	3	4	21.1899	0.0293
3	0	5	21.1899	0.0293
3	1	5	1.4569	0.0298
6	4	6	0.0000	0.0507
5	0	8	0.0000	0.0511
4	3	8	0.0000	0.0511
6	2	7	0.0000	0.0511
3	0	9	0.0000	0.0514
5	1	8	0.0000	0.0514
5	4	7	0.0000	0.0514
3	1	9	0.0000	0.0517
5	2	8	0.0000	0.0524
6	3	7	0.0000	0.0527
3	2	9	0.0000	0.0527
4	4	8	0.0000	0.0533
4	0	9	0.0000	0.0537
7	0	7	0.0000	0.0540
4	1	9	0.0000	0.0540
5	3	8	0.0000	0.0540
0	0	10	0.0000	0.0546
6	0	8	0.0000	0.0546
4	2	9	0.0000	0.0549
6	4	7	0.0000	0.0549
6	1	8	0.0000	0.0549
1	0	10	0.0000	0.0549
1	1	10	0.0000	0.0552
7	2	7	0.0000	0.0552
6	2	8	0.0000	0.0558
2	0	10	0.0000	0.0558
2	1	10	0.0000	0.0561

5	4	8	0.0000	0.0561
4	3	9	0.0000	0.0564
5	0	9	0.0000	0.0564
5	1	9	0.0000	0.0567
6	6	6	0.0000	0.0570
2	2	10	0.0000	0.0570
3	0	10	0.0000	0.0573
6	3	8	0.0000	0.0573
6	5	7	0.0000	0.0576
5	2	9	0.0000	0.0576
3	1	10	0.0000	0.0576
7	0	8	0.0000	0.0585
3	2	10	0.0000	0.0585
7	4	7	0.0000	0.0588
7	1	8	0.0000	0.0588
5	5	8	0.0000	0.0588
5	3	9	0.0000	0.0591
4	0	10	0.0000	0.0594
6	4	8	0.0000	0.0594
4	1	10	0.0000	0.0597
6	0	9	0.0000	0.0597
7	2	8	0.0000	0.0597
6	1	9	0.0000	0.0600
3	3	10	0.0000	0.0600
4	2	10	0.0000	0.0606
6	2	9	0.0000	0.0609
7	3	8	0.0000	0.0611
5	4	9	0.0000	0.0611
1	0	11	0.0000	0.0611
4	3	10	0.0000	0.0620
6	5	8	0.0000	0.0620
2	0	11	0.0000	0.0620
5	0	10	0.0000	0.0620
6	3	9	0.0000	0.0623
2	1	11	0.0000	0.0623
5	1	10	0.0000	0.0623
8	0	8	0.0000	0.0628
7	4	8	0.0000	0.0631
5	2	10	0.0000	0.0631
3	0	11	0.0000	0.0634
7	0	9	0.0000	0.0634
7	1	9	0.0000	0.0637
3	1	11	0.0000	0.0637
4	4	10	0.0000	0.0639
8	2	8	0.0000	0.0639
6	4	9	0.0000	0.0642
7	6	7	0.0000	0.0645

7	2	9	0.0000	0.0645
3	2	11	0.0000	0.0645
5	3	10	0.0000	0.0645
6	6	8	0.0000	0.0650
6	0	10	0.0000	0.0650
4	0	11	0.0000	0.0653
6	1	10	0.0000	0.0653
7	5	8	0.0000	0.0656
4	1	11	0.0000	0.0656
7	3	9	0.0000	0.0658
6	2	10	0.0000	0.0661
4	2	11	0.0000	0.0664
5	4	10	0.0000	0.0664
6	5	9	0.0000	0.0666
8	4	8	0.0000	0.0672
0	0	12	0.0000	0.0672
8	0	9	0.0000	0.0674
6	3	10	0.0000	0.0674
1	0	12	0.0000	0.0674
4	3	11	0.0000	0.0677
8	1	9	0.0000	0.0677
7	4	9	0.0000	0.0677
1	1	12	0.0000	0.0677
5	0	11	0.0000	0.0677
5	1	11	0.0000	0.0679
2	0	12	0.0000	0.0682
8	2	9	0.0000	0.0685
7	6	8	0.0000	0.0685
7	0	10	0.0000	0.0685
2	1	12	0.0000	0.0685
7	1	10	0.0000	0.0687
5	5	10	0.0000	0.0687
5	2	11	0.0000	0.0687
2	2	12	0.0000	0.0692
6	4	10	0.0000	0.0692
3	0	12	0.0000	0.0695
7	2	10	0.0000	0.0695
8	3	9	0.0000	0.0698
3	1	12	0.0000	0.0698
7	5	9	0.0000	0.0700
5	3	11	0.0000	0.0700
6	0	11	0.0000	0.0705
3	2	12	0.0000	0.0705
7	3	10	0.0000	0.0708
6	1	11	0.0000	0.0708
4	0	12	0.0000	0.0713
8	4	9	0.0000	0.0715

4	1	12	0.0000	0.0715
6	5	10	0.0000	0.0715
6	2	11	0.0000	0.0715
9	0	9	0.0000	0.0718
7	7	8	0.0000	0.0718
3	3	12	0.0000	0.0718
5	4	11	0.0000	0.0718
8	6	8	0.0000	0.0723
4	2	12	0.0000	0.0723
8	0	10	0.0000	0.0723
8	1	10	0.0000	0.0725
7	4	10	0.0000	0.0725
9	2	9	0.0000	0.0728
7	6	9	0.0000	0.0728
6	3	11	0.0000	0.0728
8	2	10	0.0000	0.0733
4	3	12	0.0000	0.0735
5	0	12	0.0000	0.0735

endf

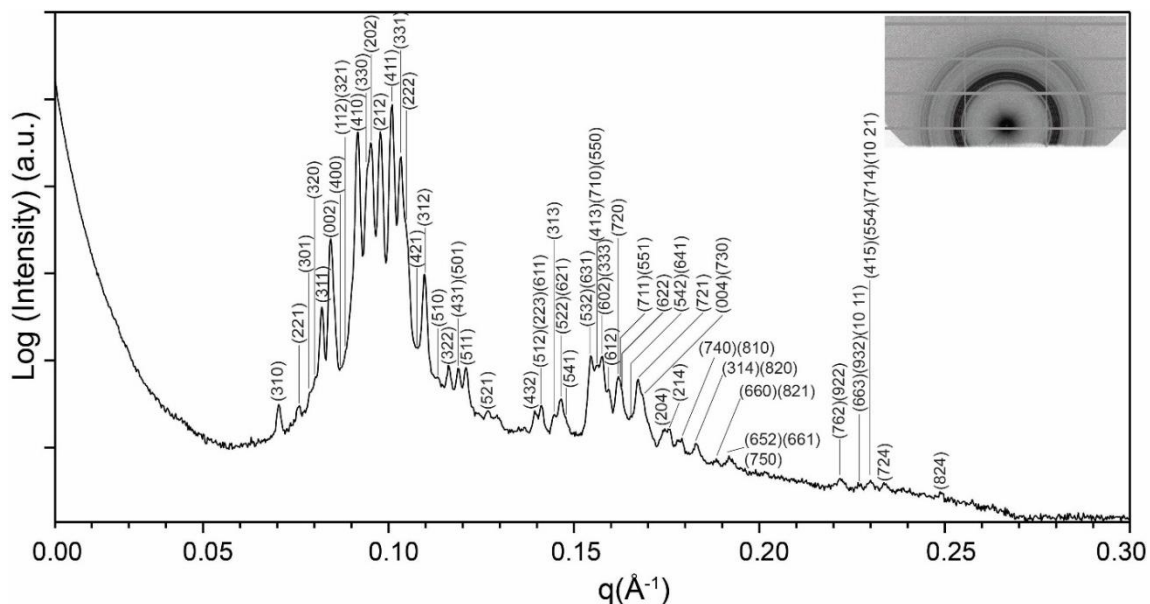


Figure A3.5 An enlarged and fully indexed SAXS pattern for the LLC FK σ phase obtained on quenching a sample comprising 58.7 wt% $C_{16}E_{20}$ from 70 °C to 25 °C and isothermally annealing it at 25 °C for 50 min. The complete assignment with indices for observed reflections are tabulated in Table A3.1. *Inset*: 2D scattering pattern which was azimuthally integrated to give the 1D plot

Table A3.1. List of the observed and calculated peak positions for the Frank-Kasper σ phase formed by quenching an aqueous LLC with 58.7 wt% C₁₆E₂₀ from 70 °C to 25 °C and annealing at 25 °C for 50 min. The corresponding tetragonal space group symmetry is $P4_2/mnm$ (#136) and unit cell parameters are $a = 28.37$ nm and $c = 14.89$ nm ($c/a = 0.525$).

For a tetragonal lattice, the scattering wavevector modulus is given by:

$$q^2 = (2\pi)^2 \left(\frac{h^2 + k^2}{a^2} + \frac{l^2}{c^2} \right)$$

Miller indices			$q_{\text{calc}} (\text{\AA}^{-1})$	$q_{\text{obs}} (\text{\AA}^{-1})$	% Residual ($\Delta q/q_{\text{calc}} \times 100$)
(h	k	l)			
3	1	0	0.0700	0.0704	-0.52
2	2	1	0.0755	0.0760	-0.62
3	0	1	0.0787	0.0788	-0.11
3	2	0	0.0799	0.0803	-0.56
3	1	1	0.0818	0.0820	-0.28
0	0	2	0.0844	0.0844	0.00
4	0	0	0.0886	0.0870	1.79
1	1	2	0.0900	0.0885	1.69
3	2	1	0.0903	0.0885	2.01
4	1	0	0.0913	0.0918	-0.53
3	3	0	0.0940	0.0945	-0.57
2	0	2	0.0953	0.0952	0.12
2	1	2	0.0979	0.0978	0.06
4	1	1	0.1006	0.1010	-0.40
3	3	1	0.1030	0.1034	-0.38
2	2	2	0.1051	0.1046	0.48
4	2	1	0.1077	0.1077	-0.04
3	1	2	0.1097	0.1096	0.07
5	1	0	0.1129	0.1132	-0.24
3	2	2	0.1162	0.1161	0.08
4	3	1	0.1185	0.1187	-0.16
5	0	1	0.1185	0.1187	-0.16
5	1	1	0.1206	0.1209	-0.28
5	2	1	0.1265	0.1269	-0.31
4	3	2	0.1392	0.1394	-0.12
5	1	2	0.1410	0.1411	-0.08
2	2	3	0.1413	0.1411	0.11

6	1	1	0.1412	0.1411	0.05
3	1	3	0.1447	0.1447	-0.01
5	2	2	0.1461	0.1466	-0.34
6	2	1	0.1463	0.1466	-0.21
5	4	1	0.1480	0.1478	0.11
6	3	0	0.1486	-	-
5	3	2	0.1543	0.1545	-0.15
6	3	1	0.1544	0.1545	-0.04
4	1	3	0.1561	0.1565	-0.26
7	1	0	0.1566	0.1565	0.07
5	5	0	0.1566	0.1565	0.07
6	0	2	0.1574	0.1577	-0.18
3	3	3	0.1577	0.1577	-0.03
6	1	2	0.1590	0.1593	-0.21
7	2	0	0.1612	0.1620	-0.47
7	1	1	0.1622	0.1625	-0.19
5	5	1	0.1622	0.1625	-0.19
6	2	2	0.1635	0.1630	0.33
5	4	2	0.1650	0.1654	-0.23
6	4	1	0.1652	0.1654	-0.13
7	2	1	0.1667	0.1673	-0.38
0	0	4	0.1688	0.1685	0.18
7	3	0	0.1687	0.1685	0.10
5	1	3	0.1696	-	-
2	0	4	0.1745	0.1740	0.30
2	1	4	0.1759	0.1759	0.01
8	1	0	0.1786	0.1791	-0.30
7	4	0	0.1786	0.1791	-0.30
3	1	4	0.1828	0.1827	0.03
8	2	0	0.1826	0.1827	-0.04
6	6	0	0.1879	0.1884	-0.25
8	2	1	0.1874	0.1884	-0.51
6	5	2	0.1925	0.1918	0.35
6	6	1	0.1926	0.1918	0.42
7	5	0	0.1905	0.1918	-0.67
9	2	2	0.2209	0.2218	-0.39
7	6	2	0.2209	0.2218	-0.39
3	1	5	0.2223	-	-
8	2	3	0.2222	-	-
9	4	1	0.2222	-	-

9	3	2	0.2264	0.2266	-0.08
6	6	3	0.2266	0.2266	0.00
10	1	1	0.2265	0.2266	-0.03
4	1	5	0.2299	0.2298	0.05
10	2	1	0.2298	0.2298	-0.01
7	1	4	0.2303	0.2298	0.20
5	5	4	0.2303	0.2298	0.20
7	2	4	0.2334	0.2334	0.01
9	2	3	0.2403	-	-
7	6	3	0.2403	-	-
8	2	4	0.2487	0.2487	0.00

***SUPERFLIP* Input File for Charge-Flipping Electron Density Reconstruction of the aqueous LLC FK σ Phase formed at 58.7 wt% C₁₆E₂₀**

The 1D-SAXS intensity $I(q)$ versus scattering wavevector q profile for the σ phase obtained upon quenching a sample comprising 58.7 wt% C₁₆E₂₀ from 70 °C to 25 °C followed by annealing at 25 °C for 2 days was scaled by multiplying the q values by 3, to expedite the calculation and rendering of the electron density map with available computing resources. Le Bail refinement of the scaled SAXS data with a 10th order polynomial fit for the X-ray background using the *JANA2006* crystallographic computing software package enabled extraction of the static structure factor intensities for each peak in the pattern in the range $q = 0.0825\text{--}0.1300 \text{ \AA}^{-1}$ (in the unscaled pattern), the Miller indices of which were assigned using the $P4_2/mnm$ space group symmetry with a scaled cubic unit cell parameter $a = 9.4577 \text{ nm}$ and $c = 4.9837 \text{ nm}$. The structure factor intensities associated with each indexed SAXS peak are given in the text file below. Application of the *SUPERFLIP* charge-flipping algorithm using the input file below in 2000 trials yielded 357 converged electron density maps with excellent figures of merit (fm) < 3 , starting from randomized initial conditions. The 357 converged maps were averaged and rendered using the VESTA software package to yield the 90% isosurface electron density maps shown in Figure 4.4A.

```

*****start_file*****
*****
title B11_1_sigma_Superflip
perform CF
outputfile "B11_1_sigma_Superflip_Try13.xplor"
outputformat xplor
dimension 3
cell 94.5767 94.5767 49.8370 90.00 90.00 90.00
spacegroup P42/mnm
centro yes
centers
0.000000 0.000000 0.000000
endcenters
symmetry
x1 x2 x3
-x1 -x2 x3
-x2+1/2 x1+1/2 x3+1/2
x2+1/2 -x1+1/2 x3+1/2
-x1+1/2 x2+1/2 -x3+1/2
x1+1/2 -x2+1/2 -x3+1/2
x2 x1 -x3
-x2 -x1 -x3
-x1 -x2 -x3
x1 x2 -x3
x2+1/2 -x1+1/2 -x3+1/2
-x2+1/2 x1+1/2 -x3+1/2
x1+1/2 -x2+1/2 x3+1/2
-x1+1/2 x2+1/2 x3+1/2
-x2 -x1 x3
x2 x1 x3
endsymmetry
composition C13440 H27360 O5040

# Keywords for charge flipping
repeatmode 2000 sumgood
bestdensities 1 symmetry
polish yes
maxcycles 1000
delta AUTO
weakratio 0.000
Biso 0.000
randomseed AUTO
searchsymmetry average
derivesymmetry no
# End of keywords for charge flipping

# EDMA-specific keywords

```

```

inputfile B11_1_sigma_Superflip.m81
outputbase B11_1_sigma_Superflip
m40forjana yes
writem40 B11_1_sigma_Superflip_tmp.m40
maxima all
fullcell no
scale fractional
plimit 0.3000 sigma
numberofatoms composition
centerofcharge yes
chlimit 0.2500
chlimlist 0.0375 relative
# End of EDMA-specific keywords

```

```

electrons 0.0000
dataitemwidths 4 15 15
dataformat intensity fwhm
fbegin

```

2	2	0	1.7759	0.0153
2	1	1	0.6081	0.0160
3	1	0	50.7322	0.0175
2	2	1	27.6748	0.0191
3	0	1	24.8614	0.0201
3	2	0	42.5197	0.0204
3	1	1	243.3518	0.0210
0	0	2	7667.8828	0.0217
4	0	0	25.9448	0.0230
1	1	2	214.5956	0.0233
3	2	1	183.7736	0.0235
4	1	0	8860.2031	0.0238
3	3	0	10000.0010	0.0245
2	0	2	7899.1997	0.0248
2	1	2	5575.9712	0.0256
4	2	0	38.2897	0.0260
4	1	1	8456.5996	0.0264
3	3	1	9312.3828	0.0271
2	2	2	2624.2578	0.0277
4	2	1	78.2934	0.0285
3	1	2	948.7307	0.0290
4	3	0	33.5163	0.0294
5	1	0	72.1135	0.0300
3	2	2	157.2879	0.0309
4	3	1	138.2182	0.0316
5	0	1	138.2182	0.0316
5	2	0	94.8668	0.0318
5	1	1	305.8773	0.0322
4	0	2	240.2753	0.0326

endf

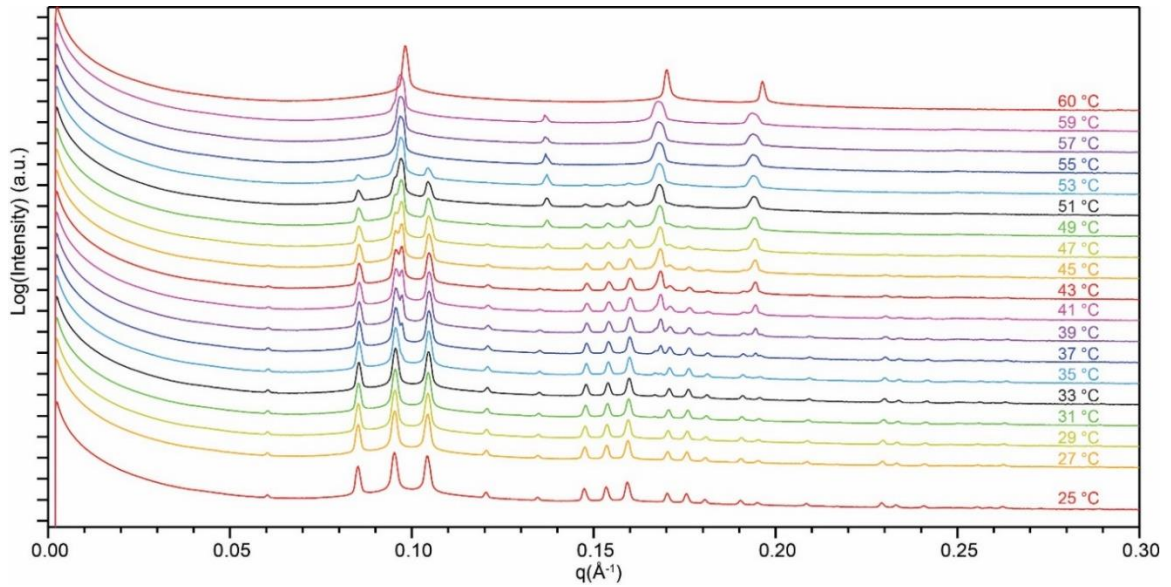


Figure A3.6 1D-SAXS intensity profiles obtained every 2 °C, on heating the aqueous LLC with 58.7 wt% $C_{16}E_{20}$ heated from 25 °C to 70 °C. Samples were equilibrated at each temperature for at least 5 min. A LLC BCC phase nucleates at 37 °C and it completely transforms to H_I at 60 °C. The σ phase is notably absent on heating, and it can only be accessed upon cooling the H_I phase.

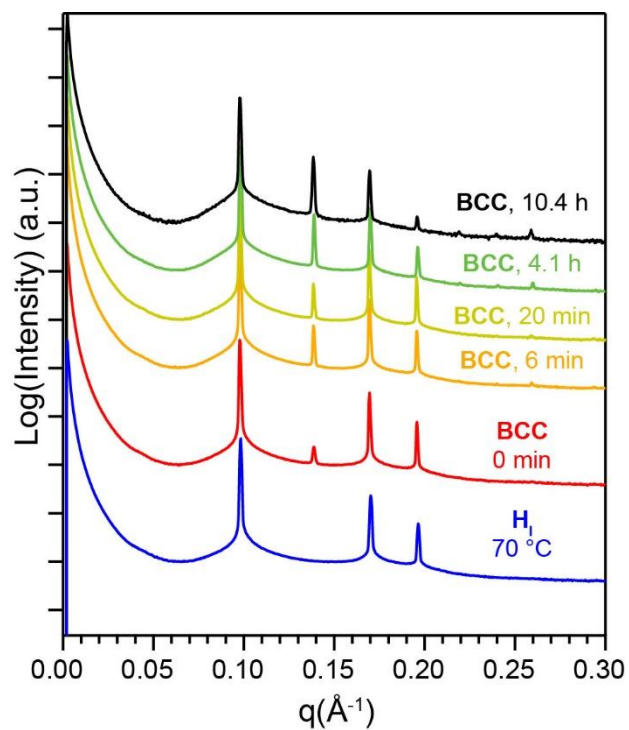


Figure A3.7 Time-resolved 1D-SAXS patterns obtained upon quenching LLC sample with 58.7 wt% C₁₆E₂₀ from 70 °C to 50 °C. H_I rapidly transforms into a BCC morphology on quenching, the latter of which remains stable for up to 10 h after annealing at 50 °C with no signs of either FK A15 or σ phase nucleation. Changes in the peak intensities with time upon extended monitoring suggest changes in the average micelle aggregation number (N_{agg}) within the BCC phase.

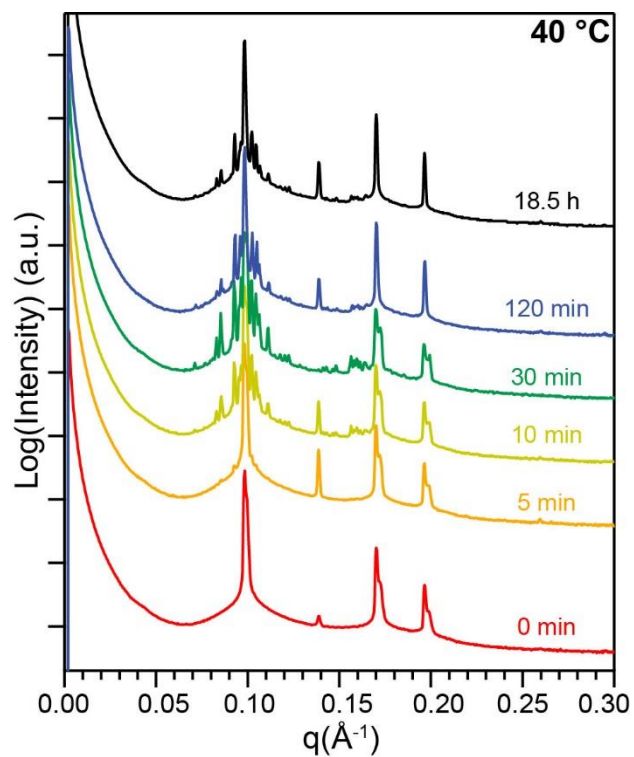


Figure A3.8 1D-SAXS patterns obtained upon quenching an LLC with 58.7 wt% C₁₆E₂₀ from 70 °C to 40 °C after various 40 °C isothermal annealing times. Prolonged annealing at 40 °C leads to decreased intensities of the “forest” or peaks which correspond to σ phase, and the peaks corresponding to BCC remain intense even after a long annealing time.

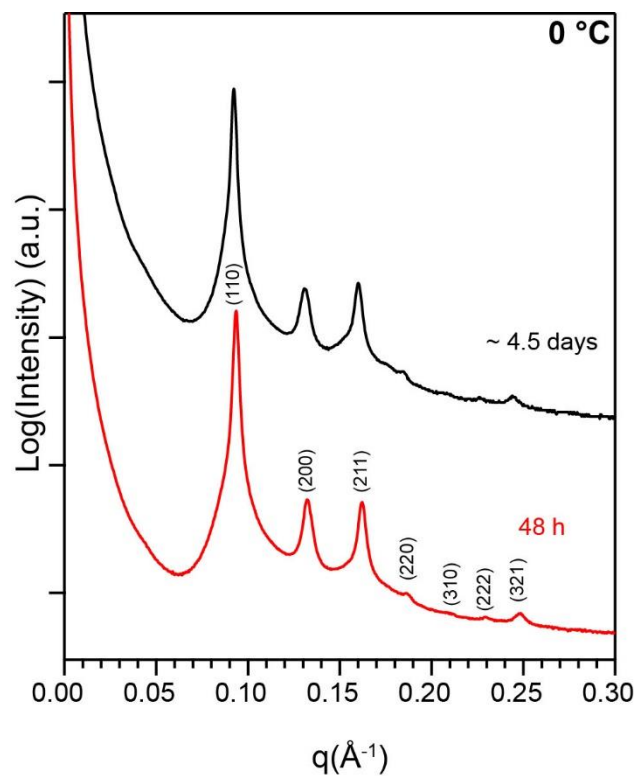


Figure A3.9 SAXS analyses of an aqueous LLC sample comprising 58.7 wt% C₁₆E quenched from 70 °C to 0 °C demonstrate the lack of nucleation of either FK σ or A15 phases upon annealing at 0 °C for > 3 days. The Miller indices corresponding to the observed peaks are marked on the plot.

Appendix 4.
Supporting information for Chapter 5. End Group-Dependent Complex
Micellar Self-assembly of Hydrated Diblock Oligomers

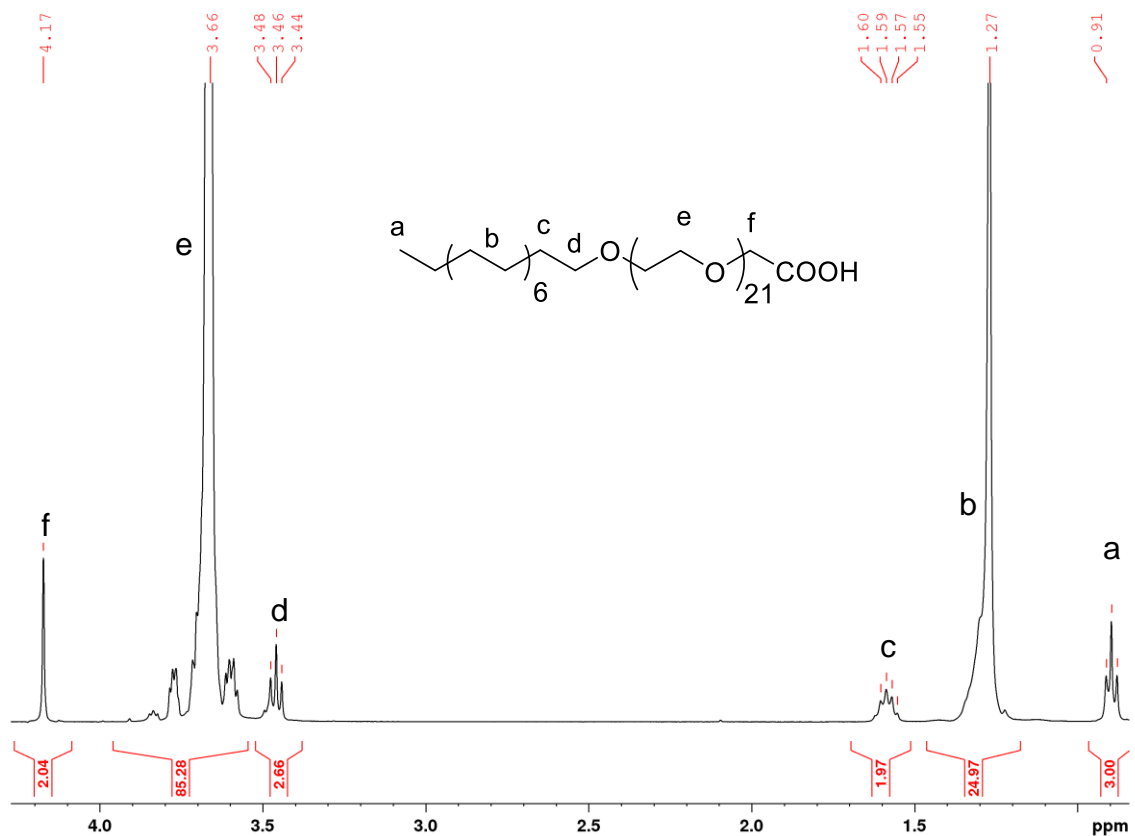


Figure A4.1. ^1H NMR spectrum obtained for $\text{C}_{16}\text{E}_{21}\text{-C}$ in CDCl_3 . The peaks of the spectrum are indexed to the protons in the structure using alphabets. The integral obtained from the methyl protons (*a*) is calibrated to 3. Completion of carboxylation of the amphiphile is apparent due to the presence of two methylene protons at 4.17 ppm (*f*).

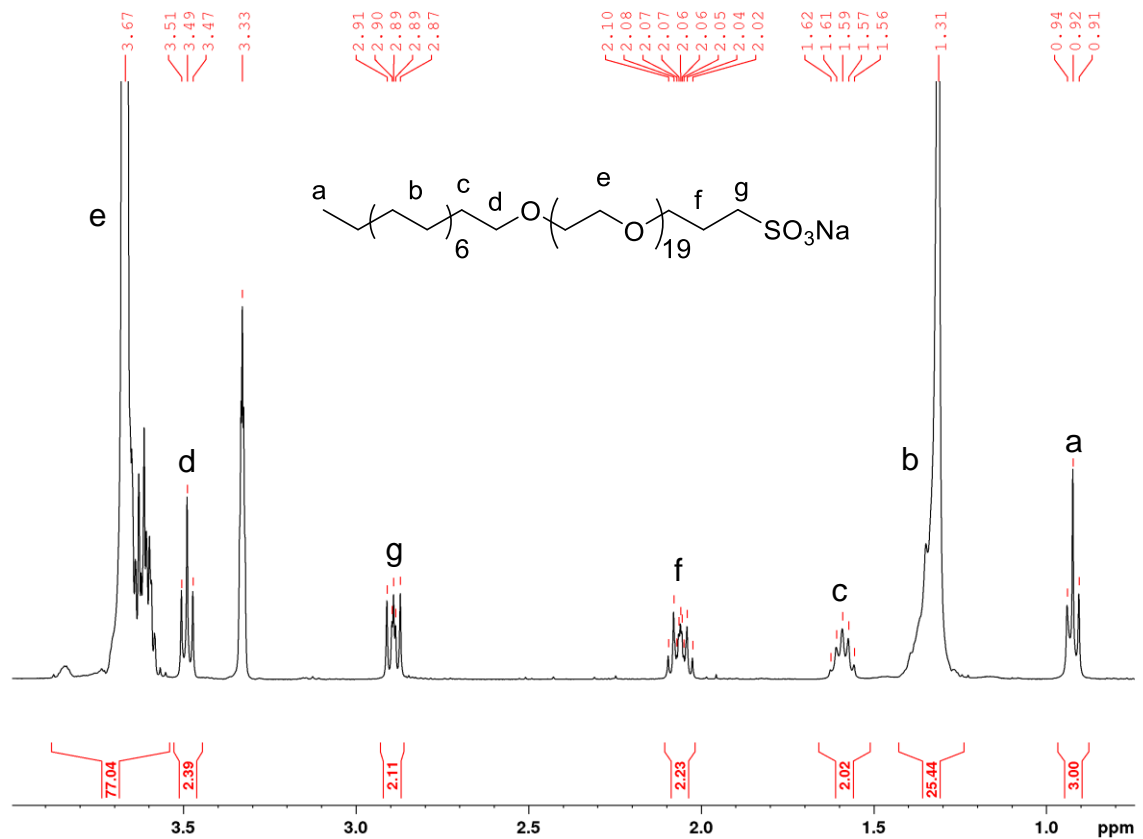


Figure A4.2. ^1H NMR spectrum of sulfonate $\text{C}_{16}\text{E}_{20}$ ($\text{C}_{16}\text{E}_{19}\text{-S}$) in $\text{CD}_4\text{OD-}d_4$. The peaks of the spectrum are assigned to the protons in the structure using alphabets. The proton integrals are calibrated such that the number of methyl protons (a) are 3. Integral of the methylene protons (f and g) is approximately 2 indicating complete modification of the $-\text{OH}$ endgroup of $\text{C}_{16}\text{E}_{20}$. The number of EO units are calculated using the integral of peak e .

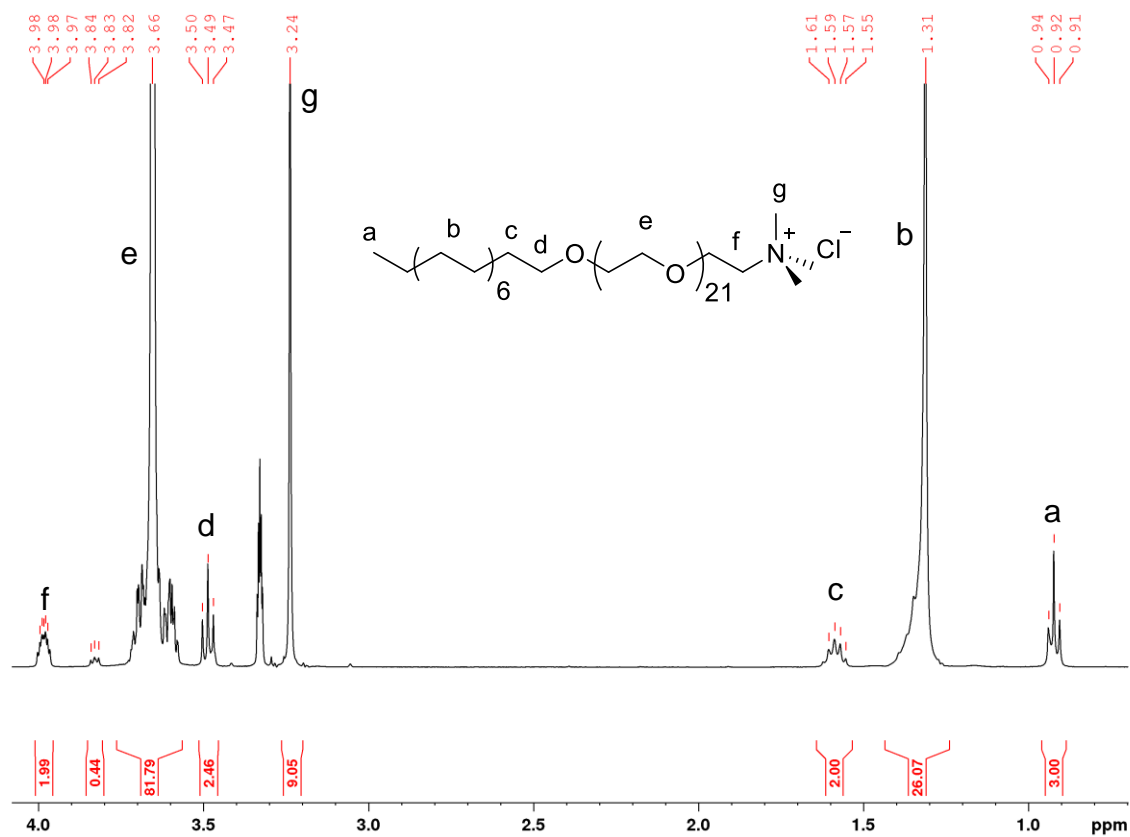


Figure A4.3. ^1H NMR spectrum of $\text{C}_{16}\text{E}_{21}\text{-N}$ in $\text{CD}_4\text{OD-}d_4$. The number of methyl protons at 0.92 ppm (*a*) is calibrated to 3 to reference the other protons. Substitution of the ammonium groups is indicated by the multiplet at 3.98 ppm (*f*) and the singlet corresponding to the methyl protons attached to N at 3.24 ppm (*g*). The extent of ion-exchange was assessed by disappearance of the tosylate peak at $\delta = 7.80$ ppm

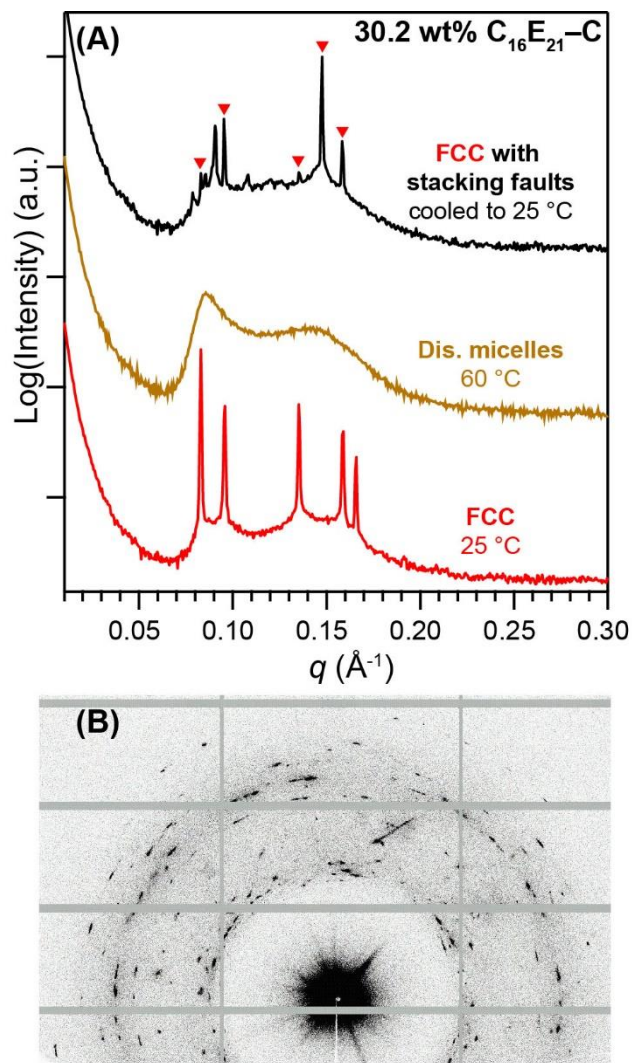


Figure A4.4. (A) 1D SAXS traces obtained from LLCs containing 30.2 wt% $C_{16}E_{21}-C$ showing the transition of an FCC arrangement of micelles to an isotropic micellar solution upon heating from 25 to 60 °C. (B) 2D SAXS pattern obtained on cooling the micellar solution from above the ODT temperature to 25 °C yields a FCC structure riddled with stacking faults, which manifest as Bragg rods.

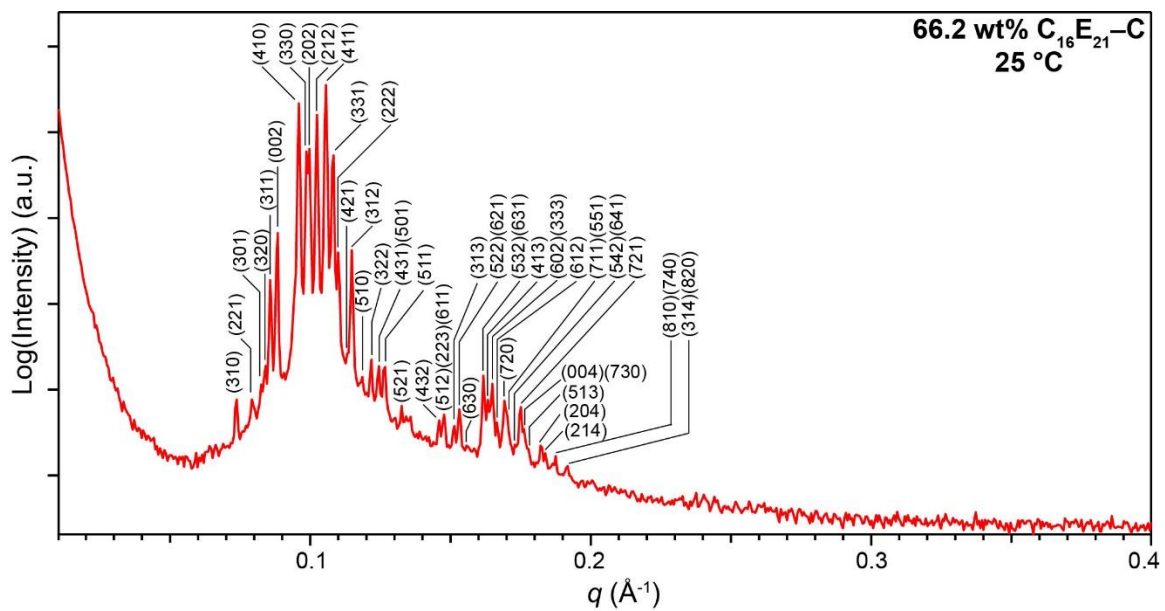


Figure A4.5. Enlarged and fully indexed pattern of a σ phase formed by LLCs containing 66.2 wt% C₁₆E₂₁-C shown in Figure 5.2A. Complete peak assignments and residuals are presented in Table A4.1.

Table A4.1. List of observed and calculated peaks positions obtained for the σ phase formed by LLCs containing 66.2 wt% $\text{C}_{16}\text{E}_{21}\text{-C}$ at 25 °C using the tetragonal space group $P4_2/mmm$ and unit cell parameters $a = 142.1 \text{ \AA}$ and $c = 271.2 \text{ \AA}$.

The scattering wavevector for a tetragonal lattice is given by:

$$q^2 = (2\pi)^2 \left(\frac{h^2 + k^2}{a^2} + \frac{l^2}{c^2} \right)$$

Miller indices			$q_{\text{calc}} (\text{\AA}^{-1})$	$q_{\text{obs}} (\text{\AA}^{-1})$	%Residual $\Delta q/q_{\text{calc}} \times 100$
(h	k	l)			
1	1	0	0.0329	-	-
2	0	0	0.0465	-	-
1	0	1	0.0499	-	-
2	1	0	0.0520	-	-
1	1	1	0.0551	-	-
2	2	0	0.0656	-	-
2	1	1	0.0682	-	-
3	1	0	0.0735	0.0738	0.38
2	2	1	0.0792	0.0792	-0.04
3	0	1	0.0826	0.0825	-0.09
3	2	0	0.0838	0.0841	0.33
3	1	1	0.0858	0.0857	-0.10
0	0	2	0.0884	0.0884	0.00
4	0	0	0.0930	-	-
1	1	2	0.0943	-	-
3	2	1	0.0948	-	-
4	1	0	0.0959	0.0959	0.04
3	3	0	0.0986	0.0986	-0.04
2	0	2	0.0999	0.0997	-0.18
2	1	2	0.1026	0.1024	-0.15
4	1	1	0.1056	0.1056	0.04
3	3	1	0.1081	0.1083	0.20
2	2	2	0.1102	0.1099	-0.25
4	2	1	0.1130	0.1132	0.20
3	1	2	0.1150	0.1148	-0.15
5	1	0	0.1185	0.1186	0.04
3	2	2	0.1218	0.1218	-0.02
4	3	1	0.1244	0.1245	0.11

5	0	1	0.1244	0.1245	0.11
5	1	1	0.1265	0.1267	0.14
5	2	1	0.1328	0.1326	-0.13
4	3	2	0.1460	0.1460	-0.03
5	1	2	0.1479	0.1477	-0.12
2	2	3	0.1480	0.1477	-0.21
6	1	1	0.1482	0.1477	-0.32
3	1	3	0.1516	0.1514	-0.14
5	2	2	0.1533	0.1531	-0.11
6	2	1	0.1535	0.1531	-0.29
5	4	1	0.1553	-	-
6	3	0	0.1560	0.1557	-0.17
5	3	2	0.1618	0.1617	-0.09
6	3	1	0.1621	0.1617	-0.25
4	1	3	0.1636	0.1633	-0.20
7	1	0	0.1644	-	-
5	5	0	0.1644	-	-
6	0	2	0.1651	0.1649	-0.15
3	3	3	0.1653	0.1649	-0.22
6	1	2	0.1668	0.1665	-0.17
7	2	0	0.1693	0.1692	-0.03
7	1	1	0.1702	0.1703	0.04
5	5	1	0.1702	0.1703	0.04
6	2	2	0.1716	-	-
5	4	2	0.1731	0.173	-0.08
6	4	1	0.1734	0.173	-0.22
7	2	1	0.1749	0.1751	0.10
0	0	4	0.1768	0.1762	-0.34
7	3	0	0.1771	-	-
5	1	3	0.1779	0.1778	-0.04
2	0	4	0.1828	0.1821	-0.39
2	1	4	0.1843	0.1838	-0.26
8	1	0	0.1874	0.1875	0.03
7	4	0	0.1874	0.1875	0.03
3	1	4	0.1915	0.1918	0.17
8	2	0	0.1917	0.1918	0.04

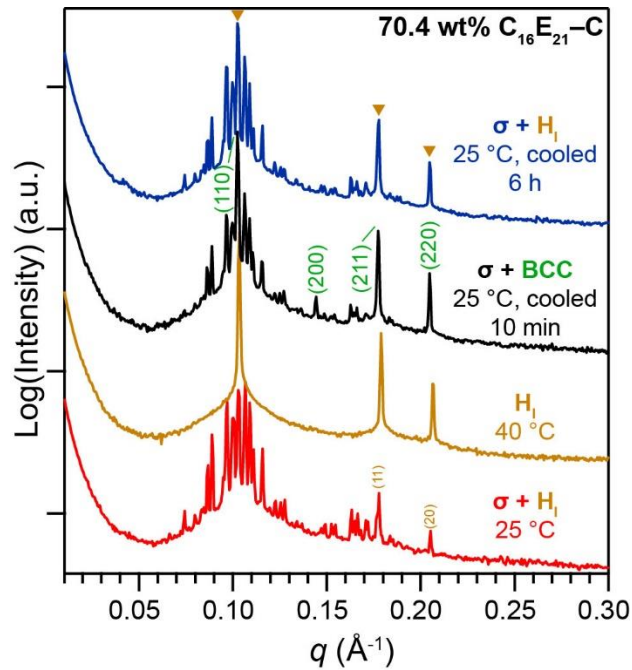


Figure A4.6. Azimuthally integrated scattering patterns obtained for an LLC containing 70.4 wt% C₁₆E₂₁-C. Coexisting σ and H_I phase formed at 25 °C transitions to pure H_I at $T = 40$ °C. Cooling the cylindrical morphology to 25 °C leads to reformation of the σ phase, which coexists with a BCC structure. SAXS maxima consistent with a BCC lattice are marked with the corresponding miller index. The sample relaxes over 6 h at 25 °C to form the initial H_I + σ morphology as evidenced by the disappearance of the (200) peak. Inverted triangles mark the peaks commensurate with the H_I phase.

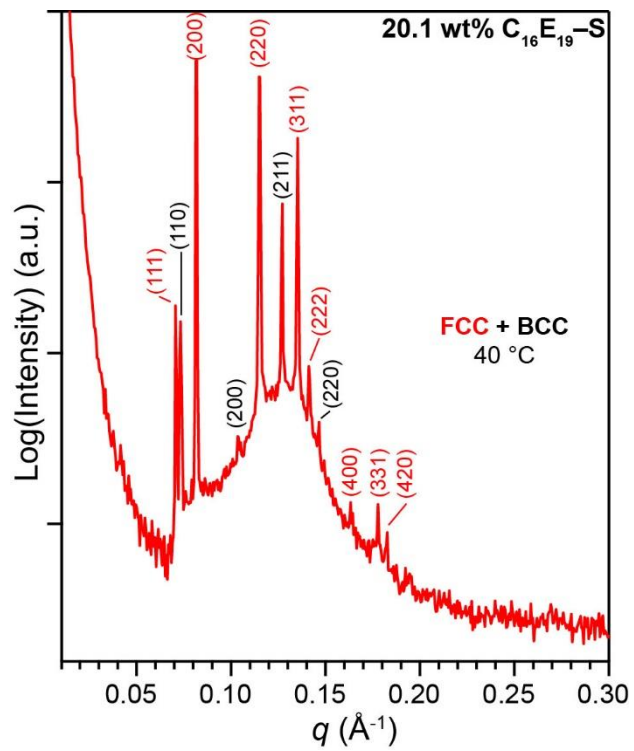


Figure A4.7. LLCs containing 20.1 wt% C₁₆E₁₉-S exhibiting coexisting FCC and BCC phases. The miller indices corresponding to the two phases are marked on the plot.

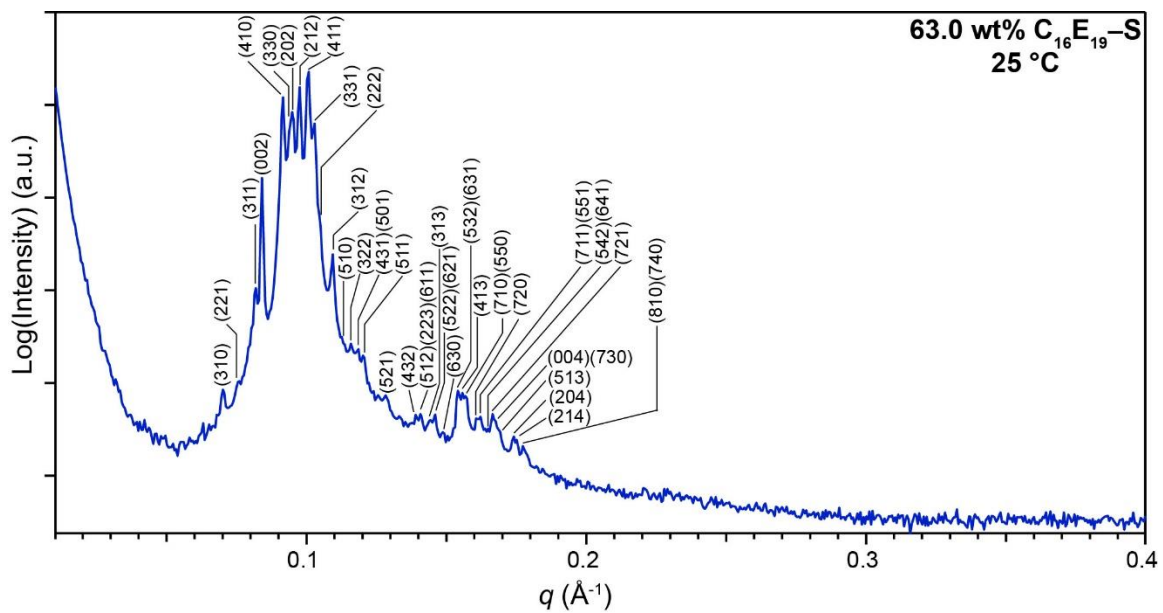


Figure A4.8. Fully indexed σ phase SAXS pattern obtained from LLC containing 63.0 wt% $C_{16}E_{19}-S$. The sample was cooled from 100 to 25 °C and annealed at 25 °C for 9 h before data acquisition. The list of miller indices and residuals are given in Table A4.2.

Table A4.2. List of observed and calculated peaks positions obtained for the σ phase formed by LLCs containing 63.0 wt% $\text{C}_{16}\text{E}_{19}\text{-S}$ at 25 °C using the tetragonal space group $P4_2/mmm$ and unit cell parameters $a = 149.4 \text{ \AA}$ and $c = 283.5 \text{ \AA}$. The sample was cooled from 100 to 25 °C and annealed for 9 h at 25 °C before data acquisition.

The scattering wavevector for a tetragonal lattice is given by:

$$q^2 = (2\pi)^2 \left(\frac{h^2 + k^2}{a^2} + \frac{l^2}{c^2} \right)$$

Miller indices			$q_{\text{calc}} (\text{\AA}^{-1})$	$q_{\text{obs}} (\text{\AA}^{-1})$	%Residual $\Delta q/q_{\text{calc}} \times 100$
(h	k	l)			
1	1	0	0.0329	-	-
2	0	0	0.0465	-	-
1	0	1	0.0499	-	-
2	1	0	0.0520	-	-
1	1	1	0.0551	-	-
2	2	0	0.0656	-	-
2	1	1	0.0682	-	-
3	1	0	0.0701	0.0706	0.74
2	2	1	0.0755	0.076	0.69
3	0	1	0.0787	-	-
3	2	0	0.0799	-	-
3	1	1	0.0817	0.0819	0.21
0	0	2	0.0841	0.0841	0.00
4	0	0	0.0886	-	-
1	1	2	0.0897	-	-
3	2	1	0.0903	-	-
4	1	0	0.0914	0.0916	0.25
3	3	0	0.0940	0.0938	-0.23
2	0	2	0.0951	0.0949	-0.17
2	1	2	0.0976	0.0976	-0.01
4	1	1	0.1006	0.1008	0.22
3	3	1	0.1030	0.1029	-0.09
2	2	2	0.1049	0.1046	-0.28
4	2	1	0.1077	-	-
3	1	2	0.1095	0.1094	-0.06
5	1	0	0.1130	0.1126	-0.35
3	2	2	0.1160	0.1159	-0.09

4	3	1	0.1185	0.1186	0.07
5	0	1	0.1185	0.1186	
5	1	1	0.1206	0.1202	-0.31
5	2	1	0.1265	0.1267	0.14
4	3	2	0.1391	0.1385	-0.44
5	1	2	0.1409	0.1407	-0.11
2	2	3	0.1409	0.1407	-0.12
6	1	1	0.1412	0.1407	-0.36
3	1	3	0.1443	0.1439	-0.28
5	2	2	0.1460	0.1460	0.00
6	2	1	0.1463	0.1460	-0.22
5	4	1	0.1480	-	-
6	3	0	0.1487	0.1487	0.03
5	3	2	0.1542	0.1541	-0.05
6	3	1	0.1545	0.1541	-0.25
4	1	3	0.1558	0.1557	-0.04
7	1	0	0.1567	0.1568	0.07
5	5	0	0.1567	0.1568	0.07
6	0	2	0.1573	-	-
3	3	3	0.1573	-	-
6	1	2	0.1589	-	-
7	2	0	0.1613	0.1611	-0.14
7	1	1	0.1622	0.1622	-0.03
5	5	1	0.1622	0.1622	-0.03
6	2	2	0.1635	-	-
5	4	2	0.1649	0.1649	-0.03
6	4	1	0.1652	0.1649	-0.21
7	2	1	0.1667	0.1665	-0.13
0	0	4	0.1682	0.1676	-0.36
7	3	0	0.1688	0.1676	-0.70
5	1	3	0.1694	0.1692	-0.09
2	0	4	0.1739	0.1735	-0.25
2	1	4	0.1753	0.1751	-0.14
8	1	0	0.1787	0.1773	-0.77
7	4	0	0.1787	0.1773	-0.77
3	1	4	0.1822	-	-
8	2	0	0.1827	-	-

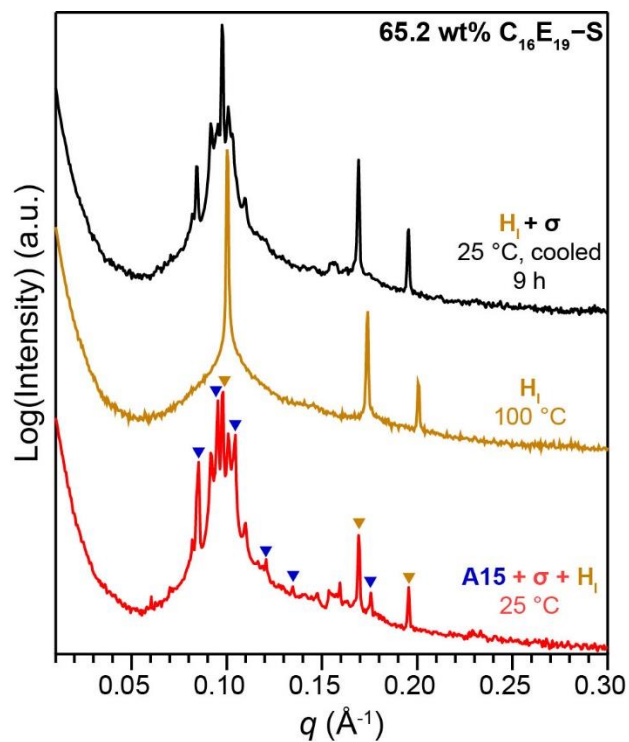


Figure A4.9. SAXS patterns obtained for LLCs containing 65.2 wt% C₁₆E₁₉-S as a function of temperature. The sample initially exhibits a non-equilibrium coexistence of A15, H₁, and σ phases at 25 °C. The peaks corresponding to A15 and H₁ morphologies are indicated using blue and yellow markers respectively. Cooling the sample from the H₁ structure at 100 °C to 25 °C leads to a transition to coexisting σ and H₁ phases indicating the metastability of the A15 structure.

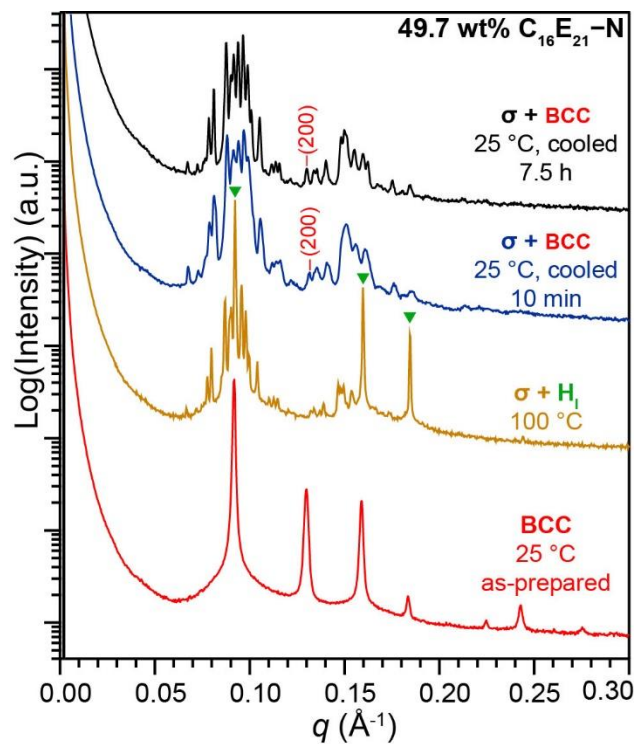


Figure A4.10. Small-angle X-ray scattering traces obtained for aqueous dispersions containing 49.7 wt% C₁₆E₂₁-N. The LLC exhibits the formation of a BCC phase at 25 °C, which upon heated to 100 °C transforms into coexisting σ + H_I phases. The peaks corresponding to the H_I phase are marked using green triangles. Cooling the sample back to 25 °C leads to retention of the σ phase while the H_I phase transitions to a BCC structure, as evidenced by the appearance of the (200) peak.

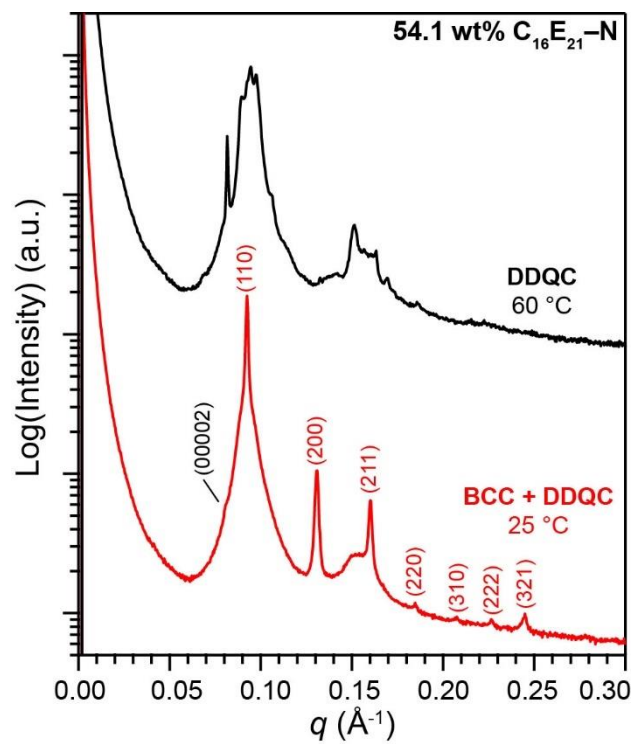


Figure A4.11. Azimuthally-integrated scattering traces obtained from LLCs containing 54.1 wt% $C_{16}E_{21}-N$. At 25 °C, the sample coexists as BCC/DDQC phases, and transitions to a pure DDQC at 60 °C.

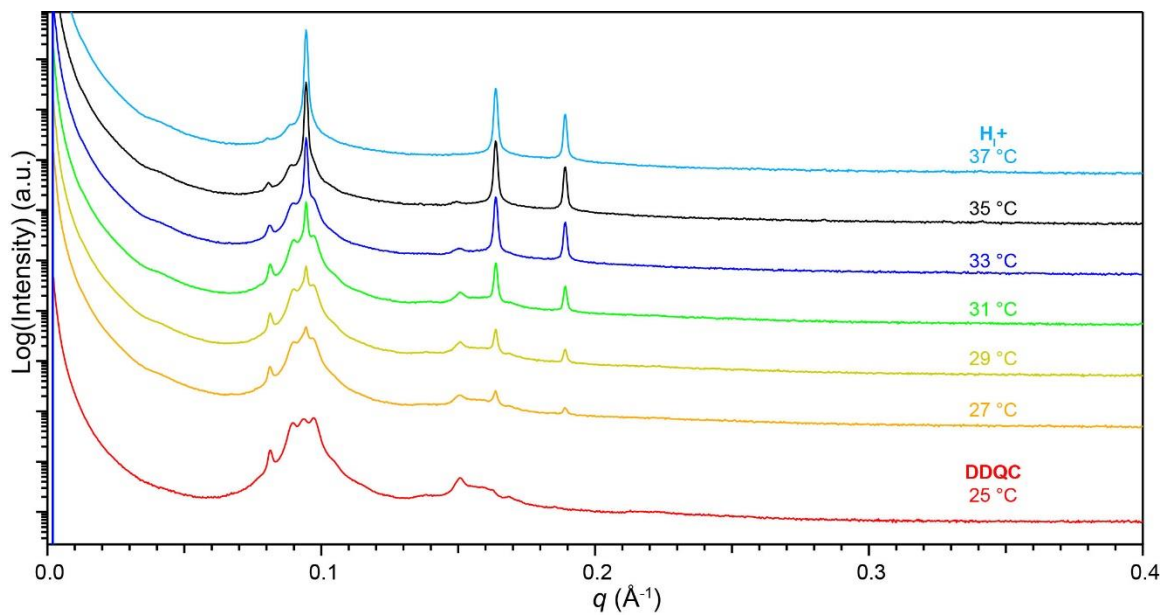


Figure A4.12. SAXS patterns obtained from sample containing 60.0 wt% C₁₆E₂₁-N as a function of temperature. The sample was equilibrated at each temperature for 5 mins before data acquisition. The sample exhibits a direct DDQC→H₁ transition when heated to 37 °C without the observation of a σ phase.

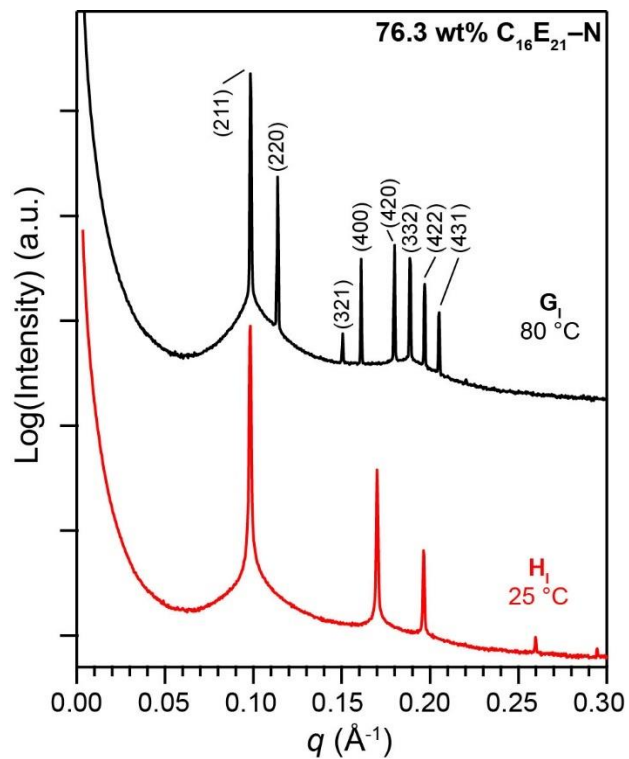


Figure A4.13. 1D SAXS patterns obtained from LLCs containing 76.3 wt% C₁₆E₂₁-N exhibiting the formation of H_I and G_I phases at 25 and 80 °C respectively. The miller indices corresponding to the G_I morphology are marked on the plot

Table A4.3. List of observed and calculated peak positions and residuals for a dodecagonal quasicrystal formed by an LLC with $[\text{C}_{16}\text{E}_{21}\text{-N}] = 60.0$ wt% at 25 °C. The miller indices correspond to the 5D space group $P12_6/mmc$ (or $P12_6/mcm$) for the quasicrystal. The intermicellar distance in the quasiperiodic plane of the DDQC is $a = 15.1$ nm with an interlayer stacking distance of $c = 15.4$ nm ($c/a = 1.02$).

The scattering wavevector positions are calculated using the following formulae:

$$\mathbf{q} = \sum_{n=1}^5 h_n \mathbf{a}_n$$

$$\mathbf{a}_n = \frac{1}{\sqrt{3}a} \left\{ i \cos \frac{(n-1)\pi}{6} + j \sin \frac{(n-1)\pi}{6} \right\} \quad \forall n \in \{1,2,3,4\}$$

$$\mathbf{a}_5 = \frac{\mathbf{k}}{c}$$

$$q_{\text{obs}} = |\mathbf{q}|$$

Miller indices					%Residual		
h_1	h_2	h_3	h_4	h_5	$q_{\text{calc}}(\text{\AA}^{-1})$	$q_{\text{obs}}(\text{\AA}^{-1})$	$\Delta q/q_{\text{calc}} \times 100$
0	0	0	0	2	0.0813	0.0813	-0.004
1	2	1	0	0	0.0894	0.0896	0.312
0	1	1	0	2	0.0936	0.0938	0.264
2	2	0	-1	1	0.0982	0.0970	-1.194
1	1	1	0	2	0.1044	0.1040	-0.304
3	3	0	-2	0	0.1346	0.1367	1.58
2	3	1	-1	2	0.1503	0.1508	0.339
3	4	0	-2	1	0.1600	0.1588	-0.776
0	0	0	0	4	0.1626	0.1623	-0.203
0	1	1	0	4	0.1691	0.1684	-0.408

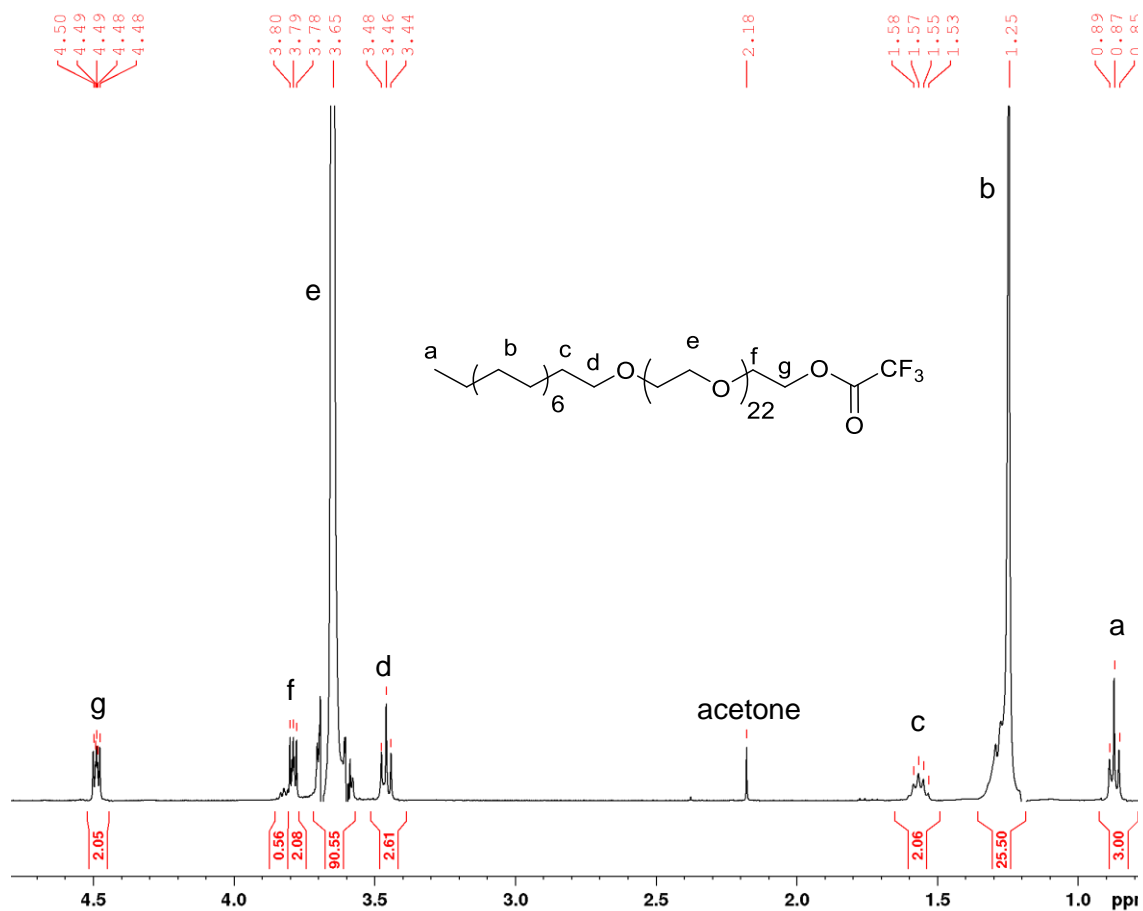


Figure A4.14. ^1H NMR spectrum obtained from precipitated $\text{C}_{16}\text{E}_{20}$ in CDCl_3 in the presence of trifluoroacetic acid. The integrals of the spectrum are calibrated such that number of methyl protons (a) is 3. The total number of EO units is obtained by summation of e, f and g protons. A peak from residual acetone in the NMR tube is observed at $\delta = 2.18$ ppm.

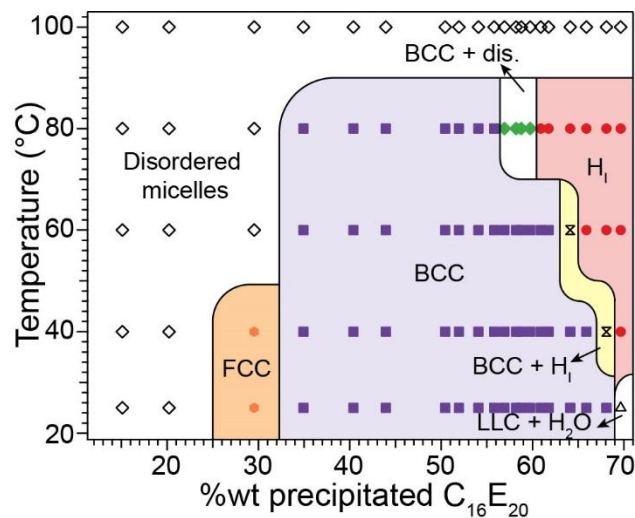


Figure A4.15. Temperature *versus* wt% diagram generated by SAXS analyses of LLCs containing $C_{16}E_{20}$ that was precipitated from hexanes twice. Only the canonical FCC, BCC and H_1 phases are observed with no evidence of any FK phases.

Table A4.4. List of laboratory notebook page numbers and synchrotron trips corresponding to molecules shown in Chapter 4.

Molecules	Notebook page number	APS trips
$C_{16}E_{21}-C$	AJ2-129	October 2018
$C_{16}E_{19}-S$	AJ2-93	October 2018
$C_{16}E_{21}-N$	AJ2-120	Dec.2018, March 2019
Precipitated $C_{16}E_{20}$	AJ2-137	March, Aug. 2019